

REVIEW ARTICLE | JULY 02 2024

Entanglement-enhanced quantum metrology: From standard quantum limit to Heisenberg limit

Jiahao Huang  ; Min Zhuang  ; Chaohong Lee  



Appl. Phys. Rev. 11, 031302 (2024)
<https://doi.org/10.1063/5.0204102>



Articles You May Be Interested In

Nonclassical light and metrological power: An introductory review

AVS Quantum Sci. (November 2019)

Quantum dense metrology by an SU(2)-in-SU(1,1) nested interferometer

Appl. Phys. Lett. (July 2020)

Quantum metrology with rotating matter waves in different geometries

AIP Conference Proceedings (September 2012)



MCL
MAD CITY LABS INC.

Closed Loop Nanopositioning Systems with Picometer precision, Low noise and High stability

Force Microscopy and Single Molecule Microscopy Instruments for Quantum, Materials, and Bioscience

Custom Design and Innovative Solutions for the Nanoscale World

Think Nano® | Positioning | Microscopy | Solutions



Entanglement-enhanced quantum metrology: From standard quantum limit to Heisenberg limit

Cite as: Appl. Phys. Rev. 11, 031302 (2024); doi: 10.1063/5.0204102

Submitted: 19 February 2024 · Accepted: 3 June 2024 ·

Published Online: 2 July 2024



Jiahao Huang,^{1,2} Min Zhuang,^{1,3} and Chaohong Lee^{1,3,a)}

AFFILIATIONS

¹Institute of Quantum Precision Measurement, State Key Laboratory of Radio Frequency Heterogeneous Integration, College of Physics and Optoelectronic Engineering, Shenzhen University, Shenzhen 518060, China

²Laboratory of Quantum Engineering and Quantum Metrology, School of Physics and Astronomy, Sun Yat-Sen University (Zhuhai Campus), Zhuhai 519082, China

³Quantum Science Center of Guangdong-Hong Kong-Macao Greater Bay Area (Guangdong), Shenzhen 518045, China

^{a)}Author to whom correspondence should be addressed: chleecn@szu.edu.cn

ABSTRACT

Entanglement-enhanced quantum metrology explores the utilization of quantum entanglement to enhance measurement precision. When particles in a probe are prepared into a suitable quantum entangled state, they may collectively accumulate information about the physical quantity to be measured, leading to an improvement in measurement precision beyond the standard quantum limit and approaching the Heisenberg limit. The rapid advancement of techniques for quantum manipulation and detection has enabled the generation, manipulation, and detection of multi-particle entangled states in synthetic quantum systems such as cold atoms and trapped ions. This article aims to review and illustrate the fundamental principles and experimental progresses that demonstrate multi-particle entanglement for quantum metrology, as well as discuss the potential applications of entanglement-enhanced quantum sensors.

© 2024 Author(s). All article content, except where otherwise noted, is licensed under a Creative Commons Attribution-NonCommercial 4.0 International (CC BY-NC) license (<https://creativecommons.org/licenses/by-nc/4.0/>). <https://doi.org/10.1063/5.0204102>

TABLE OF CONTENTS

I. INTRODUCTION.....	2	3. One-axis twisting	11
II. FUNDAMENTALS OF QUANTUM PARAMETER ESTIMATION THEORY	3	4. Two-axis counterclockwise	12
A. General procedure of quantum parameter estimation	3	5. Preparing spin-squeezed states via OAT.....	13
B. Fisher information and Cramér–Rao bound.....	5	6. Preparing spin-squeezed states beyond OAT ..	19
C. Quantum Fisher information and quantum Cramér–Rao bound.....	6	C. Twin-Fock state.....	21
D. Standard quantum limit and Heisenberg limit	6	D. Spin cat states	23
E. Strategies of quantum metrology	7	IV. INTERROGATION AND READOUT	26
III. METROLOGICALLY USEFUL ENTANGLED STATES AND THEIR PREPARATION.....	8	A. Interrogation	26
A. Metrologically useful entanglement	8	B. Conventional readout	28
B. Spin-squeezed states	9	C. Interaction-based readout	28
1. Bosonic squeezing.....	9	V. PROMISING APPLICATIONS IN QUANTUM SENSORS	33
2. Spin squeezing.....	10	A. Atomic clocks	33
		B. Magnetometers.....	36
		C. Gravimeters	39
		D. Gyroscopes.....	40
		VI. SUMMARY AND OUTLOOKS.....	41

I. INTRODUCTION

Quantum metrology is a field that harnesses quantum principles for measurement purpose, with the objective of attaining high measurement precision using quantum resources. It has emerged as an interdisciplinary science that employs fundamental principles of quantum mechanics to measure physical quantities^{1–19} and surpass the limitations of traditional measurement schemes.^{1,2,4–6,9,10,16} The precise measurement plays a critical role in advancing physics,²⁰ encompassing tasks such as testing fundamental physical principles,^{21–27} determining fundamental physical constants,^{27–30} detecting gravitational waves,^{21,31–37} and searching for dark matter.^{25,36–44} Moreover, it spurs innovation and advancements in various scientific disciplines and technologies,⁴⁵ including inertial navigation,^{46–51} groundwater monitoring,⁵² mineral exploration,⁵² and more.

Quantum parameter estimation is a fundamental aspect of quantum metrology. It involves determining unknown parameters, such as transition frequency,^{28,58–70} magnetic field,^{66,71–88} and acceleration,^{49–51,89–91} based on the combination of estimation theory and quantum mechanics. Quantum interferometry^{92–94} is the most commonly employed method for implementing high-precision parameter estimation. This approach typically involves initially preparing a quantum probe into a desired initial state, allowing the quantum probe to evolve to accumulate a phase relevant to the physical quantity to be measured, and ultimately extracting the quantity information through quantum interference and observable measurement. Choosing quantum probes of remarkable sensitivity to external fields, we can construct high-precision quantum sensors for practical purpose. By utilizing versatile quantum control techniques,^{66,72,82,95–102} high-precision measurements of numerous physical quantities have been achieved in experiments.^{14,103}

Entanglement-enhanced quantum metrology is a specialized area within quantum metrology that explores how quantum entanglement can be utilized to further enhance measurement precision. Quantum entanglement is a phenomenon where two or more particles become correlated in such a way that the state of one particle cannot be described independently of the others.^{16,104,105} This unique characteristic of quantum mechanics holds immense value as a resource that lacks classical equivalents. By combining advanced quantum interferometry techniques with quantum entanglement, it becomes possible to significantly improve measurement precision. In entanglement-enhanced quantum metrology, quantum entangled states are created and manipulated to extract more information about the parameter to be measured, thus enabling measurements with higher precision.

In conventional measurement schemes involving an ensemble of individual particles or multiple independent measurements of a single particle, the measurement precision is limited by the standard quantum limit (SQL).^{4,5,10} In statistics, the fluctuations of a measured quantity can be reduced by conducting repeated measurements and averaging them, resulting in improved precision. Using a linear generator, according to the central limit theorem, the corresponding measurement precision scales as $\Delta\theta \propto N^{-1/2}$, where $\Delta\theta$ represents the standard deviation of an estimated quantity θ and N denotes the times of repeated measurements or the number of individual particles (without entanglement) measured simultaneously as an ensemble. This precision scaling is commonly known as the shot-noise limit, also referred to as the SQL.

By employing entanglement among particles, all particles collectively accumulate the information about the physical quantity to be measured and the measurement precision may surpass the SQL.^{4,5,10}

It has been demonstrated that the SQL can be surpassed by using quantum entangled states, such as spin-squeezed states,^{106–116} twin-Fock states,^{105,117–120} spin cat states,^{74,121,122} and as input states. Notably, for an N -particle quantum probe, the utilization of a maximally entangled state¹²³ [such as Greenberger–Horne–Zeilinger (GHZ) state^{59,119,124,125}] as an input state may enhance the measurement precision to the Heisenberg limit (HL) with a scaling of N^{-1} for a linear generator.^{4,5,10} In the case of a linear generator, the HL surpasses the corresponding SQL by a factor of \sqrt{N} , leading to a \sqrt{N} -fold improvement in measurement precision.

To realize entanglement-enhanced quantum metrology, the preparation of multi-particle entangled states is a crucial step. In recent decades, rapid progresses in preparing, manipulating, and detecting multi-particle entangled states have propelled entanglement-enhanced quantum metrology into a distinct and rapidly expanding field in quantum technology.^{126,127} Numerous groundbreaking experimental breakthroughs have emerged, focusing on leveraging multi-particle entangled states to improve measurement precision from the SQL to the Heisenberg limit. These advancements encompass diverse types of entangled states, ranging from spin-squeezed states to non-Gaussian entangled states, and utilize common platforms such as cold atoms in cavities,^{120,128–130} Bose condensed atoms,^{86,112,115,116,118,127,131–134} and ultracold trapped ions.^{118,127,135–137} The successful generation of various multi-particle entangled states has laid a robust foundation for achieving entanglement-enhanced metrology.

To fully harness their potentials in quantum metrology, one has to choose appropriate methods for detecting entangled states. Conventional measurement techniques may be inadequate for precisely extracting estimated information from highly entangled states, especially in the presence of noise.^{12,18,138–144} Low-detection efficiency for large particle numbers constitutes one of the primary limitations to realizing entanglement-enhanced metrology in practice, as it obscures signals and decreases measurement precision.^{145,146} By utilizing novel readout methods such as nonlinear detection,^{8,105,111,147–154} the signal can be amplified to enable precise measurements that are robust against disruption from detection noise. Owing to rapid advances in generating, manipulating, and measuring entanglement, this field is now progressing from initial proof-of-concept experiments toward developing practical entanglement-enhanced sensing technologies.

The applications of entanglement-enhanced quantum metrology are extensive and diverse. The ultimate goal of quantum metrology is to advance the technology of quantum sensing for practical use in various fields. It aims to scrutinize the fundamental laws of physics with increased accuracy, reveal new phenomena in physics, determine physical quantities with enhanced precision, and construct practical quantum sensing devices. The research in this field not only facilitates the manipulation and detection of quantum entanglement but also opens up new opportunities in applied physics, such as the development of next-generation entanglement-enhanced quantum sensors. These sensors offer high precision and sensitivity and can include atomic clocks,^{45,64,155–165} atomic magnetometers,^{86,147,166–171} quantum gravimeters,^{47,49,51,89,90,172} quantum gyroscopes,^{173,174} and other similar devices. They can be utilized for tasks such as maintaining communication and energy network synchronization, real-time imaging of brain signals, collecting precise meteorological data for improved climate modeling, and monitoring underground water levels and volcanic eruptions.¹⁰³ Furthermore, the integration of quantum control with

quantum entanglement is expected to significantly advance the progress of entanglement-enhanced sensing technologies.

This review aims to provide a comprehensive understanding of entanglement-enhanced quantum metrology, covering its fundamental principles, experimental realization, and wide range of potential applications. In Sec. II, we introduce the fundamental concepts necessary for grasping quantum parameter estimation and precision bounds. This section is particularly valuable for readers who are new to quantum metrology and sensing. In Sec. III, we explore commonly employed entangled states that are beneficial for quantum metrology and discuss their preparation in various quantum systems, such as Bose-Einstein condensates (BECs), cold atoms in cavities, trapped ions, Rydberg tweezer arrays, and superconductors. The methods commonly used for entanglement generation include one-axis twisting, twist-and-turn dynamics, spin-mixing dynamics, and crossing through quantum phase transitions (QPTs). In Sec. IV, we delve into the techniques for effective and efficient quantum parameter estimation, focusing on interrogation and readout methods, with a special emphasis on nonlinear detection and interaction-based readout. In Sec. V, we discuss the potential applications of entanglement-enhanced quantum sensors, including atomic clocks, magnetometers, gravimeters, and gyroscopes. Finally, in Sec. VI, we provide a summary and outlook for this rapidly advancing field.

II. FUNDAMENTALS OF QUANTUM PARAMETER ESTIMATION THEORY

Quantum parameter estimation focuses on conducting measurements on a specific physical quantity and evaluating the resulting measurement precision.^{4,5,9,16} Examples of quantum parameter estimation include magnetic-field estimation,^{74,86} frequency estimation,^{62,175,176} weak force estimation,¹⁰² and so on. In a realistic measurement, the estimated parameter often relates to a phase shift, which can be measured using interferometric techniques.⁹⁴ This section primarily focuses on single-parameter estimation scenarios. We provide an overview of fundamental concepts in quantum parameter estimation, such as the general procedure,^{177–179} the Fisher information,¹⁸⁰ the Cramér-Rao bound,^{180,181} and the precision bounds represented by the standard quantum limit^{3,4,182} and the Heisenberg limit.^{3,4,182} Additionally, we illustrate different strategies of quantum metrology,⁹ emphasizing the importance of quantum entanglement in the preparation stage.

A. General procedure of quantum parameter estimation

A quantum parameter estimation process aims to measure an unknown physical parameter (denoted as θ in our review), which

could represent a field, a frequency, a force, or any other physical quantity. By leveraging the interaction between a probe and the system, it becomes possible to encode parameter-dependent information into the probe state. The fundamental procedure of quantum parameter estimation includes the following four steps (as shown in Fig. 1): (i) Preparation of a probe state ρ_0 , which is sensitive to variations in the unknown parameter θ . (ii) The probe undergoes a unitary dynamical evolution \hat{U}_θ that depends on θ . After the dynamical evolution, the state of the probe becomes $\rho_\theta = \hat{U}_\theta \rho_0 \hat{U}_\theta^\dagger$, which contains information about the unknown parameter θ . (iii) The information about θ is extracted by performing a practical measurement \hat{E} on the final state. (iv) Finally, a parameter estimation θ_{est} is derived from the obtained measurement results. Here, for simplicity, we concentrate our discussion on unitary evolution and unbiased estimators, although it can be extended to non-unitary evolution and biased estimators. Therefore, as a result of unbiased estimators, the statistical average may precisely give the true parameter value: $\theta_{\text{est}} = \theta$. To evaluate the performance of an unbiased estimation, one may analyze the measurement precision of the estimated parameter θ , which is characterized by the standard deviation $\Delta\theta = \sqrt{\langle\theta^2\rangle - \langle\theta\rangle^2}$.

Parameter estimation is commonly achieved by associating the physical parameter with a phase shift, which can be obtained through interferometry.⁹⁴ Optical interferometry involves the coherent combination of two or more light beams, resulting in interference patterns that enable the determination of their relative phase. Quantum interferometry surpasses traditional interferometry by utilizing the wave nature of particles to achieve more precise measurements, thus enhancing measurement precision compared to conventional interferometry.⁹³ In this context, we provide an introduction to two common types of quantum interferometry: SU(2) quantum interferometry and SU(1,1) quantum interferometry.^{2,139,183–190}

SU(2) quantum interferometry operates with quantum systems of SU(2) symmetry. Considering a system of N two-mode particles with the two modes labeled as $|a\rangle$ and $|b\rangle$, the system can be well described by a collective spin with length $J = \frac{N}{2}$. The collective spin operators $\hat{J}_\alpha = \frac{1}{2} \sum_{l=1}^N \sigma_\alpha^{(l)}$ with $\alpha = \{x, y, z\}$ satisfy the angular momentum commutation relations $[\hat{J}_\alpha, \hat{J}_\beta] = i\epsilon_{\alpha\beta\gamma}\hat{J}_\gamma$, where $\alpha, \beta, \gamma = \{x, y, z\}$, $\sigma_{\alpha,\beta,\gamma}^{(l)}$ are the Pauli matrices for the l th particle, and $\epsilon_{\alpha\beta\gamma}$ is the Levi-Civita symbol. The conserved quantity of the associated SU(2) group is $\hat{J}^2 = \hat{J}_x^2 + \hat{J}_y^2 + \hat{J}_z^2$, which is related to the total particle number N . The angular momentum commutation relations satisfy the SU(2) Lie algebra and so that this interferometry is called as SU(2)

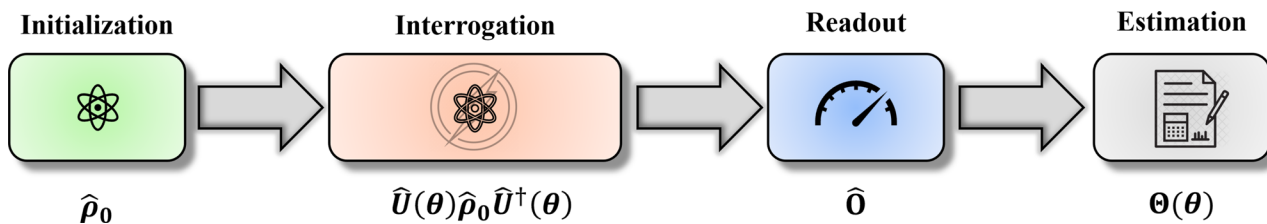


FIG. 1. General procedure of quantum parameter estimation. (i) Initialization: a desired initial probe state is prepared. (ii) Interrogation: the probe undergoes a dynamical evolution dependent on the physical parameter θ to be measured. (iii) Readout: a recombination operation is performed and the final state is readout. (iv) Estimation: the unknown parameter is finally estimated through an estimation procedure.

quantum interferometry. By using the Schwinger representation, the collective spin operators can be written as $\hat{J}_x = \frac{1}{2}(\hat{a}^\dagger \hat{b} + \hat{a} \hat{b}^\dagger)$, $\hat{J}_y = \frac{1}{2i}(\hat{a}^\dagger \hat{b} - \hat{a} \hat{b}^\dagger)$, and $\hat{J}_z = \frac{1}{2}(\hat{a}^\dagger \hat{a} - \hat{b}^\dagger \hat{b})$ with the annihilation operators \hat{a} and \hat{b} for particles in $|a\rangle$ and $|b\rangle$. Therefore, the states can be represented by using the Dicke basis $\{|J, m\rangle\}$ obeying the eigen-equation $\hat{J}_z |J, m\rangle = m |J, m\rangle$ with the half population difference between the two modes $m = \{-J, -J+1, \dots, J-1, J\}$.

A common SU(2) quantum interferometry employs two modes accumulating a relative phase encoded by the parameter to be estimated. The two modes can be either two spatial paths, such as in a SU(2) Mach-Zehnder interferometer,¹⁹¹⁻¹⁹⁴ or two hyperfine levels of an atom, such as in a Ramsey interferometer.^{85,195,196} In a Mach-Zehnder interferometer, the input particle is divided into two parts by a linear balanced beam splitter, and then, the two parts pass through two different spatial paths to accumulate a relative phase between the two parts $\theta = \theta_b - \theta_a$, as shown in Fig. 2(a). Finally, the two parts are recombined for interference via another linear balanced beam splitter to extract the relative phase from the interference fringe. A common Ramsey interferometry consists of two $\pi/2$ pulses and a free evolution process, as shown in Fig. 2(b). In comparison with a Mach-Zehnder interferometry, the two $\pi/2$ pulses act as the two beam splitters and the free evolution process accumulates the relative phase between the two involved levels. For a single two-mode particle initially prepared in the probe state $|a\rangle$, the particle is transformed to $(|a\rangle + |b\rangle)/\sqrt{2}$ by the first balanced beam splitter of the Mach-Zehnder interferometer or the first resonant $\pi/2$ pulse in a Ramsey interferometer. During the interrogation process, $|a\rangle$ and $|b\rangle$ acquire the phases $\theta_a = -\omega T/2$ and $\theta_b = \omega T/2$, respectively, determined by T the evolution time and ω the transition frequency between the two modes. Thus, the evolved state becomes $(e^{-i\theta_a}|a\rangle + e^{-i\theta_b}|b\rangle)/\sqrt{2}$ with a relative phase $\theta = \theta_b - \theta_a = \omega T$. Then, a second beam splitter or the second

resonant $\pi/2$ pulse is applied and the final state reads as $\cos(\theta/2)|a\rangle + \sin(\theta/2)|b\rangle$. Finally, through performing the half population difference measurement $\hat{J}_z = \frac{1}{2}(\hat{a}^\dagger \hat{a} - \hat{b}^\dagger \hat{b})$ on the final state, the relative phase θ can be estimated via θ -dependent expectation values $\langle \hat{J}_z \rangle = \frac{1}{2} \cos \theta$. Thus, one can obtain the unknown parameter θ by an estimator function $\theta_{\text{est}} = \arccos[2\langle \hat{J}_z \rangle]$. Generally, the evolution time T is well-controlled and so that one can infer the transition frequency $\omega = \theta_{\text{est}}/T$ from the estimated relative phase θ_{est} .

In the case of multiple two-mode particles, using the picture of a collective spin, the process of parameter estimation via quantum interferometry is similar to the single-particle case. The whole process can be represented on a generalized Bloch sphere with a radius of the collective spin length $J = \frac{N}{2}$, as shown in Fig. 2(b). First, the initial state $|\Psi_{\text{in}}\rangle$ of N two-mode particles is transformed by a balanced beam splitter, which implements a rotation $e^{i\hat{J}_x}$. Then, the system undergoes a dynamical evolution leading to a relative phase, which can be denoted by $e^{-i\theta \hat{J}_z}$. Finally, the second balanced beam splitter $e^{-i\hat{J}_x}$ is applied and the accumulated relative phase can be extracted from the half population difference \hat{J}_z . Combining the above three transformations, the final state is given as $|\Psi_f(\theta)\rangle = \hat{U} |\Psi_{\text{in}}\rangle$ with $\hat{U} = e^{-i\hat{J}_x} e^{-i\theta \hat{J}_z} e^{i\hat{J}_x}$. Therefore, the information of an unknown relative phase θ is encoded into the final state $|\Psi_f(\theta)\rangle$. The relative phase θ can be estimated by measuring the half population difference $\langle \hat{J}_z \rangle = \sum_{m=-J}^J m P(m|\theta)$ with $P(m|\theta) = |\langle \Psi_f(\theta) | J, m \rangle|^2$ denoting the conditional probability with outcome m given the relative phase θ .

SU(1, 1) quantum interferometry² works with quantum systems of SU(1, 1) symmetry. In contrast to SU(2) quantum interferometry, whose beam splitters are implemented by using linear operations, the beam splitters of SU(1, 1) interferometry are achieved by using nonlinear wave mixing of parametric amplifiers. Similar to a SU(2) quantum interferometry with linear splitters obeying SU(2) commutation

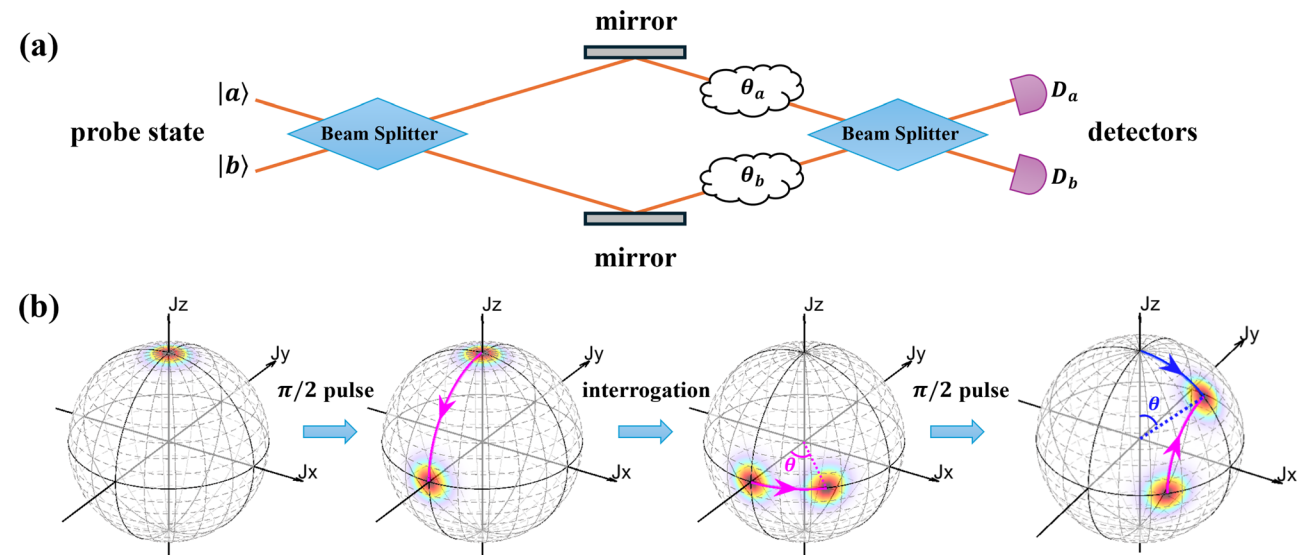


FIG. 2. Two-mode quantum interferometers. (a) two modes $|a\rangle$ and $|b\rangle$ are combined by a balanced beam splitter, followed by a relative phase shift $\theta = \theta_a - \theta_b$ between the two arms, and finally recombined on a second balanced beam splitter. (b) Equivalent representation of two-mode quantum interferometer operations as rotations of the collective spin on the generalized Bloch sphere. The initial state here is pointing toward the north pole.

relation, a $SU(1, 1)$ quantum interferometry contains two nonlinear beam splitters obeying $SU(1, 1)$ commutation relation, see Fig. 3.

In a $SU(1, 1)$ quantum interferometry,² the procedure of parameter estimation can be described by three operators: $\hat{K}_x = \frac{1}{2}(\hat{a}^\dagger \hat{b} + \hat{a} \hat{b}^\dagger)$, $\hat{K}_y = \frac{1}{2i}(\hat{a}^\dagger \hat{b}^\dagger - \hat{a} \hat{b})$, and $\hat{K}_z = \frac{1}{2}(\hat{a}^\dagger \hat{a} + \hat{b}^\dagger \hat{b})$. These operators satisfy the commutation relations: $[\hat{K}_x, \hat{K}_y] = -i\hat{K}_z$, $[\hat{K}_y, \hat{K}_z] = i\hat{K}_x$, and $[\hat{K}_z, \hat{K}_x] = i\hat{K}_y$, for a $SU(1, 1)$ group. In addition, it is easy to find that $\hat{K}_{\text{tot}}^2 = \hat{J}_z(\hat{J}_z + 1)$ and \hat{J}_z commute with all $\hat{K}_{x,y,z}$.² Different from a $SU(2)$ group, the conserved quantity (Casimir invariant) of this $SU(1, 1)$ group is given by $\hat{K}_{\text{tot}}^2 = \hat{K}_z^2 - \hat{K}_x^2 - \hat{K}_y^2$, which is related to the ever fixed atom number imbalance. In a $SU(1, 1)$ interferometer, beam splitting and recombination are implemented by using optical parametric amplification that may generate correlated photon pairs. The optical parametric amplification (OPA) can be described by $\hat{U}_{\text{OPA}} = e^{i\beta\hat{K}_y}$ with β dependent upon the effective nonlinear coupling strength. Such a beam splitter is inherently related to the parametric downconversion of a strong pump beam going through a nonlinear crystal. In parametric downconversion,¹⁹⁷ the pump beam undergoes a nonlinear process, resulting in the generation of two new beams: the signal beam and the idler beam. Due to energy conservation, we have $\nu_p = \nu_s + \nu_v$, with ν_p , ν_s , and ν_v denoting the frequencies of the pump beam, the signal beam, and the idler beam, respectively. In the degenerate case, we have $\nu_s = \nu_v = \nu_p/2$.

In Fig. 3(a), we show an optical $SU(1, 1)$ interferometer. Starting from the vacuum state $|0, 0\rangle$, the first OPA generates correlated photon pairs via \hat{U}_{OPA} . Then, the two modes accumulate phases via $\hat{U}_{\text{ph}} = e^{-i(\theta_a \hat{a}^\dagger \hat{a} + \theta_b \hat{b}^\dagger \hat{b})} = e^{-i\theta\hat{K}_z + i\bar{\theta}\hat{J}_z}$ with $\theta = \theta_a + \theta_b$ and $\bar{\theta} = \theta_a - \theta_b$. Finally, the second OPA is applied and the accumulated total phase can be extracted from the population \hat{K}_z . Therefore, the whole $SU(1, 1)$ interferometer sequence can be expressed as

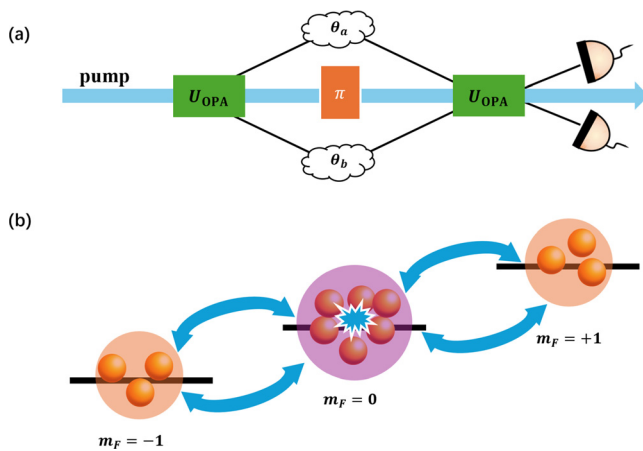


FIG. 3. Schematic of $SU(1, 1)$ quantum interferometers. (a) An optical $SU(1, 1)$ interferometer. The basic idea of this interferometric scheme is to replace the linear beam splitters of a standard interferometric scheme with OPAs that create or annihilate pairs of particles. (b) Spin-changing collisions of atoms can be regarded as an analogue of OPA in atom optics. For example, BEC in $m_F=0$ acts as the pump beam. The nonlinear spin-changing collisions populate the modes $m_F = \pm 1$, which are the analogue to the signal and idler beams.

$\hat{U} = e^{-i\beta\hat{K}_y} e^{-i\theta\hat{K}_z} e^{-i\beta\hat{K}_y}|0, 0\rangle$ and the final expectation value of \hat{K}_z is given as $\langle \hat{K}_z \rangle = (1 - \cos \theta)\sinh^2(\beta)$.

The phase sensitivity of $SU(1, 1)$ interferometer can be improved to the Heisenberg scaling.^{2,188} The difference between $SU(1, 1)$ and $SU(2)$ interferometers lies in the beam splitting and mixing processes. The parametric amplifiers are active to generate quantum fields, while the linear beam splitters are passive and rely on injection of quantum states to achieve quantum enhancements.¹⁸⁹ On the one hand, parametric amplifiers allow coherent superposition of waves and lead to amplified noises. On the other hand, parametric amplifiers may generate quantum entanglement, leading to correlated quantum noises, which can be canceled at destructive interference. This gives rise to higher signal amplification than noise amplification and thus improves the measurement precision.¹⁸⁹

In recent years, $SU(1, 1)$ interferometers have been implemented experimentally with different physical systems.^{139,184–188,198–201} Particularly, the $SU(1, 1)$ interferometry has been demonstrated by using the spin-mixing dynamics in spin-1 systems, which will be briefly illustrated in Sec. III C.

B. Fisher information and Cramér-Rao bound

Fisher information is a mathematical concept in statistics that measures the amount of information about an unknown parameter. Measurement precision refers to the degree of uncertainty with which a physical quantity can be measured. Fisher information provides a theoretical bound on the best achievable precision of an unbiased estimator for the parameter to be estimated. In practice, higher Fisher information corresponds to better measurement precision.

In a classical estimation problem with a set of measurement data from ν times of identical experiments using an unbiased estimator, the measurement precision is limited by the Cramér-Rao bound (CRB),

$$\Delta\theta \geq \frac{1}{\sqrt{\nu F(\theta)}}, \quad (1)$$

with the Fisher information

$$F(\theta) = \sum_i P(x_i|\theta) \left(\frac{\partial \ln [P(x_i|\theta)]}{\partial \theta} \right)^2 = \sum_i \frac{1}{P(x_i|\theta)} \left(\frac{\partial P(x_i|\theta)}{\partial \theta} \right)^2, \quad (2)$$

where $P(x_i|\theta)$ is the conditional probability of measuring the experimental data x_i given a specific value of θ .

In quantum mechanics, the measurement is described by a positive operator values measure (POVM).²⁰² A POVM is a set of Hermitian operators $\{\hat{E}(\mu)\}$ parameterized by μ that are positive, $E(\mu) \geq 0$. $P(\mu|\theta) = \text{Tr}[\hat{\rho}(\theta)\hat{E}(\mu)] \geq 0$, to guarantee non-negative probabilities, satisfy $\sum_\mu \hat{E}(\mu) = \hat{I}$, and ensure normalization $\sum_\mu P(\mu|\theta) = 1$. In the estimation scenario whose probe and measurement are both determined, the classical Fisher information (CFI) provides an achievable bound on measurement precision, which is a quantity able to catch the amount of information encoded in output probabilities of the estimation process.²⁰³ With the probability distribution $P(\mu|\theta)$, the CFI can be defined as follows:

$$F_C(\theta; \hat{E}) = \sum_{\mu} \frac{1}{P(\mu|\theta)} \left(\frac{\partial P(\mu|\theta)}{\partial \theta} \right)^2. \quad (3)$$

For an unbiased estimator, the measurement precision of the parameter θ is bounded by the classical CRB,²⁰⁴

$$\Delta\theta \geq \frac{1}{\sqrt{\nu F_C(\theta; \hat{E})}}, \quad (4)$$

where $\Delta\theta = \sqrt{\langle \theta^2 \rangle - \langle \theta \rangle^2}$ is the standard deviation of the estimated phase θ and ν denotes the number of trials. The CFI provides an asymptotic measure of the amount of information about the parameters of a system under specific measurements.

C. Quantum Fisher information and quantum Cramér–Rao bound

In Sec. II B, we illustrate the scenario that both probe and measurement are determined. However, the selection of $\hat{E}(\mu)$ has a significant influence on $P(\mu|\theta)$, which in turn directly impacts the CFI $F_C(\theta)$. To achieve optimal measurement precision, the POVM measurement should be carefully selected. An upper bound to the CFI can be obtained by maximizing Eq. (3) over all possible POVMs $\{\hat{E}(\mu)\}$ for the involved quantum system,¹⁸¹ leading to

$$F_Q(\theta) = \max_{\hat{E}} F_C(\theta; \hat{E}), \quad (5)$$

which is called quantum Fisher information (QFI). Therefore, the measurement precision of the parameter θ is bounded by the quantum Cramér–Rao bound (QCRB),

$$\Delta\theta \geq \frac{1}{\sqrt{\nu F_Q(\theta)}}. \quad (6)$$

Since the property $F_Q(\theta) \geq F_C(\theta; \hat{E})$, the QCRB is the ultimate achievable limit of the CRB.

According to the QCRB (6), for a given probe state and an interferometer transformation, the QFI and the QCRB allow one to calculate the ultimate achievable precision bound regardless of the measurements. A general expression of the QFI can be expressed as follows:^{180,204,205}

$$F_Q(\theta) = (\Delta\hat{L}_\theta)^2 = \text{Tr}[\hat{\rho}_\theta \hat{L}_\theta^2], \quad (7)$$

which is the variance of the symmetric logarithmic derivative operator \hat{L}_θ defined by $\partial_\theta \hat{\rho}_\theta = (\hat{\rho}_\theta \hat{L}_\theta + \hat{L}_\theta \hat{\rho}_\theta)/2$. Moreover, the QFI can be expressed in terms of the spectral decomposition of the output state $\hat{\rho}_\theta = \sum_n a_n |n_\theta\rangle \langle n_\theta|$ with θ -dependent eigenvalues $a_n \geq 0$ and eigenvectors $|n_\theta\rangle$. Thus, the QFI can be explicitly written as follows:^{206,207}

$$F_Q(\theta) = \sum_n \frac{(\partial_\theta a_n)^2}{a_n} + 2 \sum_{i \neq j} \frac{(a_i - a_j)^2}{a_i + a_j} |\langle n_i | \partial_\theta n_j \rangle|^2, \quad (8)$$

with $|\partial_\theta n_j\rangle \equiv \partial_\theta |n_j\rangle$. In Eq. (8), the first term quantifies the information about θ encoded in $|n_\theta\rangle$ and it corresponds to the Fisher information obtained via projecting on the eigenstates of $\hat{\rho}_\theta$, and the second term accounts for the change of eigenstates with θ .

According to Eq. (8), the QFI for a pure state $\hat{\rho}_\theta = |\Psi_f(\theta)\rangle \langle \Psi_f(\theta)|$ can be written as follows:²⁰⁸

$$F_Q(\theta) = 4 [\langle \partial_\theta \Psi_f(\theta) | \partial_\theta \Psi_f(\theta) \rangle - |\langle \partial_\theta \Psi_f(\theta) | \Psi_f(\theta) \rangle|^2], \quad (9)$$

with $|\partial_\theta \Psi_f(\theta)\rangle = \partial |\Psi_f(\theta)\rangle / \partial \theta$. Furthermore, if the final state is evolved from a pure initial states $\hat{\rho}_0 = |\Psi_{in}\rangle \langle \Psi_{in}|$ under an unitary evolution $U_\theta = e^{-i\hat{H}_\theta}$, the QFI can be given as follows:

$$F_Q(\theta) = 4(\Delta\hat{H}_\theta)^2, \quad (10)$$

where $(\Delta\hat{H}_\theta)^2$ is the variance of \hat{H}_θ for the initial state $|\Psi_{in}\rangle$.

However, in realistic experiments, one needs to find a suitable observable to approach the above theoretical precision bounds. For an observable \hat{O} with eigenvalue μ , we have the standard deviation of \hat{O} on the final state $\hat{\rho}_\theta$,

$$\Delta\hat{O} = \sqrt{\langle \hat{O}^2 \rangle_f - \langle \hat{O} \rangle_f^2} = \sqrt{\text{Tr}[\hat{\rho}_\theta \hat{O}^2] - \text{Tr}[\hat{\rho}_\theta \hat{O}]^2}. \quad (11)$$

For a pure final state, one can obtain

$$\langle \hat{O} \rangle_f = \sum_{\mu} \mu P(\mu|\theta) = \langle \Psi_f(\theta) | \hat{O} | \Psi_f(\theta) \rangle \quad (12)$$

and

$$\langle \hat{O}^2 \rangle_f = \sum_{\mu} \mu^2 P(\mu|\theta) = \langle \Psi_f(\theta) | \hat{O}^2 | \Psi_f(\theta) \rangle. \quad (13)$$

From the general quantum estimation theory, the measurement precision of the estimated parameters can be given via the error propagation formula¹⁸¹

$$\Delta\theta = \frac{\Delta\hat{O}}{|\partial \langle \hat{O} \rangle_f / \partial \theta|}. \quad (14)$$

D. Standard quantum limit and Heisenberg limit

In this subsection, we will illustrate how to optimize QFI over the initial states and attain the ultimate precision limits allowed by quantum mechanics.^{5,10} For simplicity, we first consider a single-particle system with a Hamiltonian $\hbar\theta$ for parameter encoding. According to Eq. (10), we have

$$4(\Delta\hat{h})^2 \leq (\lambda_{\max} - \lambda_{\min})^2, \quad (15)$$

where λ_{\max} and λ_{\min} are the maximum and minimum eigenvalues of \hat{h} , corresponding to eigenvectors $|\lambda_{\max}\rangle$ and $|\lambda_{\min}\rangle$. The variance of \hat{h} is maximized when $|\Psi_{in}\rangle = \frac{1}{\sqrt{2}}(|\lambda_{\max}\rangle + |\lambda_{\min}\rangle)$, so the maximal Fisher information is

$$F_Q(\theta) = (\lambda_{\max} - \lambda_{\min})^2. \quad (16)$$

When there are N identical systems, the whole Hamiltonian for phase encoding is given by

$$\hat{H}\theta = \left[\hat{h}^{(1)} + \hat{h}^{(2)} + \dots + \hat{h}^{(N)} \right] \theta, \quad (17)$$

where $\hat{h}^{(l)}$ is the generator for the l th system.

For N probes that are classically combined without entanglement, the whole state can be then written as $\rho = \rho^{(1)} \otimes \rho^{(2)} \dots \otimes \rho^{(N)}$, with $\rho^{(l)}$ is the state of the l th system. Using the convexity and additivity properties of QFI,¹⁶ its value for state ρ satisfies

$$F_Q(\theta) = \sum_{l=1}^N F_Q^{(l)}(\theta) \leq N \left[\lambda_{\max}^{(l)} - \lambda_{\min}^{(l)} \right]^2. \quad (18)$$

The condition for the equality is that each probe is in the same state of $|\Psi_{\text{in}}^{(l)}\rangle = (|\lambda_{\max}^{(l)}\rangle + |\lambda_{\min}^{(l)}\rangle)/\sqrt{2}$. Since $[\lambda_{\max}^{(l)} - \lambda_{\min}^{(l)}]^2$ are the same, the measurement precision vs the number of the probes N is

$$\Delta\theta \propto 1/\sqrt{N}. \quad (19)$$

Thus, for a system of N particles (labeled as $l = 1, 2, \dots, N$) and each particle regarding as a qubit with $\hat{h}^{(l)} = \frac{1}{2}\sigma_z^{(l)}$, $\lambda_{\max}^{(l)} = 1/2$, $\lambda_{\min}^{(l)} = -1/2$, one can get

$$\Delta\theta_{\text{SQL}} = 1/\sqrt{N}, \quad (20)$$

which is the so-called standard quantum limit (SQL).²⁰⁹

By employing quantum entanglement, the SQL can be surpassed.²¹⁰ For N entangled particles whose density matrix ρ cannot be expressed in the product form, the maximum and minimum eigenvalues of \hat{H} in Eq. (17) are $N\lambda_{\max}$ and $N\lambda_{\min}$, respectively. Here, the $\hat{h}^{(l)}$ for each system is in the same form with maximal and minimal eigenvalues $\hat{h}^{(l)}|\lambda_{\max}^{(l)}\rangle = \lambda_{\max}^{(l)}|\lambda_{\max}^{(l)}\rangle$ and $\hat{h}^{(l)}|\lambda_{\min}^{(l)}\rangle = \lambda_{\min}^{(l)}|\lambda_{\min}^{(l)}\rangle$. According to Eq. (18), one can obtain

$$F_Q(\theta)|_{\max} = N^2(\lambda_{\max} - \lambda_{\min})^2. \quad (21)$$

Thus, the corresponding measurement precision bound becomes

$$\Delta\theta \propto 1/N. \quad (22)$$

Similarly, for a system with N qubits with $\hat{h}^{(l)} = \frac{1}{2}\sigma_z^{(l)}$, one can obtain

$$\Delta\theta_{\text{HL}} = 1/N, \quad (23)$$

which is the so-called Heisenberg limit (HL).^{3,4,182} The HL implies a \sqrt{N} improvement of the precision scaling over the SQL. A primary goal in quantum metrology is to attain this ultimate precision limit by using optimal quantum parameter estimation process.²¹¹

E. Strategies of quantum metrology

Based on the general procedure of quantum parameter estimation, below we will introduce different strategies for implementing quantum metrology. As illustrated previously, the procedures for the parameter estimation generally contain four stages: initialization, interrogation, readout, and estimation. In analogy to quantum communication, four different scenarios are possible to be implemented:^{5,9} (i) classical–classical (CC) strategy, which do not employ quantum effects in both stages, as shown in Fig. 4(a); (ii) classical–quantum (CQ) strategy, which employs quantum effects only in the measurement stage, as shown in Fig. 4(b); (iii) quantum–classical (QC) strategy, which employs quantum effects only in the interrogation stage, as shown in Fig. 4(c); (iv) quantum–quantum (QQ) strategy, which employs quantum effects only in both stages, as shown in Fig. 4(d).

It is proved that the QC and QQ strategies that using entanglement in the preparation stage can help to improve the measurement precision while for CQ strategy where entanglement operations only in readout cannot. In the following, we give brief derivations for the ultimate precision bounds in the above four different scenarios and

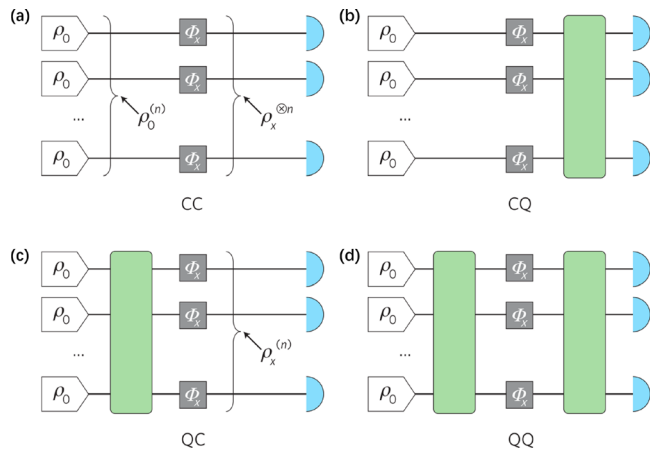


FIG. 4. Four strategies of quantum metrology.¹⁰ (a) The CC strategy. The probes are prepared in a separable state $\rho_0^{(n)}$ and local measurements are made at the output independently. (b) The CQ strategy. The probes are prepared in a separable state $\rho_0^{(n)}$, but entanglement among the probes is generated after phase encoding and before the detection. (c) The QC strategy. Entanglement among the probes is generated before phase encoding, but no entanglement resource is employed at the detection stage. (d) The QQ strategy. The entanglement can be used both at the probe preparation and detection stages. The QQ strategy provides the best performance, and the CC strategy provides the worst. Reproduced with permission from Giovannetti *et al.*, Nat. Photonics 5, 222 (2011).¹⁰ Copyright 2011 Springer Nature.

show their performances. We assume the interrogation stage for each probe is through a unitary operator $\hat{U}_\theta = e^{-i\theta\hat{h}^{(l)}}$, where θ is the parameter to be estimated and the generator for the l th probe $\hat{h}^{(l)}$ is a known Hermitian operator. Taking $\rho_0^{(N)}$ as the state of the N probes, it will be transformed into $\hat{U}_\theta^{\otimes N} \rho_0^{(N)} \hat{U}_\theta^{\dagger \otimes N}$, where $\hat{U}_\theta^{\otimes N}$ is the unitary transformation generated by $\hat{H} = \sum_{l=1}^N \hat{h}^{(l)}$. According to Eq. (10), we have

$$\Delta\theta \geq \frac{1}{2\Delta\hat{H}}. \quad (24)$$

For the CC and CQ strategies with separable state, $\Delta\hat{H} = \left[\sum_{l=1}^N \Delta^2 \hat{h}^{(l)} \right]^{1/2}$. As illustrated in Sec. II D, the maximum $\Delta\hat{H} = \sqrt{N}(\lambda_{\max} - \lambda_{\min})/2$ that can be achieved via preparing each probe in the equally weighted superpositions of the eigenvectors $|\lambda_{\max}\rangle$ and $|\lambda_{\min}\rangle$ of $\hat{h}^{(l)}$. Thus, measurement precision of parameter θ for the optimal CC and CQ strategies is

$$\Delta\theta \geq \frac{1}{\sqrt{N}(\lambda_{\max} - \lambda_{\min})}. \quad (25)$$

This result indicates that the CC strategy is as precise as the CQ strategy. Thus, for non-entangled probes, the subsequent entangled measurements have no enhancement on the precision in Eq. (25), which is just the SQL.

In contrast, for the QC and QQ strategies with entangled probes, e.g., in the maximally entangled state $\rho_0^{(N)} = |\Psi\rangle\langle\Psi|$ that maximizing $\Delta\hat{H}$

$$|\Psi\rangle = (|\lambda_{\max}\rangle^{\otimes N} + |\lambda_{\min}\rangle^{\otimes N})/\sqrt{2}, \quad (26)$$

which is the equally weighted superposition of the eigenvectors relative to the maximum and minimum eigenvalues of the global generator \hat{H} , the measurement precision of parameter θ for the optimal QC and QQ strategies can be enhanced to the Heisenberg limit

$$\Delta\theta \geq \frac{1}{N(\lambda_{\max} - \lambda_{\min})}, \quad (27)$$

with a \sqrt{N} improvement over Eq. (25). The bound of Eq. (27) is obtained by using the fact that the maximum and minimum eigenvalues both grow linearly with the number of systems N , and the maximum and minimum eigenvalues of the global generator \hat{H} are $N\lambda_{\max}$ and $N\lambda_{\min}$, respectively.

According to Eqs. (25) and (27), one can find that the ultimate measurement precision for the CC and CQ strategies just can approach the SQL, i.e., $\propto 1/\sqrt{N}$, while the ultimate measurement precision for the QC and QQ strategies can approach to the Heisenberg limit, i.e., $\propto 1/N$. This implies that quantum entanglement at the preparation stage is useful to increase the measurement precision, while the entanglement operations at the measurement stage may not. There are many different types of multi-particle entangled states that have been used to improve the precision. In Sec. III, we will introduce some typical multi-particle entangled states in practical quantum metrology.

III. METROLOGICALLY USEFUL ENTANGLED STATES AND THEIR PREPARATION

As discussed in Sec. II, entanglement plays a crucial role in enhancing the measurement precision of quantum sensors. Entanglement is a unique phenomenon in quantum mechanics that holds significant value as a resource without classical equivalents.¹³⁴ It refers to a phenomenon characterized by fascinating correlations that are exclusively observable at the minuscule scale of the quantum realm and do not manifest in our macroscopic world. In 1935, Einstein, Podolsky, and Rosen (EPR) originated the famous “EPR paradox,”^{212,213} which states that two spatially separated particles can have perfectly correlated positions and momenta. This seemingly contradicts the Heisenberg uncertainty principle, where the position and momentum of a particle cannot be simultaneously determined. The EPR argument pinpoints a contradiction between local realism and the completeness of quantum mechanics. In their attempt to support local realism, they aimed to demonstrate that the lack of precise predictions of measurement results is due to the incompleteness of quantum mechanics. Schrodinger was the first to recognize that the wavefunction of the two particles is entangled.²¹⁴ This implies that the global states of a composite system cannot be expressed as a product of the states of individual subsystems. This phenomenon, known as entanglement, serves as the foundation for quantum technology to break through bottlenecks of conventional technologies.

A. Metrologically useful entanglement

Formally, quantum entanglement is a basic phenomenon in which the quantum states of two or more particles get coupled in a manner where the state of one particle is intrinsically dependent on the state of the others. In a system of N particles, a pure quantum state $|\Psi\rangle_{sep}$ is separable if it can be expressed as a product state,²¹⁵

$$|\Psi\rangle_{sep} = |\psi^{(1)}\rangle \otimes |\psi^{(2)}\rangle \otimes \cdots \otimes |\psi^{(N)}\rangle, \quad (28)$$

with $|\psi^{(k)}\rangle$ being the k th particle’s state and the state of each individual particle is independent on the others. Such a state can be written as a density matrix, i.e.,

$$\hat{\rho} = \hat{\rho}^{(1)} \otimes \hat{\rho}^{(2)} \otimes \cdots \otimes \hat{\rho}^{(N)}, \quad (29)$$

where $\hat{\rho}^{(i)} = |\psi^{(i)}\rangle\langle\psi^{(i)}|$ describing the state of the i th subsystem. For a mixed state, it is separable if it can be expressed as a mixture of product states. More generally, a separable state of N particles, also known as a non-entangled state, is defined as a linear combination of density matrices multiplied by positive weights p_b

$$\hat{\rho} = \sum_l p_l \hat{\rho}_l^{(1)} \otimes \hat{\rho}_l^{(2)} \otimes \cdots \otimes \hat{\rho}_l^{(N)}, \quad (30)$$

where $\hat{\rho}_l^{(i)}$ is the density matrix of the i th particle in the l th term of the weighted sum. Then, quantum states that can not be expressed as product states in forms of Eqs. (28) or (30) are entangled states.¹⁶ Similarly, if we cannot write the state in the form of Eq. (30), there must be more than classical correlations and it can be considered as an entangled state. This section will provide some typical multi-particle entangled states and demonstrate the methods for generating these states in different many-body quantum systems.

For a pure state $\hat{\rho}$, we always have $\text{Tr}(\hat{\rho}^2) = 1$. If one divide the whole system into two subsystems A and B , it follows that $\hat{\rho}$ is entangled if and only if the von Neumann entropy measure

$$S[\rho] = -\text{Tr}\hat{\rho} \ln \hat{\rho} \quad (31)$$

of either reduced density matrix $\hat{\rho}^A = \text{Tr}_B \hat{\rho}$ or $\hat{\rho}^B = \text{Tr}_A \hat{\rho}$ is positive.²¹³ In the case of two particles, any quantum state is either separable or entangled. For the system containing massive number of particles, it might exhibit multi-particle entanglement and not only pairwise entanglement, which needs to be classified. Such multi-particle entanglement is best characterized by the entanglement depth,²¹⁶ which is defined as the number of particles in the largest non-separable subset of a state. A quantitative measure of entanglement in a multi-particle system is the number of elements that must at least have gone together in entangled states. We define a k -particle entangled state to be a state of N particles, which cannot be decomposed into a convex sum of products of density matrices with all density matrices involving less than k particles: at least one of the terms is a k -particle entangled density matrix.

Similar to Eq. (28), if the system state can be written as follows:

$$|\Psi_{k,sep}\rangle = |\psi_{N_1}\rangle \otimes |\psi_{N_2}\rangle \otimes \cdots \otimes |\psi_{N_M}\rangle, \quad (32)$$

where $|\psi_{N_i}\rangle$ is a state of $N_i \leq k$ particles with $\sum_{i=1}^M = N$, and the state is k -particle entangled. The state with Eq. (32) implies that there are at least one state of k particles cannot be factorized. This is also referred to an entanglement depth larger than $k - 1$. Similarly, a mixed state is k -particle entangled if it can be written in terms of a mixture of k -particle entangled pure states, i.e.,

$$\rho_{k,sep} = \sum_l p_l |\Psi_{k,sep}\rangle_{ll} \langle \Psi_{k,sep}|. \quad (33)$$

Thus, if each particle is entangled with each other completely, the system state is maximally entangled with $k = N$.

Theoretically, one can use QFI (8) or (9) to qualify the metrological usefulness of a quantum state since QFI is only related to the properties of the state. According to the QCRB of inequality (6), if the QFI of an entangled state is larger than the particle number N ,

$$F_Q > N, \quad (34)$$

the state can be metrologically useful since it has the potential to attain a measurement precision better than the SQL. An entangled state with large QFI necessitates a substantial level of entanglement depth. For a state in the form of Eq. (32), the QFI should satisfy^{217,218}

$$F_Q \leq sk^2 + r^2, \quad (35)$$

where s equals the integer part of N/k and $r = N - sk$. If the bound in Eq. (35) is violated, the state should contain $(k+1)$ -particle entanglement. When $k=N$, the QFI has an upper bound, i.e., $F_Q \leq N^2$, which corresponds to the Heisenberg limit. The state such as GHZ state that can have the maximal QFI $F_Q = N^2$ is considered to be ideal for metrological use. It should be mentioned that the condition of Eq. (34) is for the linear generator, while for nonlinear generator, the dependence of QFI on total particle number N may be different.

The relation between entanglement and metrological usefulness has been theoretically studied.^{119,133,219–223} For example, the quantum states with positive partial transpose can be useful for quantum metrology.^{220,221} However, it should be noted that not every entangled state is equally useful for quantum metrology applications.²¹⁹ While several entangled states can provide benefits for quantum metrology, their level of usefulness may be different. For instance, despite being an N -particle entangled state, the W state has a QFI of only $3N - 2$, which can only attain the SQL precision scaling when N is large.^{119,133,223} Interestingly, some of the metrologically useless states may be activated to be useful in multicopy scenarios.^{224,225}

In practice, multi-particle entangled states that typically exhibit high QFI and are thus well-suited for quantum metrology include spin-squeezed states, twin-Fock states, spin cat states, etc. These types of entangled states have the potential to surpass conventional precision limits and enable entanglement-enhanced quantum metrology.^{16,226} In addition to QFI, squeezing parameters can be used to assess the metrological usefulness of an entangled state. There are several different squeezing parameters for characterizing spin squeezing. For Gaussian entangled states, there are two commonly used squeezing parameters. The first squeezing parameter, proposed by Kitagawa and Ueda,²²⁷ is inspired by the concept of photon squeezing. The second squeezing parameter, introduced by Wineland *et al.*,²²⁸ is based on standard Ramsey spectroscopy. However, these two well-known metrological linear squeezing parameters can only quantify the sensitivity of Gaussian states, and they are insufficient to characterize the much wider class of highly sensitive non-Gaussian states.²²⁹ For non-Gaussian entangled states, a class of metrological nonlinear squeezing parameters have been introduced via optimizing measurement observables among a given set of accessible (possibly nonlinear) operators.²³⁰ These nonlinear squeezing parameters allow for the metrological characterization of non-Gaussian entangled states of both discrete and continuous variables.

The quantum features of large systems become fragile against environmental noises, leading to significant decoherence of entangled states involving many particles.^{140–143,231,232} Even a weak coupling with the environment can disrupt the quantum characteristics of such

states, causing them to exhibit classical behavior. Consequently, creating large-scale entanglement is an extremely challenging task. In 1999, experimental efforts to achieve entanglement between more than two particles began with the successful creation of a GHZ state involving three entangled photons.^{125,233} In 2000, the entanglement of four ions was demonstrated.²³⁴ Then, multi-particle entanglement has been achieved with up to 14 ions^{137,235} and eight photons.²³⁶ Other systems, such as superconducting qubits^{237,238} and nitrogen-vacancy defect centers in diamond,²³⁹ have also been utilized to create tripartite entanglement. Up to now, various multi-particle entangled states, including spin-squeezed states,^{105–114,240} twin-Fock states,^{105,117,118} and spin cat states,^{74,121} have been generated in different many-body quantum systems,^{241–245} demonstrating entanglement-enhanced measurement precisions. In Secs. III B–III D, we will introduce the experimental and theoretical advancements in this field.

B. Spin-squeezed states

Spin squeezing plays a crucial role in understanding quantum entanglement and serves as a significant quantum resource for achieving high-precision measurements. In this subsection, we will first introduce bosonic squeezing, a concept extensively investigated in the realm of quantum optics. Subsequently, we will present several definitions of spin squeezing in collective spin systems. Meanwhile, we will showcase diverse approaches employed to generate spin-squeezed states across a range of quantum many-body systems.

1. Bosonic squeezing

First, let us go over some fundamental concepts of bosonic squeezing in quantum optics. Squeezed states exist in various systems of bosonic particles such as photons, phonons, and atoms. Consider a simple harmonic oscillator obeying the Hamiltonian

$$H = \frac{\hat{p}^2}{2m} + \frac{1}{2} m\omega^2 \hat{x}^2, \quad (36)$$

where the scaled Planck constant $\hbar = h/(2\pi) = 1$, and the position operator \hat{x} and the momentum operator \hat{p} satisfy the commutation relation $[\hat{x}, \hat{p}] = i$. According to the Heisenberg uncertainty relation,

$$\Delta\hat{x}\Delta\hat{p} \geq \frac{1}{2}, \quad (37)$$

where $\Delta\hat{x}$ and $\Delta\hat{p}$ are the standard deviations of \hat{x} and \hat{p} , respectively.

To connect with number states, one may introduce the creation and annihilation operators $\hat{a}^\dagger \equiv \sqrt{\frac{m\omega}{2}}\hat{x} - i\sqrt{\frac{1}{2m\omega}}\hat{p}$ and $\hat{a} \equiv \sqrt{\frac{m\omega}{2}}\hat{x} + i\sqrt{\frac{1}{2m\omega}}\hat{p}$ for the phonons in the system. Thus, the Hamiltonian (36) reads

$$H = \omega \left(\hat{a}^\dagger \hat{a} + \frac{1}{2} \right). \quad (38)$$

The eigenstate $|n\rangle$ is a number state, that is, eigenstate of the number operator $\hat{a}^\dagger \hat{a}|n\rangle = n|n\rangle$. For convenience, we consider the following dimensionless quadrature operators:

$$\hat{X} = \sqrt{2m\omega}x = \hat{a} + \hat{a}^\dagger \quad (39)$$

and

$$\hat{P} = \sqrt{\frac{2}{m\omega}} p = \frac{\hat{a} - \hat{a}^\dagger}{i}. \quad (40)$$

One can find that $[\hat{X}, \hat{P}] = 2i$ and the corresponding Heisenberg uncertainty relation is given as

$$\Delta\hat{X}\Delta\hat{P} \geq 1. \quad (41)$$

If the quadratures of a state satisfy the minimum uncertainty

$$\Delta\hat{X} = \Delta\hat{P} = 1, \quad (42)$$

this state is a coherent state. In general, a coherent state is defined as the eigenstate of the annihilation operator $\hat{a}|\alpha\rangle = \alpha|\alpha\rangle$. Moreover, an arbitrary coherent state $|\alpha\rangle$ with the complex number $\alpha = |\alpha|e^{i\phi}$ can be generated from the vacuum state $|0\rangle$, that is,

$$|\alpha\rangle = \hat{D}(\alpha)|0\rangle, \quad (43)$$

by using the displacement operator $\hat{D}(\alpha) = \exp(\alpha\hat{a}^\dagger - \alpha^*\hat{a})$.

The Heisenberg uncertainty relation remains inviolable, but it is possible to choose a condition in which the uncertainty in either $\Delta\hat{X}$ or $\Delta\hat{P}$ is less than one, at the expense of having the uncertainty in the other variable exceed one. The state of such an uncertainty less than one is referred to as a squeezed state. An example of squeezed states is the squeezed coherent state

$$|\alpha, \eta\rangle = \hat{S}(\eta)|\alpha\rangle, \quad (44)$$

which can be generated by the nonlinear Hamiltonian

$$H = i(g\hat{a}^{12} - g^*\hat{a}^{21}). \quad (45)$$

Here, the squeezing operator is given as $\hat{S}(\eta) = \exp(-iHt) = e^{\frac{1}{2}\eta^*\hat{a}^2 - \frac{1}{2}\eta\hat{a}^{12}}$ with $r = -2|g|t$ and the complex squeezing parameter $\eta = re^{i\theta}$.

To illustrate the squeezing, one can rotate the quadrature operators by an angle $\theta/2$, and thus, the rotated quadrature operators can be expressed as follows:

$$\tilde{X} = \hat{a}^\dagger e^{\frac{\theta}{2}} + \hat{a} e^{-\frac{\theta}{2}} \quad (46)$$

and

$$\tilde{P} = i(\hat{a}^\dagger e^{\frac{\theta}{2}} - \hat{a} e^{-\frac{\theta}{2}}). \quad (47)$$

Consequently, the standard deviation for the rotated quadratures is

$$\Delta\tilde{X} = e^{-r}, \quad \Delta\tilde{P} = e^r. \quad (48)$$

Obviously, the standard deviation of \tilde{X} is decreased by a factor of e^{-r} , yet the product of the two standard deviations $\Delta\tilde{X}\Delta\tilde{P} = 1$ does not violate the Heisenberg uncertainty principle.

The use of squeezed coherent states in interferometers has shown promising potential in improving measurement precision. Initially proposed by Caves,¹ the sensitivity of optical interferometers can be improved by introducing quadrature-squeezed states. By replacing the vacuum state with squeezed states, the injection of these states into interferometers effectively reduces vacuum quantum noise.¹ This injection of squeezed states results in a reduction of detection noise below the shot-noise level, thereby enhancing phase measurement sensitivity. Notably, significant progress has been made in generating and

applying these quantum states to optical interferometry systems, as demonstrated by various experimental efforts.^{243,246–248} Recently, this technique has been employed in large-scale interferometers spanning kilometers, with the aim of improving sensitivity for gravitational wave detection.^{242,249,250} In addition, by combining unconventional nonlinear interferometers² and stimulated emission of squeezed light, a scalable scheme for achieving unconditional and robust quantum metrological advantage beyond NOON states has been proposed and demonstrated with photons,²⁵¹ making it possible for practical quantum metrology at the low-photon-flux regime.

2. Spin squeezing

Below we concentrate on spin squeezing, which refers to the phenomenon of reducing uncertainty in spin measurements. We will primarily illustrate spin squeezing using an ensemble of N indistinguishable spin-1/2 particles. The system can be described by the following collective spin operators:

$$\hat{J}_k = \frac{1}{2} \sum_{l=1}^N \sigma_k^{(l)}, \quad (49)$$

where $\sigma_k^{(l)}$ is the Pauli matrix for the l th particle and $k = \{x, y, z\}$. Similar to a coherent state, a spin coherent state consists of N identical single spin states aligned along the same direction and it can be expressed as follows:²⁵²

$$|\theta, \varphi\rangle = \otimes_{l=1}^N \left[\cos \frac{\theta}{2} |\uparrow\rangle^{(l)} + e^{i\varphi} \sin \frac{\theta}{2} |\downarrow\rangle^{(l)} \right], \quad (50)$$

where $|\uparrow\rangle^{(l)}$ and $|\downarrow\rangle^{(l)}$ are the eigenstates of $\sigma_z^{(l)}$ with eigenvalues +1 and -1, respectively. The mean spin direction is given by the vector $\vec{J} = \{\sin \theta \cos \varphi, \sin \theta \sin \varphi, \cos \theta\}$. A spin coherent state $|\theta, \varphi\rangle$ can be generated from the state $\otimes_{l=1}^N |\downarrow\rangle_l$ of all particles in spin-down state $|\downarrow\rangle_l$,²⁵² that is,

$$|\theta, \varphi\rangle = \otimes_{l=1}^N R_J(\theta, \varphi) |\downarrow\rangle_l = \otimes_{l=1}^N \exp(\xi \sigma_+^{(l)} - \xi^* \sigma_-^{(l)}) |\downarrow\rangle_l, \quad (51)$$

where $\sigma_\pm^{(l)} = \sigma_x^{(l)} \pm i\sigma_y^{(l)}$, and $\xi = \frac{\theta}{2} e^{-i\varphi}$. In the Dicke basis $\{|J, m\rangle\}$, which is defined by $\hat{J}_z |J, m\rangle = m |J, m\rangle$, the spin coherent state (51) can be written as follows:

$$|\theta, \varphi\rangle = R(\theta, \varphi) |J, -J\rangle = \exp(\xi \hat{J}_+ - \xi^* \hat{J}_-) |J, -J\rangle, \quad (52)$$

where $\hat{J}_\pm = \hat{J}_x \pm i\hat{J}_y$ and $|J, -J\rangle \equiv \otimes_{l=1}^N |\downarrow\rangle_l$ is the eigenstate of \hat{J}_z with eigenvalue $J = N/2$. After some algebra calculations, the spin coherent state can be given as follows:

$$|\theta, \varphi\rangle = \left[\frac{(2J)!}{(J+m)!(J-m)!} \right]^{1/2} \cos^{J-m} \left(\frac{\theta}{2} \right) \sin^{J+m} \left(\frac{\theta}{2} \right) e^{i(J+m)\varphi} |J, m\rangle. \quad (53)$$

When measuring the spin component that is orthogonal to the mean collective spin \vec{J} , the variance $\Delta^2 \hat{J}_\perp$ is determined by the summation of variances from individual spin-1/2 particles, resulting in $\Delta^2 \hat{J}_\perp = \frac{N}{4}$. For the spin coherent state $|\pi/2, 0\rangle = \otimes_{l=1}^N [\frac{1}{\sqrt{2}}(|\uparrow\rangle^{(l)} + |\downarrow\rangle^{(l)})]$ along x axis, its variances along two orthogonal directions are isotropic, that is,

$$\Delta^2 \hat{J}_y = \Delta^2 \hat{J}_z = \frac{N}{4}. \quad (54)$$

Spin squeezing occurs when the uncertainty in measuring the spins of a collection of particles is reduced below the limit imposed by spin coherent states. This process involves manipulating the quantum states of spinor particles to enhance their correlation and decrease the fluctuations in their collective spin. Spin-squeezed states, akin to squeezed coherent states (44), represent a kind of collective spin states that minimize the variance of spin along a specific direction while increasing the variance of the anti-squeezed spin along a perpendicular direction.^{115,228,253} Spin squeezing is currently regarded as one of the most effective means of achieving significant quantum entanglement and demonstrating measurement precision that surpasses the SQL.²⁵⁴

The degrees of spin squeezing can be characterized by squeezing parameter. According to the Heisenberg uncertainty relations for collective spin operators, a collective spin state with $\xi_H^2 = \frac{2(\Delta \hat{J}_\alpha)^2}{|\langle \hat{J}_\gamma \rangle|} < 1$ [where $\alpha \in (x, y, z)$, $\gamma \in (x, y, z)$ and $\alpha \neq \gamma$] can be regarded as a spin-squeezed state. However, the squeezing parameter ξ_H cannot indicate the optimal spin squeezing.

Inspired by the concept of photon squeezing, Kitagawa and Ueda introduced a squeezing parameter²²⁷

$$\xi_S^2 = \frac{4 \min(\Delta \hat{J}_{\vec{n}_\perp})^2}{N}, \quad (55)$$

determined by the minimum variance along the direction perpendicular to the mean collective spin direction. Therefore, a state is squeezed if $\xi_S^2 < 1$. By minimizing ξ_S over all feasible perpendicular directions \vec{n}_\perp , the optimal squeezing direction can be determined. This knowledge is crucial for implementing quantum-enhanced measurement.

Alternatively, in the context of Ramsey interferometry, Wineland *et al.* introduced a squeezing parameter

$$\xi_R^2 = \frac{\Delta\phi}{\Delta\phi_{SCS}} = \frac{N(\Delta \hat{J}_{\vec{n}_\perp})^2}{|\langle \hat{J} \rangle|^2}, \quad (56)$$

which is the ratio of the phase measurement precision obtained via the spin-squeezed state and the spin coherent state.^{228,253} Here, $(\Delta \hat{J}_{\vec{n}_\perp})^2$ can be obtained by measuring the population difference between two sensor levels and $|\langle \hat{J} \rangle|$ can be inferred from the Ramsey fringes contrast. Consequently, a squeezed state corresponds to $\xi_R^2 < 1$. As shown in Fig. 5, implementing spin-squeezed states for Ramsey interferometry, the phase measurement precision can be improved to $\Delta\phi \propto \xi_R/\sqrt{N}$. Notably, if $\xi_R = 1/\sqrt{N}$, the measurement precision attains the Heisenberg limit: $\Delta\phi \propto 1/N$.

From Eqs. (55) and (56), one can easily find the relation between the above two spin-squeezing parameters

$$\xi_R^2 = \left(\frac{N}{2|\langle \hat{J} \rangle|} \right)^2 \xi_S^2 \geq \xi_S^2. \quad (57)$$

This means that the state has $\xi_R^2 < 1$ always implying $\xi_S^2 < 1$.

Although bosonic squeezing and spin squeezing look very different, they may be connected through the Holstein–Primakoff transformation. In the limit of large particle number and small excitations, the spin squeezing can be reduced to the bosonic squeezing. Assume the total particle number $N \gg 1$ and the

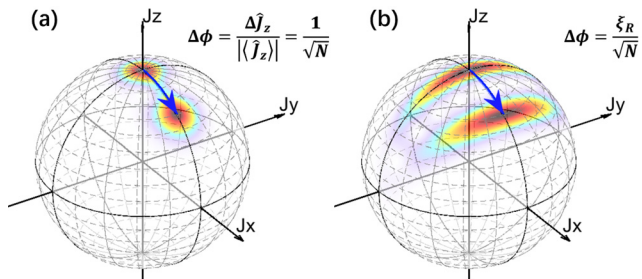


FIG. 5. Spin coherent states and spin-squeezed states.¹¹⁵ The Husimi distribution on the generalized Bloch sphere for (a) spin coherent state and (b) spin-squeezed state. Implementing spin coherent state and spin-squeezed state for Ramsey interferometry, the phase measurement precision can be achieved $\Delta\phi = \frac{1}{\sqrt{N}}$ and $\Delta\phi = \frac{\xi_R}{\sqrt{N}}$, respectively. Reproduced with permission from Ma *et al.*, Phys. Rep. **509**, 89 (2011). Copyright 2011 Elsevier.

number of excited-state particles $\langle \hat{b}^\dagger \hat{b} \rangle \ll N$, one can perform the Holstein–Primakoff transformation²⁵⁵

$$\hat{J}_+ = \hat{b} \sqrt{N - \hat{b}^\dagger \hat{b}}, \quad \hat{J}_- = \hat{b}^\dagger \sqrt{N - \hat{b}^\dagger \hat{b}}, \quad \hat{J}_z = \frac{N}{2} - \hat{b}^\dagger \hat{b}, \quad (58)$$

which is equivalent to making the mean-field approximation. As $\langle \hat{b}^\dagger \hat{b} \rangle \ll N$, $\sqrt{N - \hat{b}^\dagger \hat{b}}$ can be approximated as \sqrt{N} , therefore we have

$$\hat{J}_+ / \sqrt{N} \rightarrow \hat{b}, \quad \hat{J}_- / \sqrt{N} \rightarrow \hat{b}^\dagger, \quad 2\hat{J}_z / N \rightarrow 1. \quad (59)$$

The scaled spin operators can be mapped onto the position and momentum quadrature operators, respectively,

$$\sqrt{2/N} \hat{J}_x \rightarrow \hat{X} = (\hat{b} + \hat{b}^\dagger) / \sqrt{2} \quad (60)$$

and

$$\sqrt{2/N} \hat{J}_y \rightarrow \hat{P} = (\hat{b} - \hat{b}^\dagger) / (i\sqrt{2}). \quad (61)$$

Thus, we have

$$\xi_R^2 = 2(\Delta Q)^2, \quad (62)$$

with $\hat{Q} = (\hat{b} e^{-i\phi} + \hat{b}^\dagger e^{i\phi}) / \sqrt{2} = \hat{X} \cos \phi + \hat{P} \sin \phi$ and $0 \leq \phi < 2\pi$. This indicates that the appearance of spin squeezing $\xi_R^2 < 1$ corresponds to the variance of the quadrature below the vacuum limit $(\Delta \hat{Q})^2 < 1/2$.

3. One-axis twisting

One-axis twisting (OAT) is a widely recognized approach for producing entangled states that already have vast practical applications in quantum metrology.²⁵⁷ In principle, through the OAT dynamics from a spin coherent state, spin-squeezed states, over-squeezed states, and spin cat states can be prepared. Generally, the OAT Hamiltonian reads

$$H_{OAT} = \gamma \hat{J}_z^2, \quad (63)$$

where χ denotes the twisting strength. This Hamiltonian can be realized in various synthetic quantum systems such as BECs,^{11,116,118,126} trapped ions,¹³⁶ and cold atoms in optical cavity.^{120,128,130}

Starting from the spin coherent state $|\pi/2, 0\rangle$, the state after OAT reads

$$|\Psi(t)\rangle_{OAT} = e^{-i\chi t \hat{J}_z^2} |\pi/2, 0\rangle. \quad (64)$$

During the OAT dynamics, the uncertainties are redistributed among certain orthogonal components in the (y, z) plane based on the squeezing angle, see Fig. 6. The minimum and maximum values correspond to the spin components that are squeezed and anti-squeezed, respectively. Analytically, one can obtain the squeezing angle

$$\alpha = \frac{1}{2} \arctan(B/A), \quad (65)$$

with $A = 1 - \cos^{N-2}(2\chi t)$ and $B = 4 \sin(\chi t) \cos^{N-2}(\chi t)$. Then, the squeezed and anti-squeezed spin operators can be explicitly expressed as follows:

$$\hat{J}_s = \hat{J}_z \cos(\alpha) - \hat{J}_y \sin(\alpha) \quad (66)$$

and

$$\hat{J}_a = \hat{J}_y \cos(\alpha) + \hat{J}_z \sin(\alpha). \quad (67)$$

The expectation of the x component evolves according to

$$\langle \hat{J}_x \rangle = \frac{N}{2} \cos^{N-1}(\chi t), \quad (68)$$

where the contrast gradually diminishes. The variances of squeezed (denoted by s) and anti-squeezed (denoted by a) spin components are expressed as follows:

$$\Delta^2 \hat{J}_{s,a} = \frac{N}{4} \left[1 + \frac{1}{4} (N-1) A \mp \frac{1}{4} (N-1) \sqrt{A^2 + B^2} \right]. \quad (69)$$

Therefore, the squeezing parameter can be given as follows:

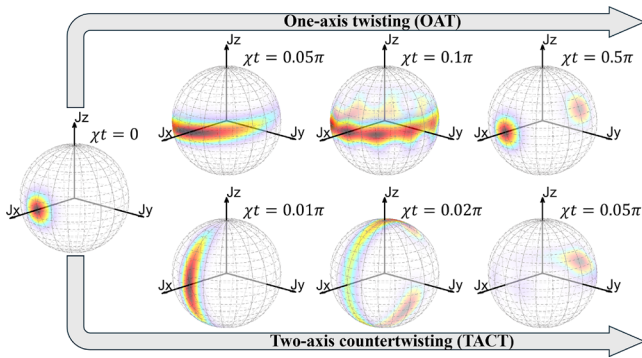


FIG. 6. State evolution via OAT and TACT dynamics.²²⁷ The Husimi distribution on the generalized Bloch sphere for (a) one-axis twisting (OAT) dynamics and (b) two-axis countertwisting (TACT) dynamics. Here, the Hamiltonian for TACT is chosen as $\tilde{H}_{TACT} = -\chi(\hat{J}_y \hat{J}_z + \hat{J}_z \hat{J}_y)$, which is obtained via a unitary transformation $\tilde{H}_{TACT} = e^{-i\tilde{\phi}_y} H_{TACT} e^{i\tilde{\phi}_y}$ on H_{TACT} .²⁵⁶ Reproduced with permission from Kitagawa and Ueda, Phys. Rev. A **47**(6), 5138 (1993).²²⁷ Copyright 1993 American Physical Society.

$$\xi_s^2 = \frac{N(\Delta \hat{J}_s)^2}{(\hat{J}_x)^2} = \frac{1 + (N-1)(A - \sqrt{A^2 + B^2})/4}{\cos^{2N-2}(\chi t)}. \quad (70)$$

In the limit of $N \gg 1$ and $\chi t \ll 1$, the variances can be approximated as follows:

$$\Delta^2 \hat{J}_s \approx \frac{N^2 \chi^2 t}{2} \quad (71)$$

and

$$\Delta^2 \hat{J}_a \approx \frac{1}{4N\chi^2 t^2} + \frac{N^3 \chi^4 t^4}{24}. \quad (72)$$

When $\chi t \leq 1/\sqrt{N}$, the state becomes spin squeezed, that is, the squeezing parameter satisfies $\xi_s^2 < 1$. Particularly, at the point of $\chi t = 3^{1/6} N^{-2/3}$, $\Delta^2 \hat{J}_{s,opt} \approx \left(\frac{3^{2/3}}{8}\right) N^{1/3}$, the spin squeezing becomes optimal,²²⁷

$$\xi_{s,opt}^2 \approx \left(\frac{3^{2/3}}{8}\right) N^{-2/3}. \quad (73)$$

Later for $\chi t > 1/\sqrt{N}$, the state stretches into an over-squeezed state, whose Husimi distribution turns to be non-Gaussian. Specifically, at the points of $\chi t = \pi/M$ ($2 \leq M < \pi\sqrt{N}/2$), the state evolves into a superposition state of M spin coherent states distributed evenly on the equator of the generalized Bloch sphere, which can be used for generating spin cat states, see Sec. III D below.

Implementing Ramsey interferometry with optimal spin-squeezed state, the best measurement precision obeys the scaling

$$\Delta\phi \propto N^{-5/6}, \quad (74)$$

which beats the SQL but does not attain the Heisenberg limit.

4. Two-axis countertwisting

The degree of spin squeezing achieved through OAT depends on the number of particles N and the duration of the evolution T , as the optimal squeezing angle varies accordingly. Furthermore, even with optimal spin squeezing, it is not possible to reach the Heisenberg limit precisely. In theory, this limitation could be overcome by simultaneously twisting clockwise and counterclockwise around two perpendicular axes within the plane perpendicular to the mean spin direction. The two orthogonal axes can be selected in the directions with $\theta = \pi/2$ and $\varphi = \pm\pi/4$. The spin operators corresponding to these two orientations are

$$\hat{J}_{\pi/2, \pm\pi/4} = \frac{1}{\sqrt{2}} (\hat{J}_x \pm \hat{J}_y). \quad (75)$$

This kind of twisting is known as two-axis countertwisting (TACT), and it obeys the following Hamiltonian:

$$H_{TACT} = \chi(\hat{J}_{\pi/2, \pi/4}^2 - \hat{J}_{\pi/2, -\pi/4}^2) = \chi(\hat{J}_x \hat{J}_y + \hat{J}_y \hat{J}_x) = \frac{\chi}{2i} (\hat{J}_+^2 - \hat{J}_-^2). \quad (76)$$

Nevertheless, the TACT model is not amenable to analytical solutions when the value of N is large. Starting from spin coherent state $|\pi, 0\rangle$, the mean spin direction is along the z axis. When the quasi-

probability Husimi distribution covers almost half of the generalized Bloch sphere, the squeezed component achieves a minimal variance of 1/2, while the anti-squeezed component reaches $N^2/8$. The optimal squeezing angle is invariant during the TACT evolution. If χt exceeds the optimal value, the quasi-probability distribution will bifurcate into two distinct components.²²⁷ Compared with OAT, the degree of spin squeezing is higher. The TACT can also be achieved from any two orthogonal axes, which can be seen in Fig. 6.

5. Preparing spin-squeezed states via OAT

Significant progress has been made in generating and applying spin-squeezed states in various physical systems. Various methods, including atom–atom collision,^{116,126,258} quantum nondemolition measurement,^{128,159,259} quantum feedback control,^{260–262} and Rydberg dressing,^{107,263} have been employed to achieve spin squeezing. Experiments involving ultracold atoms, trapped ions, and Rydberg atoms have successfully created spin-squeezed states, pushing the boundaries of what can be achieved in quantum control. Below we will explore the experimental progress made in preparing spin-squeezed states via OAT in different quantum many-body systems.

Tunable atom–atom interactions are naturally occur in BECs and offer a practical means for manipulating twisting dynamics. Considerable endeavors have been dedicated to the creation of spin-squeezed states in atomic systems. Typically, spin squeezing can be achieved using two main approaches. One method involves utilizing atomic collisions inside BECs,²⁵⁸ while the other method involves exploiting atom–photon interactions within atomic ensembles. We first discuss how to generate the OAT Hamiltonian from a two-component BEC, which can be regarded as an atomic BEC occupying two internal states, or alternatively, as a BEC confined inside a double-well potential. The former and the latter ones can be well described by the internal and external Bose–Josephson junction (BJJ), respectively, as shown in Fig. 7. Denoted the two modes by a and b , in the Swinger representation, the unified BJJ Hamiltonian can be written as follows:

$$H_{BJJ} = -\Omega \hat{J}_x + \chi \hat{J}_z^2 + \delta \hat{J}_z, \quad (77)$$

where $\hat{J}_x = \frac{\hat{a}^\dagger \hat{b} + \hat{a} \hat{b}^\dagger}{2}$, $\hat{J}_y = \frac{\hat{a}^\dagger \hat{b} - \hat{a} \hat{b}^\dagger}{2i}$, and $\hat{J}_z = \frac{\hat{a}^\dagger \hat{a} - \hat{b}^\dagger \hat{b}}{2}$.

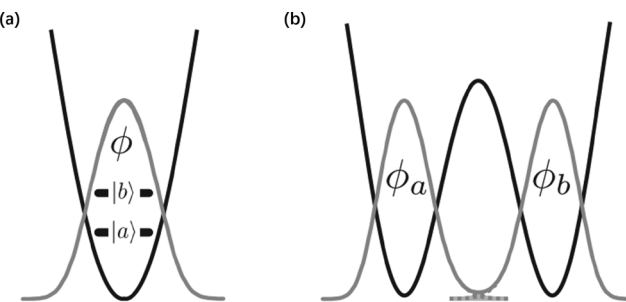


FIG. 7. Schematics of Bose–Josephson junctions.¹¹ (a) Internal Bose–Josephson junction realized with a Bose–Einstein condensate in a single-well potential occupying on two different hyperfine levels coupled by laser fields. (b) External Bose–Josephson junction realized with a BECs confined in a double-well potential. Reproduced with permission from Gross et al., J. Phys. B: At. Mol. Opt. Phys. **45**, 103001 (2012).¹¹ Copyright 2012 IOP Publishing.

For an internal BJJ, the two hyperfine states $|a\rangle$ and $|b\rangle$ are assumed in the spatial single-mode wavefunctions $\phi_a(\vec{r})$ and $\phi_b(\vec{r})$ coupled by a driving field with Rabi frequency Ω_R and detuning Δ to the resonant transition between $|a\rangle$ and $|b\rangle$. The coefficients in the many-body Hamiltonian (77) are given as $\Omega = \Omega_R \int d\vec{r} [\phi_a^*(\vec{r}) \phi_b(\vec{r})]$, $\delta = \varepsilon_b - \varepsilon_a + N(U_{bb} - U_{aa})/4$, and $\chi = U_{aa} + U_{bb} - 2U_{ab}$, with $\varepsilon_k = \int d\vec{r} [\phi_k^*(\vec{r}) (-\frac{\nabla^2}{2m} + V(\vec{r}) + \Delta_k) \phi_k(\vec{r})]$, $\Delta_{a,b} = \mp \Delta/2$, $U_{kl} = \frac{g_{kl}}{2} \int d\vec{r} |\phi_k(\vec{r})|^2 |\phi_l(\vec{r})|^2$. Here, $g_{kl} = 4\pi a_s^{kl}/m$ with a_s^{aa} , a_s^{bb} , and a_s^{ab} denoting the intraspecies and interspecies s-wave scattering lengths, and m being the atomic mass. For $g_{aa} = g_{bb}$ and $\phi_a = \phi_b = \phi$ [as shown in Fig. 7(a)], $\delta = \Delta$, $\Omega = \Omega_R$, we have $\chi \propto a_s^{aa} + a_s^{bb} - 2a_s^{ab}$. In particular for $\Omega = 0$ and $\delta = 0$, the Hamiltonian of Eq. (77) is equivalent to the OAT Hamiltonian of Eq. (63). Thus, one can tune the nonlinear interaction χ and use it for dynamical generation of spin-squeezed states.

By loading Bose condensed atoms into optical lattices, the entanglement of about 170 ^{87}Rb atoms has been successfully prepared.¹²⁶ As shown in Fig. 8(a), a BEC of ^{87}Rb atoms occupying the hyperfine state $|F = 1, m_F = -1\rangle$ was firstly prepared in an optical dipole trap. Then, through supposing a one-dimensional optical lattice potential, the dipole trap is split into six, which allows to perform six independent experiments in parallel. Before applying the first $\frac{\pi}{2}$ pulse, the atoms are swept from the state $|F = 1, m_F = -1\rangle$ to the state $|a\rangle = |F = 1, m_F = 1\rangle$. Only two hyperfine states $|a\rangle = |F = 1, m_F = 1\rangle$ and $|b\rangle = |F = 2, m_F = -1\rangle$ are involved. The effective nonlinear interaction $\chi \propto a_s^{aa} + a_s^{bb} - 2a_s^{ab}$ was tuned by changing interspecies interaction with the technique of a Feshbach resonance. By carefully tuning the magnetic field at $B = 9.10$ G, $\chi = 2\pi \times 0.063$ Hz can be achieved. The Rabi frequency Ω can be switched rapidly from 0 to $2\pi \times 600$ Hz, changing the system from Rabi regime to Fock regime. When the Rabi frequency is switched off, the system stays in the Fock regime and its state evolves under the nonlinear term. Thus, individual systems localized in each lattice site can be described by the OAT Hamiltonian with Eq. (63). The OAT evolution induces a squeezing angle α_0 with respect to the z direction. A rotation of the uncertainty ellipse around its center by $\alpha = \alpha_0 + \pi/2$ is followed. After spin-squeezing preparation, the modes $|a\rangle$ and $|b\rangle$ experience a $\tau = 2\mu\text{s}$ phase accumulation period and recombine via another $\frac{\pi}{2}$ pulse before the readout of population imbalance. In comparison with the ideal phase sensitivity obtained by spin coherent states, their experimental data show that the phase sensitivity is enhanced by 15%. With spin noise tomography, the inferred spin-squeezing parameter can be up to $\xi_R^2 = -8.2$ dB. If introducing the linear coupling between the two states, the spin squeezing can be generated faster, which will be briefly discussed at the end of this section. The experimental demonstration is shown in Figs. 8(b)–8(e).

The nonlinear interaction χ can also be tuned by controlling the spatial overlap between two spin components. Using this technique, spin-squeezed states can be generated on atomic chips. By loading Bose condensed atoms into an atomic chip and generating spin-squeezed states via OAT dynamics, the measurement precision can also be improved beyond the SQL.¹¹⁶ In the experiment, two spin states $|F = 1, m_F = -1\rangle$ and $|F = 2, m_F = 1\rangle$ of ^{87}Rb atoms are involved and the system obeys the OAT Hamiltonian of Eq. (63). Different from using a Feshbach resonance, the effective interaction is controlled by adjusting the spatial overlap between two spin

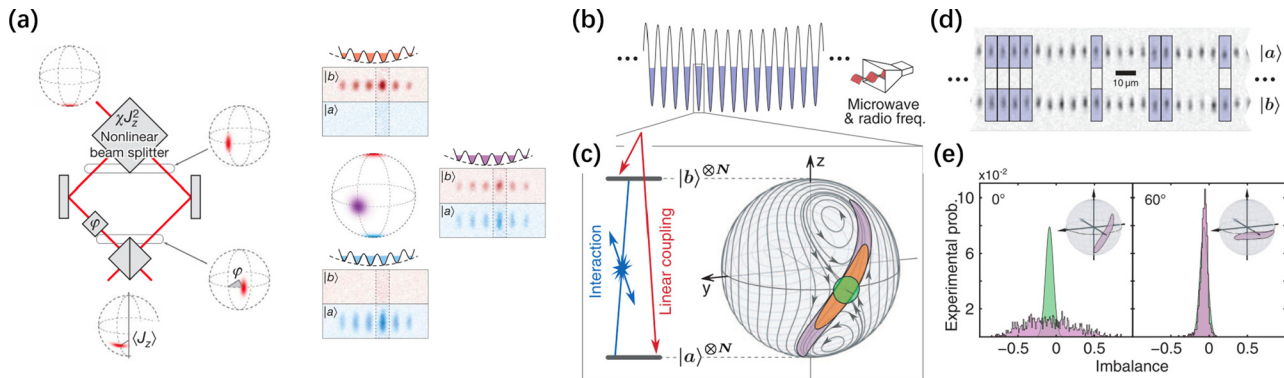


FIG. 8. Generation of spin-squeezed¹²⁶ and non-Gaussian-entangled states¹¹⁸ with BECs trapped in optical lattices. (a) The many-body Ramsey interferometry with spin-squeezed state. Six independent ^{87}Rb BECs occupying two hyperfine states in a one-dimensional optical lattice are prepared. The quantum states on the generalized Bloch sphere in one of the wells are shown. Reproduced with permission from Gross *et al.*, *Nature* **464**, 1165 (2010).¹²⁶ Copyright 2010 Springer Nature. (b) A group of BECs is manipulated inside an optical lattice potential using microwave and radio frequency fields. (c) The combination of nonlinear interaction (blue) and weak Rabi coupling (red) between the internal states leads to an unstable fixed point in the classical phase space. The gray lines represent the paths followed by the mean-field equations of motion. The initial spin coherent state (represented by the color green) undergoes an ideal transformation into a spin-squeezed state (represented by the color orange). As time progresses, the spin state further evolves into non-Gaussian states (represented by the color violet). The boundaries of the shaded regions represent the outlines of the Husimi distribution at its peak. (d) An experimental absorption image is shown, which displays the site- and state-resolved optical lattice after a Stern–Gerlach separation. (e) Displayed are histograms illustrating the disparity following the nonlinear progression of 25 ms and final rotation (as shown by the angles in the graphs), in comparison with the ideal spin coherent state of same nature (represented by the green Gaussian). Reproduced with permission from Strobel *et al.*, *Science* **345**, 424 (2014).¹¹⁸ Copyright 2014 The American Association for the Advancement of Science.

components. Except for controlling the nonlinear interaction, the procedures for spin-squeezing generation are similar, as shown in Fig. 9. First, a spin coherent state is prepared by a resonant $\frac{\pi}{2}$ pulse for 120 μs . During the pulse, the coupling term dominates, $\Omega \gg \gamma N$, so that the atom–atom interaction can be neglected. The state-dependent microwave potential is turned on within 50 μs to cause a sudden separation of trap minima for the two hyperfine states. The two components begin to oscillate oppositely, and the overlap of the modes wavefunction reduces, which leads to the decreasing of the inter-component interaction and the increasing of effective nonlinearity χ . The nonlinearity can attain $\chi = 1.5 \text{ s}^{-1}$ at the maximum separation. The two components overlap again after 12.7 ms, and the nonlinear interaction squeezing dynamics stops. The results give a spin-squeezing parameter $\xi_R^2 = -1.2 \text{ dB}$ and with detection noise subtracted $\xi_R^2 = -7.0 \text{ dB}$ can be achieved in recent experiments.

The external BJJ can be realized with BEC confined in a double-well potential $V_{dw}(\vec{r})$. For sufficiently high barrier and weak interaction, the system can be simplified by two-mode approximation. The two modes can be considered the spatial modes localized in the left and right wells constructed by the lowest two quasi-degenerate symmetric and antisymmetric eigenstates ($|\phi_g\rangle$ and $|\phi_e\rangle$) for the corresponding Gross–Pitaevskii equation, i.e., $|a\rangle = (|\phi_g\rangle + |\phi_e\rangle)/\sqrt{2}$ and $|b\rangle = (|\phi_g\rangle - |\phi_e\rangle)/\sqrt{2}$, as shown in Fig. 7(b). The corresponding wavefunctions can be written as $\phi_a = \frac{1}{\sqrt{2}}(\phi_g + \phi_e)$ and $\phi_b = \frac{1}{\sqrt{2}}(\phi_g - \phi_e)$. For a double-well with sufficiently high barrier, we have the integrals $\int d\vec{r} |\phi_g|^2 |\phi_e|^2 \approx \int d\vec{r} |\phi_g|^4 \approx \int d\vec{r} |\phi_e|^4$ and the coefficients $\Omega = \mu_e - \mu_g$ and $\chi = 2g \int d\vec{r} |\phi_g(\vec{r})|^2 |\phi_e(\vec{r})|^2$ with $\mu_{g,e} = \int d\vec{r} \left\{ [\phi_{g,e}^*(-\frac{\nabla^2}{2m}) \phi_{g,e}] + gN |\phi_{g,e}|^4 \right\}$ and $g = 4\pi a_s/m$.

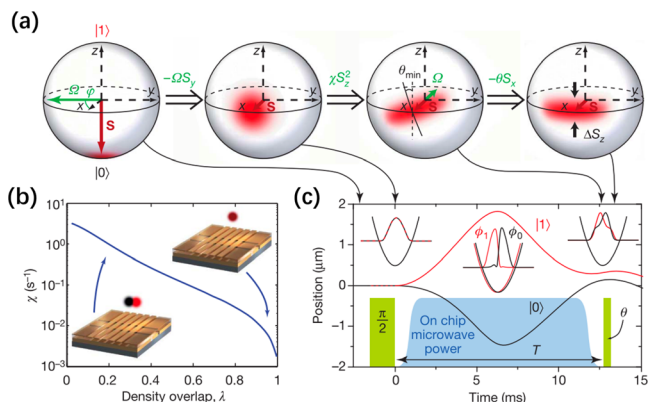


FIG. 9. Atomic spin squeezing with BEC on an atom chip.¹¹⁶ (a) The BEC internal state undergoes evolution on the generalized Bloch sphere. By first setting all atoms in the state $|0\rangle$, a $\pi/2$ -pulse is applied to create a spin coherent state. After undergoing subsequent nonlinear development, the noise circle is transformed into an ellipse, resulting in a spin-squeezed state that exhibits decreased noise at an angle θ_{\min} . A second pulse induces rotation of the state around the x axis by an angle θ , which is variable. Subsequently, the detection of half population difference occurs. (b) Manipulation of the nonlinearity χ on the atom chip. The value of χ is determined by the disparity between atomic interactions within a state and those between states. The relationship between the two BEC components is demonstrated by analyzing the normalized density overlap λ . This value is determined by evaluating the stationary mode functions in potentials with increasing spacing. (c) Sequence of experiments. During the intervals for internal-state manipulation (green), a microwave potential that depends on the state of the system is activated (blue indicates the lengths of the pulses). During the time T , it dynamically divides and merges the two BEC components, resulting in a positive value of χ . Reproduced with permission from Riedel, *Nature* **464**, 1170 (2010).¹¹⁶ Copyright 2010 Springer Nature.

In principle, the external BJJ can be realized by loading BEC in a double-well potential. However, the main challenge lies in generating a stable double-well potential. One approach utilizes the adiabatic dressed state potential, which has been used to achieve coherent splitting of a BEC and matter-wave interferometry in experiments.²⁶⁴ Another method involves employing a radio frequency dressed state potential on an atom chip, which enables the creation of double-well potentials for neutral atoms.²⁶⁵ Additionally, a double-well potential can be realized using all-optical potentials by combining a 3D harmonic trapping potential with a periodic lattice potential.²⁶⁶ The resulting potential, which combines a dipole trap and an optical lattice, exhibits a symmetric double-well shape at the center with a separation of approximately 4.4 μm between the two wells. Another demonstrated approach for establishing weak coupling between two spatially separated BECs is through the use of Bragg beams.²⁶⁷ In this setup, the atoms in the left and right wells are coupled via two Bragg beams, allowing for coherent tunneling. In an external BJJ, two important properties are the number and coherence fluctuations. As the coherence fluctuation increases with χ , it is accompanied by number squeezing, which can be considered a form of spin squeezing.

In addition to atom–atom collision, spin squeezing can also be generated through atom–light interactions. Numerous proposals focus on transferring squeezing from light to atoms as a means of generating spin squeezing. The key parameters to be controlled in this process are the atom–light coupling and the detuning between the light and atoms. In the regime of large detuning, an effective Hamiltonian can be derived that includes a dispersive interaction and a nonlinear interaction term. The magnitudes of these terms can be adjusted accordingly. The dispersive interaction between light and atoms is a type of quantum nondemolition (QND) measurement. This measurement allows for the determination of certain properties in a quantum system without disturbing or altering the system itself. The observable being measured commutes with the system’s Hamiltonian, which means that the observable and the Hamiltonian share a common set of eigenstates. Through a QND measurement, an atomic ensemble and a light beam are coupled in such a way that direct measurements on the light can provide indirect information about the atomic system. QND measurements offer a means of preparing entangled and spin-squeezed states for atomic ensembles. By performing a QND measurement on the light, the atomic ensemble can be conditioned to specific measurement outcomes, leading to squeezed states. The effective interaction between atoms is in form of an OAT interaction, which can be used to directly generate spin squeezing.

The far-off resonant dispersive interaction between an atomic ensemble and two-mode light beams can be used for implementing the QND Hamiltonian. Suppose two probe light beams coupling to different hyperfine atomic levels, respectively. In large detuning condition, the effective Hamiltonian reads²⁵⁹

$$H_{QND} = \frac{g_1^2 \Delta_1}{\gamma_1^2/4 + \Delta_1^2} \hat{c}_1^\dagger \hat{c}_1 \hat{a}^\dagger \hat{a} + \frac{g_2^2 \Delta_2}{\gamma_2^2/4 + \Delta_2^2} \hat{c}_2^\dagger \hat{c}_2 \hat{b}^\dagger \hat{b} = \Omega \left(\hat{S}_z \hat{J}_z + \frac{1}{4} \hat{n} \hat{N} \right), \quad (78)$$

where $\hat{c}_{1,2}$ are the annihilation operators for two probe light beams and $\Delta_{1,2}$ are the corresponding detunings. $g_{1,2}$ and $\gamma_{1,2}$ are the atom–light coupling constants and the spontaneous decay rates of the excited

levels. $\hat{S}_z = (\hat{c}_1^\dagger \hat{c}_1 - \hat{c}_2^\dagger \hat{c}_2)/2$ denotes the Stokes vector operator, $\hat{J}_z = (\hat{a}^\dagger \hat{a} - \hat{b}^\dagger \hat{b})/2$ stands for the collective spin operator, and $\hat{n} = \hat{c}_1^\dagger \hat{c}_1 + \hat{c}_2^\dagger \hat{c}_2$ and $\hat{N} = \hat{a}^\dagger \hat{a} + \hat{b}^\dagger \hat{b}$ are the operators for total photon number and atom number. The final form of Hamiltonian of Eq. (78) is obtained by choosing suitable detunings satisfying the following way:

$$\frac{g_1^2 \Delta_1}{\gamma_1^2/4 + \Delta_1^2} = \frac{g_2^2 \Delta_2}{\gamma_2^2/4 + \Delta_2^2} \equiv \frac{\Omega}{2}. \quad (79)$$

The Heisenberg equations can be given as follows:

$$\hat{J}_x(t) = \cos(\beta \hat{S}_z) \hat{J}_x(0) - \sin(\beta \hat{S}_z) \hat{J}_y(0), \quad (80)$$

$$\hat{J}_y(t) = \sin(\beta \hat{S}_z) \hat{J}_x(0) + \cos(\beta \hat{S}_z) \hat{J}_y(0), \quad (81)$$

$$\hat{J}_z(t) = \hat{J}_z(0), \quad (82)$$

and

$$\hat{S}_x(t) = \cos(\beta \hat{J}_z) \hat{S}_x(0) - \sin(\beta \hat{J}_z) \hat{S}_y(0), \quad (83)$$

$$\hat{S}_y(t) = \sin(\beta \hat{J}_z) \hat{S}_x(0) + \cos(\beta \hat{J}_z) \hat{S}_y(0), \quad (84)$$

$$\hat{S}_z(t) = \hat{S}_z(0), \quad (85)$$

where $\beta = \Omega t$. It is shown that the Hamiltonian acts as a Faraday rotation to the light polarization and as an artificial magnetic field to the collective spin of atoms.

When the light and atoms are both in their own spin coherent states along the x direction initially, i.e.,

$$|\psi(0)\rangle = |S, S\rangle_x |J, J\rangle_x, \quad (86)$$

the expectation

$$\langle \hat{S}_y(t) \rangle = \frac{n}{2} \langle \sin(\beta \hat{J}_z) \rangle \approx \langle \hat{S}_y(0) \rangle + \frac{n\beta}{2} \langle \hat{J}_z(0) \rangle \quad (87)$$

is related to the expectation of \hat{J}_z . Since $\langle \hat{S}_y(0) \rangle = 0$ and $\langle \hat{J}_z(0) \rangle = 0$, $\langle \hat{S}_y(t) \rangle \approx 0$ while the variance $\Delta^2 \hat{S}_y(t) \approx \langle \hat{S}_y^2(0) \rangle + \beta^2 \langle \hat{S}_x^2(0) \rangle \langle \hat{J}_z^2(0) \rangle = \frac{n}{4} + \beta^2 \frac{n^2 N}{4} = n(1 + \kappa^2)/4$ with $\kappa^2 = nN\beta^2/4$. The evolution of the system state reads

$$|\psi(t)\rangle = \exp(-i\beta \hat{S}_z \hat{J}_z) |\psi(0)\rangle = \sum_{M=-J}^J \exp(-i\beta M \hat{S}_z) \sqrt{P_J(M)} |S, S\rangle_x |J, J\rangle_x. \quad (88)$$

As shown in Fig. 10, performing the measurement of \hat{S}_y on $|\psi(t)\rangle$ with result m would cause the photon state collapsing into the eigenstate $|S, m\rangle_y$. Meanwhile, the atomic state would change according to the result m . When $N \gg 1$, the binomial distribution can be well approximated by a Gaussian distribution, i.e., $P_J(M) \approx \frac{1}{\sqrt{\pi N/2}} \exp(-\frac{2M^2}{N})$. For small rotated angle βM , one can obtain the conditional probability distribution of the atomic state given by the measurement result m of \hat{S}_y as follows:

$$P(M|m) = \frac{1}{\sqrt{\pi \xi_R^2 N/2}} \exp \left[-\frac{(M - \beta m \xi_R^2 N/2)^2}{\xi_R^2 N/2} \right], \quad (89)$$

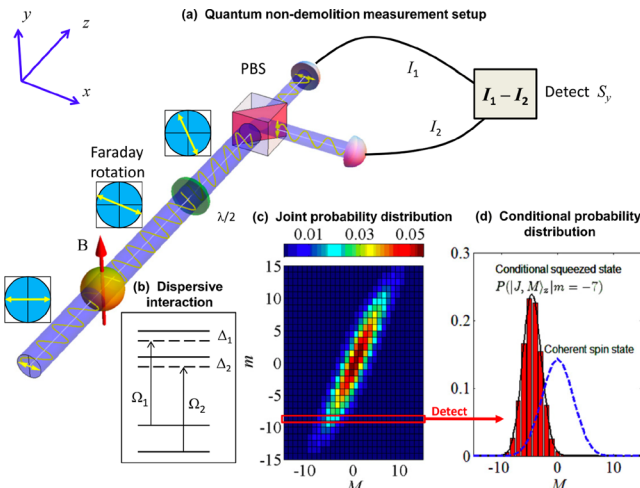


FIG. 10. Spin squeezing generation via QND measurement. (a) Diagram illustrating the schematic for the QND measurement. The input probe beam is polarized in the x direction, and the atoms are initially aligned along the x axis. The probe beam's two circularly polarized components interact with atoms in a dispersive manner, with detuning Δ_1 and Δ_2 .¹⁰⁸ Reproduced with permission from Kuzmich *et al.*, Phys. Rev. Lett. **79**(24), 4782 (1997). Copyright 1997 American Physical Society. (b) The terms Ω_1 and Ω_2 refer to the couplings between atoms and electromagnetic fields. Dispersion interactions cause a rotation of the polarization plane, known as Faraday rotation. The $\lambda/2$ wave plate, along with the subsequent PBS and two detectors, function as a QND measurement of \hat{J}_z by detecting \hat{S}_y , which is then measured by the difference in photocurrent. (c) Joint probability distributions with $N = n = 30$ and $\chi = 0.1$. (d) When the measurement of the observable \hat{S}_y yields a value of $m = -7$, the squeezed state under this condition is graphed and juxtaposed with the spin coherent state. Reproduced with permission from Ma *et al.*, Phys. Rep. **509**, 89 (2011).¹¹⁵ Copyright 2011 Elsevier.

where $\xi_R^2 = \frac{1}{1+\kappa^2}$ is the spin-squeezing parameter and $\xi_R^2 < 1$ when $t > 0$. Thus, after measuring \hat{S}_y , the atomic state becomes spin squeezed and the expectation $\langle \hat{J}_z \rangle$ is shifted to $\beta m \xi_R^2 N / 2$.

In free space, the experimental demonstration of spin squeezing via QND measurements was realized²⁶⁸ in 2009. In this experiment, the two hyperfine states $|\uparrow\rangle \equiv |F=4, m_F=0\rangle$ and $|\downarrow\rangle \equiv |F=3, m_F=0\rangle$ of Cs atoms are referred to clock levels with total atom number over 10^5 . Initially, the Cs atoms are prepared in $|\downarrow\rangle$ by using optical pumping. A resonant $\frac{\pi}{2}$ microwave pulse at the clock frequency is applied to prepare a spin coherent state. Then, successive QND measurements of the population difference $N_\uparrow - N_\downarrow$ are performed by measuring the state-dependent phase shift of the off-resonant probe light in a balanced homodyne configuration. After the QND measurement, all atoms are pumped into the $F=4$ level to determine the total atom number $N = N_\uparrow + N_\downarrow$. Two identical linear polarized beams P_\uparrow and P_\downarrow off-resonantly probe the transitions $|F=3\rangle$ to $|F'=4\rangle$ and $|F=4\rangle$ to $|F'=5\rangle$, respectively. Each beam gains a phase shift proportional to the number of atoms in the corresponding clock states,

$$\phi_\uparrow = k_\uparrow N_\uparrow, \phi_\downarrow = k_\downarrow N_\downarrow,$$

where $k_{\uparrow(\downarrow)}$ are the coupling constants and the detuning $\Delta_{\uparrow(\downarrow)}$ are tuned to make $k_\uparrow = k_\downarrow = \beta$. The phase difference between the two arms of the Mach-Zehnder interferometer is related to the measurement of J_z and the shot noise of the photons

$$\phi = \frac{\delta n}{n} + \beta(N_\uparrow - N_\downarrow) = \frac{\delta n}{n} + 2\beta J_z. \quad (90)$$

The variance of the phase difference

$$\text{Var}(\phi) = \frac{1}{n} + \beta^2 \text{Var}(N_\uparrow - N_\downarrow) = \frac{1}{n} + \beta^2 N. \quad (91)$$

The spin squeezing can be verified by estimating the correlations between two successive QND measurements. First use n_1 photons to measure \hat{J}_z and obtain a measurement result of ϕ_1 , then use n_2 photons to measure \hat{J}_z and obtain a measurement result of ϕ_2 on the same atomic ensemble. The best estimator for ϕ_2 is $\varepsilon\phi_1$, which results in a conditionally reduced variance,

$$\text{Var}(\phi_2 - \varepsilon\phi_1) = \frac{1}{n_2} + \frac{\beta^2}{1+\kappa^2} N, \quad (92)$$

with $\kappa^2 = n_1 \beta^2 N$ and $\varepsilon = \text{Cov}(\phi_1, \phi_2) / \text{Var}(\phi_1) = \frac{\kappa^2}{1+\kappa^2}$. For $\kappa^2 = 3.2$ with $N = 1.2 \times 10^5$ atoms, the projection noise can be reduced to $-(5.3 \pm 0.6)$ dB and metrologically relevant spin squeezing of $\xi_R^2 = -(3.4 \pm 0.7)$ dB on the Cs microwave clock transition has been realized. With extremely large number of atoms around 10^{11} in the vapor cell at high temperature, spin squeezing generated via stroboscopic QND measurements²⁴⁰ can further offer benefits for entanglement-enhanced magnetic field sensing.

The interaction strength between light and atoms can be enhanced by confining atomic ensemble into an optical cavity. The optical cavity allows a photon coupling with the confined atoms multiple times on successive round trips, which significantly enhances the atom-light interaction. Using high-finesse cavity, the effect of spin squeezing can be dramatically increased. The generation of spin-squeezed states of trapped ^{87}Rb atoms by cavity-aided QND measurement with a far-detuned light field was demonstrated.²⁶⁹ In addition, the application of cavity has advantages for practical applications such as atomic clocks,^{163,164,270} which will be discussed in Sec. V A.

It has been demonstrated that the strength of atom-light entanglement, regardless of light detuning or coupling strength, can be determined by multiplying the single-atom cooperativity, the normalized cavity transmission, and the total number of photons scattered by atoms into free space.¹²⁰ The entanglement between atoms and photons is primarily generated through the lowest order of atom-cavity interaction. When the laser frequency closely matches the cavity resonance and the transmission is high, the dominance lies in the atom-photon entanglement. In such cases, the measurement of the light field can generate atom-atom interaction. By transferring the atomic spin state information onto the light field, one can conditionally project the state of atoms onto an entangled state, known as the measurement-based squeezing approach. On the other hand, higher-order atom-cavity interaction can result in effective atom-atom and photon-photon interactions. When the laser detuning significantly deviates from the cavity resonance (exceeding the cavity linewidth) and the transmission is low, the atom-light entanglement weakens, and the higher-order terms become crucial in generating light-mediated atom-atom interaction. In this scenario, atomic entanglement can be unconditionally created without the need for any measurements, referred to as the cavity-feedback squeezing approach.

For example, we consider the systems of three-level atoms in a cavity. Each atom has two hyperfine levels labeled by $|a\rangle$ and $|b\rangle$ with

transition frequency ω , and an excited state $|e\rangle$ possessing a linewidth Γ . The system can be described by the following Hamiltonian:

$$H_c = \omega_c \hat{c}^\dagger \hat{c} + \frac{2g^2}{\Delta} \hat{c}^\dagger \hat{c} \hat{J}_z + \omega \hat{J}_z, \quad (93)$$

where \hat{c} is the annihilation operator for photons in the cavity, ω_c is the resonance frequency of the cavity, $\Delta = \pm \omega/2$ is the detuning between the cavity and the transition frequency of $|a\rangle \leftrightarrow |e\rangle$ and $|b\rangle \leftrightarrow |e\rangle$, g is the atom-photon effective intracavity Rabi frequency, and \hat{J}_z is the collective spin operator for the atoms. The above Hamiltonian is derived in the assumption of homogeneous interaction and large detuning with low intracavity photon number, where $\langle \hat{c}^\dagger \hat{c} \rangle \ll \Delta^2/g^2$ and $\Delta \gg \kappa_c, \Gamma, \sqrt{N}g$ with κ_c the linewidth of the cavity and N the atom number.^{271,272} By grouping the last two terms in Hamiltonian of Eq. (93), one can see that the light induces an ac Stark shift proportional to cavity photon number onto the atomic transition frequency. This shift can be detected by injecting a laser into the cavity and performing a QND measurement of \hat{J}_z . However, the performance of entanglement generation using QND measurement is generally limited by the efficiency of photon collection.

To relax the need for high-efficiency photon detection, the cavity-feedback squeezing technique has been proposed and successfully demonstrated. This method enables the unconditional squeezing of the atomic spin state and the deterministic generation of spin-squeezed states by utilizing light-mediated interactions between distant atoms within the cavity. The approach can be conceptualized as a quantum feedback process, where the atomic ensemble imprints quantum fluctuations on the light field, which in turn acts back on the atomic spin state, reducing its quantum fluctuations. The origin of spin squeezing lies in the atom-light interaction term $\frac{2g^2}{\Delta} \hat{c}^\dagger \hat{c} \hat{J}_z$, where the intracavity photon number $\hat{c}^\dagger \hat{c}$ is proportional to \hat{J}_z . This leads to the OAT Hamiltonian $H_{OAT} = \chi \hat{J}_z^2$, with an effective twisting strength χ . In 2010, the spin squeezing via cavity-based QND measurement was experimentally conducted using an ensemble of 5×10^4 ^{87}Rb atoms,¹²⁹ see Fig. 11. By preparing the atomic state in a superposition of two hyperfine clock levels, the experiment successfully generated an atomic spin-squeezed state, surpassing the SQL by achieving a 3.0 ± 0.8 dB improvement in precision. Later, a subsequent experiment using a cavity with higher cooperativity and uniform coupling between the probe light and all the atoms demonstrated spin squeezing of -20.1 ± 0.3 dB via an optical-cavity-based measurement involving a $\times 10^6$ ^{87}Rb atoms in their clock states.²⁷³

In addition to hyperfine states, spin squeezing can also be achieved between momentum states.^{274,275} This development offers a promising avenue for combining particle delocalization and entanglement in various applications such as inertial sensors, searches for new physics and particles, future precision measurements, and exploring beyond mean-field quantum many-body physics. However, the experimental realization of an entanglement-enhanced matter-wave interferometer remained elusive until the groundbreaking demonstration in 2022,¹²⁸ see Fig. 12. In that experiment, the entanglement of external degrees of freedom was successfully realized to construct a matter-wave interferometer involving 700 atoms. Remarkably, each individual atom simultaneously traversed two distinct paths while entangled with the other atoms. The experimental process involved preparing the

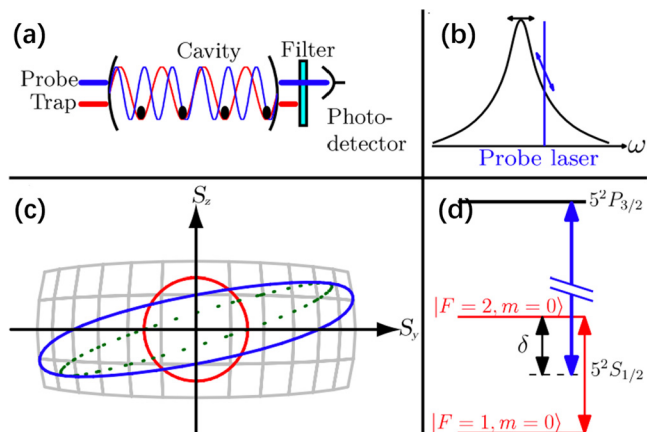


FIG. 11. Squeezing via cavity feedback.¹²⁹ (a) The atoms are confined within a dipole trap formed by a standing-wave pattern, which is located inside an optical resonator. (b) The probe laser is adjusted to be off resonance from the cavity by half of its linewidth. This allows for changes in the cavity frequency caused by atoms to affect the transmitted power in proportion to \hat{J}_z . (c) The light shift that depends on J_z causes the circular uncertainty region of the initial coherent spin state (red circle) to become an elliptical shape (dotted ellipse). The presence of photon shot noise leads to the broadening of the phase, resulting in an increase in the area of the solid ellipse. (d) The cavity is tuned halfway between the optical transition frequencies for the two clock states, where δ is the effective detuning. Reproduced with permission from Leroux *et al.*, Phys. Rev. Lett. **104**(7), 073602 (2010). Copyright 2010 American Physical Society.

atoms in superpositions of two momentum states, each associated with different hyperfine spin labels. Subsequently, both QND measurements and cavity-mediated interactions were employed to generate squeezing between momentum states. The resulting entangled state was then injected into a Mach-Zehnder light-pulse interferometer, yielding a directly observed metrological enhancement of $1.7^{+0.5}_{-0.5}$ dB, marking a significant milestone in this field.

In entanglement-enhanced atomic interferometers with momentum states, the atomic momentum states are tagged to the atomic spin states, and thus, the entanglement of spin states may map onto the entanglement of momentum states. Recently, significant progress has been made in realizing momentum-exchange interactions, wherein atoms exchange their momentum states through the collective emission and absorption of photons from a common cavity mode.²⁷⁶ This process, akin to a spin-exchange interaction, was experimentally demonstrated by pairs of atoms exchanging their momentum states via the collective emission and absorption of cavity photons.²⁷⁷ The momentum-exchange interaction manifests as an all-to-all Ising-like interaction, which proves to be instrumental in generating entanglement. This tunable momentum-exchange interaction introduces a new capability for entanglement-enhanced matter-wave interferometry, opening up avenues for exploring exotic phenomena such as simulating superconductors and dynamical gauge fields.

The van der Waals interaction between Rydberg atoms provides another resource for generating spin squeezing. The interaction between atoms in clock states is very small. In contrast, the van der Waals interaction between Rydberg atoms is strong. For atoms in a lattice clock of $\lambda = 813$ nm, the nearest-neighbor interaction C_6/r^6 between two Rydberg atoms can exceed 10 GHz.²⁷⁸ This provides an

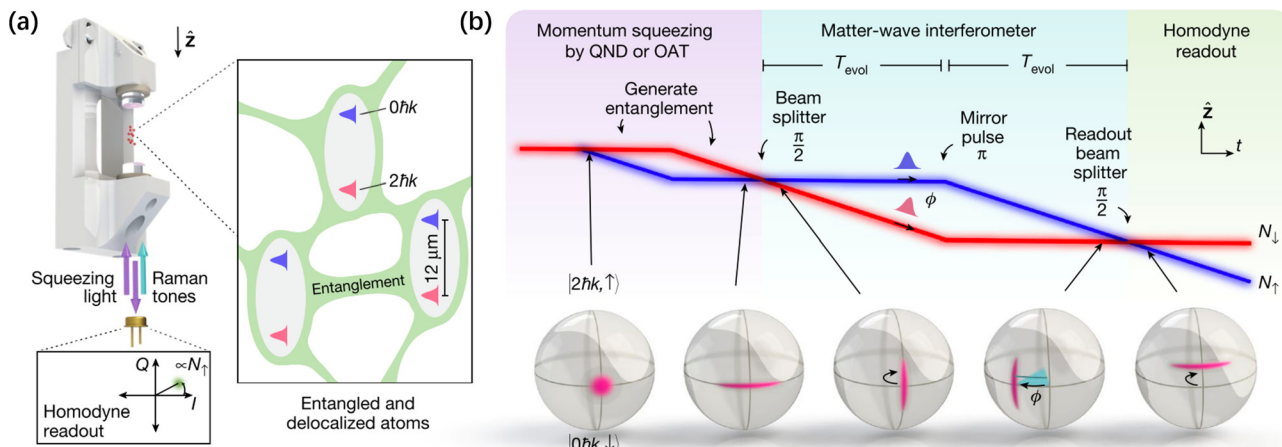


FIG. 12. Matter-wave interferometry with spin squeezing in a high-finesse cavity.¹²⁸ (a) Ultracold atoms experience controlled downward motion within a vertical chamber that has a high level of reflectivity. The atomic wave packets undergo division and subsequent fusion by the use of two-photon Raman transitions, resulting in discrete momentum impulses being imparted to the atoms. Entanglement between atoms is generated by the use of intracavity atomic probe light. This may be achieved either using OAT dynamics or QND measurements. The entanglement is created by measuring the quadrature of the reflected atomic probe field using a homodyne detector. The entanglement between atoms is observable even when the wave packets are separated by distances greater than $12\ \mu\text{m}$. (b) The entanglement is generated and injected into a Mach-Zehnder matter-wave interferometer, and this process is depicted using space-time and Bloch sphere representations. Squeezing is initially produced inside the population, and then, a Raman beam splitter pulse aligns the squeezing to improve the sensitivity of the interferometer phase. The two routes, shown by the red and blue colors, accumulate a relative phase ϕ as time progresses. The mirror pulse is used to bring the wave packets back together, while the readout beam splitter pulse generates interference that can be measured as a population difference with sub-SQRT sensitivity. The Bloch sphere displays noise distributions for different sites in the interferometer. Reproduced with permission from Greve *et al.*, *Nature* **610**, 472 (2022). Copyright 2022 licensed under a Creative Commons Attribution (CC BY) license.

excellent resource for creating entangled states. A promising approach for generating spin squeezing in optical lattice clocks has been theoretically proposed via optically coupling one clock state to a highly excited Rydberg state,²⁷⁹ which can be described by an Ising-type Hamiltonian $H_{\text{Ryd}} = \Omega \hat{J}_x + \sum_{i,j}^N V_{ij} \hat{\sigma}_z^{(i)} \hat{\sigma}_z^{(j)} + \sum_i \delta_i \hat{\sigma}_z^{(i)}$. Here, Ω is the transverse field strength, δ_i is the inhomogeneous longitudinal field strength, $V_{ij} = V_0 \frac{R_c^6}{|\vec{r}_i - \vec{r}_j|^6 + R_c^6}$ is the effective two-body interaction, and $R_c = |C_6/2\Delta|^{1/6}$ is the critical distance. The transverse and longitudinal terms can be switched on and off independently via controlling the intensities of the two laser fields. This kind of switchable atom-atom interaction provides great flexibility for the creation of entangled many-body states.

Rydberg dressing is appealing for generating entanglement in optical tweezers. Optical tweezers provide a new platform that atoms are individually trapped, and arranged in one- or two-dimensional arrays, offering high tunability and control of interatomic distance. By combining Rydberg dressing and optical tweezers, it becomes possible to finely tune atom-atom interactions, thereby enabling the realization of a wide range of interactions. This approach allows for the transformation of the interactions from an effective nearest-neighbor interaction to a nearly homogeneous interaction throughout the ensemble. Recently, an array of spin-squeezed ensembles of cesium atoms has been prepared via Rydberg dressing,¹⁰⁷ see Fig. 13. The interactions induced by Rydberg dressing can be understood as a superposition of the ac Stark shift that the dressing light imparts to each atom due to the influence of nearby atoms. This effect becomes particularly significant when considering an ensemble of N atoms confined within a critical length scale R_c where the van der Waals interaction $V_R = C_6/r^6$

surpasses the pair-state detuning 2Δ . In this limit, the system obeys the Hamiltonian $H \approx U_0 \hat{J}_z - \frac{\chi}{N} \hat{J}_z^2$, where $U_0 \approx \Omega^2/(4\Delta)$ is an overall ac Stark shift and $\chi \approx N\Omega^4/(16\Delta^3)$ is the mean-field interaction. Using spin echo, the influence of U_0 can be removed and so that one can use

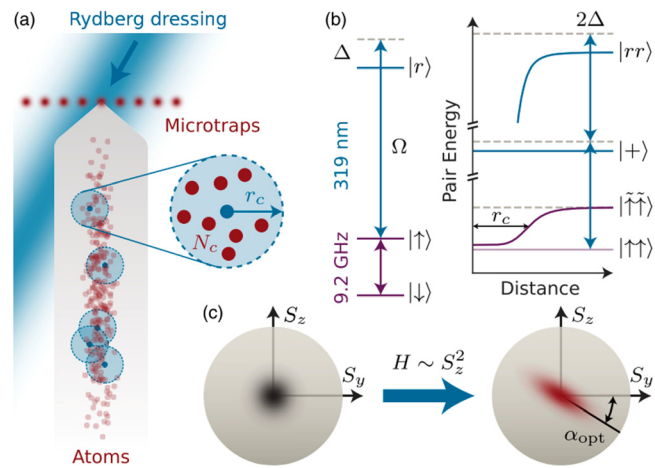


FIG. 13. Experimental setup of spin squeezing via Rydberg dressing.¹⁰⁷ (a) An array of atomic ensembles is locally illuminated with 319 nm Rydberg dressing light, inducing interactions of characteristic range r_c . (b) Level diagrams for one atom (left) and a pair of atoms (right), where $|+\rangle = (|r\uparrow\rangle + |\uparrow r\rangle)/\sqrt{2}$ and $|\langle\rangle\rangle$ denote the Rydberg-dressed state. (c) Inter-collective spin S that shears a spin coherent state (left) into a spin-squeezed state (right). Reproduced with permission from Hines *et al.*, *Phys. Rev. Lett.* **131**(6), 063401 (2023).¹⁰⁷ Copyright 2023 American Physical Society.

OAT dynamics to create spin squeezing. In the experiment, a squeezed state of $N=200$ atoms has been successfully prepared, exhibiting a squeezing parameter of $\xi_R^2 = 0.77(9)$.

Moreover, short-range interactions have been proposed^{114,280,281} and demonstrated²⁶³ for creating scalable spin squeezing. The utilization of a dipolar Rydberg quantum simulator, comprising up to $N=100$ atoms, has demonstrated the generation of spin squeezing through quench dynamics originating from a polarized initial state. The degree of spin squeezing increases with the system size, reaching a maximum of -3.5 ± 0.3 dB (prior to correcting detection errors, or roughly -5 ± 0.3 dB after correction).²⁶³ In addition, two independent refinements were introduced.²⁶³ First, a multistep spin-squeezing protocol was implemented, resulting in an additional enhancement of approximately 1 dB. Second, through the utilization of Floquet engineering to realize Heisenberg interactions, the lifetime of the squeezed state can be extended by freezing its dynamics.

Due to their clean environment and well-developed manipulation techniques, entanglement between ultracold trapped ions can be created through the Coulomb interaction. Penning traps, in particular, have emerged as a viable option for performing quantum tasks (including quantum metrology) with hundreds of ions. Experimental demonstrations of metrological spin squeezing have been achieved by using over 200 trapped ${}^9\text{Be}^+$ ions.¹²⁷ In Fig. 14, the quantum spin dynamics was observed in an engineered, homogeneous Ising interaction in a two-dimensional array in a Penning trap. Through OAT, the spin-squeezed states with multiple ions are generated. The spin-squeezing parameter ξ_R^2 was measured with different numbers of ions (N) ranging from 21 to 219, and a minimum value of $\xi_R^2 = -4.0 \pm 0.9$ dB was observed for $N=84$. Recently, the metrological utility of spin-squeezed states in a Ramsey-type interferometer was also demonstrated using 51 ions held in a macroscopic linear Paul trap.¹¹² The measurement uncertainty was reduced by -3.2 ± 0.5 dB below the SQL. In this 51-ion quantum simulator, a pseudo-spin is encoded in two electronic states of ${}^{40}\text{Ca}^+$: $|\downarrow\rangle = |\text{S}_{1/2}, m = +1/2\rangle$ and $|\uparrow\rangle = |\text{D}_{5/2}, m = +5/2\rangle$. These states are collectively coupled by a global laser beam, and spin–spin interactions between the ions are engineered using a two-tone laser that couples the ions' internal electronic states to their ground-state-cooled transverse

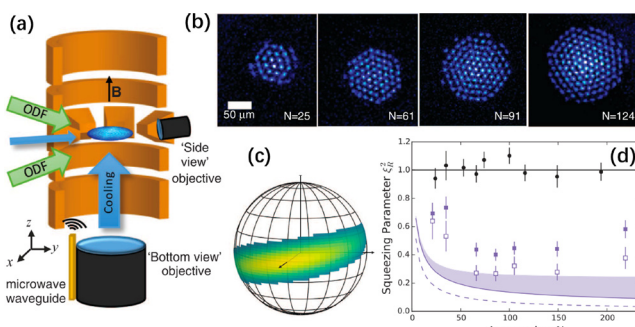


FIG. 14. Spin-squeezed states generated in a Penning trap with multiple ions.¹²⁷ The ions are restricted to the x – y plane by a powerful uniform magnetic field and axially constrained by a quadrupole electric field. The green ODF arrows represent bichromatic light fields employed for the creation of entanglement. The inset displays a depiction of a two-dimensional crystal composed of 91 ions. Reproduced with permission from Bohnet *et al.*, *Science* **352**, 1297 (2016).¹²⁷ Copyright 2016 The American Association for the Advancement of Science.

motional modes. The dynamics, under the influence of a strong driving transverse to the interaction axis, are described by the power-law transverse-field Ising model, $H_{\text{PL-TFI}} = \sum_{i < j} J_{ij} \hat{\sigma}_i^x \hat{\sigma}_j^x + B \sum_i \hat{\sigma}_i^z$. In the rotating frame of the driving, this system obeys a power-law XY model $H_{\text{PL-XY}} = \sum_{i < j} J_{ij} (\hat{\sigma}_i^+ \hat{\sigma}_j^- + \hat{\sigma}_i^- \hat{\sigma}_j^+)$, with the interaction strengths $J_{i,j} = J_0 |i-j|^{-\alpha}$ between sites i and j . The interaction strengths are parameterized in terms of the nearest-neighbor strength J_0 and a tunable exponent $0 < \alpha < 3$ describing the interaction range. Using the OAT sketched in Fig. 15(a), spin-squeezed states can be prepared. To begin, prepare a spin coherent state polarized along the $+x$ direction. Subsequently, evolve this state under the XY interaction for a variable time T . In the experiment, the interaction period is split by an echo pulse that cancels site-dependent Stark shifts along the z direction and increases the coherence time of the system.

6. Preparing spin-squeezed states beyond OAT

In addition to OAT, various schemes for generating spin squeezing have been proposed and demonstrated. To speed up the entanglement generation, one can apply an additional rotation along with the OAT, which is the so-called twist-and-turn (TNT) dynamics^{113,282,283} obeying the Hamiltonian

$$H_{\text{TNT}} = \chi \hat{j}_z^2 + \Omega \hat{j}_x, \quad (94)$$

where the turning term $\Omega \hat{j}_x$ rotates along the x axis simultaneously with the OAT interaction. The TNT dynamics is experimentally studied from the starting point of a spin coherent state pointing in the $+x$ or $-x$ direction. The interaction is suddenly switched to a finite value of $\Lambda = N \chi / \Omega$ in the presence of linear coupling. The TNT dynamics can be described as the evolution of an effective relative-number wave packet.^{16,284} Using two internal hyperfine levels of ${}^{87}\text{Rb}$ atoms, Figs. 8(b)–8(e) shows the TNT dynamics in an experiment with BEC. The nonlinearity of the system is adjusted through Feshbach resonance, while the linear coupling between the two hyperfine states is achieved using radio frequency and microwave fields. With about 400 atoms, the spin squeezing of $\xi_R^2 = -4.5 \pm 0.2$ dB was achieved. Later, spin squeezing with an inferred $\xi^2 = -7.1$ dB (taking into account the reduced mean spin length) with a single BEC and $\xi^2 = -2.8$ dB with up to 10^4 atoms was reported.¹¹³

The generation of extreme spin-squeezed states has attracted a great deal of attention since they can approach the Heisenberg limit. However, to generate extreme spin squeezing, more complex nonlinear interactions such as TACT interactions (76) are required.^{227,256} It is worth noting that the realization of TACT interactions in known quantum systems still has not been achieved. An alternative way is using the TNT dynamics augmenting the OAT interaction with a well-designed sequence of transverse coherent field. Promising analytic proposals based on this idea include transforming OAT to TACT by using a periodic train of $\pm \pi/2$ spin rotation pulses,^{285,286} or a periodically modulated transverse field.²⁸⁷ However, these scheme demand stringent experimental conditions, either requiring a large number of high-precision pulses²⁸⁵ or a high modulation frequency.²⁸⁸ One can also make use of only a few optimized pulses along the mean spin direction, but the required evolution time is greatly prolonged.²⁸⁹ To efficiently generate an extreme spin-squeezed state, one can even seek help from machine learning such as deep reinforcement learning²⁹⁰ and stochastic gradient decent,²⁹¹ which can achieve an optimized

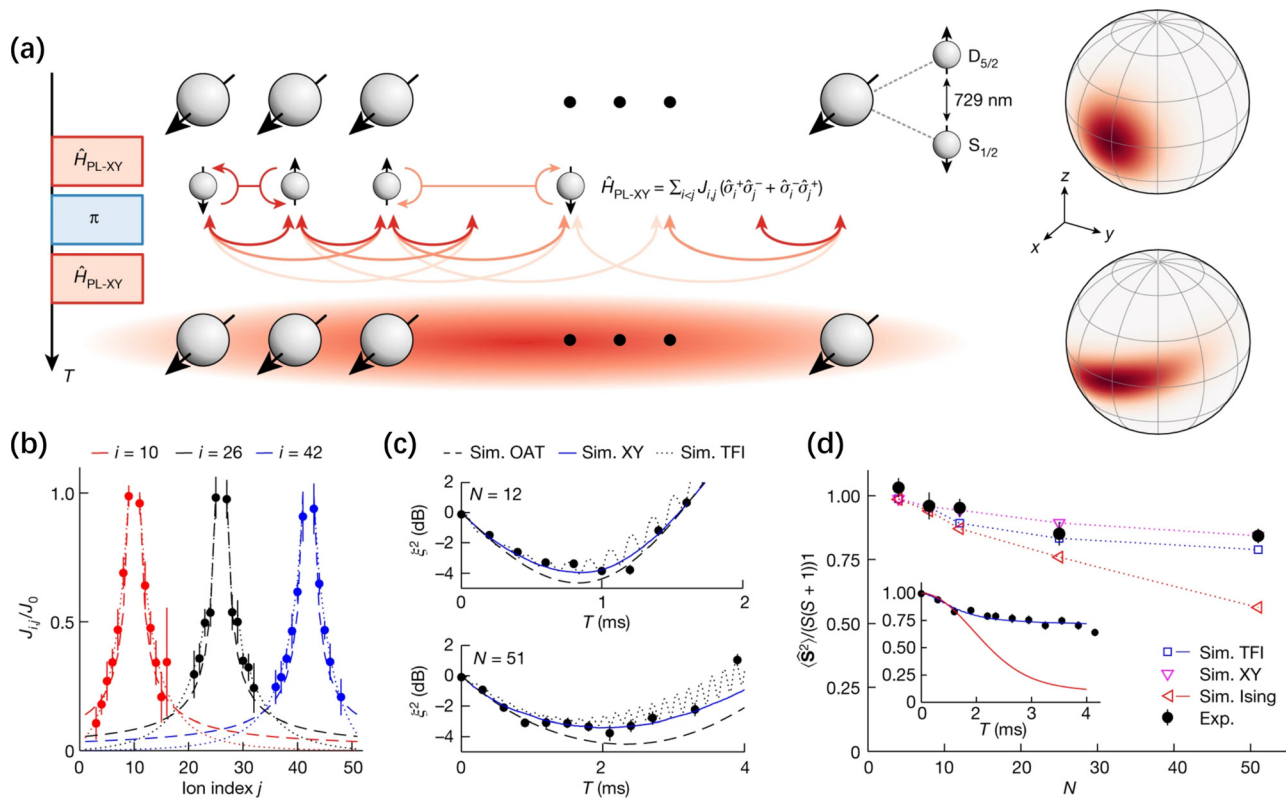


FIG. 15. Generation of spin squeezing with trapped-ion quantum simulator.¹¹² (a) Experimental sequence detailing the process of squeezing the total spin vector by exchange interaction. These interact by power-law XY interactions, where the strength of the connection diminishes as the distance between them increases. The sequence employed involves the integration of interaction pulses (red) and pulses from a global addressing beam (blue) to transform an initial spin coherent state into a spin-squeezed state, as seen on the generalized Bloch sphere. (b) The spin-spin couplings J_{ij} were measured in a 51-ion chain. The couplings were fitted using a power-law interaction with an approximate value of $\alpha \approx 0.9$. The anticipated coupling for the given mode structure and laser detuning is represented by the dashed line. (c) The squeezing measurement is shown vs the interaction time for two different scenarios. In the first scenario, the value of α is about 1, J_0 is equal to 560 rad s⁻¹, and the chain consists of 12 ions. In the second scenario, the value of α is around 0.9, J_0 is equal to 216 rad s⁻¹, and the chain consists of 51 ions. Numerical calculations are conducted to compare the dynamics of the XY model (represented by a solid blue line) with the dynamics in the presence of a finite transverse field (represented by a dotted black line). Additionally, theoretical results for the OAT model (represented by dashed black lines) is considered, including the decoherence. (d) The total spin, which is measured at the point of maximum spin-squeezing in the XY model and then normalized by its maximum value. The collective spin of 51 ions is displayed as a function of interaction time T . Theoretical findings for the Ising models, both without (red line) and with (blue line) a transverse field, are also shown for comparison. Reproduced with permission from Franke *et al.*, Nature **621**, 740 (2023).¹¹² Copyright 2023 Springer Nature.

15 February 2025 20:03:28

policy and providing perspectives and solutions that is difficult to find with analytic approach.

In cavity-QED systems, it was shown that effective two-axis twisting Hamiltonians can be realized by applying bichromatic lasers.²⁹² Spin squeezing of the atoms in the absence of dissipation can reach the ideal Heisenberg limit. However, the attainable spin squeezing is limited by collective decay and this scheme may be suited for Rydberg blockade system without strong collective decay. By using cavity-assisted Raman transitions, tunable two-axis spin model and spin squeezing may be realized in two cavities with all parameters can be tuned independently.²⁹³ The two-axis-twisting spin squeezing may also be generated by multipass quantum erasure, which may be extendable to an optical ring cavity system.²⁹⁴

Except for OAT and TACT interactions, the more general form of the quadratic collective-spin interaction can be described by the Lipkin–Meshkov–Glick (LMG) model.^{93,295–298} A way to implement

general LMG model with independent multi-parameter control as well as direct spin squeezing by both TACT and OAT is proposed, with a BEC in a ring trap with periodic angular modulation of the external potential and of the inter-particle interactions.²⁹⁹ It is also found that the squeezing properties are determined by the initial states and the anisotropic parameters. To achieve the Heisenberg-limited spin squeezing, a pulse rotation scheme is proposed to transform the model into a two-axis twisting model,³⁰⁰ while in generic coupled spin systems with collective spin–spin interactions, a universal scheme by continuous drivings is also proposed.³⁰¹

In a spin-1 BEC, the spin-squeezed ground states are recently demonstrated using a double-quench method with a final Hamiltonian tuned close to the quantum critical point.³⁰² It is related to a kind of shortcut to adiabaticity³⁰³ for the fast production of highly entangled states. In contrast to typical nonequilibrium methods by quenching through a QPT, these squeezed ground states are time

stationary. A squeezed ground state with 6–8 dB of squeezing with a constant squeezing angle is demonstrated. The spin squeezing can be maintained for over 2 s at a constant orientation angle and gradually decreases after that due to atom loss. This double-quench method can also be easily adapted to (pseudo) spin $-1/2$ systems such as bosonic Josephson junctions mentioned before.

C. Twin-Fock state

Twin-Fock state is another kind of metrological useful entangled state,^{3,304,305} which belongs to a kind of Dicke states.^{306,307} A Dicke state can be described by a specific Dicke basis $|J, m\rangle = |J+m\rangle_a|J-m\rangle_b$, which is a two-mode Fock state with $J+m$ particles in mode a and $J-m$ particles in mode b , respectively. Thus, a Dicke state has precise relative particle number between the two modes, while the relative phase is completely undefined.³ It was proposed that the depth of entanglement can be detected by using the variance and second moments of the collective spin components, which may be possible to define spin-squeezing parameters for Dicke states.²²² However, it was pointed out that a Dicke state is not spin squeezed.³⁰⁸ The Dicke states have the potential to improve the measurement precision. One can first calculate the QFI and find that

$$F_Q = \frac{N^2}{2} - 2m^2 + N. \quad (95)$$

Clearly, $m = \pm N/2$ is indeed a spin coherent state with $\theta = 0$ or π and the QFI $F_Q = N$ reduces to the case without entanglement, while for $-N/2 < m < N/2$, the QFI $F_Q > N$ indicates the metrological usefulness.

In particular, when $m = 0$ with N an even number, it corresponds to a twin-Fock state

$$|\Psi\rangle_{TWIN} = |N/2, 0\rangle = |N/2\rangle_a|N/2\rangle_b, \quad (96)$$

which is a two-mode Fock state with definite equal particle number in both modes. According to Eq. (95), the QFI for a twin-Fock state becomes $F_Q = N^2/2 + N$. When the particle number is sufficiently large $N \gg 1$, $F_Q \approx N^2/2$, the ultimate phase measurement precision bound can be

$$\Delta\phi \geq 1/\sqrt{F_Q} \sim \frac{\sqrt{2}}{N}, \quad (97)$$

approaching the Heisenberg scaling with a factor of $\sqrt{2}$ above the exact Heisenberg limit.

For a twin-Fock state, applying a $\pi/2$ pulse can convert it to a state with well-defined relative phase,

$$|\psi_{AS}\rangle = \sum_{k=0}^{N/2} (-1)^{N/2-k} \sqrt{\frac{1}{2^N} C_k^{2k} C_{N/2-k}^{N-k}} |N/2, -N/2+2k\rangle, \quad (98)$$

which is called the arcsine state³⁰⁵ and can be visualized as a ring around the equator of the generalized Bloch sphere. Then, accumulating phase ϕ between two modes and applying another $\pi/2$ pulse can finalize a whole Ramsey process. In practice, one cannot directly exploit the population difference measurement to extract the phase information since $\langle \hat{J}_z \rangle$ always equals 0. An effective way to extract the phase is using the square of the population difference \hat{J}_z^2 . When $\phi \approx 0$, one can find that \hat{J}_z^2 can attain the ultimate phase measurement

precision bound of the twin-Fock state.¹¹⁷ Theoretically, it was proposed that the parity measurement $\hat{\Pi} = (-1)^{N-\hat{J}_z}$, which distinguishes the population number in one mode either even or odd is also capable to estimate ϕ .³⁰⁵ However, in systems with large particle number, parity measurement is not feasible to be realized in experiments.

In spinor BECs, colliding atoms can exchange spin. The spin-exchange collisions can generate entangled atom pairs, which is suitable for generating twin-Fock state.^{117,131} The many-body Hamiltonian for a spin-1 BEC under the spin-exchanging interaction can be expressed as follows:

$$H_{SM} = 2c(\hat{a}_0^\dagger \hat{a}_0^\dagger \hat{a}_1 \hat{a}_{-1} + \hat{a}_0 \hat{a}_0 \hat{a}_1^\dagger \hat{a}_{-1}^\dagger) + [q + c(2\hat{N}_0 - 1)](\hat{N}_{+1} + \hat{N}_{-1}), \quad (99)$$

where \hat{a}_{m_F} ($\hat{a}_{m_F}^\dagger$) denotes annihilation (creation) operator and $\hat{N}_{m_F} = \hat{a}_{m_F}^\dagger \hat{a}_{m_F}$ is the atom number in m_F component with the total atom number $N = \sum_{m_F} N_{m_F}$ with $m_F = 0, \pm 1$. The Hamiltonian is obtained under the assumption of all the three spin components being in the same spatial wavefunction $\phi(\vec{r})$. $c = \frac{2\pi(a_2 - a_0)}{3m} \int d\vec{r} |\phi(\vec{r})|^4$ denotes spin-dependent collision energy where atoms in $m_F = 0$ can be transferred to $m_F = \pm 1$ in pairs and vice versa. Here, m is the atomic mass, and a_0 and a_2 denote the s-wave scattering length for total spin $G = 0$ and $G = 2$ allowed by two-particle collisions, respectively.³⁰⁹ $c < 0$ ($c > 0$) corresponds to ferromagnetic (antiferromagnetic) interaction, respectively.³¹⁰ q is an effective quadratic Zeeman shift, which can be tuned by the external magnetic field (proportional to the square of magnetic field strength) or near-resonant microwave dressing field.¹³¹ In the language of angular momentum with conserved magnetization $\hat{N}_{+1} - \hat{N}_{-1} = 0$, the Hamiltonian of Eq. (99) can be rewritten as follows:

$$H_{SM} = c\hat{L}^2 - q\hat{N}_0, \quad (100)$$

where $\hat{L} = \{\hat{L}_x, \hat{L}_y, \hat{L}_z\}$, $\hat{L}_\mu = \sum_{m,n} \hat{a}_m^\dagger [f_\mu]_{mn} \hat{a}_n$ ($\mu = x, y, z$ and $m, n = 0, \pm 1$) with $[f_\mu]_{mn}$ the matrix element for spin-1 angular momentum. The ground state of Hamiltonian with Eq. (99) is determined by the competition between c and q . It is convenient to express the system state in the three-mode Fock basis $|N-2k\rangle_0|k\rangle_{-1}|k\rangle_{+1}$ with $k = 0, 1, \dots, N/2$.

For a ferromagnetic BEC with $c < 0$, the ground state can be divided into three distinct phases. For $q \gg 2|c|$, the ground state $|N\rangle_0|0\rangle_{-1}|0\rangle_{+1}$ is in the polar phase with all atoms condensed in the $m_F = 0$ component. For $q \ll -2|c|$, the ground state $|0\rangle_0|N/2\rangle_{-1}|N/2\rangle_{+1}$ becomes a twin-Fock state with the atoms equally partitioned into the $m_F = \pm 1$ components. In the middle, two critical points $q = \pm 2|c|$ correspond to the broken-axisymmetry phase whose ground state acquires a transverse magnetization, spontaneously breaking the SO(2) symmetry of the system.

To generate a twin-Fock state, one can start in the polar phase and ramp down $q(t)$ adiabatically from $q \gg 2|c|$ to $q \ll -2|c|$ crossing the two critical points $q = \pm 2|c|$.³¹¹ At the QPT points, the energy gap $\Delta E \sim 1/N^{1/3}$. The energy gap decreases slowly with the total particle number N , which suggests the possibility to maintain the adiabaticity even for $N \sim 10^5$. It had been demonstrated that near-deterministic generation of a twin-Fock state with more than 10 000 atoms can be achieved with ⁸⁷Rb BEC as shown in Fig. 16.¹³¹ Later, in a subsequent experiment,¹³² an interferometric precision of 2.42 dB

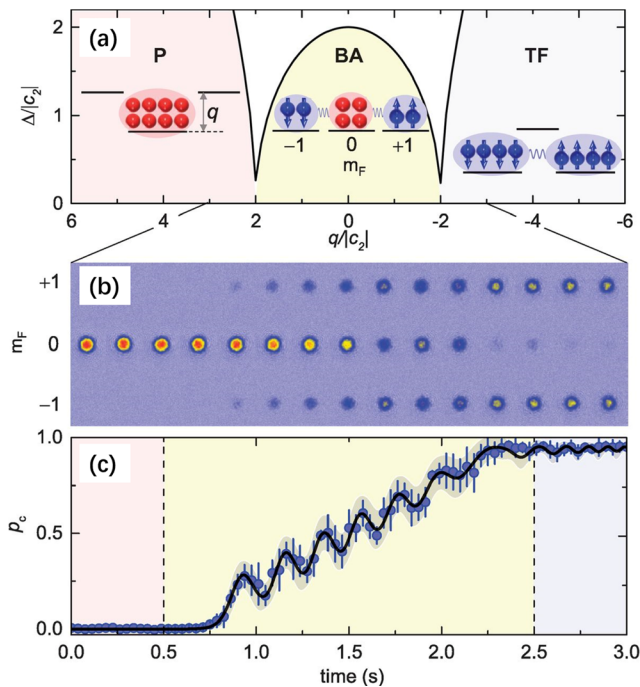


FIG. 16. Generation of twin-Fock state via adiabatic sweeping.¹³¹ (a) The thick black solid line denotes the gap Δ between the first excited and the ground state of Hamiltonian. The two minima at $q = \pm 2|c_2|$ defines three quantum phases, illustrated by their atom distributions in the three spin components. Here, c_2 is the same as the spin-dependent collision energy c . The first-order Zeeman shifts are not shown because they are inconsequential for a system with zero magnetization. (b) Absorption images of atoms in the three spin components after Stern–Gerlach separation, showing efficient conversion of a condensate from a polar state into a twin-Fock state by adiabatic sweeping. (c) Conversion efficiency as a function of time. Reproduced with permission from Luo *et al.*, Science **355**, 620 (2017).¹³¹ Copyright 2017 The American Association for the Advancement of Science.

beyond the three-mode SQL, using balanced spin-1 (three-mode) Dicke states containing thousands of entangled atoms are demonstrated. The input quantum states are also deterministically generated by controlled QPT and exhibit close to ideal quality. This work also demonstrated an interferometric precision of 8.44 dB beyond the two-mode SQL.

For an antiferromagnetic BEC with $c > 0$, the system exhibits two phases of ground state. In the limit of $N \rightarrow \infty$, the ground state is a polar state $|N\rangle_0|0\rangle_{-1}|0\rangle_{+1}$ when $q > 0$ and a twin-Fock state $|0\rangle_0|N/2\rangle_{-1}|N/2\rangle_{+1}$ when $q < 0$. For a finite total particle number N , the minimal energy gap $\Delta E \sim 1/N$ occurs at the critical point $q/c = 3.7688/N^2$, which is close to $q = 0$ if N is large.¹⁰⁴ Ideally, by adiabatically tuning the effective quadratic Zeeman energy q from positive infinity to negative infinity, the twin-Fock state can be generated. However, since the energy gap decreases inversely proportional to N , which drops much faster than the one in a ferromagnetic spin-1 BEC, the adiabatic evolution is difficult to realize in experiment. It was suggested that utilizing the adiabatic and multilevel-oscillation method,¹⁰⁴ the high-fidelity twin-Fock state can be efficiently generated. By partially replacing the adiabatic evolution near the QPT point with multi-level oscillations, this method accelerates the state generation process

and relaxes the requirement on the control accuracy of quadratic Zeeman splitting from microgauss to milligauss.

In this many-body system with Eq. (100), excited-state quantum phase transitions (ESQPTs) can also be appealing, which refers to quantum criticality aroused in ground state. The existence of QPTs and ESQPTs in an antiferromagnetic spin-1 condensate are shown and their correspondence with dynamical phase transition is demonstrated, which can be characterized by the QFI.³¹² The dynamical phase transition with the condensate initially prepared in a spin coherent state can be used to probe the quantum criticality in excited states, which gives rise to a peak value of the QFI. It can also be used to implement sub-SQL estimation on the effective quadratic Zeeman energy q . It is interesting to note that the ground-state phase transitions from symmetry-broken states to the symmetry-restored spin-singlet state can also be indicated by the dynamical phase transition.

In the approximation that $N_0 \approx N \gg 1$, the initial condensate of $m_F = 0$ can serve as an unlimited pump source for parametric amplification of the output modes $m_F = \pm 1$. In this case, one can make use of the parametric approximation $\hat{a}_0 \approx \sqrt{N_0}$ and the Hamiltonian (99) becomes

$$H_{SM} \approx A(\hat{a}_1\hat{a}_{-1} + \hat{a}_1^\dagger\hat{a}_{-1}^\dagger) + B(\hat{a}_1^\dagger\hat{a}_1 + \hat{a}_{-1}^\dagger\hat{a}_{-1}), \quad (101)$$

where $A = 2cN_0$ and $B = q + c(2N_0 - 1)$. Evolving from $|0\rangle_{+1}|0\rangle_{-1}$ under Hamiltonian in the form of Eq. (101), a two-mode squeezed vacuum state (a superposition state of multiple twin-Fock state with different total particle number) can be obtained.¹⁷⁵

In particular for the resonance case with $B = 0$, the spin-mixing Hamiltonian becomes

$$H_{SM} = 2cN_0(\hat{a}_1\hat{a}_{-1} + \hat{a}_1^\dagger\hat{a}_{-1}^\dagger), \quad (102)$$

and the evolved state can be calculated as follows:

$$|\psi_{SM}(t)\rangle = \sum_{n=0}^{\infty} \frac{(-it\text{anh}r)^n}{\cosh r} |n\rangle_{+1} |n\rangle_{-1}, \quad (103)$$

where $r = 2cN_0 t$. Projecting onto a certain total particle number $2n = N$, one can immediately get the twin-Fock state $|N/2\rangle_{+1}|N/2\rangle_{-1}$.

The quantum interferometry with twin-Fock state had been experimentally demonstrated with spin-1 BEC via spin mixing, as shown in Fig. 16.¹¹⁷ In the experiment, spin dynamics in BECs was used to create large ensembles of pair-correlated atoms with an interferometric sensitivity beyond SQL. The experiment starts with creating a ^{87}Rb condensate of 2.8×10^4 atoms in the hyperfine state $|F = 2, m_F = 0\rangle$ in an optical dipole trap. Then, the spin-exchange collision gradually produces correlated pairs of atoms with spins up and down. The total number of the correlated pairs of atoms in $|F = 2, m_F = \pm 1\rangle$ increases exponentially with time due to spin mixing. Afterward, the trap is switched off and the three hyperfine states are split by a strong magnetic field gradient, and all three hyperfine states are recorded by absorption imaging. As the hyperfine states $|F = 2, m_F = \pm 1\rangle$ are generated in pairs, twin-Fock state in these two modes is prepared. The twin-Fock state was effectively obtained by post-selection of a certain particle number.

Spin-mixing dynamics in cold atoms can also be used to realize a SU(1, 1) interferometer,^{313,314} which is analogous to parametric down-conversion in optics. As shown in Fig. 3(b), for spin-1 BEC, the spin-exchanging collision plays the role of Kerr nonlinearity, and the condensate atoms in $m_F = 0$ can be regarded as the optical pump field. The atoms that transferred to $m_F = \pm 1$ correspond to the signal and

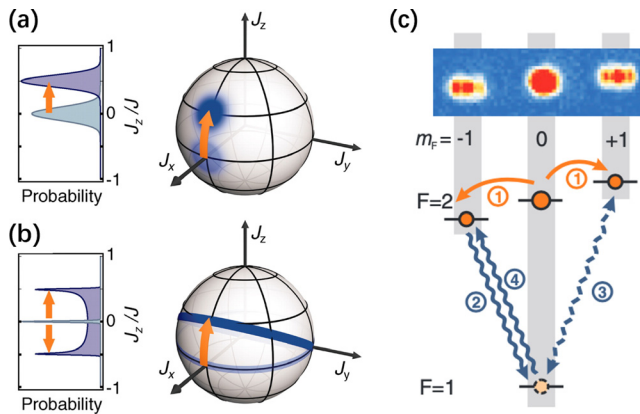


FIG. 17. Matter-wave interferometry with twin-Fock state generated through spin-mixing dynamics.¹¹⁷ (a) An unentangled spin coherent state and the corresponding state after rotation. (b) An input twin-Fock state and the corresponding state after rotation. (c) Schematic of the sequence of the realization of the beam splitter. Three microwave pulses are sequentially applied to achieve the coupling of the two hyperfine states $|F=2, m_F=\pm 1\rangle$. The total effect is equivalent to a rotation around the x axis by an angle. Reproduced with permission from Lücke *et al.*, Science **334**, 773 (2011).¹¹⁷ Copyright 2011 The American Association for the Advancement of Science.

idler beams. Similar to the optical parametric downconversion, the amplification can be triggered by the fluctuations of spin orientation. Let us indicate with N the total average number of atoms transferred in pairs from a condensate prepared in $m_F=0$ to the initially empty $m_F=\pm 1$ modes. After spin mixing, the system acquires a relative phase $\theta = 2\theta_0 - (\theta_{+1} + \theta_{-1})$ between $m_F=0$ and $m_F=\pm 1$ modes. A second spin-mixing dynamics ends up the interferometer. The final populations in $m_F=0, \pm 1$ depend on θ . A nonlinear SU(1, 1) interferometry with $F=2$ manifold of ^{87}Rb atoms was experimentally demonstrated.¹⁴⁹ The phase imprinting is achieved via adding a second-order Zeeman shift and readout by counting the mean atom number in $m_F=\pm 1$. In addition, if one apply a linear coupling among the $m_F=0, \pm 1$ before and after phase imprinting, realizing the so-called “pumped-up” SU(1, 1) interferometer,¹⁵⁰ the measurement precision may be further improved.

D. Spin cat states

Spin cat states are promising candidates for achieving Heisenberg-limited quantum metrology.^{122,146} A spin cat state is a typical kind of macroscopic superposition of spin coherent states (MSSCS).^{315–317} Generally, an MSSCS is a superposition of multiple spin coherent states,^{317–320} which can be written in the form of

$$|\Psi(\theta, \varphi)\rangle_M = \mathcal{N}_C (|\theta, \varphi\rangle + |\pi - \theta, \varphi\rangle), \quad (104)$$

where \mathcal{N}_C is the normalization factor and $|\theta, \varphi\rangle$ denotes a spin coherent state. Here, without loss of generality, we assume $\varphi=0$ and expressing in terms of Dicke basis

$$|\Psi(\theta)\rangle_M = \mathcal{N}_C \left[\sum_{m=-J}^J c_m(\theta) (|J, m\rangle + |J, -m\rangle) \right]. \quad (105)$$

Since $c_m(\theta) = c_{-m}(\pi - \theta)$, the coefficients are symmetric about $m=0$.

The properties of the MSSCS depend on θ , see Fig. 18. When $\theta = \pi/2$, it corresponds to a spin coherent state $|\pi/2, 0\rangle$. As θ decreases, the two superposition spin coherent states become separated. When $\theta \leq \theta_c \equiv \sin^{-1}\{2[(J-1)!^2]^{1/2J}\}$ is sufficiently small,^{122,146} the two spin coherent states become quasi-orthogonal (or orthogonal), and the MSSCS can be regarded as a spin cat state. In this case, we abbreviate the spin cat states as $|\Psi(\theta)\rangle_{\text{CAT}}$, and it can be approximated as follows:

$$\begin{aligned} |\Psi(\theta)\rangle_{\text{CAT}} &\approx \frac{1}{\sqrt{2}} (|\theta, 0\rangle + |\pi - \theta, 0\rangle) \\ &= \frac{1}{\sqrt{2}} \left[\sum_{m=-J}^J c_m(\theta) (|J, m\rangle + |J, -m\rangle) \right]. \end{aligned} \quad (106)$$

Note that spin cat states can be understood as a superposition of GHZ states with different spin length. Particularly, when $\theta=0$, it reduces to a GHZ state, i.e., $|\Psi(0)\rangle_{\text{CAT}} = \frac{1}{\sqrt{2}} (|J, -J\rangle + |J, J\rangle)$. The expectation of \hat{J}_z for a spin cat state $|\Psi(\theta)\rangle_{\text{CAT}} \langle \Psi(\theta) | \hat{J}_z | \Psi(\theta) \rangle_{\text{CAT}} = \sum_m m c_m^*(\theta) c_m(\theta) = 0$. Hence, the variance of a spin cat state becomes $\Delta^2 \hat{J}_z = \langle \Psi(\theta) | \hat{J}_z^2 | \Psi(\theta) \rangle_{\text{CAT}} = \sum_m m^2 c_m^*(\theta) c_m(\theta)$. The variance can be analytically obtained $\Delta^2 \hat{J}_z \approx \frac{1}{4} N^2 \cos^2 \theta$, which only depends on θ and N . If spin cat state is input for quantum interferometry, the QFI for the output state can be computed as follows:

$$I_Q^{\text{CAT}} = 4\Delta^2 \hat{J}_z \approx N^2 \cos^2 \theta, \quad (107)$$

and the corresponding measurement precision can achieve the Heisenberg-limited scaling $\propto \frac{1}{N \cos \theta}$.

OAT is one of the well-known strategies for generating entanglement in many-body quantum systems. Under the time evolution of

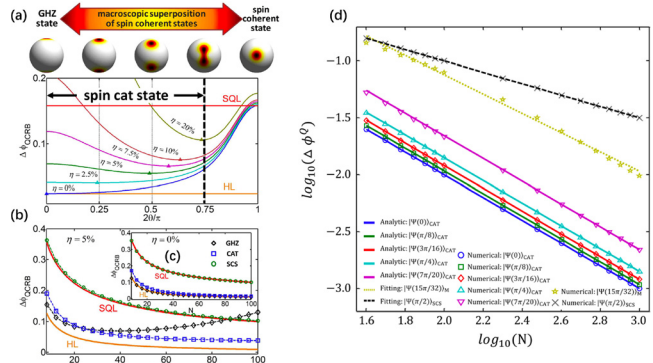


FIG. 18. Measurement precisions offered by spin cat states.^{122,146} (a) The achievable precisions vs θ for different atom loss ratios. The triangles denote the best optimal precisions. The precision becomes worse when the atom loss ratio becomes larger. For nonzero loss ratio, instead of the GHZ state, the optimal state becomes a spin cat states with modest θ . Here, the initial total atomic number $N=40$. The left side of the thick black dashed line indicates the region of spin cat states. (b) The achievable precisions vs the initial total atomic number N for three typical input states (GHZ state, modest spin cat state and the spin coherent state under loss ratio $\eta=5\%$). (c) The measurement precision vs N for the three input states in the absence of loss (i.e., $\eta=0\%$). Reproduced with permission from Huang *et al.*, Sci. Rep. **5**, 17894 (2015).¹²² Copyright 2015 licensed under a Creative Commons Attribution (CC BY) license. (d) The ultimate measurement precision of spin cat states. Reproduced with permission from Huang *et al.*, Phys. Rev. A **98**(1), 012129 (2018).¹⁴⁶ Copyright 2018 American Physical Society.

OAT interaction [Eq. (63)], an initial spin coherent state (without entanglement) can evolve to spin-squeezed states, over-squeezed states, and other kinds of nonclassical states.¹⁶ For evolution times beyond the optimal spin-squeezing time, the Husimi distribution of the evolved state in the OAT model starts to develop into the non-Gaussian regime. In particular, when $\chi t = \pi/2$, it evolves to the GHZ state.³²¹ Recently, in a trapped-ion quantum simulator, the multi-headed cat states are successfully prepared with $N=12$ ions.¹¹² Yet, the generation of spin cat state with this method^{182,318,322,323} requires long evolution times and the generated states are not deterministically prepared. So far, experiments have demonstrated the generation of spin-squeezed^{116,126} and slightly non-Gaussian states¹¹⁸ in ultracold atomic ensembles. The generation of spin cat states in an engineered Dicke model may also be achieved.³²⁴ In an appropriate limit of the Dicke model, one can obtain OAT dynamics that leads to the generation of spin cat states. Additionally, the quantum jump trajectories that generate “kitten” states in a random fashion are investigated. In addition, the effects of decoherence are also explored on spin cat state generation and the experimental feasibility in trapped ions and atom ensembles with cavity-mediated Raman transitions is discussed.

An effective and deterministic way to generate spin cat states is the adiabatic evolution.^{6,122,325} As shown in Fig. 19, adiabatic evolution crossing QPTs can be used for generating non-Gaussian entangled states. The process can be described by a time-dependent Hamiltonian³²⁵

$$H_{BS1}(t) = R_1(t)H_1 + R_2(t)H_2. \quad (108)$$

Here, the Hamiltonians H_1 and H_2 are interpolated with the time-varying parameters $R_1(t)$ and $R_2(t)$. One can choose proper Hamiltonians such that the ground state of $R_1(0)H_1$ is non-degenerate, while the ground state of $R_2(T)H_2$ at time T is multi-fold degenerate. Defining the ratio $\lambda(t) = R_1(t)/R_2(t)$, there exists a QPT at the critical point λ_c that is, $R_1(t)H_1$ dominates the system when $|\lambda(t)| > |\lambda_c|$ and $R_2(t)H_2$ dominates the system when $0 \leq |\lambda(t)| < |\lambda_c|$. Thus, starting from the non-degenerate ground state of $R_1(0)H_1 + R_2(0)H_2$, an entangled ground state can be obtained with high fidelity if λ is adiabatically swept through λ_c . For instance,

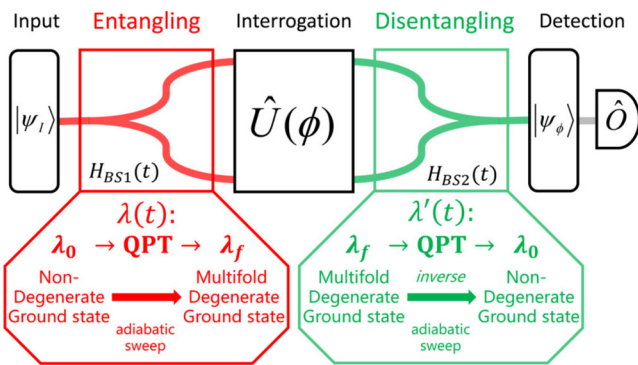


FIG. 19. Schematic of quantum phase estimation via driving through quantum phase transitions. The two beam splitters are achieved by driving the parameter forwardly and inversely across the critical point.³²⁵ In the first beam splitter, an entangled state can be prepared while in the second beam splitter, the state is gradually disentangled. Reproduced with permission from Huang *et al.*, Phys. Rev. A **97** (3), 032116 (2018). Copyright 2018 American Physical Society.

preparing the ground state of a BEC trapped in a double-well potential with attractive interaction,³²⁶ or in an ion crystal.³²⁷ By adiabatic sweeping the control parameter across the spontaneous symmetry-breaking transition, spin cat states with different degree of entanglement can be prepared. However, due to the degeneracy of the spectrum, this method may be fragile to symmetry-breaking perturbations and finite temperature.^{328,329} It should be mentioned that, by driving the parameter inversely across the critical point again, one can realize recombination as a kind of nonlinear detection, which will be illustrated in Sec. IV C.

For the Hamiltonian of Eq. (77) with $\delta=0$, when $|\Omega/N\chi| \gg 1$, the system ground state is an SU(2) spin coherent state. The sign of χ determines the properties of the ground state when Ω is not large enough. When $\chi > 0$ and $|\Omega/N\chi| \ll 1$, the ground state is a spin-squeezed state, while for $\chi < 0$, the ground state becomes a spin cat state when $|\Omega/N\chi| \ll 1$.²⁹⁸ To generate a spin cat state, it is natural to prepare the ground state of Hamiltonian (77) in the limit of $|\Omega/N\chi| \ll 1$ with $\chi < 0$. For atomic BEC system, the negative twisting strength can be achieved by tuning the interspecies s-wave scattering length via Feshbach resonance.³³⁰

Under the transformation $\hat{a}(\hat{b}) \rightarrow \hat{b}(\hat{a})$, $\hat{J}_x \rightarrow \hat{J}_z$, $\hat{J}_z \rightarrow -\hat{J}_z$, the Hamiltonian of Eq. (77) with $\delta=0$ remains unchanged. Thus, this Hamiltonian possesses a parity symmetry and it guarantees the symmetry-protected adiabatic evolution.^{331,332} Adiabatic evolution occurs due to the presence of a finite minimum energy gap between instantaneous eigenstates of the same parity. With negative χ , one can generate spin cat states via the adiabatic evolution. Initially, we set $\Omega(0)$ to be sufficiently large, and the ground state is nearly a spin coherent state along x axis with even parity. By sweeping the Rabi frequency across the critical point $|\Omega/N\chi| = 1$, the two lowest eigenstates change from non-degenerate to degenerate. Through adiabatically sweeping $\Omega(t)$ to zero, the evolved state will stay in the instant ground state and spin cat states can be prepared.

For the sweeping, one can linearly change $\Omega(t) = \Omega(0) + vt$ from the non-degenerate regime across to the degenerate regime with the fixed sweeping rate v . If v is sufficiently small, the adiabatic evolution of the ground state can still be achieved with high fidelity. However, this linear sweeping scheme is not time-saving. In order to accelerate ground state adiabatic evolution, the sweeping rate can be modified temporally in accordance with the instantaneous energy gaps separating the ground state and the second excited state (both possessing the same parity), while maintaining the adiabatic parameter ε . It is one of the nonlinear sweeping schemes. Since ε is fixed, it is called adiabatic-parameter-fixed sweeping.³³² It is shown that adiabatic-parameter-fixed sweeping can generate spin cat states with high fidelity.³³³

In this scheme, the time-varying Rabi frequency

$$\Omega(t) = \Omega(0) + \int_0^t v(t')dt', \quad (109)$$

where $v(t) = \dot{\Omega}(t)$ is the instant sweeping rate of the Rabi frequency. Since the parity symmetry, for adiabatic-parameter-fixed sweeping,

$$v(t) = \frac{\varepsilon[E_1(t) - E_3(t)]^2}{|\langle\phi_1(t)|\hat{J}_x|\phi_3(t)\rangle|.} \quad (110)$$

Here, $E_1(t)$ and $E_3(t)$ represent the energy of instant ground state $\phi_1(t)$ and the second excited state $\phi_3(t)$ of Hamiltonian with Eq. (77),

respectively. Based on the adiabatic-parameter-fixed sweeping scheme, the total time for adiabatic evolution can be reduced compared with the naive linear sweeping. The fidelities can exceed 0.9 with $\varepsilon = 0.05$ and total atom number $N = 100$.

However, the adiabatic sweeping still demands the control parameter vary slowly to let the evolved state follow the instant ground state of the system. Due to the limited coherence time in experiments, adiabatic process may be time-consuming and not easy to realize. Shortcut to adiabaticity is a well-known approach for quickly achieving the target state.^{106,303,334} However, for many-body quantum state generation, this method is not simple and may necessitate some approximations (such as in the semiclassical limit) in order to get the analytical best solution. To accelerate state preparation process, TNT dynamics is proposed in which an additional rotation is introduced along with OAT interaction as shown in Sec. III B. One may also use TNT dynamics with time-dependent rotation sequence for the preparation of spin cat states. Moreover, to obtain the better performance, one can apply piecewise time-modulation of rotations designed via machine optimization.³³³ When comparing adiabatic evolution, the fidelity to the spin cat states can be increased while also significantly reducing the needed evolution time. It does not require large modification to the existing experimental setups and can be realized with state-of-the-art techniques in a BEC system or an optical cavity system with light-mediated interactions.

In a spin-1 BEC, which is described by Hamiltonian of Eq. (99), a proposal for generating macroscopic superposition states of a large number of atoms is presented.³³⁵ As shown in Fig. 20, measuring the number of particles in one mode prepares with large probability highly entangled macroscopic superposition states in the two remaining modes. The macroscopic superposition states are heralded by the measurement outcome. This protocol is robust under realistic conditions in current experiments, including finite adiabaticity, particle loss, and measurement uncertainty. It is demonstrated that MSSCS of a large number of atoms, $N > 100$, can be heralded with large success probability-in a ferromagnetic spin-1 BEC. First, one can consider the preparation of the ground state of the three-mode condensate by the quasiadiabatic crossing over a QPT point, as demonstrated experimentally.^{131,336} Once the ground state is prepared, MSSCS can be generated stochastically, with up to 90% probability, by measuring the number of

atoms in one of the modes. The state preparation is nondestructive—the spin cat states can be manipulated after its generation. Remarkably, a numerical simulation of the proposed procedure reveals that the structure of the MSSCS survives under experimentally realistic conditions. Nonadiabatic crossing of the QPT and particle loss reduce the Fisher information to about 50% of its ideal value, which still implies significant entanglement and metrological sensitivity above the classical limit.

In an optical cavity with multi-atom ensemble, an entanglement-creation scheme named entanglement amplification is proposed, converting unentangled states into entangled states and amplifying less-entangled ones to maximally entangled GHZ states whose fidelity is logarithmically dependent on the atom number and robust against common experimental noises.¹²⁴ As shown in Fig. 21, the scheme starts with a multi-atom ensemble initialized in a spin coherent state. By shifting the energy of a particular Dicke state, the Hilbert space of the ensemble is broken into two isolated subspaces to tear the spin coherent state into two components so that entanglement is introduced. After that, the isolated subspaces are utilized to further enhance the entanglement by coherently separating the two components. By single-particle Rabi drivings on atoms in a high-finesse optical cavity illuminated by a single-frequency light,³³⁷ 2000-atom GHZ states can be created with a fidelity above 80% in an experimentally achievable system. This may make resources of ensembles at Heisenberg limit practically available for quantum metrology.

In experimental trapped-ion systems, GHZ state can also be generated and used for precision measurement. In 2001, an experiment demonstrated that the sensitivity of rotation angle estimation with a Ramsey spectroscopy can be improved by using entangled trapped ions.³³⁸ The experiment used two ${}^9\text{Be}^+$ ions that are confined in a linear radio frequency trap. Two hyperfine states $|F = 1, m_F = -1\rangle \equiv |\uparrow\rangle$ and $|F = 2, m_F = -2\rangle \equiv |\downarrow\rangle$ form the basis of an effective spin-1/2 system. $|\uparrow\rangle$ and $|\downarrow\rangle$ are coupled by two-photon Raman transitions. The detection of the ions in states $|\uparrow\rangle$ and $|\downarrow\rangle$ is done by state-sensitive fluorescence. The use of entangled states for parity measurement and Ramsey spectroscopy has been demonstrated with $|\Psi_P\rangle = (e^{i\phi}|\uparrow\uparrow\rangle + |\downarrow\downarrow\rangle)/\sqrt{2}$ and $|\Psi_R\rangle = (|\uparrow\downarrow\rangle + |\downarrow\uparrow\rangle)/\sqrt{2}$, respectively. The experimental data show the measurement sensitivity

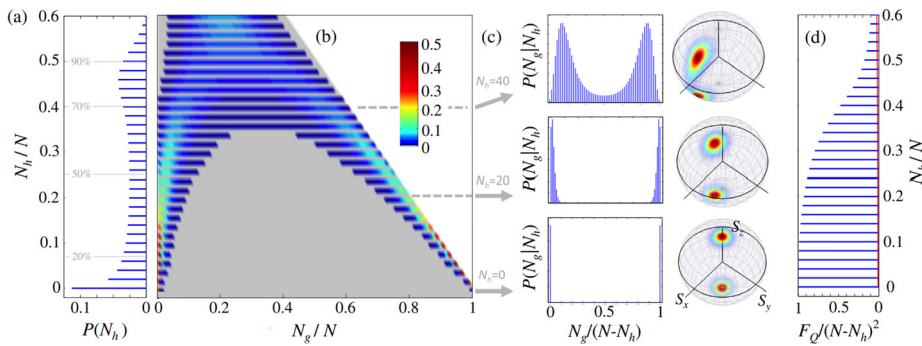


FIG. 20. Stochastic generation of spin cat states under ideal conditions.³³⁵ (a) The probability of measuring N_h particles in the ground state is represented by bars. The dashed lines represent cumulative probability thresholds. (b) Conditional probability to find N_g particles in the g mode given a heralded measurement of N_h particles in the h mode. The g and h modes are defined as the symmetric and antisymmetric combinations of $|m_F = +1\rangle$ and $|m_F = -1\rangle$. (c) Examples of probability (left) and Husimi distributions on the Bloch sphere (right) of rotated heralded states for different values of N_h . (d) QFI of the heralded states as a function of N_h . In all panels $N = 100$. Reproduced with permission from Pezze et al., Phys. Rev. Lett. **123**(26), 260403 (2019). Copyright 2019 American Physical Society.

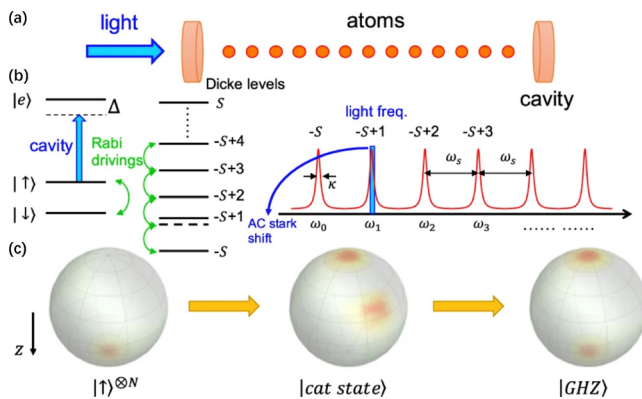


FIG. 21. Entanglement amplification for GHZ state generation with atomic ensemble trapped in an optical cavity.¹²⁴ (a) A collection of N atoms is connected to a high-finesse optical cavity. The cavity is exposed to a single-frequency light that can be switched on or off. (b) The atomic levels and the spectra of cavity transmission. The Rabi drivings pair the states $| \uparrow \rangle$ and $| \downarrow \rangle$. The cavity mode exhibits coupling between the state $| \uparrow \rangle$ and $| e \rangle$, characterized by a detuning Δ . Since the intense connection between the atom and the cavity, each atom in the state $| \uparrow \rangle$ causes a shift in the resonance of the cavity. This shift is equal to $\omega_s = g^2/\Delta$, which is more than κ . Therefore, the incoming light with a frequency of $\omega_1 = \omega_c + \omega_s$ only alters the energy of the Dicke state $| -S + 1 \rangle$ and establishes a boundary in the Hilbert space at this state with S the total spin length. (c) The Husimi-Q function is observed on the generalized Bloch sphere before, during, and after the process of entanglement amplification. Reproduced with permission from Zhao et al., npj Quantum Inf. 7, 24 (2021).¹²⁴ Copyright 2021 licensed under a Creative Commons Attribution (CC BY) license.

is improved beyond the SQL and close to the Heisenberg limit. Later, the Ramsey spectroscopy with three entangled ${}^9\text{Be}^+$ ions in the GHZ state was demonstrated. The experimental data show that the spectroscopic sensitivity is 1.45(2) times as high as that of a perfect experiment with three independent ions, which approaches the Heisenberg limit.³³⁹ Then, the precision spectroscopy of a pair of trapped Ca^+ ions in a decoherence-free subspace of specifically designed entangled states¹³⁵ was demonstrated. In addition to the enhancement of signal-to-noise ratio in frequency measurements, a suitably designed pair of ions enables atomic clock measurements in the presence of magnetic field noise. Later, there have been many other experiments^{112,340,341} about the preparation of GHZ state with trapped atomic ions for quantum metrology.

Multi-particle GHZ states have also been experimentally generated in other quantum systems. The deterministic generation of an 18-qubit GHZ state and multi-component atomic spin cat states of up to 20 qubits have been demonstrated with a superconducting quantum processor interconnected by a bus resonator.³⁴² By engineering an OAT Hamiltonian, the system of qubits, once initialized, coherently evolves to multi-component atomic spin cat states, which are superpositions of atomic coherent states including the GHZ state at specific time intervals as expected. Moreover, a highly scalable method for producing multipartite cat states, also known as flying cat states, for itinerant microwave photons has also been presented.³⁴³ By reflecting coherent-state photon pulses from a microwave cavity containing a superconducting qubit, flying cat states of microwave photons containing up to four photonic modes are successfully prepared. In addition, the GHZ states of 20 Rydberg atoms have been demonstrated by

exploiting optimal control methods to optimize the preparation time.³⁴⁴ The entanglement manipulation by using GHZ states to distribute entanglement to distant sites in the array has been demonstrated, establishing important ingredients for quantum metrology.

IV. INTERROGATION AND READOUT

Apart from state preparation, interrogation and readout are two important processes in quantum metrology. The interrogation process is provided by a dynamical evolution of the probe, and it determines the QCRB for the parameter θ with a probe state ρ_0 . On the other hand, the readout process determines the CRB and the measurement precision through practical observable measurements. In this section, we will discuss the advancements made in investigating the interrogation and readout processes. Regarding the interrogation process, the signal can either be time-invariant or time-varying. Therefore, we will review both the interrogation process with time-independent Hamiltonians and the one with time-dependent Hamiltonians. Regarding the readout process, we will cover both conventional readout methods and the recent developments in interaction-based readout.

A. Interrogation

The parameters to be estimated are typically embedded within the Hamiltonian or within the dynamics of a physical system. During the interrogation process, these parameters are encoded into quantum states by evolving the probe state ρ_0 under the influence of the corresponding Hamiltonians or physical dynamics, represented by \hat{U}_θ (as shown in Fig. 1). Here, we illustrate the interrogation process with time-independent Hamiltonians^{177,345} and time-dependent Hamiltonians,^{346–349} respectively.

A commonly studied and straightforward example in quantum metrology involves estimating a multiplicative parameter within a Hamiltonian. For example, estimating the parameter θ in a unitary evolution $\hat{U}_\theta = e^{-i\theta\hat{H}}$, where the generator \hat{H} is time-independent. In this case, if a quantum probe with a pure state $\rho_0 = |\Psi\rangle\langle\Psi|$ undergoing a unitary evolution $\hat{U}_\theta = e^{-i\theta\hat{H}}$ with $\theta = \omega T$, the QFI that determines the ultimate measurement precision of ω can be given as $F_\omega^Q = T^2(\Delta\hat{H})^2$ and its maximum is $F_\omega^Q|_{\max} = T^2(\lambda_{\max} - \lambda_{\min})^2$ with λ_{\max} and λ_{\min} , respectively, denoting the maximal and minimal eigenvalues of \hat{H} . For a many-body SU(2) quantum interferometry involving N two-mode particles, one can choose a linear or nonlinear coupling of collective spin operators as the generator \hat{H} .

In most cases, one may choose a linear operator such as $\hat{H} = \hat{J}_z$ as the generator, which is commonly used in quantum metrology¹⁶ including magnetic field measurement,^{72,82,101} frequency measurement,^{59,66,350} and more. The maximal and minimal eigenvalues are $\lambda_{\max} = N/2$ and $\lambda_{\min} = -N/2$, respectively. Thus, the maximum quantum Fisher information is $F_\omega^Q|_{\max} = T^2(\lambda_{\max} - \lambda_{\min})^2 = T^2N^2$, which corresponds to the Heisenberg limit (HL). Achieving the HL with the linear generator $H = \hat{J}_z$ requires the probe to be initialized in a maximally entangled state.

In the case of a nonlinear generator $\hat{H} = (\hat{J}_z)^k$ (where the exponent $k > 1$), the measurement precision can reach a scaling of N^{-k} . When k is an even number, the maximal and minimal eigenvalues of \hat{H} are $\lambda_{\max} = (\frac{N}{2})^k$ and $\lambda_{\min} = 0$, respectively. The corresponding maximum of QFI and QCRB of ω is $F_\omega^Q|_{\max} = T^2(\frac{N}{2})^{2k}$ and

$\omega_{\text{QCRB}} = \frac{2^k}{T} \frac{1}{N^k}$, respectively. When k is an odd number, the maximal and minimal eigenvalues of \hat{H} are $\lambda_{\max} = (\frac{N}{2})^k$ and $\lambda_{\min} = -(\frac{N}{2})^k$, respectively. The corresponding maximum of QFI and QCRB of ω is $F_{\omega}^Q = 4T^2(\frac{N}{2})^{2k}$ and $\omega_{\text{QCRB}} = \frac{2^{k-1}}{T} \frac{1}{N^k}$, respectively. Mathematically, when $k > 1$, the scaling of N^{-k} is better than the Heisenberg scaling N^{-1} for the case of linear generators.^{345,351–353} However, this does not mean that the measurement precision breaks the Heisenberg uncertainty relation. The measurement precision offered by a nonlinear generator still obeys the Heisenberg uncertainty relation. In other words, when we unify the definitions of HL for both linear and nonlinear generators as the ultimate precision limit dictated by the Heisenberg uncertainty relation, the scaling of HL depends on the form of the associated generator. With this unified definition, it should be noted that the HL remains unbreakable regardless of the protocol employed. A realistic possibility for taking advantage of nonlinear generator is the case of $k = 2$, such as a quadratic OAT Hamiltonian $\hat{H} = \chi_z^2$.

Extensive studies have been dedicated to quantum metrology utilizing time-independent Hamiltonians. However, the investigation of time-dependent Hamiltonians is crucial in order to broaden the applicability of quantum metrology to more complex scenarios. Below, we consider the quantum metrology with time-dependent Hamiltonians $\hat{H}_{\theta}(t)$.³⁴⁶ A system is initialized in a state $|\Psi\rangle$ and then evolves under the time-dependent Hamiltonian $\hat{H}_{\theta}(t)$ for a time duration of T , and its final state reads

$$|\Psi_{\theta}(T)\rangle = \hat{U}_{\theta}(T)|\Psi\rangle, \quad (111)$$

where $\hat{U}_{\theta}(T) = e^{-i \int_0^T \mathcal{T} \hat{H}_{\theta}(t) dt}$ is the unitary evolution under the Hamiltonian $\hat{H}_{\theta}(t)$ with the time-ordering operator \mathcal{T} . According to Eq. (9), the QFI of $|\Psi_{\theta}(T)\rangle$ for estimating θ can be written as

$$F_{\theta}^Q = 4 \left[\langle \Psi | \hat{h}_{\theta}^2(T) | \Psi \rangle - \langle \Psi | \hat{h}_{\theta}(T) | \Psi \rangle^2 \right], \quad (112)$$

where $\hat{h}_{\theta}(T) = i \hat{U}_{\theta}(T)^{\dagger} [\partial_{\theta} \hat{U}_{\theta}(T)]$. Therefore, the maximum F_{θ}^Q is the squared gap between the maximum and minimum eigenvalues of $\hat{h}_{\theta}(T)$, similar to the case of a static Hamiltonian. This means that the key to give the optimal estimation precision is finding the maximum and minimum eigenvalues of $\hat{h}_{\theta}(T)$. To obtain the maximum QFI, one can take an alternative approach that breaks the unitary evolution $\hat{U}_{\theta}(T)$ into products of small time intervals dt and takes the limit $dt \rightarrow 0$. That is,

$$\hat{h}_{\theta}(T) = \int_0^T \hat{U}_{\theta}(t)^{\dagger} \partial_{\theta} \hat{H}_{\theta} \hat{U}_{\theta}(t) dt. \quad (113)$$

Thus, one can decompose the global optimization of the eigenvalues of $\hat{h}_{\theta}(T)$ into the local optimizations at each time instant t . As $\hat{U}_{\theta}(t)$ is unitary, $\hat{U}_{\theta}(t)|\psi\rangle$ is a normalized state and the upper bound of $\langle \Psi | \hat{U}_{\theta}(t)^{\dagger} \partial_{\theta} \hat{H}_{\theta}(t) \hat{U}_{\theta}(t) | \Psi \rangle$ must be the maximum eigenvalue $\lambda_{\max}(t)$ of $\partial_{\theta} \hat{H}_{\theta}(t)$ at time t . Consequently, the maximum eigenvalue and the minimum eigenvalue of $\hat{h}_{\theta}(T)$ are bounded by $\int_0^T \lambda_{\max}(t) dt$ and $\int_0^T \lambda_{\min}(t) dt$, respectively. Therefore, the upper bound of the QFI can be given as

$$F_{\theta}^Q(T) \leq \left[\int_0^T (\lambda_{\max}(t) - \lambda_{\min}(t)) dt \right]^2. \quad (114)$$

This indicates that the upper bound of $F_{\theta}^Q(T)$ is determined by the integral of the gap between the maximum and minimum eigenvalues of $\partial_{\theta} \hat{H}_{\theta}(t)$ over the time interval from 0 to T .

From Eq. (114), in the case of a time-independent Hamiltonian $\hat{H}_{\theta} = \theta \hat{H}$, it reduces to $F_{\theta}^Q(T)|_{\max} = T^2(\lambda_{\max} - \lambda_{\min})^2$. For a time-dependent Hamiltonian $\hat{H}_{\theta}(t)$, a convenient way to achieve the upper bound of QFI is to introduce a control Hamiltonian $\hat{H}_c(t)$, which is independent of the parameter θ , to the original Hamiltonian. That is, the system will evolve under the total Hamiltonian is $\hat{H}_{\text{tot}} = \hat{H}_{\theta}(t) + \hat{H}_c(t)$. By applying the control Hamiltonian $\hat{H}_c(t)$, the state evolution under the total Hamiltonian will always stay in the instantaneous eigenstates of $\partial_{\theta} \hat{H}_{\theta}(t)$. To realize the above target, the optimal control Hamiltonian $\hat{H}_c(t)$ can be chosen as follows:

$$\hat{H}_c(t) = \sum_k f_k(t) |\Psi_k(t)\rangle \langle \Psi_k| - \hat{H}_{\theta}(t) + i \sum_k |\partial_t \Psi_k(t)\rangle \langle \Psi_k|, \quad (115)$$

where $f_k(t)$ are arbitrary real functions, and $|\Psi_k\rangle$ is the k th eigenstate of $\partial_{\theta} \hat{H}_{\theta}(t)$. The aim of applying this control Hamiltonian is to guide the state evolution governed by the total Hamiltonian \hat{H}_{tot} , following the paths traced by the instantaneous eigenstates of $\partial_{\theta} \hat{H}_{\theta}(t)$. This approach allows for acquiring the maximum amount of information about θ . Figure 22 illustrates a schematic diagram for the state evolution under the optimal control Hamiltonian $\hat{H}_c(t)$. This control approach can also be extended to multi-particle systems. However, the optimal control Hamiltonian may become more complex and challenging to implement.

By employing the above method, the precision of measuring the field amplitude and frequency of a rotating magnetic field can be significantly improved. Similar ideas of steering quantum state evolution along specific trajectories have also been used in other studies.^{106,354–356} A simple case is that the Hamiltonian is still time-independent but the parameter to estimate is not multiplicative, such

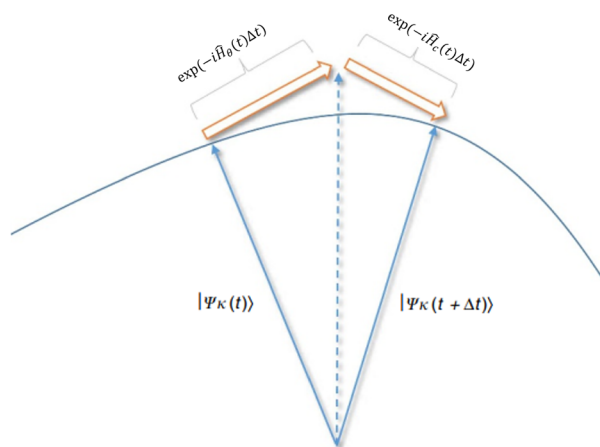


FIG. 22. Optimal Hamiltonian control scheme.³⁴⁶ To achieve the maximal Fisher information, the optimal control Hamiltonian needs to keep the state evolution under the total Hamiltonian \hat{H}_{tot} evolving along the tracks of the eigenstates of $\partial_{\theta} \hat{H}_{\theta}(t)$ at all times t . Reproduced with permission from Pang and Jordan, Nat. Commun. **8**, 041006 (2017).³⁴⁶ Copyright 2017 licensed under a Creative Commons Attribution (CC BY) license.

as a spin-1/2 particle in a DC vector magnetic field.³⁴⁸ In this case, the Hamiltonian can be represented as $\hat{H}_\theta(t) = \hat{H}_\theta$, and one have $|\partial_t \Psi_k(t)\rangle = 0$. Thus, the optimal control Hamiltonian can be chosen as $\hat{H}_c(t) = \sum_k f_k(t)|\Psi_k(t)\rangle\langle\Psi_k| - \hat{H}_\theta(t)$.

In realistic entanglement-enhanced metrology, the time required to prepare entangled states is typically not short.^{357,358} Especially for highly entangled states, the preparation time is comparable with the interrogation time. Hence, the simultaneous state preparation and signal interrogation becomes an effective approach to optimize time utilization in quantum metrology.³⁵⁸ In this approach, it is more advantageous to allocate the entire duration for the entanglement generation and signal interrogation, rather than dividing the time between creating an entangled state and separately using the prepared state for signal interrogation. Intuitively, this approach can enhance sensitivity by accumulating a larger phase shift due to the extended time duration involved. However, it generally depends on the trade-off between entanglement generation and signal interrogation.³⁵⁸ For instance, in the scenario of magnetic field sensing with twisted states, it is more advantageous to allocate the entire duration to the sensing process if the twisting strength is relatively weak or the total time available is limited. However, if the twisting strength is strong, it allows the twisting dynamics and the magnetic field sensing operate concurrently will be more effective. Moreover, chaotic dynamics can be utilized to achieve this purpose and develop the quantum chaotic sensors.^{359,360} Meanwhile, the machine optimized concurrent state preparation and signal interrogation are developed,^{361–363} which can provide better measurement precision in a shorter time compared to traditional schemes.

B. Conventional readout

In addition to the preparation of multi-particle entangled states, the readout of such states poses a significant challenge in achieving entanglement-enhanced quantum metrology. In a SU(2) quantum interferometry, it is usually to measure the population difference $n \equiv n_\uparrow - n_\downarrow$ between the two involved modes $|\uparrow\rangle$ and $|\downarrow\rangle$. The population uncertainty Δn limits the attainable measurement precision $\Delta\theta = \Delta n / (\partial\langle n \rangle / \partial\theta)$. In situations involving non-entangled states, population measurement works well and can achieve the optimal measurement precision provided by the input state. However, when dealing with entangled states, approaching the optimal measurement precision (especially the Heisenberg limit) requires single-particle-resolved state detection. This task becomes progressively more challenging as the number of atoms increases.

For Gaussian entangled states, population measurement can still make the measurement precision beyond the SQL. As an example, inputting a spin-squeezed state and measuring the population difference measurement \hat{J}_z , the measurement precision reads

$$\Delta\theta = \frac{\Delta\hat{J}_z}{|\partial\langle\hat{J}_z\rangle/\partial\theta|} = \frac{\xi_R}{|\sin\theta|\sqrt{N}}, \quad (116)$$

with ξ_R being the squeezing parameter for the input state. If $\theta = \pi/2$, the measurement precision $\Delta\theta$ reaches its minimum $\Delta\theta = \frac{\xi_R}{\sqrt{N}}$. This means that spin-squeezed states may be used to beat the SQL if $\xi_R < 1$. In particular, if the input state is squeezed to $\xi_R \propto 1/\sqrt{N}$, the measurement precision can reach the Heisenberg scaling: $\Delta\theta \propto 1/N$.

For non-Gaussian entangled states, such as twin-Fock states, spin cat states, and over-squeezed states, the population difference measurement cannot fully exploit their nonclassical features and achieve the optimal measurement precisions. To resolve this issue, one can implement the parity measurement $\hat{\Pi} = e^{i\pi b^\dagger b}$. According to the error propagation formula, the measurement precision with parity measurement can be given as follows:^{358,305,364}

$$\Delta\theta = \frac{\Delta\hat{\Pi}}{|\partial\langle\hat{\Pi}\rangle/\partial\theta|}. \quad (117)$$

For a twin-Fock state,³⁰⁵ the phase uncertainty $\Delta\theta$ vs the particle number N approaches the Heisenberg limit $\Delta\theta = 1/(2N)$ when $\theta \rightarrow 0$. For certain values of θ , the measurement precision $\Delta\theta$ may significantly increase for specific total particle numbers, while for other total particle numbers, it continues to approach the Heisenberg limit. For a GHZ state, the measurement precision with parity measurement is always $\Delta\theta = 1/N$, which is independent of the values of θ .³⁵⁸ However, in order to achieve entanglement-enhanced quantum metrology with parity measurement, the requirement of single-particle resolved detection poses a challenge, especially at larger atom numbers, and it also serves as a bottleneck in practical experiments. Moreover, the fragility of quantum entangled states under inevitable sources of noises,^{122,319} such as phase or detection noises, presents a major obstacle that hinders the enhancement of measurement precision.

C. Interaction-based readout

In addition to conventional readout protocols, which involve directly measuring the states output from an interferometer, interaction-based readout protocols have been introduced. In interaction-based readout protocols,^{8,105,111,146–154,365–369} the states output from an interferometer undergo a unitary operation through specific nonlinear interactions before measurement takes place. The introduction of nonlinear operation before implementing measurement efficiently eliminates the need for single-particle resolved detection.

In Fig. 23, we show how interaction-based readout works. In the preparation stage, an unentangled initial state undergoes a unitary evolution \hat{U}_1 into a nonclassical state. Then, the estimated physical parameter θ is encoded onto the state via the interrogation stage, which is described by the unitary operator \hat{U}_θ . The interaction-based readout is then implemented by applying another unitary operator \hat{U}_2 before the final measurement. Therefore, the final state reads

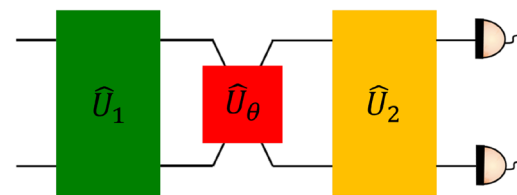


FIG. 23. Schematic of interaction-based readout. First, an unentangled initial state undergoes a unitary evolution \hat{U}_1 into a nonclassical state. Then, the estimated physical parameter θ is encoded onto the state in the interrogation stage via the unitary operator \hat{U}_θ . Finally, another unitary operator \hat{U}_2 is applied before the final measurement.

$$|\Psi_{\text{final}}(\theta)\rangle = \hat{U}_2 \hat{U}_\theta \hat{U}_1 |\Psi_{\text{in}}\rangle. \quad (118)$$

The QFI is just dependent on the unitary operator \hat{U}_1 and the initial state. Although \hat{U}_2 does not alter the QFI, it may affect the CFI when a measurement is made in a particular basis. Specifically, several studies have demonstrated that the protocol with perfectly time reverse the initial unitary operator, i.e., $\hat{U}_2 = \hat{U}_1^\dagger$, the projection measurement onto the initial state is optimal, which can saturate the QCRB.^{148–151,367} The corresponding interferometry also called time-reversed nonlinear interferometry. Meanwhile, the protocols with $\hat{U}_2 \neq \hat{U}_1^\dagger$ can also improve robustness against detection noise.^{152,368–370} Below we introduce these two interaction-based readout protocols.

First, we introduce the interaction-based readout protocols of $\hat{U}_2 = \hat{U}_1^\dagger$ via OAT.¹⁴⁷ The dynamics under an OAT Hamiltonian $\hat{H}_{\text{OAT}}(\chi) = \chi \hat{j}_z^2$ can generate different entangled states. For spins initially polarized along x direction, the lowest-order effect of \hat{H}_{OAT} can generate spin-squeezed state. For a short twisting time, the generated state is a Gaussian state. However, for a long twisting time, the generated state becomes a non-Gaussian state, such as spin cat state and over-squeezed state. In particular, a GHZ state appears at $\chi t = \pi/2$. Then the generated state undergoes a dynamical evolution to encode the information of the parameter θ to be estimated. Before implementing measurement, a unitary operation via another OAT Hamiltonian $\hat{H}_{\text{OAT}}(-\chi) = -\chi \hat{j}_z^2$ is applied.

In Fig. 24(a), we show the schematic of interaction-based readout with OAT. From a spin coherent state along the x direction $|\hat{x}\rangle$, applying $\hat{H}_{\text{OAT}}(\chi)$ for a duration t yields an entangled state $|\Psi_e\rangle = e^{-i\hat{H}_{\text{OAT}}t}|\hat{x}\rangle$. Then, the parameter θ is encoded into the entangled state via a unitary operation $\hat{U}_\theta = e^{-i\theta\hat{j}_y}$. Subsequently, one can use the interaction-based readout to undo the twisting by applying $\hat{H}_{\text{OAT}}(-\chi)$. When $\theta = 0$, the

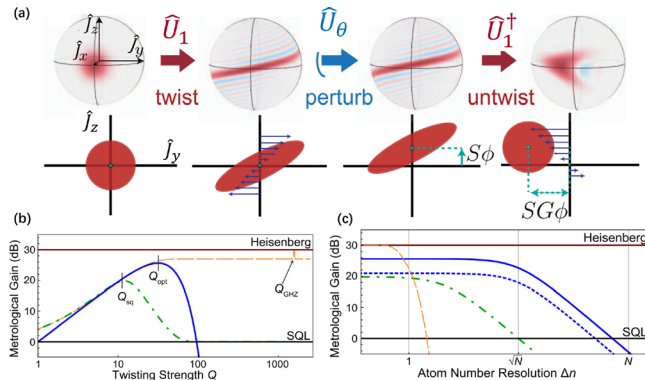


FIG. 24. Interaction-based readout via one-axis twisting.¹⁴⁷ (a) A spin coherent state evolves under $\hat{H}_{\text{OAT}}(\chi)$ into an over-squeezed state $|\Psi_e\rangle$. Then, rotating $|\Psi_e\rangle$ about \hat{x} by a small angle θ . Finally, amplifying the perturbation into a large displacement by applying $\hat{H}_{\text{OAT}}(-\chi)$. (b) Metrological gain $1/[N(\Delta\theta)^2]$ vs twisting strength Q for the unitary twisting echo (solid blue), compared to spin squeezing (dot-dashed green) and the quantum Cramér–Rao bound (QCRB) on phase sensitivity (dashed orange). (c) Metrological gain $1/[N(\Delta\theta)^2]$ vs measurement uncertainty Δn for echo with twisting strength Q_{opt} (solid blue) or Q_{sq} (dotted blue), compared to direct detection of the squeezed state at Q_{sq} (dot-dashed green) and projective measurements with the GHZ state. Reproduced with permission from Davis *et al.*, Phys. Rev. Lett. **116**(5), 053601 (2016). Copyright 2016 American Physical Society.

final state is identical to the original spin coherent state. When $\theta \neq 0$, the \hat{j}_z -dependent spin precession can produce a large final value of $\langle \hat{j}_y \rangle$. Through measuring \hat{j}_y , the measurement precision of θ is given by

$$\Delta\theta = \frac{\Delta\hat{j}_y}{|\partial\langle\hat{j}_y\rangle/\partial\theta|}. \quad (119)$$

The resulting metrological gain depends on the “shearing strength” $Q \equiv 2J\chi t$, see Fig. 24(b). At the optimal shearing strength $Q_{\text{opt}} = 2J\arccot(\sqrt{2J-1})$ for $N \gg 1$, the protocol yields the optimal measurement precision

$$\Delta\theta_{\text{min}} = \frac{\sqrt{e}}{N}, \quad (120)$$

which is very close to the Heisenberg limit. The scheme is highly robust against detection noise, as the “untwisting” amplifies the spin rotation signal. This implies that the measurement precision may achieve the Heisenberg limit, even when the detection resolution of atom number is approximately $\Delta n \approx \sqrt{N}$, see Fig. 24(c).

Interaction-based readout with OAT interaction is also suitable for effective detection of non-Gaussian entangled states.^{146,367} It is shown that the interaction-based readout enables spin cat states to saturate their ultimate precision bounds of Eq. (107). Compared with the twisting echo scheme on spin-squeezed states, the scheme with spin cat states via interaction-based readout is more robust against detection noise.¹⁴⁶

In addition to OAT, one may employ TNT to achieve interaction-based readout. As mentioned earlier in Sec. III B, the TNT interaction exhibits a remarkable ability to generate entanglement at a faster rate compared to the OAT interaction. Additionally, it enables the rapid production of both spin-squeezed states and entangled non-Gaussian spin states. Figure 25 shows an interaction-based readout protocol with TNT Hamiltonian.³⁶⁸ The TNT Hamiltonian is

$$\hat{H}_{\text{TNT}} = \chi \hat{j}_z^2 - \Omega \hat{j}_x, \quad (121)$$

such that $\hat{U}_1 = e^{-i\hat{H}_{\text{TNT}}t_1}$ with the adjustable parameter t_1 is the state preparation time. To align the interferometer along the optimal Fisher information direction, one choose $\hat{U}_\theta = e^{-i\theta\hat{j}_n}$ with $\hat{j}_n = \alpha\hat{j}_y + \beta\hat{j}_z$ that normal to the mean spin direction \hat{j}_x . Thus, the final state after the interaction-based readout is

$$|\Psi_{\text{final}}\rangle = \hat{U}_2 e^{-i\theta\hat{j}_n} \hat{U}_1 |\Psi_{\text{in}}\rangle. \quad (122)$$

In general, the choices of \hat{U}_2 may affect the CFI for a measurement is made with a particular basis. For a measurement that projects into the \hat{j}_x eigenbasis (which can saturate the QCRB), we have $F_C(\theta) = \sum_{m_x} \frac{1}{P_{m_x}(\theta)} (\frac{\partial P_{m_x}(\theta)}{\partial \theta})^2$ with $P_{m_x}(\theta) = |\langle m_x | \Psi_{\text{final}} \rangle|^2$ being the ideal conditional probability via projecting into the eigenbasis $|m_x\rangle$ for a given parameter θ . Furthermore, the robustness to detection noise with different \hat{U}_2 is shown in Figs. 25(b) and 25(c). To model detection noise, one can take the convolution of the probability distribution with a Gaussian distribution under detection noise $\sigma^{148,150,151,367}$ and it is $\tilde{P}_{m_x}(\theta) = \sum_{m'_x} C_{m'_x} e^{-(m_x - m'_x)^2/2\sigma^2} P_{m'_x}(\theta)$ with $C_{m'_x}$ being a normalization factor, and the conditional probability depends on the detection noise σ . F_C as a function of detection noise for different choices of \hat{U}_2 are shown in Figs. 25(b) and 25(c). Interestingly, the optimal interaction-based

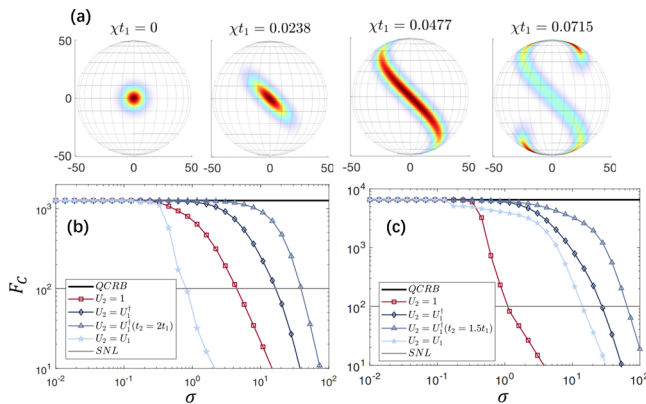


FIG. 25. Twist-and-turn entanglement with interaction-based readout.³⁶⁸ (a) Husimi-Q function for the state $|\Psi_{in}\rangle$ under TNT, where $|\Psi_{in}\rangle$ is chosen as the eigenstate of \hat{J}_x with minimum eigenvalue. Time evolution of the CFI for a many-body entangled state produced by the TNT Hamiltonian in the presence of detection noise σ for (b) $\chi t_1 = 0.027$ and (c) $\chi t_1 = 0.072$ with $\hat{U}_2 = 1$ (red squares), a time-reversal echo $\hat{U}_2 = \hat{U}_1^\dagger$ (dark blue diamonds), an asymmetric echo $\hat{U}_2 \neq \hat{U}_1^\dagger$ (light blue triangles), and a pseudo-echo $\hat{U}_2 = \hat{U}_1$ (light turquoise pentagons). Reproduced with permission from Mirkhalaf et al., Phys. Rev. A **97**(10), 053618 (2018).³⁶⁸ Copyright 2018 American Physical Society.

readout may not be the case of perfect time-reversal echo. In particular for weakly entangled initial states, using an asymmetric echo provides better robustness than the symmetric case.

Interaction-based readout can also be realized via driving through quantum phase transitions (QPTs). As shown in Fig. 19, a nonlinear beam splitting process, in which an initial non-degenerate ground state evolves into a highly entangled state, can be achieved by adiabatically driving the system through a QPT.⁶²⁹⁸ Inversely, by driving the system from the entangled state back across the QPT again to the non-degenerate regime, the state becomes gradually disentangled.³²⁵ The reversed driving through QPTs can be regarded as a kind of nonlinear detection. Finally, the phase shift accumulated in the interrogation process can be easily inferred via population measurement without single-particle resolution.^{68,325}

Moreover, one may also use cyclic nonlinear dynamics to achieve the interaction-based readout. Different from the time-reversed dynamics that drives a system back to its starting point, the cyclic nonlinear interferometer accomplish the same by forcing the system to travel along a “closed loop” instead of explicitly tracing back its antecedent path. For a TNT Hamiltonian of Eq. (121), using a spin coherent state as the input, the first stage of the nonlinear dynamics $\hat{U}_1 = e^{-i\hat{H}_{TNT}t_1}$ serves as nonlinear splitting leading to the non-Gaussian entangled state. After sensing a spin rotation, the system undergoes a second stage of TNT dynamics $\hat{U}_2 = e^{-i\hat{H}_{TNT}t_2}$ for nonlinear recombination. The non-Gaussian entangled input state evolves directly back to the vicinity of the initial state. Compared with a direct linear readout of the non-Gaussian entangled state, the quasi-cyclic nonlinear readout can magnify the encoded signal and refocus the associated quantum noise, leading to a better signal-to-noise ratio (SNR), see Fig. 26. It is found that the optimal metrological gain with population measurement nearly saturates the QCRB and follows the Heisenberg-limited scaling.³⁶⁹ Meanwhile, the interaction-based readout with cyclic nonlinear dynamics of TACT Hamiltonian is also investigated.

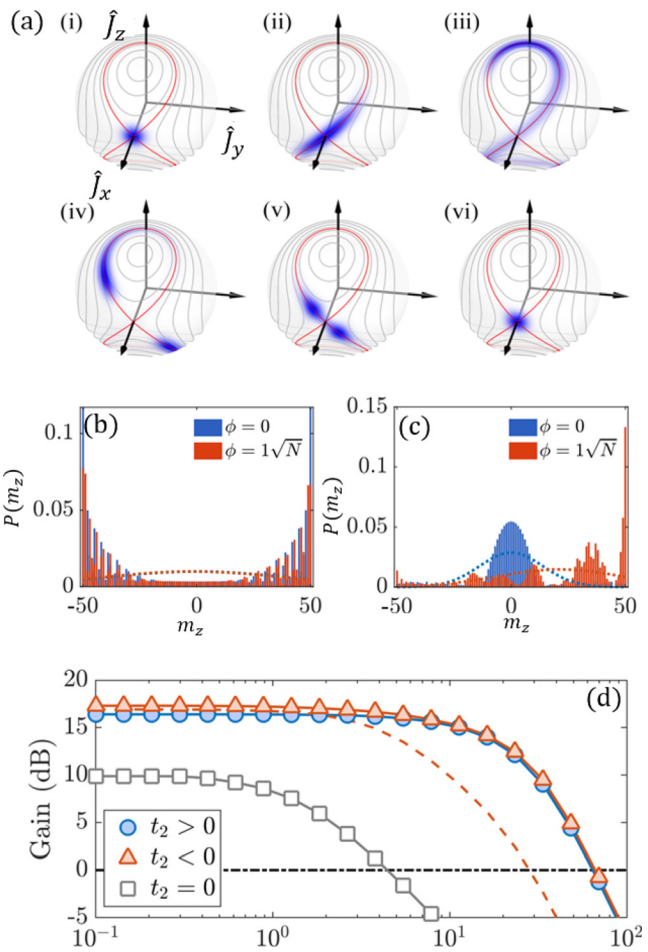


FIG. 26. Quantum metrology with cyclic nonlinear dynamics. (a) Husimi representations of states with quasi-cyclic dynamics in the TNT model.³⁶⁹ Spin coherent state (i) evolves into spin-squeezed state (ii), non-Gaussian entangled states (iii)–(v), and back to the vicinity of the initial point (vi) in succession. (b) Probability distributions of the probe states with the rotation θ in the \hat{J}_z eigenbasis. Dashed lines denote the Gaussian fitting curves. (c) Probability distributions of the output states with the rotation θ via nonlinear detection with cyclic dynamics. (d) Robustness to detection noise for the TNT Hamiltonian. The nonlinear cyclic readout protocol (blue circles), the linear readout scheme (gray squares), and exact time-reversal scheme with $t_2 = -t_1$ (red dashed line). Reproduced with permission from Liu et al., Phys. Rev. A **107**(5), 052613 (2023).³⁶⁹ Copyright 2023 American Physical Society.

At the same time of generating multi-particle entangled states in experiments, numerous interaction-based readout protocols have been demonstrated for achieving entanglement-enhanced quantum metrology with Bose condensed atoms,^{149,152} cavity-QED systems,¹⁰⁵ and ultracold trapped ions.¹⁵⁴

With a spin-1 BEC, its spin-exchange collision has been utilized to realize the time-reversal interaction-based readout.¹⁴⁹ The spin-exchange collision is analog to the parametric amplification, in which both the sign and the strength of the nonlinear coupling can be experimentally adjustable, see Fig. 27(a). As shown in Fig. 27(b), the nonlinear detection is experimentally demonstrated by exploiting

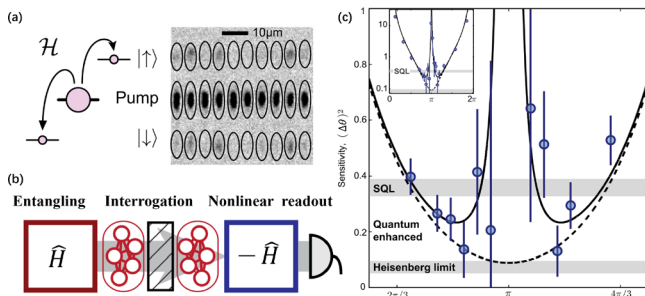


FIG. 27. Entanglement-enhanced sensing based on time reversal of nonlinear dynamics in a spin-1 BEC.¹⁴⁹ (a) Spin-changing collisions in a BEC are used as the nonlinear process. Atom numbers are detected by high-resolution absorption imaging after Stern–Gerlach separation. (b) The interaction-based readout scheme exploits a time-reversal sequence. The Hamiltonian \hat{H} used for entangled state generation is inverted and reapplied for readout. (c) The phase sensitivity is experimentally extracted by Gaussian error propagation. The SQL (gray horizontal bar) is surpassed in close vicinity of phase $\theta = \pi$. At phase π , the sensitivity diverges due to the vanishing slope of the signal. Reproduced with permission from Linnemann *et al.*, Phys. Rev. Lett. 117(1), 013001 (2016).¹⁴⁹ Copyright 2016 American Physical Society.

time-reversal dynamics to disentangle continuous variable entangled states for feasible readout. As both preparation and readout of entangled states consisting of parametric amplification, an active atom SU(1, 1) interferometer is constructed, which is capable of utilizing the quantum entanglement by only detecting the mean atom numbers. The phase sensitivity $(\Delta\theta)^2$ can surpass the SQL in the vicinity of $\theta = \pi$, see Fig. 27(c). Moreover, the time-reversal readout can also be achieved by a state flip operation. Similar to the spin echo with a π -pulse state flip that reverses linear dynamics, this process switches the squeezing and anti-squeezing axes of the probe state, leading to effectively time-reversed nonlinear dynamics to realize the echo-based spin-nematic interferometry.¹⁵³ A sensitivity of 15.6 ± 0.5 dB beyond the SQL for detecting small-angle Rabi rotation, as well as 16.6 ± 1.1 dB for phase sensing in a nonlinear Ramsey-like interferometry, is observed.

In addition to the time-reversal dynamics, interaction-based readout can be achieved by the quasi-cyclic dynamics resulted from spin-exchange collision. It has demonstrated that a three-mode nonlinear interferometer with quasi-cyclic dynamics can attain a metrological gain of 5.01 dB over the classical limit for a total of 26,500 atoms can be achieved.¹⁵² As shown in Fig. 28, utilizing the spin-mixing dynamics \hat{U}_1 at the beginning, paired atoms are created in $|1, \pm 1\rangle$

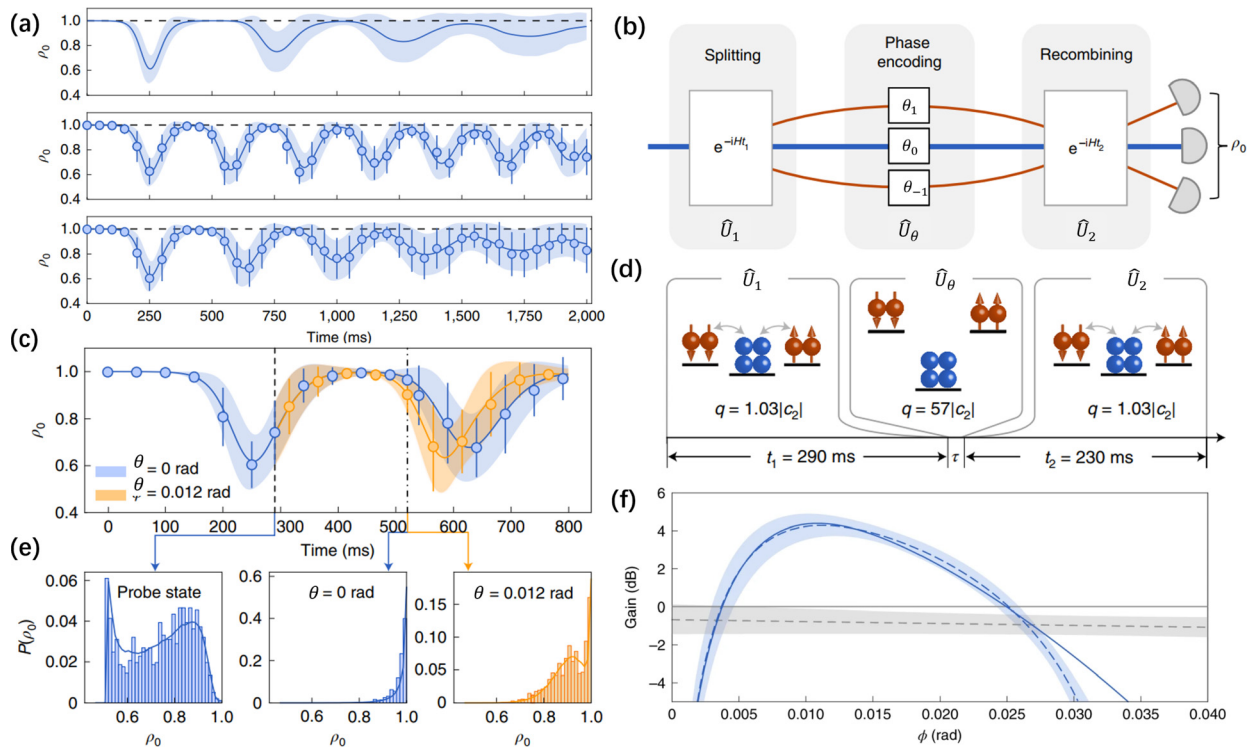


FIG. 28. Quantum metrology with quasi-cyclic dynamics in a spin-1 BEC.¹⁵² (a) The quasi-cyclic dynamics. Temporal evolution of ρ_0 starting from the polar state with all atoms in the $|1, 0\rangle$ component. The upper panel denotes the ideal case without atom loss or technical noises. The middle and lower panels present experimentally measured data. (b) Schematic of the three-mode cyclic dynamics nonlinear interferometry based on spin-mixing dynamics. (c) Temporal evolution of ρ_0 for different spinor phase θ encoded at the instant marked by the vertical dashed black line. (d) The specific sequence to implement the experiments with “path” splitting (\hat{U}_1) and recombining (\hat{U}_2) both from time-forward spin-mixing dynamics for $t_1 = 290$ ms and $t_2 = 230$ ms, respectively. (e) Probability distributions of ρ_0 for the probe state and for the final states. (f) Metrological gain $20 \log_{10} [\Delta\phi / \Delta\phi_{SQL}]$ ($\Delta\phi_{SQL} = 2/\sqrt{N}$) obtained from error propagation formula. Reproduced with permission from Liu *et al.*, Nat. Phys. 18(2), 167 (2022).¹⁵² Copyright 2022 Springer Nature.

components from the $|1, 0\rangle$. Then, the dressing microwave is switched on and encodes a spinor phase $\theta = \theta_1 + \theta_{-1} - 2\theta_0$ via $\hat{U}_\theta = e^{i\theta\hat{N}_0/2}$. At last, the microwave field is turned off and the spin-mixing dynamics \hat{U}_2 is used again to annihilates paired atoms in $|1, \pm 1\rangle$ components into the $|1, 0\rangle$. The encoded spinor phase θ can be extracted from the measured fractional population ρ_0 in the end. The time evolution of the measured ρ_0 for different phase θ is shown in Fig. 28(c). Without an encoded phase, the system nearly returns to its initial state at the end of the interferometry. However, a nonzero phase shift of $2/\sqrt{N} \approx 0.012$ rad causes an evident decrease in the mean value of ρ_0 , as well as broadening of its distribution, as shown in Fig. 28(e). The metrological gain for different phase θ is shown in Fig. 28(f). In particular, a maximal gain of $4.28_{-0.58}^{+0.56}$ dB beyond the SQL at $= 0.011$ rad is observed.

With a cavity-QED system of ^{171}Yb atoms, it has been experimentally demonstrated that the phase sensitivity can achieve a Heisenberg scaling of (b/N) at a fixed distance $b = 12.6$ dB from the Heisenberg limit by employing interaction-based readout with the OAT interaction.¹⁰⁵ In particular, when used in a Ramsey sequence via an atomic interferometer, the highest metrological gain over the SQL with 11.8 ± 0.5 dB can be achieved. As shown in Fig. 29, an entangling light pulse is passed through the cavity to generate the nonlinear OAT

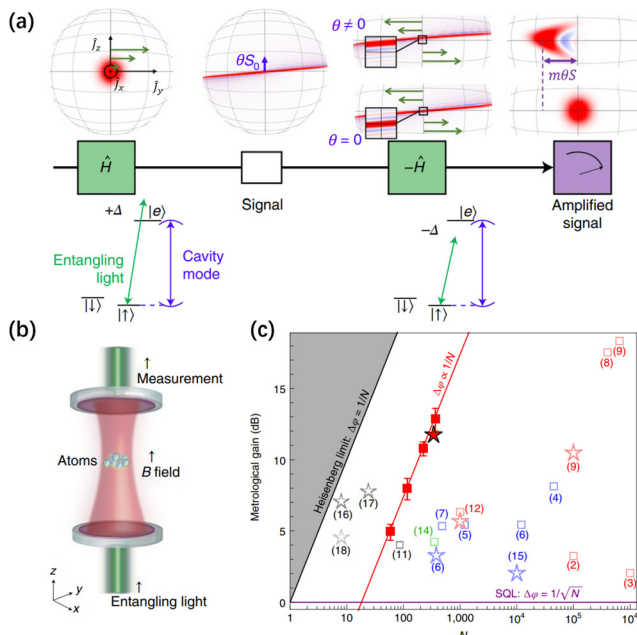


FIG. 29. Time-reversal-based quantum metrology with entangled atoms in cavity.¹⁰⁵ (a) The sequence of the interaction-based readout protocol. The protocol sequence with the quantum state evolution (top) and relevant energy levels and cavity mode (bottom). The Wigner quasi-probability distribution functions describing the collective quantum states. (b) ^{171}Yb atoms are trapped inside an optical cavity in an optical lattice. (c) The scaling of the sensitivity with the atom number and a comparison with previous results. A comparison with previous results including BECs experiments (blue), thermal atoms (red), ions (dark gray), and Rydberg atoms (light gray). The green point shows the squeezing generated in an optical lattice clock. Squares show expected metrological gains obtained by quantum state characterization. Stars indicate directly measured phase sensitivity gains. Solid symbols are obtained in this work. Reproduced with permission from Colombo *et al.*, Nat. Phys. **18**(8), 925 (2022).¹⁰⁵ Copyright 2022 Springer Nature.

Hamiltonian $\hat{H} = \chi\hat{J}_z^2$, which shears the initial spin coherent state. A rotation θ about the \hat{J}_y axis displaces the state such that $\langle \hat{J}_z \rangle = \theta S_0$ with $S_0 = N/2$. Subsequently, a (dis)entangling light pulse is sent through the cavity, which generates the negative OAT Hamiltonian $-\hat{H}$ causing the quantum state to evolve effectively “backwards in time.” For a small angle ($\theta \neq 0$), the final state is displaced by an angle $m\theta$ from the original spin coherent state, where m is the signal amplification. The scaling of the sensitivity with the atom number N is shown in Fig. 29(c), when the particle number N varies between 50 and 370, a gain over the SQL is measured, which can achieve the Heisenberg scaling. More recently, a time-reversal protocol is used to observe a simultaneous exponential growth of both the metrological gain and the out-of-time-order correlation, thereby experimentally verifying the relation between quantum metrology and quantum information scrambling.³⁷¹

With a trapped-ion mechanical oscillator, interaction-based readout has been employed to amplify and detect coherent motional displacements that are considerably smaller than the quantum zero-point fluctuations.¹⁵⁴ As shown in Fig. 30(a), by squeezing the motional state first, one can suppress the quantum fluctuations along a particular phase space quadrature. Then, a small displacement α_i is applied along the squeezed axis. Finally, by reversing the squeezing interaction, the oscillator returns to a minimum-uncertainty coherent state with a larger amplitude $\alpha_f = G\alpha_i$ with G is the gain. The maximum amplification is achieved when the displacement is along the squeezed axis. To demonstrate experimentally, a single trapped $^{25}\text{Mg}^+$ ion is used. In each experiment, the ion is initialized in the electronic and motional ground state $| \downarrow \rangle | 0 \rangle$ via optical pumping, sideband laser cooling and microwave pulses. The pulse sequence for displacement sensing protocol is shown in Fig. 30(b). The displacement α_f is obtained by

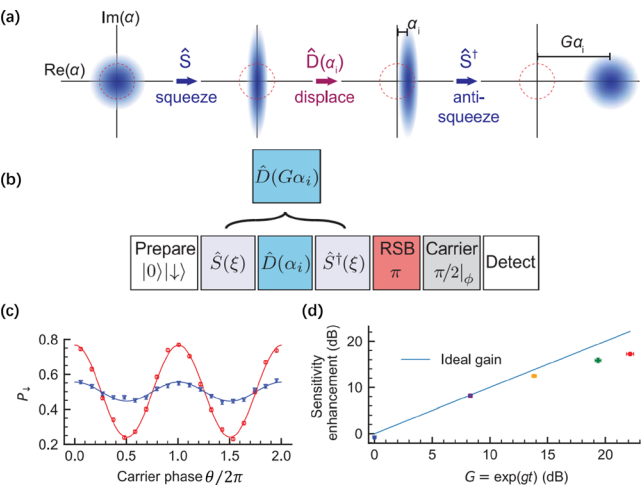


FIG. 30. Quantum amplification in a trapped-ion mechanical oscillator.¹⁵⁴ (a) Conceptual illustration of the amplification protocol. Each panel shows a Wigner function phase space distribution. A displacement α_i of an initially squeezed ground state is amplified by subsequent anti-squeezing, resulting in a final coherent state with amplitude $G\alpha_i$ with no added noise. (b) Pulse sequence for displacement sensing protocol with phase-sensitive red sideband (PSRSB) detection. (c) Population P_d as a function of the carrier $\pi/2$ pulse phase with no squeezing (blue inverted triangles) and amplification (red circles). (d) Measurement sensitivity enhancement in the linear small-displacement regime as a function of the ideal gain $G = \exp(gt)$. Reproduced with permission from Burd *et al.*, Science **364**, 1163 (2019).¹⁵⁴ Copyright 2019 The American Association for the Advancement of Science.

measuring probability into state $| \downarrow \rangle$ with $P_{\downarrow} = \frac{1}{2}[1 - C(|\alpha_f|) \cos \phi]$, where $C(|\alpha_f|)$ is the signal contrast and ϕ is the phase of a carrier $\pi/2$ pulse. Without amplification, $\alpha_i = \alpha_f$ and the contrast is $C(|\alpha_i|)$. However, the initial displacement amplitude α_i is increased by utilizing the anti-squeezing and the contrast become $C(|G\alpha_i|)$. This increase in contrast is shown in Fig. 30(c). Especially, if the displacement is along the squeezed axis, the measurement sensitivity enhancement as a function of the ideal gain $G = \exp(gt)$ in the linear small-displacement regime, as shown in Fig. 30(d). More recently, by modulating the trapping potential at close to twice of the center-of-mass mode frequency, a motional squeezing of 5.4 ± 0.9 dB below the ground-state motion has been achieved via a stroboscopic protocol.³⁷²

V. PROMISING APPLICATIONS IN QUANTUM SENSORS

Recent technological advancements have paved the way for the development of highly stable and precise instruments such as lasers, optical frequency combs, and microwave electronics. These advancements have enabled the creation of quantum interferometers with unprecedented sensitivity and the world's most accurate and precise clocks. In these devices, the stable quantum states of atoms play a crucial role. By harnessing controlled atomic entanglement, it is possible to achieve entanglement-enhanced atom interferometry, surpassing the precision limits of conventional methods. Entanglement-enhanced atom interferometry allows for the precise measurement of various physical quantities, including frequency, magnetic field, gravity, acceleration, and rotation. This breakthrough has significant implications for the development of atomic clocks, quantum magnetometers, quantum gravimeters, and quantum gyroscopes, offering unprecedented levels of precision in these applications. Quantum sensors, empowered by the remarkable precision offered by quantum entanglement, have emerged as highly promising tools in various domains. They hold great potential in fields such as inertial navigation, mineral exploration, groundwater monitoring, dark matter detection, and space-based experiments aimed at testing theories of general relativity or quantum gravity. Below we will introduce the exciting and promising applications of entanglement in the realm of quantum sensors.

A. Atomic clocks

Atomic clocks are the most accurate and precise clocks that have been developed to date. Atomic clocks utilize the reliable transition frequency of stable long-lived energy levels found in atoms. They work by comparing the frequency of a local oscillator (LO) to the reference atomic transition frequency. This comparison is used to ensure that the ticking period of the LO remains stable, as shown in Fig. 31(a). For atomic clocks, the selected states are often magnetically insensitive internal states. It makes them excellent frequency references as they do not experience the aging process observed in mechanical clocks. The atomic transition frequency is universally present and highly suitable for usage as a standard frequency. For example, the current major frequency standard relies on the hyperfine transition in ^{133}Cs , which is utilized to precisely define the SI second.⁶⁰ The systematic error achieved by a solitary optical clock based on an aluminum ion³⁷³ can be 9.4×10^{-19} . Nevertheless, as systematic effects are fully understood and accounted for, atomic clocks that make use of a large number of atoms have the capacity to far exceed the performance of clocks that rely on a single ion. Atomic clocks with a performance beating the SQL have been demonstrated in several experiments.^{62,67,126,374}

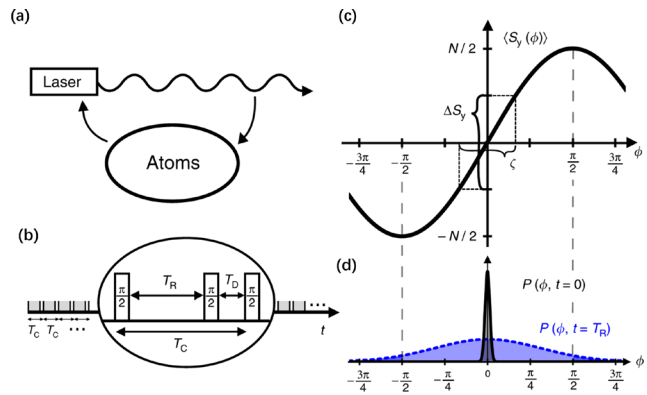


FIG. 31. Measurement noises of a squeezing-enhanced atomic clock.⁶⁷ (a) Measurement and feedback loop to stabilize the laser frequency to an atomic transition. (b) Periodic measurements with Ramsey time T_R and dead time T_D in each cycle of total time T_C lead to increased instability from the Dick effect. (c) Quantum projection noise for N particles limits the clock stability for short interrogation times but can be decreased with squeezed states thus reducing the inferred phase uncertainty where ζ is the Wineland spin squeezing parameter of Eq. (56). (d) For longer T_R , the distribution of phases broadens substantially due to the laser's decoherence. Inefficient feedback for phases outside the interval gives the coherence time limit. Reproduced with permission from Schulte et al., Nat. Commun. 11, 5955 (2020). Copyright 2020 licensed under a Creative Commons Attribution (CC BY) license.

Entanglement-enhanced microwave-frequency clocks have been achieved using neutral atoms with spin-squeezed states as input.^{86,126,175,273,375} Although these proof-of-principle experiments serve as spectacular examples of entanglement-enhanced atomic clocks, they have not yet achieved the same level of frequency stability as state-of-the-art fountain clocks. This is mostly due to their Ramsey interrogation time (limited by the noise of the microwave LO) is much shorter than the ones typically operating in fountain clocks using uncorrelated individual atoms.³⁷⁶

The performance of atomic clocks could be greatly improved if the reference transition occurred in the optical range instead of the microwave range.³⁷⁷ Typically, optical frequencies are approximately 10^4 times higher than microwave frequencies, resulting in a corresponding improvement of the fractional stability by a factor of 10^4 . With the advent of optical frequency combs spanning a wide range of octaves,³⁷⁸ there has been notable progress in optical clock technology.¹⁵⁶ The lasers consist of a series of closely spaced spectral lines in frequency space. The separation between these lines is a few hundred MHz, and it is dictated by the repetition rate of the femtosecond laser. Therefore, by utilizing a frequency comb as an intermediate stage, two lasers operating at distinct wavelengths might effectively compete. The usage of optical frequency comb in an optical atomic clock enables an experimentally feasible way to measuring optical transition frequencies and comparing optical clocks.

Optical transition-based atomic clocks have gained significant attention in recent years due to their remarkable precision and stability.^{155,379} Currently, optical atomic clocks are the most precise and accurate clocks. These clocks generally interrogate the optical transitions with groups of atoms that are confined in an optical lattice. So far, the optical transition atomic clocks can reach fractional stability below 10^{-18} ,^{163–165} and approaching 10^{-19} .^{380,381} Technical noises from imperfect readout, intrinsic atom–atom interactions, or aliased

frequency noise of the interrogating clock laser pose challenges for observing clock performance at the quantum projection noise (QPN) limit. Since the atomic collisions would disturb the transition frequency and the resulted collision shift would decrease the accuracy of the atomic clocks. Thus, the collision shifts impose a limit on the total number of atoms used in atomic clocks. Typically, the atomic number is about 10^2 – 10^4 . At such relatively small atom number, the SQL places a significant constraint on the clock frequency measurement.

By using suitable entangled states such as spin-squeezed states, the performance of optical atomic clocks can be improved beyond the SQL. The spin squeezing has been used to improve an optical lattice clock of ^{171}Yb atoms.¹⁷⁶ The strategy used is to generate a spin-squeezed state in the ground state of ^{171}Yb atoms and then transfer it to the ultra-narrow optical clock transition by applying an optical π pulse, see Fig. 32. Using the spin-squeezed state on the optical transition as the input state, a Ramsey interferometry is performed in the optical domain with a five-order improved Q-factor compared to the microwave transitions. After the Ramsey interference, the spin-squeezed state is mapped back onto the ground state and readout via the cavity. As a result, a measurement precision of 4.4 dB below the SQL is demonstrated, corresponding to a 2.8-fold reduction of the

averaging time. More recently, a protocol based on time-reversal dynamics called Signal Amplification through Time-Reversal Interaction was demonstrated for optical atomic clocks approaching the Heisenberg limit. As shown in Sec. IVB, a non-Gaussian over-squeezed state is generated under a prolonged OAT dynamics and with a time-reversal process for readout, it enables one to reach near-Heisenberg sensitivity.

The clock stability can be assessed by its Allan deviation, which depends on several factors such as the transition frequency, interrogation time, dead time, average time, and input state. For optical atomic clocks, the laser is stabilized by a control loop to an optical atomic transition of frequency ν_0 , as shown in Fig. 31(a). The Ramsey interrogation T_R and the dead time T_D comprise of the duration $T_C = T_R + T_D$ for each cycle. By measuring the spin component $\langle \hat{S}_y \rangle$, one can get the information of ν_0 from the laser frequency. The measurement result is converted into an error signal that is used to correct the laser frequency. Averaging over a long time $\tau \gg T_C$, the clock stability can be measured in terms of Allan deviation $\sigma_y(\tau)$. For an atomic clock with spin squeezing, the stability limited only by the QPN of the spin measurement results in the Allan deviation

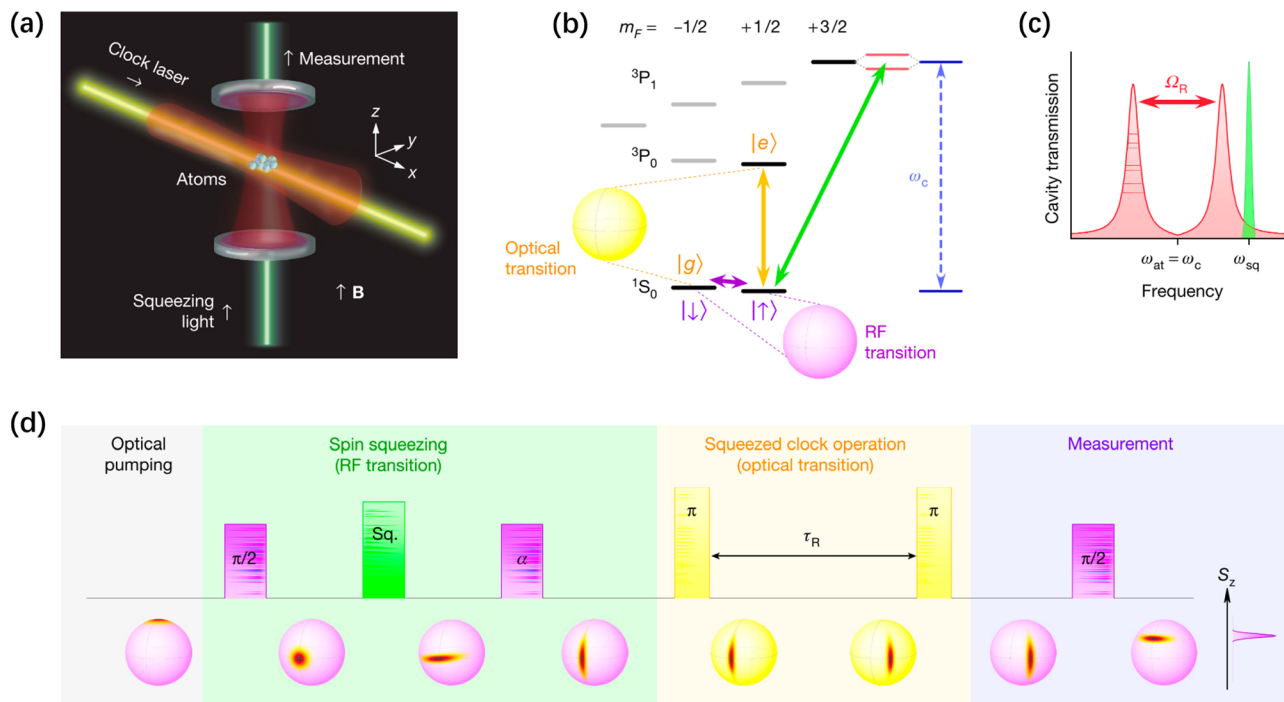


FIG. 32. Optical atomic clock operated with spin squeezing.¹⁷⁶ (a) ^{171}Yb atoms are confined within an optical cavity in a two-dimensional magic-wavelength optical lattice, namely, in the x and z directions (shown by the color red). The optical pumping and spin squeezing light (green) is directed parallel to the cavity axis z, while the clock laser (yellow) travels parallel to the x axis. (b) Levels of energy and changes between them. The ground-state RF transition $|l\rangle \rightarrow |u\rangle$ is shown by purple pulses, the squeezing transition at ω_{at} is represented by green pulses, and the optical clock transition $|l\rangle \rightarrow |e\rangle$ is represented by yellow pulses. The system undergoes evolution inside either the ground-state manifold (the purple Bloch sphere) or the clock-state manifold (the yellow Bloch sphere). The resonance of the squeezing transition is achieved by adjusting the cavity frequency ω_c . (c) The atoms' strong interaction with the cavity leads to the division of the cavity resonance into two distinct peaks, known as vacuum Rabi splitting (red peaks). A laser is used at a frequency ω_{sq} (green peak) that is detuned from the Rabi peak. This laser is employed to generate a spin-squeezed state by cavity feedback. (d) Squeezed-clock sequence. A spin-squeezed state is initially created in the lowest energy level and then rotated by an angle α . It is then moved to the clock energy level and undergoes a Ramsey sequence for a duration of τ_R . Finally, it is mapped back to the states $|l\rangle, |u\rangle$ and a measurement of the state is made. The quantum state's development is illustrated on the Bloch spheres, representing the RF (purple) and optical (yellow) transitions. Reproduced with permission from Pedrozo-Penafiel *et al.*, Nature **588**, 414 (2020).¹⁷⁶ Copyright 2020 Springer Nature.

$$\sigma_{QPN}(\tau) = \frac{1}{2\pi\nu_0 T_R} \sqrt{\frac{T_C}{\tau}} \frac{\xi_R}{\sqrt{N}}, \quad (123)$$

where N is the number of atoms participating in the clock, and ξ_R is the Wineland spin-squeezing parameter. It is important to note that under practical conditions, optical atomic clocks are not exclusively limited by QPN.

In practice, the overall stability of a clock is influenced by various sources of noise, including laser phase noise and dead time. Among these factors, the Dick effect and the laser coherence time limit play significant roles in compromising the stability. The Dick effect arises from the interrupted interrogation of the atomic system, while the finite laser coherence time contributes to the stability with an additional diffusion process, which refers to the laser coherence time limit. Incorporating these effects, the optimal operating point of the control loop is determined by a trade-off between QPN, Dick effect, and coherence time limit. This trade-off is achieved by minimizing the combined stability.⁶⁷

$$\sigma_y(\tau) = \sqrt{\sigma_{QPN}^2(\tau) + \sigma_{Dick}^2(\tau) + \sigma_{CTL}^2(\tau)}. \quad (124)$$

Considering all these critical factors of the instability, it has been revealed that a typical single-ensemble Ramsey clock holds the potential for improving performance through spin squeezing, especially in systems with relatively low atom numbers.⁶⁷ The primary limitations arise from the instability of the lasers in the system. However, these limitations can be addressed by employing an adaptive measurement scheme.¹⁶² This scheme involves performing a weak measurement of the collective spin state, followed by a feedback process that rotates the state by an amount determined by the measurement outcome. By doing so, the measurement backaction is minimized, resulting in a final state that remains unaffected by undesired noises.

Using two clock ensembles for comparison, the common-mode noises such as the LO decoherence can be canceled and so that the Dick effect can be completely eliminated.¹⁶⁵ Likewise, employing cascaded systems with multiple ensembles can effectively mitigate the impact of laser coherence limit.^{161,383} An experimental implementation of a “multiplexed” one-dimensional optical lattice clock has been realized, where spatially resolved ensembles of strontium atoms are trapped in the same optical lattice, allowing for simultaneous interrogation by a shared clock laser and parallel readout processes.³⁸⁰ The results of these experiments showcase that applications involving optical clock comparisons can overcome the limitations imposed by LO instability, making it a viable option for implementing a quantum network of clocks as well.³⁸⁴

To improve spin-squeezing-enhanced atomic clocks, it is crucial to consider the coupling of anti-squeezing, as it couples with the measurement projection, and then introduce extra noise and reduce the contrast. To overcome this problem, one may utilize adaptive measurement for a single clock ensemble,^{162,385,386} or combination of measurement and feed forward for multiple clock ensembles.^{161,350,387} Recently, the protocol of multiple clock ensembles with feedback was analyzed,^{350,388} where one squeezed clock was considered together with another unentangled clock. It is shown that by feeding forward the measurement result of the unentangled ensemble to the squeezed ensemble, it is possible to sustain the entanglement enhancement for extended periods of time, even when there is LO noise present.

The two methods can thereby increase the interrogation times that still allow an enhancement due to spin squeezing.

Through integrating an optical clock platform with collective strong-coupling cavity QED for QND measurements, the direct comparison of two spin-squeezed optical clock ensembles has been achieved.³⁷⁴ The QND measurements of the clock state³⁸⁹ can be implemented for spin squeezing and clock readout. Optimizing the competition between spin measurement precision and loss of coherence, a metrological enhancement for a large ensemble of atoms beyond the initial spin coherent state can be measured. Using a movable lattice, the cavity can individually address two independent sub-ensembles, enabling one to spin squeeze two clock ensembles successively and compare their performance without the influence of clock laser noise. Although the clock comparison remains above the effective SQL, the performance directly verifies 1.9(2) dB clock stability enhancement at the 10^{-17} level without subtracting any technical noise contributions. Moreover, resonant electric dipole-dipole interactions in a cubic array of atoms in the many-excitation limit has been observed directly.³⁹⁰ With the ⁸⁷Sr atoms loaded in a cubic optical lattice, the effects of resonant dipole-dipole interactions is measured. The ensemble-averaged shifts can be suppressed below the level of evaluated systematic uncertainties for optical atomic clocks. It is found that the interactions caused a tiny clock shift, the magnitude of which could be controlled by varying the relative orientation of the probe light and the atomic dipoles.

In comparison with an optical lattice clock, the trapped-ion clock offers the advantage of less dead time. This is because that the same ion can be trapped and interrogated for extended durations due to the presence of a strong confinement potential. Despite their lower signal-to-noise ratios when compared to optical lattice clocks, ion clocks remain among the most stable clocks now accessible. The physics component of trapped-ion clock systems is much more amenable to miniaturization, and ongoing attempts are being made to enable the transmission and reception of light from the ions through phonics integrated into the trap structure itself.⁶⁷ In recent, several promising trapped ion-based clocks such as highly charged ion clocks³⁹¹ and nuclear clocks⁴³ are being pursued and they offer further improvement in the performance of these types of clocks. In particular, the enhanced frequency comparisons using an elementary quantum network of two entangled trapped-ion atomic clocks have been demonstrated.⁶² The network’s ability to generate entanglement with high fidelity and speed, resulting in a large signal and an efficient duty cycle, demonstrates the potential for practical enhancements in atomic clocks. Furthermore, as shown in Fig. 14, a potential avenue for leveraging large-scale entanglement is demonstrated on an optical transition by utilizing one-dimensional chains of ions. The observation of emergent collective behaviors related to OAT with finite-range interactions represents a significant milestone in the integration of entanglement into high-performance ion clocks that operate with a large number of ions.

Another intriguing avenue for clock applications involves utilizing long-range Rydberg-dressing interactions to generate spin-squeezed and non-Gaussian entangled states. With the versatile capabilities of optical tweezer arrays in manipulating atomic ensembles, optical clocks have been developed using current breakthroughs in optical tweezers.^{69,382,392} The tweezer array optical clocks combine the advantages of both single-ion-based optical clocks and optical lattice clocks. They incorporate the superb isolation and high duty cycles

demonstrated by single-ion-based optical clocks, while also benefiting from the large ensembles and consequent low QPN characteristic of optical lattice clocks. The demonstration of a half-minute-scale atomic coherence and high relative stability in a tweezer clock, as reported in a recent experiment,⁶⁹ lays a solid foundation for the engineering of entanglement on an optical clock transition. The utilization of expansive 2D arrays and close proximities in this context is crucial for utilizing limited-range Rydberg interactions. This approach enables for the study of larger samples with enhanced interconnections, more potent interactions, and therefore, increased entanglement. Despite the exponential decline in many-body entanglement due to single-particle decoherence, the coherence times demonstrated in the experiment show remarkable potential for achieving a highly precise entangled optical clock. This clock may operate with tens of atoms and interrogation durations lasting several seconds, making it suitable for metrological applications. Furthermore, by incorporating precise control and detection of individual particles along with a diverse set of tunable entangling interactions, the experimental generation of spin squeezing was achieved in an optical atomic clock. It has been demonstrated that such a clock can be built upon a programmable array of interacting optical qubits,³⁸² see Fig. 33. In subarrays of 16 atoms and 70 atoms, spin-squeezed states with $\xi_R^2 = -3.8$ and $\xi_R^2 = -3.4$ dB have been prepared, respectively. This enables the performance of a synchronous clock comparison with a stability that surpasses the SQL by up to 3.5 dB, which paves an avenue to entanglement-enhanced optical clocks.

B. Magnetometers

The precise measurement of magnetic fields with high sensitivity is a critical requirement in various domains, including physics,^{76,84,393} biology,^{394,395} and medical applications,^{73,396,397} among others. For instance, it is essential for detecting geomagnetic anomalies, studying magnetic fields in space, and mapping electric and magnetic fields

generated in the brain for bio-magnetic measurements. Quantum magnetometry uses the principles of quantum mechanics to measure magnetic fields with high precision and sensitivity. Based upon the interaction between quantum systems and external magnetic fields, various quantum systems including atoms, superconducting quantum interference devices, and nitrogen-vacancy centers have been employed to detect magnetic fields. The atomic magnetometers mainly include optical Faraday magnetometers,^{147,167–169,398,399} coherent-population-trapping magnetometers,^{400–405} spin-exchange relaxation-free magnetometers,^{406–412} and cold-atom magnetometers.^{86,168–170} Below, we will highlight the progresses in entanglement-enhanced magnetometry.

Optical Faraday magnetometers operate by measuring the polarization rotation of light as it traverses a group of atoms exposed to a magnetic field.¹⁶⁷ Generally, the device consists of N spin- F atoms initially optically pumped into a fully polarized state (pointing along the y axis, for instance), such that the collective spin of the ensemble has length F_N . A weak magnetic field along the x axis causes the precession of the collective spin in the y - z plane at a rate $g\gamma B$, where g is the gyromagnetic ratio, γ is the in Bohr magneton, and B is the magnetic field strength. Polarization of light propagating along z will be rotated proportional to the collective atomic spin J_z due to the Faraday effect. Thus, the atomic spin precession is detected by measuring transmission or rotation of the polarized probe light, as shown in Fig. 34(a). The rotation of the polarized probe light is described via the Stokes parameters S_x, S_y, S_ϕ , and the detected signal is⁴¹³

$$S_y^{\text{out}} = S_y^{\text{in}} + S_x(\nu B_z + \alpha J_z)l, \quad (125)$$

where ν is the Verdet constant of the vapor, B is the magnetic field, α is proportional to the vector component of the atomic polarizability, and l is the length of the medium. Quantum mechanics sets fundamental limits on the best sensitivity that can be achieved in a magnetic-field measurement. According to Eq. (125), the sensitivity of these magnetometers is fundamentally limited by quantum noise main

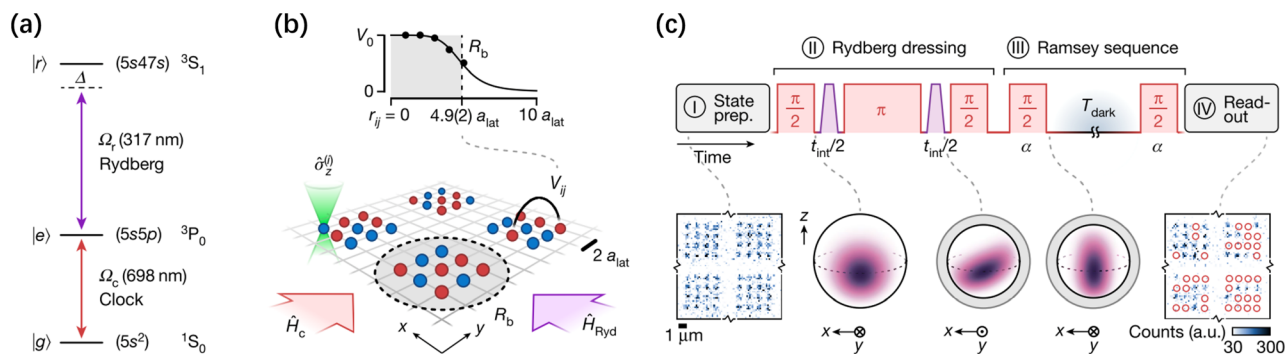


FIG. 33. Generation of spin squeezing in a Rydberg-dressed array of ⁸⁸Sr atoms.³⁸² (a) Atomic states (black lines) and transitions (colored arrows) of ⁸⁸Sr relevant for clock interrogation and Rydberg dressing. (b) Diagram illustrating the configuration of the experimental arrangement. The spacing of a_{lat} is approximately 575 nm, and it is organized into several subarrays. The upper plot illustrates the relationship between atoms at a distance r_{ij} , which is defined by the potential energy V_{ij} . The black circles represent the data points. The solid black line represents a numerical fit. The laser beams that connect the states in (a) are shown by colored arrows and correspond to the Hamiltonians H_c and H_{Ryd} . Optical tweezers, which have a green double cone shape and operate at a wavelength of 515 nm, allow for the application of the operator $\hat{\sigma}_z^{(i)}$ to a specific atom i . (c) Diagram depicting the procedural method for generating spin-squeezed states in an experimental setting. The pulse sequences for (II) and (III) display clock and Rydberg laser pulses in the colors red and purple, respectively. In this context, the symbol α represents the phase of the clock laser relative to a reference. Individual photographs are captured after the process of preparing the state (located at the bottom left) and for the purpose of determining the atomic populations (located at the bottom right). In this context, the red circles represent atoms in the state $|g\rangle$ that have been deliberately eliminated prior to the final imaging. The generalized Bloch spheres, located in the bottom center, depict the progression of the atomic state for a subarray consisting of 16 atoms, where $N = 4 \times 4$. Reproduced with permission from Eckner et al., Nature 621, 734 (2023). Copyright 2023 Springer Nature.

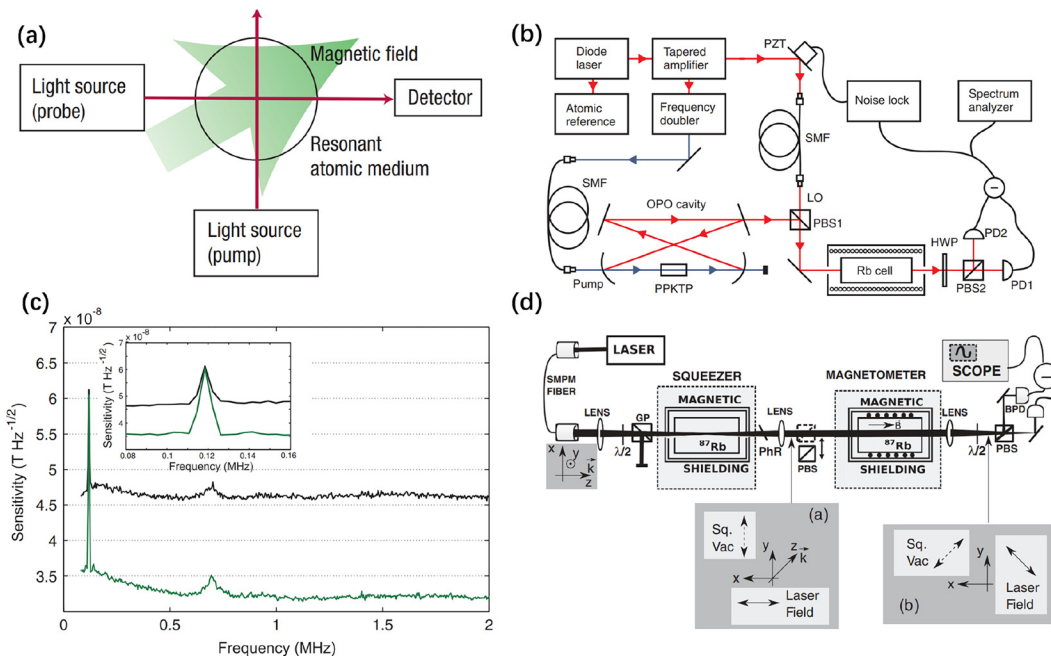


FIG. 34. Optical Faraday magnetometers. (a) The schematic of an all-optical atomic magnetometer.¹⁶⁷ Pump light polarizes the atoms, atomic evolves in the magnetic field, and the resultant state of the atoms is detected by the probe light. Reproduced with permission from Budker and Romalis, Nat. Phys. 3(4), 227 (2007).¹⁶⁷ Copyright 2007 Springer Nature. (b) Experimental setup of optical atomic magnetometer with optical parametric oscillator.⁴¹³ Rb cell, rubidium vapor cell with magnetic coil and magnetic shielding; OPO, optical parametric oscillator; PPKTP, phase-matched nonlinear crystal; LO, local oscillator beam; PBS, polarizing beam splitter; HWP, half-wave plate; SMF, single-mode fiber; PD, photodiode. Reproduced with permission from Wolfgramm *et al.*, Phys. Rev. Lett. **105**(5), 053601 (2010).⁴¹³ Copyright 2010 American Physical Society. (c) Faraday rotation measurement. The black curve shows the sensitivity with a polarized (but not squeezed) probe. The green line depicts the sensitivity with a polarization-squeezing probe. A zoomed view around the calibration peak at 120 kHz is shown in the inset.⁴¹³ Reproduced with permission from Wolfgramm *et al.*, Phys. Rev. Lett. **105**(5), 053601 (2010).⁴¹³ Copyright 2010 American Physical Society. (d) Experimental setup of optical atomic magnetometer with atomic squeezer.⁴¹⁴ The squeezer prepares an optical field with reduced noise properties, which is used as a probe for the magnetometer. SMPM fiber: single-mode polarization maintaining fiber; $\lambda/2$: half-wave plate; PhR: phase-retarding wave plate; PBS: polarizing beam splitter; GP: Glan-Laser polarizer; BPD: balanced photodetector. Insets show the polarization of the squeezed vacuum field and the laser field before the magnetometer cell (a) and right before the last PBS (b). Reproduced with permission from Horrom *et al.*, Phys. Rev. A **86**(2), 023803 (2012).⁴¹⁴ Copyright 2012 American Physical Society.

in the form of photon shot noise presented in S_y^{in} and atomic projection noise presented in J_z . It is obvious that one can realize the entanglement-enhanced magnetic-field measurement via using a squeezed state in S_y as an input.

In experiments, the improvement in magnetic field sensing via using polarization-squeezed probe lights has been demonstrated with Rb atoms.^{147,414} By using off-resonant, polarization-squeezed probe light, the sensitivity of the magnetometer is improved by 3.2 dB. The magnetometer consists of a source of polarization-squeezed light, a rubidium vapor cell at room temperature, and a shot-noise-limited polarimeter. The experimental setup is shown schematically in Fig. 34(b). First, the squeezed vacuum state is produced by pumping a sub-threshold optical parametric oscillator (OPO). The nonlinear medium in the OPO is used to polarize the squeezed vacuum. Then, the polarization-squeezed light is sent through an atomic cell at room temperature. At last, the optical rotation is detected by a shot-noise-limited polarimeter. The sensitivity of the Faraday rotation measurement is shown in Fig. 34(c). Moreover, one can also use an atomic squeezer to generate the squeezed probe light, which is based on the polarization self-rotation (PSR) effect.⁴¹⁴ The setup is depicted in Fig. 34(d), the atomic squeezer can generate about 2 dB of noise reduction, and the magnetometer with sensitivities close to $1\text{ pT}/\sqrt{\text{Hz}}$.

More recently, by using squeezed probe light and evasion of measurement backaction, one can enhance the sensitivity and measurement bandwidth of the magnetometer at sensitivity-optimal atom number density.³⁹⁹

Cold-atom magnetometers generally operate based on the measurement of the collective spin of an ensemble of atoms after a Ramsey interferometry. The device consists of N two-mode particles (single-particle states) and the two modes are labeled as $|a\rangle$ and $|b\rangle$. According to the description of the Ramsey interferometry in Sec. II, the magnetic field to be estimated is encoded in the quantum system during the interrogation process. After the beam splitter, the information of the magnetic field can be obtained via measuring the collective spin. For atomic ensembles, trapped BECs are particularly well suited for sensing applications requiring both high sensitivity and spatial resolution, taking advantage of their small size, high degree of coherence, and the availability of sophisticated techniques for precise controlling of motional degrees of freedom.¹⁷⁰ Recently, Ramsey interferometry using spin-squeezed states, which generated via OAT dynamics with BEC,^{126,170} has applied to sense magnetic fields.

With small BECs on an atom chip, one can overcome the SQL by 4 dB and yield a microwave magnetic field sensitivity of 77 pT via using the spin-squeezed state as input.⁸⁶ The experimental schematic

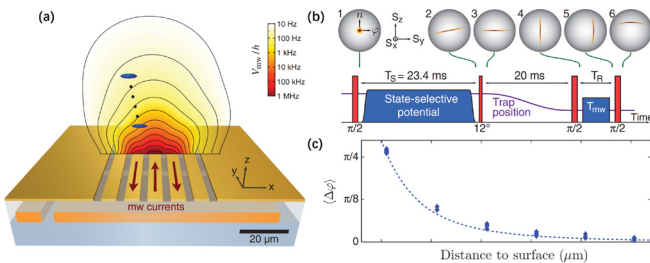


FIG. 35. Entanglement-enhanced magnetic field sensing with an atom chip.⁸⁶ (a) Experimental setup. Central region of the atom chip is the atomic probe and the scanning trajectory. The probe is used to measure the magnetic near-field potential generated by an on-chip microwave guide. (b) Experimental sequence of the scanning probe interferometer, showing Rabi (red) and on-chip microwave (blue) pulses and the trap position (purple). Spheres show the Wigner function of the collective spin state at different stages of the Ramsey experiment. (c) Measured phase shift $\langle \varphi \rangle$ induced by a microwave near-field pulse as a function of the atom-surface distance. Reproduced with permission from Ockeloen *et al.*, Phys. Rev. Lett. **111**(14), 143001 (2013).⁸⁶ Copyright 2013 licensed under a Creative Commons Attribution (CC BY) license.

of the scanning probe interferometer is shown in Fig. 35. First, a spin coherent state on the equator of the generalized Bloch sphere is created via a $\pi/2$ pulse. Then, applying OAT Hamiltonian $\hat{H}_{\text{OAT}} = \gamma \hat{J}_z^2$ to generate spin-squeezed state. Next, applying a suitable rotation around the \hat{J}_x axis to align the anti-squeezed quadrature with the equator. A full Ramsey interferometer sequence consists of a $\pi/2$ pulse to make it maximally phase sensitive, a free evolution with time T_R for phase accumulation $\phi \propto B T_R$, and a final $\pi/2$ pulse mapping ϕ onto the population difference. The measurements as a function of the atom-surface distance are shown in Fig. 35(c). For all positions, the

interferometer performs well below the SQL, and the microwave field sensitivity approach to $\Delta B = 2.4 \mu\text{T}$.

With BECs in an optical lattice, one can achieve a quantum-enhanced single-shot sensitivity of $310(47) \text{ pT}$ for a static magnetic field in a probe volume as small as $90 \mu\text{m}^3$.¹⁷⁰ The experimental schematic and results of the entanglement-enhanced magnetometer are shown in Fig. 36. First, generating the spin-squeezed state in the levels $|a\rangle$ and $|b\rangle$ under OAT Hamiltonian $\hat{H}_{\text{OAT}} = \gamma \hat{J}_z^2$, the state is rotated to achieve the maximum phase sensitivity. Subsequently, a microwave π pulse transfers the squeezing to a magnetic-field-sensitive hyperfine transition. After magnetic field-dependent phase evolution with a hold time, swapping the state back to the original level to readout. During this sequence, the state acquires a phase $\phi \propto B$. At last, a Ramsey fringe is obtained by a final $\pi/2$ pulse, as shown in Fig. 36(d). Magnetic field sensitivity of the Ramsey magnetometer vs interrogation time is shown in Fig. 36(c), and the entanglement-enhanced sensitivity can be maintained up to interrogation time of 342 ms. The array configuration is particularly well suited for differential measurements and magnetic-field gradiometry.

Using synthesized QND measurements in an ensemble of laser-cooled spin-1 Rb atoms, the spin-squeezed state has been generated and employed to perform high-precision magnetic measurement.⁸³ Based upon a Ramsey sequence, the squeezing-enhanced field measurement in a volume of $V = 3.7 \times 10^{-6} \text{ cm}^3$ can achieve a sensitivity of $\Delta B = 105 fT \sqrt{\text{cm}^3 \text{Hz}}$ in single-shot measurements. The experimental geometry is shown in Fig. 37(a), an ensemble of laser-cooled ^{87}Rb atoms in the ground state. Then, the spin-squeezed state is generated via utilizing the pulses sequence, as shown in Fig. 37(b). These pulses are used in pairs to synthesize the QND measurement or singly for the alignment-to-orientation conversion measurement. The Ramsey sequence for field measurement is shown in Fig. 37(c). First, using synthesized QND measurements to prepares a spin-squeezed

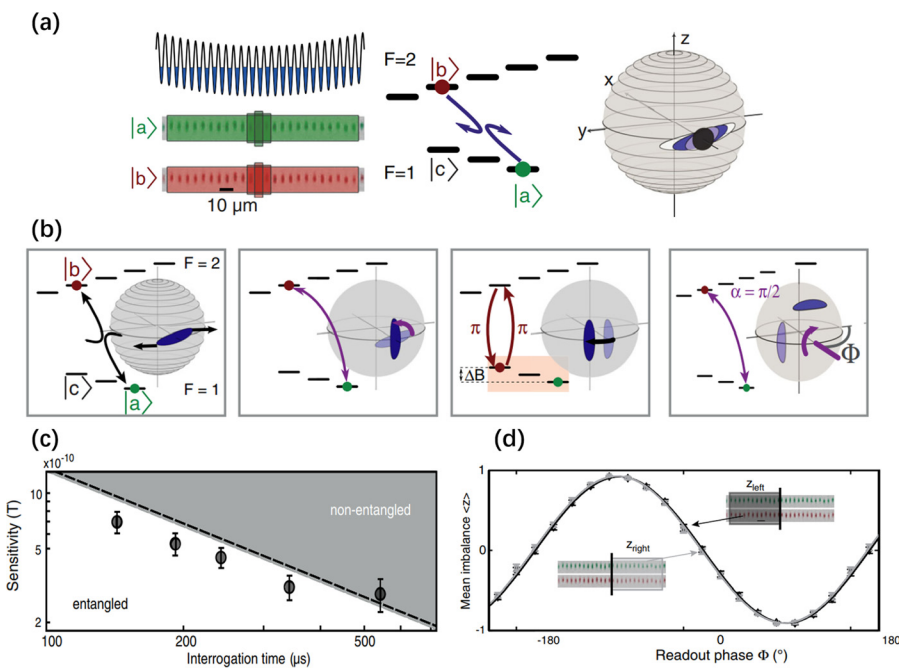


FIG. 36. Quantum-enhanced magnetometry with BECs in an optical lattice.⁷⁰ (a) Independent squeezing of 25 binary BECs in a 1D lattice. (b) The implemented experimental sequence for entanglement-enhanced magnetometer, which are displayed on generalized Bloch sphere. (c) Ramsey fringes for left and right parts of the full sample. (d) Magnetic field sensitivity of the Ramsey magnetometer vs interrogation time. Reproduced with permission from Muessel *et al.*, Phys. Rev. Lett. **113**(10), 103004 (2014).¹⁷⁰ Copyright 2014 American Physical Society.

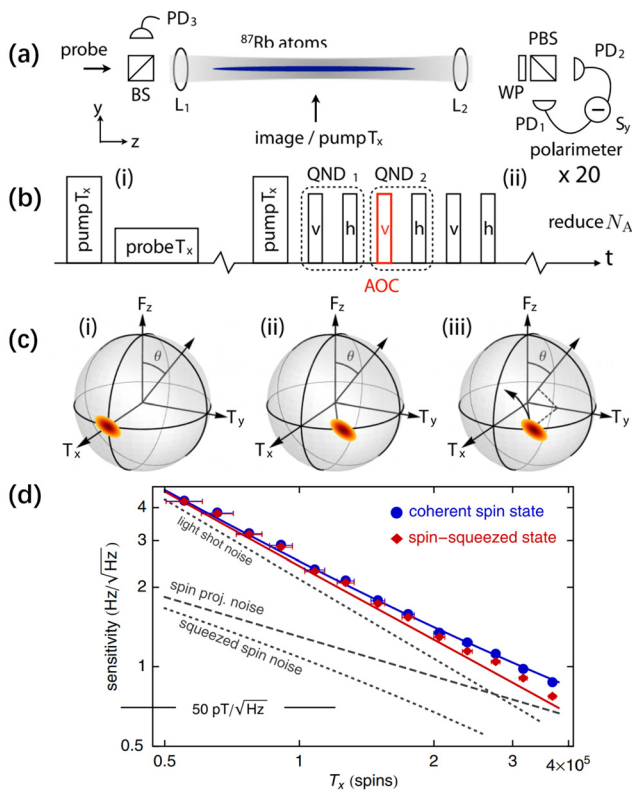


FIG. 37. Squeezing-enhanced magnetic field sensing with cold atomic ensembles.⁸³ (a) Experimental geometry. PD: photodiode; L: lens; WP: wave plate; BS: beam splitter; PBS: polarizing beam splitter. (b) Measurement sequence for generating spin-squeezed state. (c) Entanglement-enhanced field measurement. (d) Log-log plot of measurement sensitivity with an input spin coherent state (blue circles) and spin-squeezed state (red diamonds). Reproduced with permission from Sewell et al., Phys. Rev. Lett. **109**(25), 253605 (2012).⁸³ Copyright 2012 American Physical Society.

state. Then, the state is allowed to evolve for a time due to Zeeman shifts. Finally, a pulse is used for measurement, giving an integrated signal proportional to the Zeeman shift. The measurement sensitivity with an input spin coherent state and spin-squeezed state is shown in Fig. 37(d).

In recent, through combining the techniques of optical pumping and continuous QND measurement, a sustained spin-squeezed state with 4×10^{10} hot atoms has been achieved.⁴¹⁵ The steady spin squeezing with $\xi_R^2 = -3.23 \pm 0.24$ dB is prepared by applying the prediction and retrodiction QND protocol and can be maintained for about one day. The entanglement enhancement due to the steady spin squeezing is utilized by the atomic magnetometer. The system can be employed to track different types of continuous time-fluctuating magnetic fields, in which deep learning models are constructed to decode the measurement records from the optical signals. This work represents an important progress toward using long-lived quantum entanglement resources in realistic sensors.

In principle, utilizing well-developed Ramsey techniques, one can detect DC magnetic fields with ultrahigh sensitivity, while for the measurement of AC magnetic fields, just using Ramsey techniques is

insufficient, and various modulations need to be employed. It has been demonstrated that dynamical decoupling method, one of the well-known quantum control techniques, provides an excellent tool for measuring AC magnetic fields.^{56,72,82,95–102} In particular, by combining many-body Ramsey interferometry and rapid periodic π pulses, one can estimate DC and AC magnetic fields simultaneously. Meanwhile, the measurement precisions of DC and AC components can both exhibit Heisenberg scaling simultaneously for entangled particles in GHZ state.⁸⁸ Moreover, the dynamical decoupling method can be used to realize quantum lock-in measurement for high-precision magnetometers^{66,101} and force detector.¹⁰² Utilizing many-body entanglement, one can realize many-body quantum lock-in amplifiers, measuring the AC magnetic field with Heisenberg-limited scaling even under a strongly noisy background.⁴¹⁶

C. Gravimeters

Quantum gravimeters make use of quantum systems, such as ultracold atoms or molecules, to probe the gravity and achieve high sensitivity via using quantum resources. The first-generation quantum atomic gravimeter^{89,417} was developed in 1990s. With the unprecedented precision offered by quantum resources, atomic gravimeters are capable of detecting extremely small changes in the gravitational field and provide broad applications in geophysics, geodesy, metrology, and exploration of fundamental physics. Below we will introduce the progresses in entanglement-enhanced atomic gravimeters.

The basic principle of a quantum gravimeter involves the interferometric measurement of the phase shift induced by gravity on a matter wave.^{87,418} As an example, Fig. 38 shows a schematic of quantum gravimetry on an atom chip.¹⁷² Different from atomic clocks and

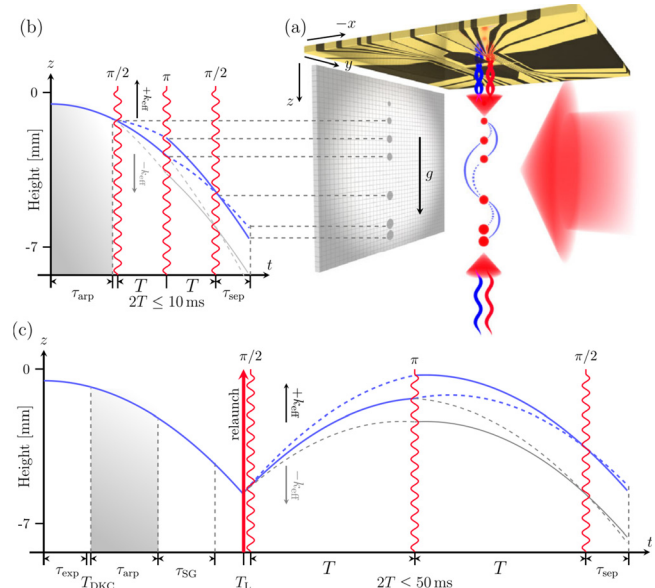


FIG. 38. Quantum gravimetry on an atom chip.¹⁷² (a) Schematic diagram of atom interferometry for gravity measurement. (b) Pulse sequence of atom interferometry. (c) Relaunch mechanism using Bloch oscillation and double Bragg mechanism to increase the sensitivity. Reproduced with permission from Abend et al., Phys. Rev. Lett. **117**(20), 203003 (2016).¹⁷² Copyright 2016 American Physical Society.

magnetometers, quantum gravimeters are a type of inertial sensors and they generally require distinct spatial paths. Generally, quantum gravimeters are implemented via standard Mach-Zehnder interferometers,^{419,420} in which beam splitters ($\pi/2$ pulses) and mirrors (π pulses) are achieved via Raman transitions. The Raman transitions are realized with two counter-propagating lasers of wave vector k_L , which coherently couple two internal states. As a result of momentum conservation, a transition between the two internal states will impart a momentum of $2\hbar k_L$ to an atom, giving the momentum separation needed for gravity measurement. The phase of an interferometer is related to the gravity acceleration g as $\Phi = k_{\text{eff}} \cdot gT^2$ with the effective wave vector k_{eff} and the evolution time T .

To improve the precision of quantum gravimeters, in addition to large momentum transfer⁴¹⁸ via Bloch oscillations or double Bragg diffraction, multi-particle entangled momentum states^{128,274,421,422} have been introduced. It has been demonstrated that one can increase the interferometric area via using large momentum transfer.^{90,423–427} This allows to improve the sensitivity by increasing the effective separation between the two interfering atomic samples. However, there may appear extra phase noises induced by the effective multi-photon process for achieving large momentum transfer. Quantum entanglement offers another promising route to improve their measurement precision. Using spin-squeezed states, the sensitivity can be given as follows:

$$\Delta g = \frac{\xi_R}{\sqrt{N}k_{\text{eff}} T^2}, \quad (126)$$

where N is the number of atoms, and ξ_R is the squeezing parameter. In an atom interferometer with entangled momentum states,⁴²¹ a spin squeezing of -3.1 dB has been achieved in experiments. Thus, quantum-enhanced atomic inertial sensors in a more matured form should be promising in the near future.¹²⁸

With currently available experimental techniques, a theoretical study⁴²⁸ shows that spin-squeezed ultracold atoms can improve the sensitivity up to 14 dB beyond the SQL. As shown in Fig. 39(b), before the standard Mach-Zehnder interference process, an initial state preparation generating spin squeezing via the interatomic interactions during the expansion period is introduced. Unlike the trapped schemes, where interatomic collisions cause unwanted multimode dynamics that make it difficult to match the two modes upon recombination,⁴²⁹ a BEC's spatial mode is almost perfectly preserved under free expansion, even for large atom numbers and collisional energies. Furthermore, since the collision energy is converted to kinetic energy during expansion, the interatomic interactions effectively “switch off” after ~ 10 ms, minimizing their effect during most of the interferometer sequence. This scheme allows high-precision gravimetry up to a factor of five below the SQL and is robust to a range of experimental imperfections.

Due to its compact size, the atomic interferometer via Bloch oscillations^{430–432} provides another excellent candidate for building quantum gravimeters. In such a setup, cold atoms are held in a vertical optical lattice tilted by the gravity. Therefore, the cold atoms will undergo Bloch oscillations whose frequency is determined by the gravity and the lattice constant. To harness entanglement, a scheme has been developed utilizing an ensemble of ultracold atoms in tilted spin-dependent optical lattices along the direction of gravity.⁴³³ The fast coherent separation and recombination of atoms can be realized via polarization-synthesized optical lattices. The input atomic wave packet

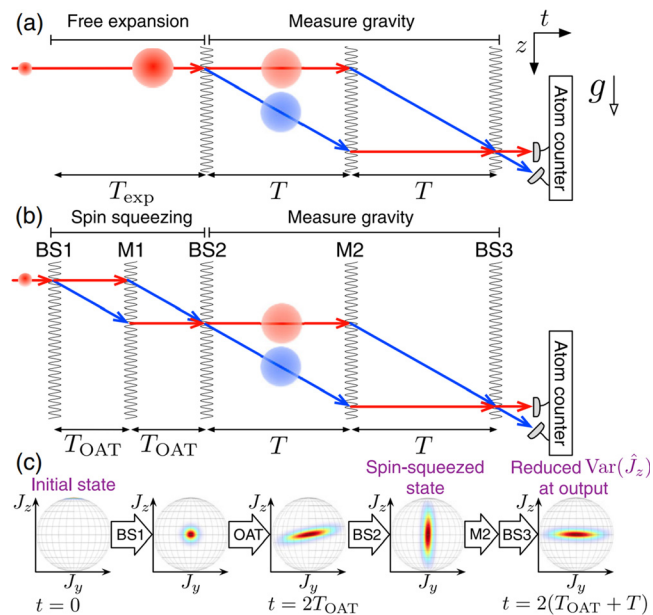


FIG. 39. Entanglement-enhanced gravity measurement with BEC.⁴²⁸ (a) Space-time diagram illustrating gravimetry with a BEC attaining the SQL. Unwanted interatomic interactions are reduced by freely expanding the BEC for duration T_{exp} . A $\pi/2 - \pi - \pi/2$ Raman pulse sequence then creates a Mach-Zehnder interferometer of interrogation time T . The two interferometer modes correspond to internal states $|1\rangle$ (red) and $|2\rangle$ (blue) with momentum separation. (b) Quantum-enhanced ultracold-atom gravimetry. During initial expansion duration, the BEC's interatomic interactions generate spin squeezing via OAT. (c) Bloch sphere representation of state during entanglement-enhanced gravimetry. Reproduced with permission from Szegedi et al., Phys. Rev. Lett. **125**(10), 100402 (2020).⁴²⁸ Copyright 2020 American Physical Society.

is coherently split into two parts by a spin-dependent shift and a subsequent $\pi/2$ pulse. Then, the two parts are held for accumulating a relative phase related to the gravity. Finally, the two parts are recombined for interference by a $\pi/2$ pulse and a subsequent spin-dependent shift. The pulses not only preclude the spin-dependent energies in the accumulated phase, but also avoid the error sources, such as dislocation of optical lattices in the holding process. In particular, by using entangled states as initial states, the measurement precision of such an interferometer can beat the SQL.

However, even in laboratory-based proof-of-principle apparatus, there is still a considerable gap to overcome in demonstrating entanglement-enhanced gravimetry. The main challenge stems from the fact that most methods of generating entangled atomic states do not meet the stringent requirements of precision gravimetry. Most cold-atom gravimeters necessitate the creation and precise control of distinct and well-isolated atomic matter-wave momentum modes. To achieve a significant fringe contrast, it is crucial to maintain coherence between these modes for extended periods during the interrogation process, while also ensuring proper alignment of the modes at the output of the interferometer.

D. Gyroscopes

High-performance gyroscopes for rotation sensing are crucial for navigation in a wide range of air, ground, marine, and space

applications. Rotation frequency is commonly measured by using the Sagnac effect, which is the accumulation of a rotation-dependent phase difference by two counter-propagating waves in a revolving loop. Gyroscopes operate with either lasers (an ensemble of photons—a type of massless particles) or massive particle such as atoms.

Usually, an optical gyroscope uses two counter-propagating laser beams to sense a rotation. If the setup rotates with an angular velocity Ω , the two laser beams will accumulate a relative phase $\Phi = 4M\Omega A_o / (\lambda c)$ with M the number of rounds, A_o the area enclosed by the gyroscope parallel to the rotation direction, λ the wavelength, and c the speed of light. However, the conventional SQL still places a limit on their precision, which is proportional to the surface area contained by the optical path. In a recent theoretical proposal, the utilization of distributed quantum sensing is envisioned as a means to enhance the performance of fiber gyroscopes specifically for navigation applications.¹⁷³ The idea is to inject quantum-optical squeezed vacuum light, like what was utilized in a RF-sensing experiment,⁷⁰ into to an array of fiber gyroscopes to improve the scaling of measurement precisions. The idea is to inject quantum-optical squeezed vacuum light, like what was utilized in the RF-sensing experiment,⁷⁰ into to an array of fiber gyroscopes to improve the scaling of the measurement noise. Moreover, such a configuration can also be applied to improve the readout signal-to-noise ratio of an array of optomechanical transducers used in inertial sensing⁵¹ and atomic force microscopes.⁴³⁴

Similar to an optical gyroscope, in an atomic gyroscope, two counter-propagating atomic beams accumulate a relative phase $\Phi = 2m\Omega A_a / \hbar$ with m the atomic mass, the angular velocity Ω , and A_a the area enclosed by the gyroscope parallel to the rotation direction. Theoretically, the sensitivity of an atom interferometer is about ten orders of magnitude larger than the optical counterpart due to m/\hbar is much larger than $1/(\lambda c)$. However, the optical interferometers have much larger interferometric area than the atom interferometers, i.e., $4MA_o \gg 2A_a$, practically the sensitivity can be improved by about 3–4 orders of magnitude gain. Atomic gyroscopes have made significant advancements since their early demonstrations,^{417,435} achieving a short-term sensitivity of 6×10^{-10} (rad/s) / $\sqrt{\text{Hz}}$ with a one-second interrogation time.⁴³⁵ Using two counter-propagating atomic beam geometries, one can isolate the phase shifts respectively caused by acceleration and rotation. By removing phase shifts caused by non-inertial effects such as magnetic field and ac Stark shift, the long-term sensitivity can be further improved.⁴³⁶ To counteract systematic effects and long-term drift, they employed a technique of regularly inverting the propagation vector k_{eff} which resulted in an opposite sign for the inertial phase while preserving the sign of the non-inertial phase. By utilizing this approach, the system was able to improve its sensitivity to 3×10^{-10} (rad/s) $\sqrt{\text{Hz}}$ during a 5-h interrogation duration.

To improve the long-term stability and shorten dead times of atomic gyroscopes, atomic beam source can be replaced by laser-cooled atoms. By using two cold atomic clouds launched in curved parabolic trajectories in a counter-propagating directions, a cold atomic gyroscope has been demonstrated experimentally,⁴³⁷ in which the short-term sensitivities of acceleration and rotation were 4.7×10^{-6} and 2.2×10^{-6} (rad/s) / $\sqrt{\text{Hz}}$, respectively. Instead of employing continuously running beams, it utilizes three pulsed Raman beams oriented in three orthogonal directions. In a similar experiment,⁴³⁸ the long-term stability after an integration time of 1000 s was shown to be limited by the QPN, 1×10^{-8} (rad/s) / $\sqrt{\text{Hz}}$. In recent years, there

appear numerous advancements in cold atomic gyroscopes. A zero dead time gyroscope was presented, where continuous operation contributed to enhancing the short-term sensitivity to 1×10^{-7} (rad/s) / $\sqrt{\text{Hz}}$.⁴³⁹ A Sagnac interferometry with a single-atom clock⁴⁴⁰ had been proposed by combining the techniques of state-dependent manipulations and Ramsey pulses. Based upon an interleaved atom interferometry with a sampling rate of 3.75 Hz and an interrogation time of 801 ms, in which three atomic clouds are simultaneously interrogated, the sensitivity has been improved to 3×10^{-10} (rad/s) / $\sqrt{\text{Hz}}$, which competes with the best results achieved using fiber-optic gyroscopes.⁴⁴¹ In addition, several compact designs utilizing atom chips^{442,443} have shown preliminary rotation sensing capabilities through double Bragg diffraction. Furthermore, using the nitrogen-vacancy center in diamonds,^{174,444} it is possible to perform rotational measurements, which in turn paves the way for the realization of microchip-size gyroscopes.

Beyond the conventional scheme with individual particles, it is interesting to investigate how to exploit many-body quantum entanglement in measuring rotation frequency. Ultracold atomic system provides a feasible experimental platform for achieving this objective.^{445–447} A spin-squeezed rotation sensor utilizing the Sagnac effect in a spin-1 BEC in a ring trap was proposed.⁴⁴⁵ By employing Laguerre–Gauss beams and Raman pulses, the two input states are initially prepared and subsequently amplified through the bosonic enhancement of spin-exchange collisions. This process leads to spin-squeezing, which in turn offers quantum enhancement for rotation sensing. An alternative multi-particle scheme utilizing two-mode Bose condensed atoms was also proposed.⁴⁴⁶ In this scheme, an ensemble of entangled two-state Bose atoms is transported in a ring-shaped path using a state-dependent rotating potential. Subsequently, the atoms are recombined for interference by employing Ramsey pulses. The duration of phase accumulation is controlled by the state-dependent rotating potential. The ultimate sensitivity to rotation can be enhanced to reach the Heisenberg limit by utilizing entangled initial internal degrees of freedom. By implementing parity measurement, the measurement precision can be maximized, and the achieved precisions approach the Heisenberg limit. However, this scheme requires parity measurement based upon single-atom resolution detection. The non-linear detection in Sec. IV C may be helpful for removing the need of single-atom resolution detection.

The journey toward practical entanglement-enhanced quantum sensors may be long and unpredictable. A hard and crucial initial step involves surpassing the SQL in measurements to demonstrate the feasibility of a specific inertial quantity. Advancements in entanglement-enhanced clocks provide valuable insights that inform the development of design strategies to achieve this goal. Furthermore, quantum sensors for acceleration, rotation, gravity, and magnetic fields can be integrated into position, navigation, and timing systems for applications in underwater and underground environments. In such applications, quantum sensors surpass their classical counterparts by offering reduced bias, improved precision, and greater stability. This may enable navigation with meter-level accuracy without relying on global satellite systems.¹⁰³

VI. SUMMARY AND OUTLOOKS

In summary, the utilization of multi-particle entanglement offers promising potentials to improve measurement precision beyond conventional shot-noise limit. This has sparked an active and dynamic research field focused on characterizing, manipulating, and utilizing

entangled multi-particle quantum states.^{448–450} With the rapid progress in creating and detecting multi-particle entangled state, quantum metrology is emerging as a domain capable of achieving quantum advantages over conventional measurements and sensing for practical applications in the near future. The field of entanglement-enhanced quantum metrology is poised to shift from theoretical studies⁴⁵¹ to experimental demonstrations and practical applications, specifically in the realm of precise measurements involving frequency,⁶⁸ electromagnetic fields,^{61,452} and forces. Nevertheless, there remain several challenges in constructing entanglement-enhanced quantum sensors for real-world applications.

Developing a practical entanglement-enhanced quantum sensor poses a significant challenge, not in generating entanglement itself, but in generating entanglement that meets the precise sensing requirements of a particular application. These requirements, such as particle number and interrogation time, impose constraints on achievable measurement precision. One of the difficulties lies in scalability with particle number, as an increase in particles tends to rapidly amplify errors and complicate the experiment. If only a limited number of particles can achieve a certain degree of entanglement, the improvement over the SQL may not be readily apparent. Similarly, if entanglement can only persist for a short interrogation time or is susceptible to weak experimental noises, it may not lead to a significant enhancement in practical sensing tasks. Future research should prioritize utilizing entanglement to surpass the SQL and focus on developing entanglement-enhanced quantum metrology protocols specifically tailored for practical sensing scenarios.

It is worth noting that, while many experiments demonstrate improved precision scaling in entanglement-enhanced metrology, their absolute measurement precisions for certain quantities still do not match the highest levels achieved by state-of-the-art measurements performed without entanglement. Although various quantum entanglement has been successfully generated in experiments, utilizing quantum entanglement for realistic measurements continues to encounter several challenges, resulting in performance that lags behind state-of-the-art methods without involving entanglement. Exhilaratingly, a recent experiment of optical lattice clock comparison³⁷⁴ has demonstrated a stability performance at the level of 10^{-17} , which is close to the best state-of-the-art clocks.²⁶ With the growing capabilities of quantum control for engineering many-body entangled states,²⁰ the prospect of transitioning from demonstration to achieving genuine quantum advantage in the near future is increasingly promising.

Quantum entanglement is highly susceptible to decoherence,^{140–143,453} leading to a significant reduction in achievable measurement precision.^{142,454,455} This fragility is particularly evident when employing long interrogation times to achieve high precision. Theoretical investigations have demonstrated the detrimental impact of decoherence on surpassing the SQL.^{59,456} Typically, measurement precision returns to the SQL during an optimal transient interrogation period but diverges in the long-interrogation-time regime due to the effects of decoherence. To mitigate the negative effects of decoherence on quantum metrology, various strategies have been proposed.^{260–262,347,453,457–467} These include adaptive^{162,468,469} and quantum nondemolition measurements,⁴⁷⁰ correlated decoherence,⁴⁵⁴ and dynamical control,^{471–473} aiming to restore the Heisenberg limit. With

advancements in strategies such as quantum reservoir engineering,⁴⁷⁴ Floquet engineering,⁴⁶⁷ quantum error mitigation,^{475,476} and other techniques, quantum metrology is on the verge of transitioning from the laboratory to practical use. Additionally, quantum feedback,^{260–262,347} quantum error correction,^{458–462} and other techniques^{463,464,468,477–479} can be employed to extend coherence time and achieve robust high-precision measurements in experiments. Moreover, various modulation techniques such as periodic modulation,^{66,100} quantum heterodyne,⁷¹ quantum mixing,⁶⁵ and quantum lock-in amplification measurement^{101,416} enable high-precision frequency estimation even in noisy environments. The combination of these quantum control techniques with quantum entanglement holds the potential for significant advancements in the field of entanglement-enhanced sensing technologies.

On the other hand, while enhancing measurement precision, it is crucial to improve measurement accuracy by minimizing systematic errors. In general, systematic errors always introduce inaccuracies that impact the overall performance of measurements.^{19,480} For instance, in atomic optical clocks, system errors arising from laser probe frequency or intensity instabilities can lead to systematic frequency shifts, compromising clock accuracy. To mitigate the effects of laser intensity variations and reduce corresponding frequency shifts, composite pulse sequences can be employed,^{158,481,482} improving measurement accuracy. Other sources of systematic errors, such as collision shifts, Doppler shifts, Stark shifts, and blackbody radiation shifts, can also have adverse effects.¹⁵⁶ Therefore, it is important to assess systematic errors throughout the process of quantum parameter estimation and develop methods to suppress specific system errors in many-body sensing systems.

To optimize the performance of a practical quantum metrology, in addition to conventional optimization tools, machine learning has emerged as a powerful tool.^{483,484} Machine learning may optimize various aspects of a quantum metrology process,³⁶³ including generation of entangled states, signal accumulation, entangled state readout, and parameter estimation. In scenarios with limited resources, such as limited coherence time or measurement times, machine learning approaches like reinforcement learning^{290,484,485} quantum algorithms,^{486–489} and Bayesian inference^{490–493} can guide us in determining the most effective strategies for conducting metrology.⁴⁹⁴ The exploration of quantum metrology protocols augmented by machine learning offers an alternative pathway toward achieving practical high-precision measurements.

In addition to the typical entangled states discussed in Sec. III, strong types of quantum correlations such as EPR steering and Bell nonlocality are also useful for quantum metrology.⁴⁹⁵ It has been demonstrated that EPR-assisted metrology may precisely estimate a local phase shift and its generating observable.^{496,497} Bell nonlocality seems to be linked to high QFI, implying a potential connection to metrological advantages.^{498,499} Moreover, nonclassical states of atomic ensembles can be spatially distributed in different positions,^{500–504} which allows for quantum-enhanced distributed sensing.

In addition, associated with quantum entanglement, quantum criticality has been recognized as a novel quantum resource for enhancing quantum metrology.^{15,508–511} On the one hand, quantum systems prepared near the critical point exhibit extreme sensitivity to small perturbations.⁵¹² By leveraging the criticality associated with quantum phase transitions, high-precision measurements of physical

quantities can be achieved. Systems near a quantum phase transition display a divergent susceptibility, indicating the potential for achieving remarkably high precision by utilizing quantum critical systems as probes for parameter estimation.^{262,513} On the other hand, parameter estimation can be accomplished by measuring the equilibrium state or dynamical properties of the system when it is driven close to the critical point of a quantum phase transition.^{514,515} Furthermore, the response of eigenstates in non-Hermitian systems to small perturbations at singularities can also be utilized to detect specific physical quantities.^{516–526}

At last, it is important to note that multi-parameter estimation^{138,527–533} is a crucial problem in both fundamental research and practical applications,^{534–536} alongside single-parameter estimation. It has been extensively employed for various purpose, including vector field detection^{537,538} and imaging and biological sensing.^{539,540} Several studies have demonstrated that a multi-parameter approach can outperform the optimal quantum individual estimation scheme⁵²⁸ and offer advantages in the presence of noise.^{539,540} Although progress has been made in multi-parameter estimation scenarios,^{532–534,539–544} including finding the optimal measurement strategies,^{545–547} how to experimentally achieve the optimal multi-parameter measurement in the presence of noise remains a challenge. Furthermore, the development of entanglement-enhanced multi-parameter estimation is crucial for practical quantum sensing, such as vector magnetometers^{537,538} and multimode quantum imaging.^{489,528}

ACKNOWLEDGMENTS

The authors acknowledged Matteo Fadel, Kaoru Yamamoto, Geza Toth, Yingkai Ouyang, and Chao-Yang Lu for their valuable suggestions. The authors thank Jihao Ma, Jungeng Zhou, Sijie Chen, Yi Shen, Yuehua Pang, and Jinye Wei for critical reading and helpful suggestions. This work was supported by the National Natural Science Foundation of China (Grant Nos. 12025509 and 12305022) and the National Key Research and Development Program of China (Grant No. 2022YFA1404104).

AUTHOR DECLARATIONS

Conflict of Interest

The authors have no conflicts to disclose.

Author Contributions

J. Huang and M. Zhuang contributed equally to this work.

Jiahao Huang: Conceptualization (equal); Data curation (equal); Formal analysis (equal); Investigation (equal); Methodology (equal); Resources (equal); Software (equal); Validation (equal); Visualization (equal); Writing—original draft (equal); Writing—review & editing (equal). **Min Zhuang:** Conceptualization (equal); Data curation (equal); Formal analysis (equal); Investigation (equal); Methodology (equal); Resources (equal); Software (equal); Validation (equal); Visualization (equal); Writing—original draft (equal); Writing—review & editing (equal). **Chaohong Lee:** Conceptualization (equal); Funding acquisition (equal); Investigation (equal); Methodology (equal); Project administration (equal); Supervision (equal); Validation (equal); Writing—original draft (equal); Writing—review & editing (equal).

DATA AVAILABILITY

Data sharing is not applicable to this article as no new data were created or analyzed in this study.

REFERENCES

- ¹C. M. Caves, “Quantum-mechanical noise in an interferometer,” *Phys. Rev. D* **23**, 1693–1708 (1981).
- ²B. Yurke, S. L. McCall, and J. R. Klauder, “SU(2) and SU(1,1) interferometers,” *Phys. Rev. A* **33**, 4033–4054 (1986).
- ³M. J. Holland and K. Burnett, “Interferometric detection of optical phase shifts at the Heisenberg limit,” *Phys. Rev. Lett.* **71**, 1355–1358 (1993).
- ⁴V. Giovannetti, “Quantum-enhanced measurements: Beating the standard quantum limit,” *Science* **306**, 1330–1336 (2004).
- ⁵V. Giovannetti, S. Lloyd, and L. Maccone, “Quantum metrology,” *Phys. Rev. Lett.* **96**, 010401 (2006).
- ⁶C. Lee, “Adiabatic Mach-Zehnder interferometry on a quantized Bose-Josephson junction,” *Phys. Rev. Lett.* **97**, 150402 (2006).
- ⁷S. Boixo, A. Datta, M. J. Davis, S. T. Flammia, A. Shaji, and C. M. Caves, “Quantum metrology: Dynamics versus entanglement,” *Phys. Rev. Lett.* **101**, 040403 (2008).
- ⁸P. M. Anisimov, G. M. Raterman, A. Chiruvelli, W. N. Plick, S. D. Huver, H. Lee, and J. P. Dowling, “Quantum metrology with two-mode squeezed vacuum: Parity detection beats the Heisenberg limit,” *Phys. Rev. Lett.* **104**, 103602 (2010).
- ⁹L. Maccone and V. Giovannetti, “Quantum metrology: Beauty and the noisy beast,” *Nat. Phys.* **7**, 376–377 (2011).
- ¹⁰V. Giovannetti, S. Lloyd, and L. Maccone, “Advances in quantum metrology,” *Nat. Photonics* **5**, 222–229 (2011).
- ¹¹C. Gross, “Spin squeezing, entanglement and quantum metrology with Bose-Einstein condensates,” *J. Phys. B* **45**, 103001 (2012).
- ¹²R. Demkowicz-Dobroński and L. Maccone, “Using entanglement against noise in quantum metrology,” *Phys. Rev. Lett.* **113**, 250801 (2014).
- ¹³P. Sekatski, M. Skotiniotis, J. J. Kolodynski, and W. Dür, “Quantum metrology with full and fast quantum control,” *Quantum* **1**, 27 (2016).
- ¹⁴C. L. Degen, F. Reinhard, and P. Cappellaro, “Quantum sensing,” *Rev. Mod. Phys.* **89**, 035002 (2017).
- ¹⁵M. M. Rams, P. Sierant, O. Dutta, P. Horodecki, and J. Zakrzewski, “At the limits of criticality-based quantum metrology: Apparent super-Heisenberg scaling revisited,” *Phys. Rev. X* **8**, 021022 (2018).
- ¹⁶L. Pezzè, A. Smerzi, M. K. Oberthaler, R. Schmied, and P. Treutlein, “Quantum metrology with nonclassical states of atomic ensembles,” *Rev. Mod. Phys.* **90**, 035005 (2018).
- ¹⁷L. Garbe, M. Bina, A. Keller, M. G. A. Paris, and S. Felicetti, “Critical quantum metrology with a finite-component quantum phase transition,” *Phys. Rev. Lett.* **124**, 120504 (2020).
- ¹⁸X. Long, W.-T. He, N.-N. Zhang, K. Tang, Z. Lin, H. Liu, X. Nie, G. Feng, J. Li, T. Xin, Q. Ai, and D. Lu, “Entanglement-enhanced quantum metrology in colored noise by quantum Zeno effect,” *Phys. Rev. Lett.* **129**, 070502 (2022).
- ¹⁹Y. L. Len, T. Gefen, A. Retzker, and J. J. Kolodynski, “Quantum metrology with imperfect measurements,” *Nat. Commun.* **13**, 6971 (2022).
- ²⁰J. Ye and P. Zoller, “Essay: Quantum sensing with atomic, molecular, and optical platforms for fundamental physics,” *Phys. Rev. Lett.* **132**, 190001 (2024).
- ²¹R. Schnabel, N. Mavalvala, D. E. McClelland, and P. K. Lam, “Quantum metrology for gravitational wave astronomy,” *Nat. Commun.* **1**, 121 (2010).
- ²²G. Rosi, G. D. Amico, L. Cacciapuoti, F. Sorrentino, M. Prevedelli, M. Zych, C. Brukner, and G. M. Tino, “Quantum test of the equivalence principle for atoms in coherent superposition of internal energy states,” *Nat. Commun.* **8**, 15529 (2017).
- ²³M. Takamoto, I. Ushijima, N. Ohmae, T. Yahagi, K. Kokado, H. Shinkai, and H. Katori, “Test of general relativity by a pair of transportable optical lattice clocks,” *Nat. Photonics* **14**, 411–415 (2020).
- ²⁴M. S. Safranova and D. Budker, “Quantum technologies and the elephants,” *Quantum Sci. Technol.* **6**, 040401 (2021).

- ²⁵K. Lehnert, "Quantum enhanced metrology in the search for fundamental physical phenomena," *SciPost Phys. Lect. Notes* **40**, 1–20 (2022).
- ²⁶T. Bothwell, C. J. Kennedy, A. Aepli, D. Kedar, J. M. Robinson, E. Oelker, A. Staron, and J. Ye, "Resolving the gravitational redshift across a millimetre-scale atomic sample," *Nature* **602**, 420–424 (2022).
- ²⁷D. DeMille, N. R. Hutzler, A. M. Rey, and T. Zelevinsky, "Quantum sensing and metrology for fundamental physics with molecules," *Nat. Phys.* **20**, 741–749 (2024).
- ²⁸T. Rosenband, D. B. Hume, P. O. Schmidt, C. W. Chou, A. Brusch, L. Lorini, W. H. Oskay, R. E. Drullinger, T. M. Fortier, J. E. Stalnaker, S. A. Diddams, W. C. Swann, N. R. Newbury, W. M. Itano, D. J. Wineland, and J. C. Bergquist, "Frequency ratio of Al⁺ and Hg⁺ single-ion optical clocks: Metrology at the 17th decimal place," *Science* **319**, 1808–1812 (2008).
- ²⁹C. Yu, W. Zhong, B. Estey, J. Kwan, R. H. Parker, and H. Müller, "Atom-interferometry measurement of the fine structure constant," *Ann. Phys.* **531**, 1800346 (2019).
- ³⁰L. Morel, Z. Yao, P. Clade, and S. Guellati-Khelifa, "Determination of the fine-structure constant with an accuracy of 81 parts per trillion," *Nature* **588**, 61–65 (2020).
- ³¹T. Zhang, H. Yang, D. Martynov, P. Schmidt, and H. Miao, "Gravitational-wave detector for postmerger neutron stars: Beyond the quantum loss limit of the Fabry–Pérot–Michelson interferometer," *Phys. Rev. X* **13**, 021019 (2023).
- ³²S. Kolkowitz, I. Pikovski, N. Langellier, M. D. Lukin, R. L. Walsworth, and J. Ye, "Gravitational wave detection with optical lattice atomic clocks," *Phys. Rev. D* **94**, 124043 (2016).
- ³³P. W. Graham, J. M. Hogan, M. A. Kasevich, and S. Rajendran, "New method for gravitational wave detection with atomic sensors," *Phys. Rev. Lett.* **110**, 171102 (2013).
- ³⁴F. Y. Khalili and E. S. Polzik, "Overcoming the standard quantum limit in gravitational wave detectors using spin systems with a negative effective mass," *Phys. Rev. Lett.* **121**, 031101 (2018).
- ³⁵M. Tse, H. Yu, N. Kijbunchoo, A. Fernandez-Galiana, P. Dupej, L. Barsotti, C. D. Blair, D. D. Brown, S. E. Dwyer, A. Effler, M. Evans, P. Fritschel, V. V. Frolov, A. C. Green, G. L. Mansell, F. Matichard, N. Mavalvala, D. E. McClelland, L. McCuller, T. McRae, J. Miller, A. Mullavey, E. Oelker, I. Y. Phinney, D. Sigg, B. J. J. Slagmolen, T. Vo, R. L. Ward, C. Whittle, R. Abbott, C. Adams, R. X. Adhikari, A. Ananyeva, S. Appert, K. Arai, J. S. Areeda, Y. Asali, S. M. Aston, C. Austin, A. M. Baer, M. Ball, S. W. Ballmer, S. Banagiri, D. Barker, J. Bartlett, B. K. Berger, J. Betzwieser, D. Bhattacharjee, G. Billingsley, S. Biscans, R. M. Blair, N. Bode, P. Booker, R. Bork, A. Bramley, A. F. Brooks, A. Buikema, C. Cahillane, K. C. Cannon, X. Chen, A. A. Ciobanu, F. Clara, S. J. Cooper, K. R. Corley, S. T. Countryman, P. B. Covas, D. C. Coyne, L. E. H. Datrier, D. Davis, C. Di Fronzo, J. C. Driggers, T. Etzel, T. M. Evans, J. Feicht, P. Fulda, M. Fyffe, J. A. Giaime, K. D. Giardina, P. Godwin, E. Goetz, S. Gras, C. Gray, R. Gray, A. Gupta, E. K. Gustafson, R. Gustafson, J. Hanks, J. Hanson, T. Hardwick, R. K. Hasskew, M. C. Heintze, A. F. Helmling-Cornell, N. A. Holland, J. D. Jones, S. Kandhasamy, S. Karki, M. Kasprzack, K. Kawabe, P. J. King, J. S. Kissel, R. Kumar, M. Landry, B. B. Lane, B. Lantz, M. Laxen, Y. K. Lecoeuche, J. Leviton, J. Liu, M. Lormand, A. P. Lundgren, R. Macas, M. MacInnis, D. M. Macleod, S. Márrka, Z. Márrka, D. V. Martynov, K. Mason, T. J. Massinger, R. McCarthy, S. McCormick, J. McIver, G. Mendell, K. Merfeld, E. L. Merilh, F. Meylahn, T. Mistry, R. Mittleman, G. Moreno, C. M. Mow-Lowry, S. Mozzon, T. J. N. Nelson, P. Nguyen, L. K. Nuttall, J. Oberling, R. J. Oram, B. O'Reilly, C. Osthelder, D. J. Ottawa, H. Overmier, J. R. Palamos, W. Parker, E. Payne, A. Pele, C. J. Perez, M. Pirello, H. Radkins, K. E. Ramirez, J. W. Richardson, K. Riles, N. A. Robertson, J. G. Rollins, C. L. Romel, J. H. Romie, M. P. Ross, K. Ryan, T. Sadecki, E. J. Sanchez, L. E. Sanchez, T. R. Saravanan, R. L. Savage, D. Schaetzl, R. Schnabel, R. M. S. Schofield, E. Schwartz, D. Sellers, T. J. Shaffer, J. R. Smith, S. Soni, B. Sorazu, A. P. Spencer, K. A. Strain, L. Sun, M. J. Szczepańczyk, M. Thomas, P. Thomas, K. A. Thorne, K. Toland, C. I. Torrie, G. Taylor, A. L. Urban, G. Vajente, G. Valdes, D. C. Vander-Hyde, P. J. Veitch, K. Venkateswara, G. Venugopalan, A. D. Viets, C. Vorick, M. Wade, J. Warner, B. Weaver, R. Weiss, B. Willke, C. C. Wipf, L. Xiao, H. Yamamoto, M. J. Yap, H. Yu, L. Zhang, M. E. Zucker, and J. Zweizig, "Quantum-enhanced advanced LIGO detectors in the era of gravitational-wave astronomy," *Phys. Rev. Lett.* **123**, 231107 (2019).
- ³⁶Y. Jiang, M. Abe, P. Adamson, M. Borcean, D. Bortolotto, K. Bridges, S. P. Carman, S. Chattopadhyay, J. Coleman, N. M. Curfman, K. Derose, T. Deshpande, S. Dimopoulos, C. J. Foot, J. C. Frisch, B. E. Garber, S. Geer, V. Gibson, J. Glick, P. W. Graham, S. R. Hahn, R. Harnik, L. Hawkins, S. Hindley, J. M. Hogan, Y. Jiang, M. A. Kasevich, R. J. Kellett, M. Kiburg, T. Kovachy, J. D. Lykken, J. March-Russell, J. Mitchell, M. Murphy, M. Nantel, L. E. Nobrega, R. K. Plunkett, S. Rajendran, J. Rudolph, N. Sachdeva, M. Safdari, J. K. Santucci, A. G. Schwartzman, I. Shipsey, H. Swan, L. R. Valerio, A. Vasonis, Y. Wang, and T. Wilkason, "Matter-wave atomic gradiometer interferometric sensor (MAGIS-100)," *Quantum Sci. Technol.* **6**, 044003 (2021).
- ³⁷L. Badurina, O. Buchmueller, J. Ellis, M. Lewicki, C. McCabe, and V. Vaskonen, "Prospective sensitivities of atom interferometers to gravitational waves and ultralight dark matter," *Philos. Trans. R. Soc. A* **380**, 20210060 (2022).
- ³⁸Y. V. Stadnik and V. V. Flambaum, "Searching for dark matter and variation of fundamental constants with laser and maser interferometry," *Phys. Rev. Lett.* **114**, 161301 (2015).
- ³⁹A. Arvanitaki, J. Huang, and K. Van Tilburg, "Searching for dilaton dark matter with atomic clocks," *Phys. Rev. D* **91**, 015015 (2015).
- ⁴⁰K. M. Backes, D. A. Palken, S. A. Kenany, B. M. Brubaker, S. B. Cahn, A. Droster, G. C. Hilton, S. Ghosh, H. Jackson, S. K. Lamoreaux, A. F. Leder, K. W. Lehnert, S. M. Lewis, M. Malnou, R. H. Maruyama, N. M. Rapidis, M. Simanovskia, S. Singh, D. H. Speller, I. Urdinaran, L. R. Vale, E. C. van Assendelft, K. van Bibber, and H. Wang, "A quantum enhanced search for dark matter axions," *Nature* **590**, 238–242 (2021).
- ⁴¹A. O. Sushkov, "Quantum science and the search for axion dark matter," *PRX Quantum* **4**, 020101 (2023).
- ⁴²A. J. Brady, C. Gao, R. Harnik, Z. Liu, Z. Zhang, and Q. Zhuang, "Entangled sensor-networks for dark-matter searches," *PRX Quantum* **3**, 030333 (2022).
- ⁴³E. Peik, T. Schumm, M. S. Safronova, A. Palfy, J. Weitenberg, and P. G. Thirolf, "Nuclear clocks for testing fundamental physics," *Quantum Sci. Technol.* **6**, 034002 (2021).
- ⁴⁴A. V. Dixit, S. Chakram, K. He, A. Agrawal, R. K. Naik, D. I. Schuster, and A. Chou, "Searching for dark matter with a superconducting qubit," *Phys. Rev. Lett.* **126**, 141302 (2021).
- ⁴⁵R. Bondarescu, M. Bondarescu, G. Hetenyi, L. Boschi, P. Jetzer, and J. Balakrishna, "Geophysical applicability of atomic clocks: Direct continental geoid mapping," *Geophys. J. Int.* **191**, 78–82 (2012).
- ⁴⁶B. Adams, C. Macrae, M. Entezami, K. Ridley, A. Kubba, Y.-H. Lien, S. Kinge, and K. Bongs, "The development of a high data rate atom interferometric gravimeter (Hidrag) for gravity map matching navigation," in *International Symposium on Inertial Sensors and Systems (INERTIAL)* (IEEE, 2021), pp. 1–4.
- ⁴⁷X. Wu, Z. Pagel, B. S. Malek, T. H. Nguyen, F. Zi, D. S. Scheirer, and H. Müller, "Gravity surveys using a mobile atom interferometer," *Sci. Adv.* **5**, aax0800 (2019).
- ⁴⁸P. Dutta, S. S. Maurya, K. Patel, K. Biswas, J. Mangaonkar, S. Sarkar, and U. D. Rapol, "A decade of advancement of quantum sensing and metrology in India using cold atoms and ions," *J. Indian Inst. Sci.* **103**, 609–632 (2023).
- ⁴⁹J. C. Saywell, M. S. Carey, P. S. Light, S. S. Szigeti, A. R. Milne, K. S. Gill, M. L. Goh, V. S. Perunicic, N. M. Wilson, C. D. Macrae, A. Rischka, P. J. Everitt, N. P. Robins, R. P. Anderson, M. R. Hush, and M. J. Biercuk, "Enhancing the sensitivity of atom-interferometric inertial sensors using robust control," *Nat. Commun.* **14**, 7626 (2023).
- ⁵⁰C. Jekeli, "Navigation error analysis of atom interferometer inertial sensor," *Navigation* **52**, 1–14 (2005).
- ⁵¹A. Hines, L. Richardson, H. Wisniewski, and F. Guzman, "Optomechanical inertial sensors," *Appl. Opt.* **59**, G167 (2020).
- ⁵²B. Stray, A. Lamb, A. Kaushik, J. Vovrosh, A. Rodgers, J. Winch, F. Hayati, D. Boddice, A. Stabrawa, A. Niggebaum, M. Langlois, Y.-H. Lien, S. Lellouch, S. Roshanmanesh, K. Ridley, G. de Villiers, G. Brown, T. Cross, G. Tuckwell, A. Faramarzi, N. Metje, K. Bongs, and M. Holynski, "Quantum sensing for gravity cartography," *Nature* **602**, 590–594 (2022).
- ⁵³L. Maccone and C. Ren, "Quantum radar," *Phys. Rev. Lett.* **124**, 200503 (2020).

- ⁵⁴A. Karsa, G. Spedalieri, Q. Zhuang, and S. Pirandola, "Quantum illumination with a generic Gaussian source," *Phys. Rev. Res.* **2**, 023414 (2020).
- ⁵⁵A. Widera, O. Mandel, M. Greiner, S. Kreim, T. W. Hänsch, and I. Bloch, "Entanglement interferometry for precision measurement of atomic scattering properties," *Phys. Rev. Lett.* **92**, 160406 (2004).
- ⁵⁶V. Giovannetti, S. Lloyd, and L. Maccone, "Quantum-enhanced positioning and clock synchronization," *Nature* **412**, 417–419 (2001).
- ⁵⁷G. Y. Xiang, B. L. Higgins, D. W. Berry, H. M. Wiseman, and G. J. Pryde, "Entanglement-enhanced measurement of a completely unknown optical phase," *Nat. Photonics* **5**, 43–47 (2011).
- ⁵⁸J. J. Bollinger, W. M. Itano, D. J. Wineland, and D. J. Heinzen, "Optimal frequency measurements with maximally correlated states," *Phys. Rev. A* **54**, R4649 (1996).
- ⁵⁹S. F. Huelga, C. Macchiavello, T. Pellizzari, A. K. Ekert, M. B. Plenio, and J. I. Cirac, "Improvement of frequency standards with quantum entanglement," *Phys. Rev. Lett.* **79**, 3865–3868 (1997).
- ⁶⁰W. Markowitz, R. G. Hall, L. Essen, and J. V. L. Parry, "Frequency of cesium in terms of ephemeris time," *Phys. Rev. Lett.* **1**, 105–107 (1958).
- ⁶¹M. T. Simons, A. B. Artusio-Glimpse, A. K. Robinson, N. Prajapati, and C. L. Holloway, "Rydberg atom-based sensors for radio-frequency electric field metrology, sensing, and communications," *Measurement* **18**, 100273 (2021).
- ⁶²B. C. Nichol, R. Srinivas, D. P. Nadlinger, P. Drmota, D. Main, G. Araneda, C. J. Ballance, and D. M. Lucas, "An elementary quantum network of entangled optical atomic clocks," *Nature* **609**, 689–694 (2022).
- ⁶³G. K. Campbell, A. D. Ludlow, S. Blatt, J. W. Thomsen, M. J. Martin, M. H. De Miranda, T. Zelevinsky, M. M. Boyd, J. Ye, S. A. Diddams, T. P. Heavner, T. E. Parker, and S. R. Jefferts, "The absolute frequency of the ⁸⁷Sr optical clock transition," *Metrologia* **45**, 539 (2008).
- ⁶⁴B. C. Nichol, R. Srinivas, D. P. Nadlinger, P. Drmota, D. Main, G. Araneda, C. J. Ballance, and D. M. Lucas, "Entanglement-enhanced frequency comparison of two optical atomic clocks," in *Conference on Lasers and Electro-Optics/Europe (CLEO/Europe 2023) and European Quantum Electronics Conference (EQEC 2023)* (Optica Publishing Group, 2023), p. ed_5_1.
- ⁶⁵G. Wang, Y.-X. Liu, J. M. Schloss, S. T. Alsid, D. A. Braje, and P. Cappellaro, "Sensing of arbitrary-frequency fields using a quantum mixer," *Phys. Rev. X* **12**, 021061 (2022).
- ⁶⁶J. M. Boss, K. S. Cujia, J. Zopes, and C. L. Degen, "Quantum sensing with arbitrary frequency resolution," *Science* **356**, 837–840 (2017).
- ⁶⁷M. Schulte, C. Lisdat, P. O. Schmidt, U. Sterr, and K. Hammerer, "Prospects and challenges for squeezing-enhanced optical atomic clocks," *Nat. Commun.* **11**, 5955 (2020).
- ⁶⁸M. Zhuang, H. Huo, Y. Qiu, W. Liu, J. Huang, and C. Lee, "Heisenberg-limited frequency estimation via driving through quantum phase transitions," *Phys. Rev. Appl.* **16**, 064056 (2021).
- ⁶⁹A. W. Young, W. J. Eckner, W. R. Milner, D. Kedar, M. A. Norcia, E. Oelker, N. Schine, J. Ye, and A. M. Kaufman, "Half-minute-scale atomic coherence and high relative stability in a tweezer clock," *Nature* **588**, 408–413 (2020).
- ⁷⁰Y. Xia, W. Li, W. Clark, D. Hart, Q. Zhuang, and Z. Zhang, "Demonstration of a reconfigurable entangled radio-frequency photonic sensor network," *Phys. Rev. Lett.* **124**, 150502 (2020).
- ⁷¹J. Meinel, V. Vorobyov, B. Yavkin, D. Dasari, H. Sumiya, S. Onoda, J. Isoya, and J. Wrachtrup, "Heterodyne sensing of microwaves with a quantum sensor," *Nat. Commun.* **12**, 2737 (2021).
- ⁷²S. Schmitt, T. Gefen, F. M. St rner, T. Unden, G. Wolff, C. Muller, J. Scheuer, B. Naydenov, M. Markham, S. Pezzagna, J. Meijer, I. Schwarz, M. Plenio, A. Retzker, L. P. McGuinness, and F. Jelezko, "Submillihertz magnetic spectroscopy performed with a nanoscale quantum sensor," *Science* **356**, 832–837 (2017).
- ⁷³T. J. Yen, W. J. Padilla, N. Fang, D. C. Vier, D. R. Smith, J. B. Pendry, D. N. Basov, and X. Zhang, "Terahertz magnetic response from artificial materials," *Science* **303**, 1494–1496 (2004).
- ⁷⁴J. A. Jones, S. D. Karlen, J. Fitzsimons, A. Ardavan, S. C. Benjamin, G. A. D. Briggs, and J. J. L. Morton, "Magnetic field sensing beyond the standard quantum limit using 10-Spin NOON states," *Science* **324**, 1166–1168 (2009).
- ⁷⁵P. Ripka, "Magnetic sensors and magnetometers," *Meas. Sci. Technol.* **13**, 645 (2002).
- ⁷⁶M. Diaz-Michelena, "Small magnetic sensors for space applications," *Sensors* **9**, 2271–2288 (2009).
- ⁷⁷A. Balogh, "Planetary magnetic field measurements: Missions and instrumentation," *Space. Sci. Rev.* **152**, 23–97 (2010).
- ⁷⁸W. Zheng, H. Wang, R. Schmiege, A. Oesterle, and E. S. Polzik, "Entanglement-enhanced magnetic induction tomography," *Phys. Rev. Lett.* **130**, 203602 (2023).
- ⁷⁹C. L. Degen, "Scanning magnetic field microscope with a diamond single-spin sensor," *Appl. Phys. Lett.* **92**, 243111 (2008).
- ⁸⁰M. Loretz, S. Pezzagna, J. Meijer, and C. L. Degen, "Nanoscale nuclear magnetic resonance with a 1.9-nm-deep nitrogen-vacancy sensor," *Appl. Phys. Lett.* **104**, 033102 (2014).
- ⁸¹H. J. Mamin, M. Kim, M. H. Sherwood, C. T. Rettner, K. Ohno, D. D. Awschalom, and D. Rugar, "Nanoscale nuclear magnetic resonance with a nitrogen-vacancy spin sensor," *Science* **339**, 557–560 (2013).
- ⁸²J. R. Maze, P. L. Stanwick, J. S. Hodges, S. Hong, J. M. Taylor, P. Cappellaro, L. Jiang, M. V. G. Dutt, E. Togan, A. S. Zibrov, A. Yacoby, R. L. Walsworth, and M. D. Lukin, "Nanoscale magnetic sensing with an individual electronic spin in diamond," *Nature* **455**, 644–647 (2008).
- ⁸³R. J. Sewell, M. Koschorreck, M. Napolitano, B. Dubost, N. Behbood, and M. W. Mitchell, "Magnetic sensitivity beyond the projection noise limit by spin squeezing," *Phys. Rev. Lett.* **109**, 253605 (2012).
- ⁸⁴H. J. Mamin, M. Poggio, C. L. Degen, and D. Rugar, "Nuclear magnetic resonance imaging with 90-nm resolution," *Nat. Nanotechnol.* **2**, 301–306 (2007).
- ⁸⁵N. F. Ramsey, *Molecular-Beam Magnetic Resonance Methods* (Oxford University Press, 1986).
- ⁸⁶C. F. Ockeloen, R. Schmid, M. F. Riedel, and P. Treutlein, "Quantum metrology with a scanning probe atom interferometer," *Phys. Rev. Lett.* **111**, 143001 (2013).
- ⁸⁷K. S. Hardman, P. J. Everitt, G. D. McDonald, P. Manju, P. B. Wigley, M. A. Sooriyabandara, C. C. N. Kuhn, J. E. Debs, J. D. Close, and N. P. Robins, "Simultaneous precision gravimetry and magnetic gradiometry with a Bose-Einstein condensate: A high precision, quantum sensor," *Phys. Rev. Lett.* **117**, 138501 (2016).
- ⁸⁸M. Zhuang, J. Huang, and C. Lee, "Simultaneous measurement of DC and AC magnetic fields at the Heisenberg limit," *Phys. Rev. Appl.* **13**, 044049 (2020).
- ⁸⁹A. Peters, K. Y. Chung, and S. Chu, "Measurement of gravitational acceleration by dropping atoms," *Nature* **400**, 849–852 (1999).
- ⁹⁰P. A. Altin, M. T. Johnsson, V. Negnevitsky, G. R. Dennis, R. P. Anderson, J. E. Debs, S. S. Szigeti, K. S. Hardman, S. Bennetts, G. D. McDonald, L. D. Turner, J. D. Close, and N. P. Robins, "Precision atomic gravimeter based on Bragg diffraction," *New J. Phys.* **15**, 023009 (2013).
- ⁹¹D. Braun, G. Adesso, F. Benatti, R. Floreanini, U. Marzolino, M. W. Mitchell, and S. Pirandola, "Quantum-enhanced measurements without entanglement," *Rev. Mod. Phys.* **90**, 035006 (2018).
- ⁹²S. Abend, M. Gersemann, C. Schubert, D. Schlippe, E. M. Rasel, M. Zimmermann, M. A. Efremov, A. Roura, F. A. Narducci, and W. P. Schleich, "Atom interferometry and its applications," in *Foundations of Quantum Theory*, Proceedings of the International School of Physics "Enrico Fermi" Vol. 197 (IOS Press, 2020).
- ⁹³C. Lee, J. Huang, H. Deng, H. Dai, and J. Xu, "Nonlinear quantum interferometry with Bose condensed atoms," *Front. Phys.* **7**, 109–130 (2012).
- ⁹⁴Z. Hradil and J. Reháček, "Quantum interference and Fisher information," *Phys. Lett. A* **334**, 267–272 (2005).
- ⁹⁵G. de Lange, Z. H. Wang, D. Rist, V. V. Dobrovitski, and R. Hanson, "Universal dynamical decoupling of a single solid-state spin from a spin bath," *Science* **330**, 60–63 (2010).
- ⁹⁶M. J. Biercuk, H. Uys, A. P. VanDevender, N. Shiga, W. M. Itano, and J. J. Bollinger, "Experimental Uhrig dynamical decoupling using trapped ions," *Phys. Rev. A* **79**, 062324 (2009).
- ⁹⁷P. C. Maurer, G. Kucsko, C. Latta, L. Jiang, N. Y. Yao, S. D. Bennett, F. Pastawski, D. Hunger, N. Chisholm, M. Markham, D. J. Twitchen, J. I. Cirac, and M. D. Lukin, "Room-temperature quantum bit memory exceeding one second," *Science* **336**, 1283–1286 (2012).
- ⁹⁸S. Choi, N. Y. Yao, and M. D. Lukin, "Dynamical engineering of interactions in qudit ensembles," *Phys. Rev. Lett.* **119**, 183603 (2017).

- ⁹⁹L. Jiang and A. Imambekov, "Universal dynamical decoupling of multiqubit states from environment," *Phys. Rev. A* **84**, 060302 (2011).
- ¹⁰⁰W.-J. Kuo and D. A. Lidar, "Quadratic dynamical decoupling: Universality proof and error analysis," *Phys. Rev. A* **84**, 042329 (2011).
- ¹⁰¹S. Kotler, N. Akerman, Y. Glickman, A. Keselman, and R. Ozeri, "Single-ion quantum lock-in amplifier," *Nature* **473**, 61–65 (2011).
- ¹⁰²R. Shaniv and R. Ozeri, "Quantum lock-in force sensing using optical clock doppler velocimetry," *Nat. Commun.* **8**, 14157 (2017).
- ¹⁰³K. Bongs, S. Bennett, and A. Lohmann, "Quantum sensors will start a revolution if we deploy them right," *Nature* **617**, 672–675 (2023).
- ¹⁰⁴P. Xu, S. Yi, and W. Zhang, "Efficient generation of many-body entangled states by multilevel oscillations," *Phys. Rev. Lett.* **123**, 073001 (2019).
- ¹⁰⁵S. Colombo, E. Pedrozo-Peña, A. F. Adiyatullin, Z. Li, E. Mendez, C. Shu, and V. Vuletić, "Time-reversal-based quantum metrology with many-body entangled states," *Nat. Phys.* **18**, 925–930 (2022).
- ¹⁰⁶A. Ruschhaupt, X. Chen, D. Alonso, and J. G. Muga, "Optimally robust shortcuts to population inversion in two-level quantum systems," *New J. Phys.* **14**, 093040 (2012).
- ¹⁰⁷J. A. Hines, S. V. Rajagopal, G. L. Moreau, M. D. Wahrman, N. A. Lewis, O. Marković, and M. Schleier-Smith, "Spin squeezing by Rydberg dressing in an array of atomic ensembles," *Phys. Rev. Lett.* **131**, 063401 (2023).
- ¹⁰⁸A. Kuzmich, K. Mølmer, and E. S. Polzik, "Spin squeezing in an ensemble of atoms illuminated with squeezed light," *Phys. Rev. Lett.* **79**, 4782–4785 (1997).
- ¹⁰⁹Y.-C. Zhang, X.-F. Zhou, X. Zhou, G.-C. Guo, and Z.-W. Zhou, "Cavity-assisted single-mode and two-mode spin-squeezed states via phase-locked atom-photon coupling," *Phys. Rev. Lett.* **118**, 083604 (2017).
- ¹¹⁰G. Vasilakis, K. Shen, H. Jensen, M. Balabas, D. Salart, B. Chen, and E. S. Polzik, "Generation of a squeezed state of an oscillator by stroboscopic back-action-evasive measurement," *Nat. Phys.* **11**, 389–392 (2015).
- ¹¹¹O. Hosten, R. Krishnakumar, N. J. Engelsen, and M. A. Kasevich, "Quantum phase magnification," *Science* **352**, 1552–1555 (2016).
- ¹¹²J. Franke, S. R. Muleady, R. Kaubruegger, F. Kranzl, R. Blatt, A. M. Rey, M. K. Joshi, and C. F. Roos, "Quantum-enhanced sensing on optical transitions through finite-range interactions," *Nature* **621**, 740–745 (2023).
- ¹¹³W. Muessel, H. Strobel, D. Linnemann, T. Zibold, B. Juliá-Díaz, and M. K. Oberthaler, "Twist-and-turn spin squeezing in Bose-Einstein condensates," *Phys. Rev. A* **92**, 023603 (2015).
- ¹¹⁴M. A. Perlin, C. Qu, and A. M. Rey, "Spin squeezing with short-range spin-exchange interactions," *Phys. Rev. Lett.* **125**, 223401 (2020).
- ¹¹⁵J. Ma, X. Wang, C. Sun, and F. Nori, "Quantum spin squeezing," *Phys. Rep.* **509**, 89–165 (2011).
- ¹¹⁶M. F. Riedel, P. Böhi, Y. Li, T. W. Hänsch, A. Sinatra, and P. Treutlein, "Atom-chip-based generation of entanglement for quantum metrology," *Nature* **464**, 1170–1173 (2010).
- ¹¹⁷B. Lücke, M. Scherer, J. Kruse, L. Pezzè, F. Deuretzbacher, P. Hyllus, O. Topic, J. Peise, W. Ertmer, J. Arlt, L. Santos, A. Smerzi, and C. Klempert, "Twin matter waves for interferometry beyond the classical limit," *Science* **334**, 773–776 (2011).
- ¹¹⁸H. Strobel, W. Muessel, D. Linnemann, T. Zibold, D. B. Hume, L. Pezzè, A. Smerzi, and M. K. Oberthaler, "Fisher information and entanglement of non-Gaussian spin states," *Science* **345**, 424–427 (2014).
- ¹¹⁹Y. Li and P. Li, "Detection of genuine n-qubit W state, GHZ state and twin-Fock state via quantum Fisher information," *Phys. Lett. A* **384**, 126413 (2020).
- ¹²⁰Z. Li, B. Braverman, S. Colombo, C. Shu, A. Kawasaki, A. F. Adiyatullin, E. Pedrozo-Peña, E. Mendez, and V. Vuletić, "Collective spin-light and light-mediated spin-spin interactions in an optical cavity," *PRX Quantum* **3**, 020308 (2022).
- ¹²¹Y.-A. Chen, X.-H. Bao, Z.-S. Yuan, S. Chen, B. Zhao, and J.-W. Pan, "Heralded generation of an atomic NOON state," *Phys. Rev. Lett.* **104**, 043601 (2010).
- ¹²²J. Huang, X. Qin, H. Zhong, Y. Ke, and C. Lee, "Quantum metrology with spin cat states under dissipation," *Sci. Rep.* **5**, 17894 (2015).
- ¹²³J. P. Dowling, "Quantum optical metrology the lowdown on high-NOON states," *Contemp. Phys.* **49**, 125–143 (2008).
- ¹²⁴Y. Zhao, R. Zhang, W. Chen, X. B. Wang, and J. Hu, "Creation of Greenberger-Horne-Zeilinger states with thousands of atoms by entanglement amplification," *npj Quantum Inf.* **7**, 24 (2021).
- ¹²⁵D. Bouwmeester, J.-W. Pan, M. Daniell, H. Weinfurter, and A. Zeilinger, "Observation of three-photon Greenberger-Horne-Zeilinger entanglement," *Phys. Rev. Lett.* **82**, 1345–1349 (1999).
- ¹²⁶C. Gross, T. Zibold, E. Nicklas, J. Estève, and M. K. Oberthaler, "Nonlinear atom interferometer surpasses classical precision limit," *Nature* **464**, 1165–1169 (2010).
- ¹²⁷J. G. Bohnet, B. C. Sawyer, J. W. Britton, M. L. Wall, A. M. Rey, M. Foss-Feig, and J. J. Bollinger, "Quantum spin dynamics and entanglement generation with hundreds of trapped ions," *Science* **352**, 1297–1301 (2016).
- ¹²⁸G. P. Greve, C. Luo, B. Wu, and J. K. Thompson, "Entanglement-enhanced matter-wave interferometry in a high-finesse cavity," *Nature* **610**, 472–477 (2022).
- ¹²⁹I. D. Leroux, M. H. Schleier-Smith, and V. Vuletić, "Implementation of cavity squeezing of a collective atomic spin," *Phys. Rev. Lett.* **104**, 073602 (2010).
- ¹³⁰Y.-L. Zhang, C.-L. Zou, X.-B. Zou, L. Jiang, and G.-C. Guo, "Detuning-enhanced cavity spin squeezing," *Phys. Rev. A* **91**, 033625 (2015).
- ¹³¹X.-Y. Luo, Y.-Q. Zou, L.-N. Wu, Q. Liu, M.-F. Han, M. K. Tey, and Y. Li, "Deterministic entanglement generation from driving through quantum phase transitions," *Science* **355**, 620–623 (2017).
- ¹³²Y.-Q. Zou, L.-N. Wu, Q. Liu, X.-Y. Luo, S.-F. Guo, J.-H. Cao, M. K. Tey, and L. You, "Beating the classical precision limit with spin-1 Dicke states of more than 10,000 atoms," *Proc. Natl. Acad. Sci. U. S. A.* **115**, 6381–6385 (2018).
- ¹³³L. Pezzè, Y. Li, W. Li, and A. Smerzi, "Witnessing entanglement without entanglement witness operators," *Proc. Natl. Acad. Sci. U. S. A.* **113**, 11459–11464 (2016).
- ¹³⁴L. Amico, R. Fazio, A. Osterloh, and V. Vedral, "Entanglement in many-body systems," *Rev. Mod. Phys.* **80**, 517–576 (2008).
- ¹³⁵C. F. Roos, M. Chwalla, K. Kim, M. Riebe, and R. Blatt, "Designer atoms for quantum metrology," *Nature* **443**, 316–319 (2006).
- ¹³⁶K. A. Gilmore, M. Affolter, R. J. Lewis-Swan, D. Barberena, E. Jordan, A. M. Rey, and J. J. Bollinger, "Quantum-enhanced sensing of displacements and electric fields with two-dimensional trapped-ion crystals," *Science* **373**, 673–678 (2021).
- ¹³⁷T. Monz, P. Schindler, J. T. Barreiro, M. Chwalla, D. Nigg, W. A. Coish, M. Harlander, W. Hänsel, M. Hennrich, and R. Blatt, "14-qubit entanglement: Creation and coherence," *Phys. Rev. Lett.* **106**, 130506 (2011).
- ¹³⁸E. Polino, M. Riva, M. Valeri, R. Silvestri, G. Corrielli, A. Crespi, N. Spagnolo, R. Osellame, and F. Sciarrino, "Experimental multiphase estimation on a chip," *Optica* **6**, 288–295 (2019).
- ¹³⁹J. Kong, F. Hudelist, Z. Y. Ou, and W. Zhang, "Cancellation of internal quantum noise of an amplifier by quantum correlation," *Phys. Rev. Lett.* **111**, 033608 (2013).
- ¹⁴⁰Q.-J. Tong, J.-H. An, H.-G. Luo, and C. H. Oh, "Mechanism of entanglement preservation," *Phys. Rev. A* **81**, 052330 (2010).
- ¹⁴¹J.-H. An and W.-M. Zhang, "Non-Markovian entanglement dynamics of noisy continuous-variable quantum channels," *Phys. Rev. A* **76**, 042127 (2007).
- ¹⁴²Q.-K. Wan, H.-L. Shi, X. Zhou, X.-H. Wang, and W.-L. Yang, "Decoherence dynamics of entangled quantum states in the XXX central spin model," *Quantum Inf. Process.* **19**, 400 (2020).
- ¹⁴³A. W. Chin, S. F. Huelga, and M. B. Plenio, "Quantum metrology in non-Markovian environments," *Phys. Rev. Lett.* **109**, 233601 (2012).
- ¹⁴⁴L. Jiao, W. Wu, S. Y. Bai, and J. H. An, "Quantum metrology in the noisy intermediate-scale quantum era," *Adv. Quantum Technol.* **2023**, 2300218.
- ¹⁴⁵A. Datta, L. Zhang, N. Thomas-Peter, U. Dorner, B. J. Smith, and I. A. Walmsley, "Quantum metrology with imperfect states and detectors," *Phys. Rev. A* **83**, 063836 (2011).
- ¹⁴⁶J. Huang, M. Zhuang, B. Lu, Y. Ke, and C. Lee, "Achieving Heisenberg-limited metrology with spin cat states via interaction-based readout," *Phys. Rev. A* **98**, 012129 (2018).
- ¹⁴⁷E. Davis, G. Bentzen, and M. Schleier-Smith, "Approaching the Heisenberg limit without single-particle detection," *Phys. Rev. Lett.* **116**, 053601 (2016).
- ¹⁴⁸F. Fröwis, P. Sekatski, and W. Dür, "Detecting large quantum Fisher information with finite measurement precision," *Phys. Rev. Lett.* **116**, 090801 (2016).
- ¹⁴⁹D. Linnemann, H. Strobel, W. Muessel, J. Schulz, R. J. Lewis-Swan, K. V. Kheruntsyan, and M. K. Oberthaler, "Quantum-enhanced sensing based on time reversal of nonlinear dynamics," *Phys. Rev. Lett.* **117**, 013001 (2016).

- ¹⁵⁰S. S. Szigeti, R. J. Lewis-Swan, and S. A. Haine, "Pumped-up SU(1,1) interferometry," *Phys. Rev. Lett.* **118**, 150401 (2017).
- ¹⁵¹S. P. Nolan, S. S. Szigeti, and S. A. Haine, "Optimal and robust quantum metrology using interaction-based readouts," *Phys. Rev. Lett.* **119**, 193601 (2017).
- ¹⁵²Q. Liu, L.-N. Wu, J.-H. Cao, T.-W. Mao, X.-W. Li, S.-F. Guo, M. K. Tey, and L. You, "Nonlinear interferometry beyond classical limit enabled by cyclic dynamics," *Nat. Phys.* **18**, 167–171 (2022).
- ¹⁵³T.-W. Mao, Q. Liu, X.-W. Li, J.-H. Cao, F. Chen, W.-X. Xu, M. K. Tey, Y.-X. Huang, and L. You, "Quantum-enhanced sensing by echoing spin-nematic squeezing in atomic Bose Einstein condensate," *Nat. Phys.* **19**, 1585–1590 (2023).
- ¹⁵⁴S. C. Burd, R. Srinivas, J. J. Bollinger, A. C. Wilson, D. J. Wineland, D. Leibfried, D. H. Slichter, and D. T. C. Allcock, "Quantum amplification of mechanical oscillator motion," *Science* **364**, 1163–1165 (2019).
- ¹⁵⁵S. Colombo, E. Pedrozo-Peñaflor, and V. Vuletić, "Entanglement-enhanced optical atomic clocks," *Appl. Phys. Lett.* **121**, 210502 (2022).
- ¹⁵⁶A. D. Ludlow, M. M. Boyd, J. Ye, E. Peik, and P. O. Schmidt, "Optical atomic clocks," *Rev. Mod. Phys.* **87**, 637–701 (2015).
- ¹⁵⁷R. B. Hutson, A. Goban, G. E. Marti, L. Sonderhouse, C. Sanner, and J. Ye, "Engineering quantum states of matter for atomic clocks in shallow optical lattices," *Phys. Rev. Lett.* **123**, 123401 (2019).
- ¹⁵⁸T. Zanon-Willette, R. Lefevre, R. Metzdorff, N. Sillitoe, S. Almonacil, M. Minissale, E. de Clercq, A. V. Taichenachev, V. I. Yudin, and E. Arimondo, "Composite laser-pulses spectroscopy for high-accuracy optical clocks: review of recent progress and perspectives," *Rep. Prog. Phys.* **81**, 094401 (2018).
- ¹⁵⁹D. Meiser, J. Ye, and M. J. Holland, "Spin squeezing in optical lattice clocks via lattice-based QND measurements," *New J. Phys.* **10**, 073014 (2008).
- ¹⁶⁰A. André, A. S. Sørensen, and M. D. Lukin, "Stability of atomic clocks based on entangled atoms," *Phys. Rev. Lett.* **92**, 230801 (2004).
- ¹⁶¹J. Borregaard and A. S. Sørensen, "Efficient atomic clocks operated with several atomic ensembles," *Phys. Rev. Lett.* **111**, 090802 (2013).
- ¹⁶²J. Borregaard and A. S. Sørensen, "Near-Heisenberg-limited atomic clocks in the presence of decoherence," *Phys. Rev. Lett.* **111**, 090801 (2013).
- ¹⁶³B. J. Bloom, T. L. Nicholson, J. R. Williams, S. L. Campbell, M. Bishof, X. Zhang, W. Zhang, S. L. Bromley, and J. Ye, "An optical lattice clock with accuracy and stability at the 10^{-18} level," *Nature* **506**, 71–75 (2014).
- ¹⁶⁴E. Oelker, R. B. Hutson, C. J. Kennedy, L. Sonderhouse, T. Bothwell, A. Goban, D. Kedar, C. Sanner, J. M. Robinson, G. E. Marti, D. G. Matei, T. Legero, M. Giunta, R. Holzwarth, F. Riehle, U. Sterr, and J. Ye, "Demonstration of 4.8×10^{-17} stability at 1s for two independent optical clocks," *Nat. Photonics* **13**, 714–719 (2019).
- ¹⁶⁵M. Schioppo, R. C. Brown, W. F. McGrew, N. Hinkley, R. J. Fasano, K. Beloy, T. H. Yoon, G. Milani, D. Nicolodi, J. A. Sherman, N. B. Phillips, C. W. Oates, and A. D. Ludlow, "Ultrastable optical clock with two cold-atom ensembles," *Nat. Photonics* **11**, 48–52 (2017).
- ¹⁶⁶J. F. Barry, J. M. Schloss, E. Bauch, M. J. Turner, C. A. Hart, L. M. Pham, and R. L. Walsworth, "Sensitivity optimization for NV-diamond magnetometry," *Rev. Mod. Phys.* **92**, 015004 (2020).
- ¹⁶⁷D. Budker and M. Romalis, "Optical magnetometry," *Nat. Phys.* **3**, 227–234 (2007).
- ¹⁶⁸M. Koschorreck, M. Napolitano, B. Dubost, and M. W. Mitchell, "Sub-projection-noise sensitivity in broadband atomic magnetometry," *Phys. Rev. Lett.* **104**, 093602 (2010).
- ¹⁶⁹W. Wasilewski, K. Jensen, H. Krauter, J. J. Renema, M. V. Balabas, and E. S. Polzik, "Quantum noise limited and entanglement-assisted magnetometry," *Phys. Rev. Lett.* **104**, 133601 (2010).
- ¹⁷⁰W. Muessel, H. Strobel, D. Linnemann, D. B. Hume, and M. K. Oberthaler, "Scalable spin squeezing for quantum-enhanced magnetometry with Bose-Einstein condensates," *Phys. Rev. Lett.* **113**, 103004 (2014).
- ¹⁷¹J. B. Brask, R. Chaves, and J. Kołodyński, "Improved quantum magnetometry beyond the standard quantum limit," *Phys. Rev. X* **5**, 031010 (2015).
- ¹⁷²S. Abend, M. Gebbe, M. Gersemann, H. Ahlers, H. Müntinga, E. Giese, N. Gaaloul, C. Schubert, C. Lämmerzahl, W. Ertmer, W. P. Schleich, and E. M. Rasel, "Atom-chip fountain gravimeter," *Phys. Rev. Lett.* **117**, 203003 (2016).
- ¹⁷³M. R. Grace, C. N. Gagatsos, Q. Zhuang, and S. Guha, "Quantum-enhanced fiber-optic gyroscopes using quadrature squeezing and continuous-variable entanglement," *Phys. Rev. Appl.* **14**, 034065 (2020).
- ¹⁷⁴M. P. Ledbetter, K. Jensen, R. Fischer, A. Jarmola, and D. Budker, "Gyroscopes based on nitrogen-vacancy centers in diamond," *Phys. Rev. A* **86**, 052116 (2012).
- ¹⁷⁵I. Kruse, K. Lange, J. Peise, B. Lücke, L. Pezzè, J. Arlt, W. Ertmer, C. Lisdat, L. Santos, A. Smerzi, and C. Klempert, "Improvement of an atomic clock using squeezed vacuum," *Phys. Rev. Lett.* **117**, 143004 (2016).
- ¹⁷⁶E. Pedrozo-Peñaflor, S. Colombo, C. Shu, A. F. Adiyatullin, Z. Li, E. Mendez, B. Braverman, A. Kawasaki, D. Akamatsu, Y. Xiao, and V. Vuletić, "Entanglement on an optical atomic-clock transition," *Nature* **588**, 414–418 (2020).
- ¹⁷⁷S. Pang and T. A. Brun, "Quantum metrology for a general Hamiltonian parameter," *Phys. Rev. A* **90**, 022117 (2014).
- ¹⁷⁸X.-X. Jing, J. Liu, H.-N. Xiong, and X. Wang, "Maximal quantum Fisher information for general SU(2) parametrization processes," *Phys. Rev. A* **92**, 012312 (2015).
- ¹⁷⁹J. Liu, X.-X. Jing, and X. Wang, "Quantum metrology with unitary parametrization processes," *Sci. Rep.* **5**, 8565 (2015).
- ¹⁸⁰C. W. Helstrom, "Quantum detection and estimation theory," *J. Stat. Phys.* **1**, 231–252 (1969).
- ¹⁸¹S. L. Braunstein and C. M. Caves, "Statistical distance and the geometry of quantum states," *Phys. Rev. Lett.* **72**, 3439–3443 (1994).
- ¹⁸²L. Pezzé and A. Smerzi, "Entanglement, nonlinear dynamics, and the Heisenberg limit," *Phys. Rev. Lett.* **102**, 100401 (2009).
- ¹⁸³Y. Gao, "Quantum optical metrology in the lossy SU(2) and SU(1,1) interferometers," *Phys. Rev. A* **94**, 023834 (2016).
- ¹⁸⁴J. Jing, C. Liu, Z. Zhou, Z. Y. Ou, and W. Zhang, "Realization of a nonlinear interferometer with parametric amplifiers," *Appl. Phys. Lett.* **99**, 011110 (2011).
- ¹⁸⁵J. Kong, Z. Y. Ou, and W. Zhang, "Phase-measurement sensitivity beyond the standard quantum limit in an interferometer consisting of a parametric amplifier and a beam splitter," *Phys. Rev. A* **87**, 023825 (2013).
- ¹⁸⁶J. Kong, J. Jing, H. Wang, F. Hudelist, C. Liu, and W. Zhang, "Experimental investigation of the visibility dependence in a nonlinear interferometer using parametric amplifiers," *Appl. Phys. Lett.* **102**, 011130 (2013).
- ¹⁸⁷F. Hudelist, J. Kong, C. Liu, J. Jing, Z. Y. Ou, and W. Zhang, "Quantum metrology with parametric amplifier-based photon correlation interferometers," *Nat. Commun.* **5**, 3049 (2014).
- ¹⁸⁸D. Li, C.-H. Yuan, Z. Y. Ou, and W. Zhang, "The phase sensitivity of an SU(1,1) interferometer with coherent and squeezed-vacuum light," *New J. Phys.* **16**, 073020 (2014).
- ¹⁸⁹Z. Y. Ou and X. Li, "Quantum SU(1,1) interferometers: Basic principles and applications," *APL Photonics* **5**, 080902 (2020).
- ¹⁹⁰M. Barbieri, "Optical quantum metrology," *PRX Quantum* **3**, 010202 (2022).
- ¹⁹¹S. van Frank, A. Negretti, T. Berrada, R. Bücker, S. Montangero, J.-F. Schaff, T. Schumm, T. Calarco, and J. Schmiedmayer, "Interferometry with non-classical motional states of a Bose-Einstein condensate," *Nat. Commun.* **5**, 4009 (2014).
- ¹⁹²L. Pezzé and A. Smerzi, "Mach-Zehnder interferometry at the Heisenberg limit with coherent and squeezed-vacuum light," *Phys. Rev. Lett.* **100**, 073601 (2008).
- ¹⁹³J. G. Rarity, P. R. Tapster, E. Jakeman, T. Larchuk, R. A. Campos, M. C. Teich, and B. E. A. Saleh, "Two-photon interference in a Mach-Zehnder interferometer," *Phys. Rev. Lett.* **65**, 1348–1351 (1990).
- ¹⁹⁴J.-W. Pan, Z.-B. Chen, C.-Y. Lu, H. Weinfurter, A. Zeilinger, and M. Żukowski, "Multiphoton entanglement and interferometry," *Rev. Mod. Phys.* **84**, 777–838 (2012).
- ¹⁹⁵N. F. Ramsey, "The method of successive oscillatory fields," *Phys. Today* **33**(7), 25–30 (1980).
- ¹⁹⁶B. Dalton and S. Ghanbari, "Two mode theory of Bose-Einstein condensates: interferometry and the Josephson model," *J. Mod. Opt.* **59**, 287–353 (2012).
- ¹⁹⁷C. K. Hong, Z. Y. Ou, and L. Mandel, "Measurement of subpicosecond time intervals between two photons by interference," *Phys. Rev. Lett.* **59**, 2044–2046 (1987).
- ¹⁹⁸E. Flurin, N. Roch, F. Mallet, M. H. Devoret, and B. Huard, "Generating entangled microwave radiation over two transmission lines," *Phys. Rev. Lett.* **109**, 183901 (2012).
- ¹⁹⁹B. Chen, C. Qiu, S. Chen, J. Guo, L. Q. Chen, Z. Y. Ou, and W. Zhang, "Atom-light hybrid interferometer," *Phys. Rev. Lett.* **115**, 043602 (2015).

- ²⁰⁰M. Manceau, G. Leuchs, F. Khalili, and M. Chekhova, "Detection loss tolerant supersensitive phase measurement with an SU(1,1) interferometer," *Phys. Rev. Lett.* **119**, 223604 (2017).
- ²⁰¹D. Linnemann, J. Schulz, W. Muessel, P. Kunkel, M. Prüfer, A. Frolian, H. Strobel, and M. K. Oberthaler, "Active SU(1,1) atom interferometry," *Quantum Sci. Technol.* **2**, 044009 (2017).
- ²⁰²M. A. Nielsen and I. L. Chuang, *Quantum Computation and Quantum Information: 10th Anniversary Edition* (Cambridge University Press, 2010).
- ²⁰³R. A. Fisher, "Theory of statistical estimation," *Math. Proc. Cambridge Philos. Soc.* **22**, 700–725 (1925).
- ²⁰⁴C. Helstrom, *Quantum Detection and Estimation Theory* (Academic Press (New York), 1976).
- ²⁰⁵C. M. Care, "Probabilistic and statistical aspects of quantum theory: North-holland series in statistics and probability," *Phys. Bull.* **34**, 395 (1983).
- ²⁰⁶S. L. Braunstein, C. M. Caves, and G. Milburn, "Generalized uncertainty relations: Theory, examples, and Lorentz invariance," *Ann. Phys.* **247**, 135–173 (1996).
- ²⁰⁷X.-M. Lu, X. Wang, and C. P. Sun, "Quantum Fisher information flow and non-Markovian processes of open systems," *Phys. Rev. A* **82**, 042103 (2010).
- ²⁰⁸A. Fujiwara and H. Nagaoka, "Quantum Fisher metric and estimation for pure state models," *Phys. Lett. A* **201**, 119–124 (1995).
- ²⁰⁹Z. Y. Ou, "Fundamental quantum limit in precision phase measurement," *Phys. Rev. A* **55**, 2598–2609 (1997).
- ²¹⁰G. M. D'Ariano, P. Lo Presti, and M. G. A. Paris, "Using entanglement improves the precision of quantum measurements," *Phys. Rev. Lett.* **87**, 270404 (2001).
- ²¹¹J. T. Reilly, J. D. Wilson, S. B. Jäger, C. Wilson, and M. J. Holland, "Optimal generators for quantum sensing," *Phys. Rev. Lett.* **131**, 150802 (2023).
- ²¹²A. Einstein, B. Podolsky, and N. Rosen, "Can quantum-mechanical description of physical reality be considered complete?," *Phys. Rev.* **47**, 777–780 (1935).
- ²¹³M. D. Reid, P. D. Drummond, W. P. Bowen, E. G. Cavalcanti, P. K. Lam, H. A. Bachor, U. L. Andersen, and G. Leuchs, "Colloquium: The Einstein-Podolsky-Rosen paradox: From concepts to applications," *Rev. Mod. Phys.* **81**, 1727–1751 (2009).
- ²¹⁴E. Schrödinger, "Die gegenwärtige situation in der quantenmechanik," *Die Naturwissenschaften* **23**, 807–812 (1935).
- ²¹⁵R. Horodecki, P. Horodecki, M. Horodecki, and K. Horodecki, "Quantum entanglement," *Rev. Mod. Phys.* **81**, 865–942 (2009).
- ²¹⁶A. S. Sørensen and K. Mølmer, "Entanglement and extreme spin squeezing," *Phys. Rev. Lett.* **86**, 4431–4434 (2001).
- ²¹⁷P. Hyllus, W. Laskowski, R. Krischek, C. Schwemmer, W. Wieczorek, H. Weinfurter, L. Pezzé, and A. Smerzi, "Fisher information and multiparticle entanglement," *Phys. Rev. A* **85**, 022321 (2012).
- ²¹⁸G. Tóth, "Multipartite entanglement and high-precision metrology," *Phys. Rev. A* **85**, 022322 (2012).
- ²¹⁹P. Hyllus, O. Gühne, and A. Smerzi, "Not all pure entangled states are useful for sub-shot-noise interferometry," *Phys. Rev. A* **82**, 012337 (2010).
- ²²⁰G. Tóth and T. Vértesi, "Quantum states with a positive partial transpose are useful for metrology," *Phys. Rev. Lett.* **120**, 020506 (2018).
- ²²¹K. F. Pál, G. Tóth, E. Bene, and T. Vértesi, "Bound entangled singlet-like states for quantum metrology," *Phys. Rev. Res.* **3**, 023101 (2021).
- ²²²G. Vitagliano, I. Apellaniz, M. Kleinmann, B. Lücke, C. Klempf, and G. Tóth, "Entanglement and extreme spin squeezing of unpolarized states," *New J. Phys.* **19**, 013027 (2017).
- ²²³F. Ozaydin, "Phase damping destroys quantum Fisher information of W states," *Phys. Lett. A* **378**, 3161–3164 (2014).
- ²²⁴G. Tóth, T. Vértesi, P. Horodecki, and R. Horodecki, "Activating hidden metrological usefulness," *Phys. Rev. Lett.* **125**, 020402 (2020).
- ²²⁵R. Trényi, Á. Lukács, P. Horodecki, R. Horodecki, T. Vértesi, and G. Tóth, "Activation of metrologically useful genuine multipartite entanglement," *New J. Phys.* **26**, 023034 (2024).
- ²²⁶G. Toth and I. Apellaniz, "Quantum metrology from a quantum information science perspective," *J. Phys. A* **47**, 424006 (2014).
- ²²⁷M. Kitagawa and M. Ueda, "Squeezed spin states," *Phys. Rev. A* **47**, 5138–5143 (1993).
- ²²⁸D. J. Wineland, J. J. Bollinger, W. M. Itano, F. L. Moore, and D. J. Heinzen, "Spin squeezing and reduced quantum noise in spectroscopy," *Phys. Rev. A* **46**, R6797–R6800 (1992).
- ²²⁹M. Walschaers, "Non-Gaussian quantum states and where to find them," *PRX Quantum* **2**, 030204 (2021).
- ²³⁰M. Gessner, A. Smerzi, and L. Pezzè, "Metrological nonlinear squeezing parameter," *Phys. Rev. Lett.* **122**, 090503 (2019).
- ²³¹Y. Li, Y. Castin, and A. Sinatra, "Optimum spin squeezing in Bose-Einstein condensates with particle losses," *Phys. Rev. Lett.* **100**, 210401 (2008).
- ²³²Y. Li, P. Treutlein, J. Reichel, and A. Sinatra, "Spin squeezing in a bimodal condensate: Spatial dynamics and particle losses," *Eur. Phys. J. B* **68**, 365–381 (2009).
- ²³³Y.-F. Huang, B.-H. Liu, L. Peng, Y.-H. Li, L. Li, C.-F. Li, and G.-C. Guo, "Experimental generation of an eight-photon Greenberger-Horne-Zeilinger state," *Nat. Commun.* **2**, 546 (2011).
- ²³⁴C. A. Sackett, D. Kielpinski, B. E. King, C. Langer, V. Meyer, C. J. Myatt, M. Rowe, Q. A. Turchette, W. M. Itano, D. J. Wineland, and C. Monroe, "Experimental entanglement of four particles," *Nature* **404**, 256–259 (2000).
- ²³⁵H. Häffner, W. Hänsel, C. F. Roos, J. Benhelm, D. Chek-al-kar, M. Chwalla, T. Körber, U. D. Rapol, M. Riebe, P. O. Schmidt, C. Becher, O. Gühne, W. Dür, and R. Blatt, "Scalable multiparticle entanglement of trapped ions," *Nature* **438**, 643–646 (2005).
- ²³⁶X.-C. Yao, T.-X. Wang, P. Xu, H. Lu, G.-S. Pan, X.-H. Bao, C.-Z. Peng, C.-Y. Lu, Y.-A. Chen, and J.-W. Pan, "Observation of eight-photon entanglement," *Nat. Photonics* **6**, 225–228 (2012).
- ²³⁷L. DiCarlo, M. D. Reed, L. Sun, B. R. Johnson, J. M. Chow, J. M. Gambetta, L. Frunzio, S. M. Girvin, M. H. Devoret, and R. J. Schoelkopf, "Preparation and measurement of three-qubit entanglement in a superconducting circuit," *Nature* **467**, 574–578 (2010).
- ²³⁸M. Neeley, R. C. Bialczak, M. Lenander, E. Lucero, M. Mariantoni, A. D. O. Connell, D. Sank, H. Wang, M. Weides, J. Wenner, Y. Yin, T. Yamamoto, A. N. Cleland, and J. M. Martinis, "Generation of three-qubit entangled states using superconducting phase qubits," *Nature* **467**, 570–573 (2010).
- ²³⁹P. Neumann, N. Mizuochi, F. Rempp, P. Hemmer, H. Watanabe, S. Yamasaki, V. Jacques, T. Gaebel, F. Jelezko, and J. Wrachtrup, "Multipartite entanglement among single spins in diamond," *Science* **320**, 1326–1329 (2008).
- ²⁴⁰H. Bao, J. Duan, S. Jin, X. Lu, P. Li, W. Qu, M. Wang, I. Novikova, E. E. Mikhailov, K.-F. Zhao, K. Mølmer, H. Shen, and Y. Xiao, "Spin squeezing of 10^{11} atoms by prediction and retrodiction measurements," *Nature* **581**, 159–163 (2020).
- ²⁴¹G. J. Pryde and A. G. White, "Creation of maximally entangled photon-number states using optical fiber multiports," *Phys. Rev. A* **68**, 052315 (2003).
- ²⁴²H. Grote, K. Danzmann, K. L. Dooley, R. Schnabel, J. Slutsky, and H. Vahlbruch, "First long-term application of squeezed states of light in a gravitational-wave observatory," *Phys. Rev. Lett.* **110**, 181101 (2013).
- ²⁴³P. Grangier, R. E. Slusher, B. Yurke, and A. LaPorta, "Squeezed-light-enhanced polarization interferometer," *Phys. Rev. Lett.* **59**, 2153–2156 (1987).
- ²⁴⁴T. Xie, Z. Zhao, X. Kong, W. Ma, M. Wang, X. Ye, P. Yu, Z. Yang, S. Xu, P. Wang, Y. Wang, F. Shi, and J. Du, "Beating the standard quantum limit under ambient conditions with solid-state spins," *Sci. Adv.* **7**, eabg9204 (2021).
- ²⁴⁵Y. Zhong, H.-S. Chang, A. Bienfait, É. Dumur, M.-H. Chou, C. R. Conner, J. Grebel, R. G. Povey, H. Yan, D. I. Schuster, and A. N. Cleland, "Deterministic multi-qubit entanglement in a quantum network," *Nature* **590**, 571–575 (2021).
- ²⁴⁶E. S. Polzik, J. Carri, and H. J. Kimble, "Spectroscopy with squeezed light," *Phys. Rev. Lett.* **68**, 3020–3023 (1992).
- ²⁴⁷M. Xiao, L.-A. Wu, and H. J. Kimble, "Precision measurement beyond the shot-noise limit," *Phys. Rev. Lett.* **59**, 278–281 (1987).
- ²⁴⁸A. Vaartjes, A. Kringshøj, W. Vine, T. Day, A. Morello, and J. J. Pla, "Strong microwave squeezing above 1 Tesla and 1 Kelvin," *Nat. Commun.* **15**, 4229 (2024).
- ²⁴⁹T. L. S. Collaboration, "A gravitational wave observatory operating beyond the quantum shot-noise limit," *Nat. Phys.* **7**, 962–965 (2011).
- ²⁵⁰R. Schnabel, "Squeezed states of light and their applications in laser interferometers," *Phys. Rep.* **684**, 1–51 (2017).
- ²⁵¹J. Qin, Y.-H. Deng, H.-S. Zhong, L.-C. Peng, H. Su, Y.-H. Luo, J.-M. Xu, D. Wu, S.-Q. Gong, H.-L. Liu, H. Wang, M.-C. Chen, L. Li, N.-L. Liu, C.-Y. Lu, and J.-W. Pan, "Unconditional and robust quantum metrological advantage beyond n0n states," *Phys. Rev. Lett.* **130**, 070801 (2023).

- ²⁵²F. T. Arecchi, E. Courtens, R. Gilmore, and H. Thomas, "Atomic coherent states in quantum optics," *Phys. Rev. A* **6**, 2211–2237 (1972).
- ²⁵³D. J. Wineland, J. J. Bollinger, W. M. Itano, and D. J. Heinzen, "Squeezed atomic states and projection noise in spectroscopy," *Phys. Rev. A* **50**, 67–88 (1994).
- ²⁵⁴B. Braverman, A. Kawasaki, E. Pedrazzo-Peñaflor, S. Colombo, C. Shu, Z. Li, E. Mendez, M. Yamoah, L. Salvi, D. Akamatsu, Y. Xiao, and V. Vuletić, "Near-unitary spin squeezing in ^{171}Yb ," *Phys. Rev. Lett.* **122**, 223203 (2019).
- ²⁵⁵T. Holstein and H. Primakoff, "Field dependence of the intrinsic domain magnetization of a ferromagnet," *Phys. Rev.* **58**, 1098–1113 (1940).
- ²⁵⁶D. Kajtoch and E. Witkowska, "Quantum dynamics generated by the two-axis countertwisting Hamiltonian," *Phys. Rev. A* **92**, 013623 (2015).
- ²⁵⁷G.-R. Jin, Y.-C. Liu, and W.-M. Liu, "Spin squeezing in a generalized one-axis twisting model," *New J. Phys.* **11**, 073049 (2009).
- ²⁵⁸E. A. Burt, R. W. Ghrist, C. J. Myatt, M. J. Holland, E. A. Cornell, and C. E. Wieman, "Coherence, correlations, and collisions: What one learns about Bose–Einstein condensates from their decay," *Phys. Rev. Lett.* **79**, 337–340 (1997).
- ²⁵⁹A. Kuzmich, N. P. Bigelow, and L. Mandel, "Atomic quantum non-demolition measurements and squeezing," *Europhys. Lett.* **42**, 481–486 (1998).
- ²⁶⁰A. A. Berni, T. Gehring, B. M. Nielsen, V. Handchen, M. G. A. Paris, and U. L. Andersen, "Ab initio quantum-enhanced optical phase estimation using real-time feedback control," *Nat. Photonics* **9**, 577–581 (2015).
- ²⁶¹A. Fallani, M. A. C. Rossi, D. Tamascelli, and M. G. Genoni, "Learning feedback control strategies for quantum metrology," *PRX Quantum* **3**, 020310 (2022).
- ²⁶²R. Salvia, M. Mehboudi, and M. Perarnau-Llobet, "Critical quantum metrology assisted by real-time feedback control," *Phys. Rev. Lett.* **130**, 240803 (2023).
- ²⁶³G. Bornet, G. Emperauger, C. Chen, B. Ye, M. Block, M. Bintz, J. A. Boyd, D. Barredo, T. Comparin, F. Mezzacapo, T. Roscilde, T. Lahaye, N. Y. Yao, and A. Browaeys, "Scalable spin squeezing in a dipolar Rydberg atom array," *Nature* **621**, 728–733 (2023).
- ²⁶⁴T. Schumm, S. Hofferberth, L. M. Andersson, S. Wildermuth, S. Groth, I. Bar-Joseph, J. Schmiedmayer, and P. Krüger, "Matter-wave interferometry in a double well on an atom chip," *Nat. Phys.* **1**, 57–62 (2005).
- ²⁶⁵T. Schumm, P. Krüger, S. Hofferberth, I. Lesanovsky, S. Wildermuth, S. Groth, I. Bar-Joseph, L. M. Andersson, and J. Schmiedmayer, "A double well interferometer on an atom chip," *Quantum Inf. Process.* **5**, 537–558 (2006).
- ²⁶⁶R. Gati, B. Hemmerling, J. Fölling, M. Albiez, and M. K. Oberthaler, "Noise thermometry with two weakly coupled Bose–Einstein condensates," *Phys. Rev. Lett.* **96**, 130404 (2006).
- ²⁶⁷Y. Shin, G.-B. Jo, M. Saba, T. A. Pasquini, W. Ketterle, and D. E. Pritchard, "Optical weak link between two spatially separated Bose–Einstein condensates," *Phys. Rev. Lett.* **95**, 170402 (2005).
- ²⁶⁸J. Appel, P. J. Windpassinger, D. Oblak, U. B. Hoff, N. Kjargaard, and E. S. Polzik, "Mesoscopic atomic entanglement for precision measurements beyond the standard quantum limit," *Proc. Natl. Acad. Sci. U.S.A.* **106**, 10960–10965 (2009).
- ²⁶⁹M. H. Schleier-Smith, I. D. Leroux, and V. Vuletić, "States of an ensemble of two-level atoms with reduced quantum uncertainty," *Phys. Rev. Lett.* **104**, 073604 (2010).
- ²⁷⁰R. J. Lewis-Swan, M. A. Norcia, J. R. K. Cline, J. K. Thompson, and A. M. Rey, "Robust spin squeezing via photon-mediated interactions on an optical clock transition," *Phys. Rev. Lett.* **121**, 070403 (2018).
- ²⁷¹M. H. Schleier-Smith, I. D. Leroux, and V. Vuletić, "Squeezing the collective spin of a dilute atomic ensemble by cavity feedback," *Phys. Rev. A* **81**, 021804 (2010).
- ²⁷²F. Reiter and A. S. Sørensen, "Effective operator formalism for open quantum systems," *Phys. Rev. A* **85**, 032111 (2012).
- ²⁷³O. Hosten, N. J. Engelsen, R. Krishnakumar, and M. A. Kasevich, "Measurement noise 100 times lower than the quantum-projection limit using entangled atoms," *Nature* **529**, 505–508 (2016).
- ²⁷⁴A. Shankar, L. Salvi, M. L. Chiofalo, N. Poli, and M. J. Holland, "Squeezed state metrology with Bragg interferometers operating in a cavity," *Quantum Sci. Technol.* **4**, 045010 (2019).
- ²⁷⁵J. D. Wilson, S. B. Jäger, J. T. Reilly, A. Shankar, M. L. Chiofalo, and M. J. Holland, "Beyond one-axis twisting: Simultaneous spin-momentum squeezing," *Phys. Rev. A* **106**, 043711 (2022).
- ²⁷⁶C. Luo, H. Zhang, V. P. W. Koh, J. D. Wilson, A. Chu, M. J. Holland, A. M. Rey, and J. K. Thompson, "Momentum-exchange interactions in a Bragg atom interferometer suppress doppler dephasing," *Science* **384**, 551–556 (2024).
- ²⁷⁷H. Zhang, A. Chu, C. Luo, J. K. Thompson, and A. M. Rey, "Control and amplification of Bloch oscillations via photon-mediated interactions," *Phys. Rev. Res.* **5**, L032039 (2023).
- ²⁷⁸C. L. Vaillant, M. P. Jones, and R. M. Potvliege, "Long-range Rydberg interactions in calcium, strontium and ytterbium," *J. Phys. B* **45**, 135004 (2012).
- ²⁷⁹L. I. R. Gil, R. Mukherjee, E. M. Bridge, M. P. A. Jones, and T. Pohl, "Spin squeezing in a Rydberg lattice clock," *Phys. Rev. Lett.* **112**, 103601 (2014).
- ²⁸⁰T. Comparin, F. Mezzacapo, and T. Roscilde, "Multipartite entangled states in dipolar quantum simulators," *Phys. Rev. Lett.* **129**, 150503 (2022).
- ²⁸¹T. Comparin, F. Mezzacapo, M. Robert-de Saint-Vincent, and T. Roscilde, "Scalable spin squeezing from spontaneous breaking of a continuous symmetry," *Phys. Rev. Lett.* **129**, 113201 (2022).
- ²⁸²C. K. Law, H. T. Ng, and P. T. Leung, "Coherent control of spin squeezing," *Phys. Rev. A* **63**, 055601 (2001).
- ²⁸³G. Sorelli, M. Gessner, A. Smerzi, and L. Pezzè, "Fast and optimal generation of entanglement in bosonic Josephson junctions," *Phys. Rev. A* **99**, 022329 (2019).
- ²⁸⁴B. Juliá-Díaz, T. Zibold, M. K. Oberthaler, M. Melé-Meseguer, J. Martorell, and A. Polls, "Dynamic generation of spin-squeezed states in bosonic Josephson junctions," *Phys. Rev. A* **86**, 023615 (2012).
- ²⁸⁵Y. C. Liu, Z. F. Xu, G. R. Jin, and L. You, "Spin squeezing: Transforming one-axis twisting into two-axis twisting," *Phys. Rev. Lett.* **107**, 013601 (2011).
- ²⁸⁶J.-Y. Zhang, X.-F. Zhou, G.-C. Guo, and Z.-W. Zhou, "Dynamical spin squeezing via a higher-order Trotter–Suzuki approximation," *Phys. Rev. A* **90**, 013604 (2014).
- ²⁸⁷W. Huang, Y.-L. Zhang, C.-L. Zou, X.-B. Zou, and G.-C. Guo, "Two-axis spin squeezing of two-component Bose–Einstein condensates via continuous driving," *Phys. Rev. A* **91**, 043642 (2015).
- ²⁸⁸L.-N. Wu, M. K. Tey, and L. You, "Persistent atomic spin squeezing at the Heisenberg limit," *Phys. Rev. A* **92**, 063610 (2015).
- ²⁸⁹C. Shen and L.-M. Duan, "Efficient spin squeezing with optimized pulse sequences," *Phys. Rev. A* **87**, 051801 (2013).
- ²⁹⁰F. Chen, J.-J. Chen, L.-N. Wu, Y.-C. Liu, and L. You, "Extreme spin squeezing from deep reinforcement learning," *Phys. Rev. A* **100**, 041801 (2019).
- ²⁹¹S. C. Carrasco, M. H. Goerz, Z. Li, S. Colombo, V. Vuletić, and V. S. Malinovsky, "Extreme spin squeezing via optimized one-axis twisting and rotations," *Phys. Rev. Appl.* **17**, 064050 (2022).
- ²⁹²J. Borregaard, E. J. Davis, G. S. Bentsen, M. H. Schleier-Smith, and A. S. Sørensen, "One- and two-axis squeezing of atomic ensembles in optical cavities," *New J. Phys.* **19**, 093021 (2017).
- ²⁹³L. Yu, C. Li, J. Fan, G. Chen, T.-C. Zhang, and S. Jia, "Tunable two-axis spin model and spin squeezing in two cavities," *Chin. Phys. B* **25**, 050301 (2016).
- ²⁹⁴M. Wang, W. Qu, P. Li, H. Bao, V. Vuletić, and Y. Xiao, "Two-axis-twisting spin squeezing by multipass quantum erasure," *Phys. Rev. A* **96**, 013823 (2017).
- ²⁹⁵H. J. Lipkin, N. Meshkov, and A. J. Glick, "Validity of many-body approximation methods for a solvable model: (i). exact solutions and perturbation theory," *Nucl. Phys.* **62**, 188–198 (1965).
- ²⁹⁶N. Meshkov, A. J. Glick, and H. J. Lipkin, "Validity of many-body approximation methods for a solvable model: (ii). linearization procedures," *Nucl. Phys.* **62**, 199–210 (1965).
- ²⁹⁷A. J. Glick, H. J. Lipkin, and N. Meshkov, "Validity of many-body approximation methods for a solvable model: (iii). diagram summations," *Nucl. Phys.* **62**, 211–224 (1965).
- ²⁹⁸C. Lee, "Universality and anomalous mean-field breakdown of symmetry-breaking transitions in a coupled two-component Bose–Einstein condensate," *Phys. Rev. Lett.* **102**, 070401 (2009).
- ²⁹⁹T. Opatrný, M. Kolář, and K. K. Das, "Spin squeezing by tensor twisting and Lipkin–Meshkov–Glick dynamics in a toroidal Bose–Einstein condensate with spatially modulated nonlinearity," *Phys. Rev. A* **91**, 053612 (2015).

- ³⁰⁰Z. Hu, Q. Li, X. Zhang, L.-G. Huang, H.-b Zhang, and Y.-C. Liu, "Spin squeezing with arbitrary quadratic collective-spin interactions," *Phys. Rev. A* **108**, 023722 (2023).
- ³⁰¹L.-G. Huang, X. Zhang, Y. Wang, Z. Hua, Y. Tang, and Y.-C. Liu, "Heisenberg-limited spin squeezing in coupled spin systems," *Phys. Rev. A* **107**, 042613 (2023).
- ³⁰²L. Xin, M. Barrios, J. T. Cohen, and M. S. Chapman, "Long-lived squeezed ground states in a quantum spin ensemble," *Phys. Rev. Lett.* **131**, 133402 (2023).
- ³⁰³D. Guéry-Odelin, A. Ruschhaupt, A. Kiely, E. Torrontegui, S. Martínez-Garaot, and J. G. Muga, "Shortcuts to adiabaticity: Concepts, methods, and applications," *Rev. Mod. Phys.* **91**, 045001 (2019).
- ³⁰⁴J. A. Dunningham, K. Burnett, and S. M. Barnett, "Interferometry below the standard quantum limit with Bose-Einstein Condensates," *Phys. Rev. Lett.* **89**, 150401 (2002).
- ³⁰⁵R. A. Campos, C. C. Gerry, and A. Benmoussa, "Optical interferometry at the Heisenberg limit with twin Fock states and parity measurements," *Phys. Rev. A* **68**, 023810 (2003).
- ³⁰⁶W. Wieczorek, R. Krischek, N. Kiesel, P. Michelberger, G. Tóth, and H. Weinfurter, "Experimental entanglement of a six-photon symmetric Dicke state," *Phys. Rev. Lett.* **103**, 020504 (2009).
- ³⁰⁷B. Lücke, J. Peise, G. Vitagliano, J. Arlt, L. Santos, G. Tóth, and C. Klempt, "Detecting multiparticle entanglement of Dicke states," *Phys. Rev. Lett.* **112**, 155304 (2014).
- ³⁰⁸X. Wang and K. Mølmer, "Pairwise entanglement in symmetric multi-qubit systems," *Eur. Phys. J. D* **18**, 385–391 (2002).
- ³⁰⁹B. Lücke, "Multi-particle entanglement in a spinor Bose-Einstein condensate for quantum-enhanced interferometry," Ph.D. thesis, Gottfried Wilhelm Leibniz Universität Hannover, 2014.
- ³¹⁰L.-N. Wu and L. You, "Using the ground state of an antiferromagnetic spin-1 atomic condensate for Heisenberg-limited metrology," *Phys. Rev. A* **93**, 033608 (2016).
- ³¹¹Z. Zhang and L.-M. Duan, "Generation of massive entanglement through an adiabatic quantum phase transition in a spinor condensate," *Phys. Rev. Lett.* **111**, 180401 (2013).
- ³¹²L. Zhou, J. Kong, Z. Lan, and W. Zhang, "Dynamical quantum phase transitions in a spinor Bose-Einstein condensate and criticality enhanced quantum sensing," *Phys. Rev. Res.* **5**, 013087 (2023).
- ³¹³A. M. Marino, N. V. Corzo Trejo, and P. D. Lett, "Effect of losses on the performance of an SU(1,1) interferometer," *Phys. Rev. A* **86**, 023844 (2012).
- ³¹⁴M. Gabrielli, L. Pezzè, and A. Smerzi, "Spin-mixing interferometry with Bose-Einstein condensates," *Phys. Rev. Lett.* **115**, 163002 (2015).
- ³¹⁵H. W. Lau, Z. Dutton, T. Wang, and C. Simon, "Proposal for the creation and optical detection of spin cat states in Bose-Einstein condensates," *Phys. Rev. Lett.* **113**, 090401 (2014).
- ³¹⁶S. P. Nolan and S. A. Haine, "Quantum Fisher information as a predictor of decoherence in the preparation of spin-cat states for quantum metrology," *Phys. Rev. A* **95**, 043642 (2017).
- ³¹⁷S. P. Nolan and S. A. Haine, "Generating macroscopic superpositions with interacting Bose-Einstein condensates: Multimode speedups and speed limits," *Phys. Rev. A* **98**, 063606 (2018).
- ³¹⁸A. Micheli, D. Jaksch, J. I. Cirac, and P. Zoller, "Many-particle entanglement in two-component Bose-Einstein condensates," *Phys. Rev. A* **67**, 013607 (2003).
- ³¹⁹G. Ferrini, D. Spaehner, A. Minguzzi, and F. W. J. Hekking, "Noise in Bose Josephson junctions: Decoherence and phase relaxation," *Phys. Rev. A* **82**, 033621 (2010).
- ³²⁰D. Spaehner, K. Pawłowski, G. Ferrini, and A. Minguzzi, "Effect of one-, two-, and three-body atom loss processes on superpositions of phase states in Bose-Josephson junctions," *Eur. Phys. J. B* **87**, 157 (2014).
- ³²¹L. You, "Creating maximally entangled atomic states in a Bose-Einstein condensate," *Phys. Rev. Lett.* **90**, 30402 (2003).
- ³²²F. Piazza, L. Pezzè, and A. Smerzi, "Macroscopic superpositions of phase states with Bose-Einstein condensates," *Phys. Rev. A* **78**, 051601 (2008).
- ³²³K. Pawłowski, M. Fadel, P. Treutlein, Y. Castin, and A. Sinatra, "Mesoscopic quantum superpositions in bimodal Bose-Einstein condensates: Decoherence and strategies to counteract it," *Phys. Rev. A* **95**, 063609 (2017).
- ³²⁴C. Groiseau, S. J. Masson, and S. Parkins, "Generation of spin cat states in an engineered Dicke model," *Phys. Rev. A* **104**, 053721 (2021).
- ³²⁵J. Huang, M. Zhuang, and C. Lee, "Non-Gaussian precision metrology via driving through quantum phase transitions," *Phys. Rev. A* **97**, 032116 (2018).
- ³²⁶A. Trenkwalder, G. Spagnoli, G. Semeghini, S. Coop, M. Landini, P. Castilho, L. Pezzè, G. Modugno, M. Inguscio, A. Smerzi, and M. Fattori, "Quantum phase transitions with parity-symmetry breaking and hysteresis," *Nat. Phys.* **12**, 826–829 (2016).
- ³²⁷A. Safavi-Naini, R. J. Lewis-Swan, J. G. Bohnet, M. Gärttner, K. A. Gilmore, J. E. Jordan, J. Cohn, J. K. Freericks, A. M. Rey, and J. J. Bollinger, "Verification of a many-ion simulator of the Dicke model through slow quenches across a phase transition," *Phys. Rev. Lett.* **121**, 040503 (2018).
- ³²⁸B. Dakić and M. Radonjić, "Macroscopic superpositions as quantum ground states," *Phys. Rev. Lett.* **119**, 090401 (2017).
- ³²⁹M. Gabrielli, A. Smerzi, and L. Pezzè, "Multipartite entanglement at finite temperature," *Sci. Rep.* **8**, 15663 (2018).
- ³³⁰C. Chin, R. Grimm, P. Julienne, and E. Tiesinga, "Feshbach resonances in ultracold gases," *Rev. Mod. Phys.* **82**, 1225–1286 (2010).
- ³³¹H. Xing, A. Wang, Q.-S. Tan, W. Zhang, and S. Yi, "Heisenberg-scaled magnetometer with dipolar spin-1 condensates," *Phys. Rev. A* **93**, 043615 (2016).
- ³³²M. Zhuang, J. Huang, Y. Ke, and C. Lee, "Symmetry-protected quantum adiabatic evolution in spontaneous symmetry-breaking transitions," *Ann. Phys.* **532**, 1900471 (2020).
- ³³³J. Huang, H. Huo, M. Zhuang, and C. Lee, "Efficient generation of spin cat states with twist-and-turn dynamics via machine optimization," *Phys. Rev. A* **105**, 062456 (2022).
- ³³⁴T. Hatomura and K. Pawłowski, "Superadiabatic generation of cat states in bosonic Josephson junctions under particle losses," *Phys. Rev. A* **99**, 043621 (2019).
- ³³⁵L. Pezzè, M. Gessner, P. Feldmann, C. Klempt, L. Santos, and A. Smerzi, "Heralded generation of macroscopic superposition states in a spinor Bose-Einstein condensate," *Phys. Rev. Lett.* **123**, 260403 (2019).
- ³³⁶T. M. Hoang, H. M. Bharath, M. J. Boguslawski, M. Anquez, B. A. Robbins, and M. S. Chapman, "Adiabatic quenches and characterization of amplitude excitations in a continuous quantum phase transition," *Proc. Natl. Acad. Sci. U. S. A.* **113**, 9475–9479 (2016).
- ³³⁷W. Chen, J. Hu, Y. Duan, B. Braverman, H. Zhang, and V. Vuletić, "Carving complex many-atom entangled states by single-photon detection," *Phys. Rev. Lett.* **115**, 250502 (2015).
- ³³⁸V. Meyer, M. A. Rowe, D. Kielpinski, C. A. Sackett, W. M. Itano, C. Monroe, and D. J. Wineland, "Experimental demonstration of entanglement-enhanced rotation angle estimation using trapped ions," *Phys. Rev. Lett.* **86**, 5870–5873 (2001).
- ³³⁹D. Leibfried, M. D. Barrett, T. Schaetz, J. Britton, J. Chiaverini, W. M. Itano, J. D. Jost, C. Langer, and D. J. Wineland, "Toward Heisenberg-limited spectroscopy with multiparticle entangled states," *Science* **304**, 1476–1478 (2004).
- ³⁴⁰N. Friis, O. Marty, C. Maier, C. Hempel, M. Holzäpfel, P. Jurcevic, M. B. Plenio, M. Huber, C. Roos, R. Blatt, and B. Lanyon, "Observation of entangled states of a fully controlled 20-qubit system," *Phys. Rev. X* **8**, 021012 (2018).
- ³⁴¹I. Pogorelov, T. Feldker, C. D. Marciniak, L. Postler, G. Jacob, O. Kriegelsteiner, V. Podlesnic, M. Meth, V. Negnevitsky, M. Stadler, B. Höfer, C. Wächter, K. Lakhmanskii, R. Blatt, P. Schindler, and T. Monz, "Compact ion-trap quantum computing demonstrator," *PRX Quantum* **2**, 020343 (2021).
- ³⁴²C. Song, K. Xu, H. Li, Y.-R. Zhang, X. Zhang, W. Liu, Q. Guo, Z. Wang, W. Ren, J. Hao, H. Feng, H. Fan, D. Zheng, D.-W. Wang, H. Wang, and S.-Y. Zhu, "Generation of multicomponent atomic Schrödinger cat states of up to 20 qubits," *Science* **365**, 574–577 (2019).
- ³⁴³Z. Wang, Z. Bao, Y. Wu, Y. Li, W. Cai, W. Wang, Y. Ma, T. Cai, X. Han, J. Wang, Y. Song, L. Sun, H. Zhang, and L. Duan, "A flying Schrödinger's cat in multipartite entangled states," *Sci. Adv.* **8**, eabn1778 (2022).
- ³⁴⁴A. Omran, H. Levine, A. Keesling, G. Semeghini, T. T. Wang, S. Ebadi, H. Bernien, A. S. Zibrov, H. Pichler, S. Choi, J. Cui, M. Rossignolo, P. Rembold, S. Montangero, T. Calarco, M. Endres, M. Greiner, V. Vuletić, and M. D. Lukin, "Generation and manipulation of Schrödinger cat states in Rydberg atom arrays," *Science* **365**, 570–574 (2019).
- ³⁴⁵S. Boixo, S. T. Flammia, C. M. Caves, and J. Geremia, "Generalized limits for single-parameter quantum estimation," *Phys. Rev. Lett.* **98**, 090401 (2007).

- ³⁴⁶S. Pang and A. N. Jordan, "Optimal adaptive control for quantum metrology with time-dependent Hamiltonians," *Nat. Commun.* **8**, 14695 (2017).
- ³⁴⁷H. Yuan and C.-H. F. Fung, "Optimal feedback scheme and universal time scaling for Hamiltonian parameter estimation," *Phys. Rev. Lett.* **115**, 110401 (2015).
- ³⁴⁸H. Yuan, "Sequential feedback scheme outperforms the parallel scheme for hamiltonian parameter estimation," *Phys. Rev. Lett.* **117**, 160801 (2016).
- ³⁴⁹Z. Hou, R.-J. Wang, J.-F. Tang, H. Yuan, G.-Y. Xiang, C.-F. Li, and G.-C. Guo, "Control-enhanced sequential scheme for general quantum parameter estimation at the Heisenberg limit," *Phys. Rev. Lett.* **123**, 040501 (2019).
- ³⁵⁰L. Pezzè and A. Smerzi, "Heisenberg-limited noisy atomic clock using a hybrid coherent and squeezed state protocol," *Phys. Rev. Lett.* **125**, 210503 (2020).
- ³⁵¹X. Nie, J. Huang, Z. Li, W. Zheng, C. Lee, X. Peng, and J. Du, "Experimental demonstration of nonlinear quantum metrology with optimal quantum state," *Sci. Bull.* **63**, 469–476 (2018).
- ³⁵²S. M. Roy and S. L. Braunstein, "Exponentially enhanced quantum metrology," *Phys. Rev. Lett.* **100**, 220501 (2008).
- ³⁵³M. J. W. Hall and H. M. Wiseman, "Does nonlinear metrology offer improved resolution? Answers from quantum information theory," *Phys. Rev. X* **2**, 041006 (2012).
- ³⁵⁴D. A. Garanin and R. Schilling, "Inverse problem for the Landau-Zener effect," *Europhys. Lett.* **59**, 7 (2002).
- ³⁵⁵M. V. Berry, "Transitionless quantum driving," *J. Phys. A* **42**, 365303 (2009).
- ³⁵⁶E. Barnes, "Analytically solvable two-level quantum systems and Landau-Zener interferometry," *Phys. Rev. A* **88**, 013818 (2013).
- ³⁵⁷S. Dooley, W. J. Munro, and K. Nemoto, "Quantum metrology including state preparation and readout times," *Phys. Rev. A* **94**, 052320 (2016).
- ³⁵⁸A. J. Hayes, S. Dooley, W. J. Munro, K. Nemoto, and J. Dunningham, "Making the most of time in quantum metrology: Concurrent state preparation and sensing," *Quantum Sci. Technol.* **3**, 035007 (2018).
- ³⁵⁹L. J. Fiderer and D. Braun, "Quantum metrology with quantum-chaotic sensors," *Nat. Commun.* **9**, 1351 (2018).
- ³⁶⁰W. Liu, M. Zhuang, B. Zhu, J. Huang, and C. Lee, "Quantum metrology via chaos in a driven Bose-Josephson system," *Phys. Rev. A* **103**, 023309 (2021).
- ³⁶¹S. A. Haine and J. J. Hope, "Machine-designed sensor to make optimal use of entanglement-generating dynamics for quantum sensing," *Phys. Rev. Lett.* **124**, 060402 (2020).
- ³⁶²J. Schuff, L. J. Fiderer, and D. Braun, "Improving the dynamics of quantum sensors with reinforcement learning," *New J. Phys.* **22**, 035001 (2020).
- ³⁶³H. Huo, M. Zhuang, J. Huang, and C. Lee, "Machine optimized quantum metrology of concurrent entanglement generation and sensing," *Quantum Sci. Technol.* **7**, 025010 (2022).
- ³⁶⁴C. C. Gerry and J. Mimih, "Heisenberg-limited interferometry with pair coherent states and parity measurements," *Phys. Rev. A* **82**, 013831 (2010).
- ³⁶⁵T. Macri, A. Smerzi, and L. Pezzè, "Loschmidt echo for quantum metrology," *Phys. Rev. A* **94**, 010102 (2016).
- ³⁶⁶F. Anders, L. Pezzè, A. Smerzi, and C. Klempert, "Phase magnification by two-axis counter twisting for detection-noise robust interferometry," *Phys. Rev. A* **97**, 043813 (2018).
- ³⁶⁷S. A. Haine, "Using interaction-based readouts to approach the ultimate limit of detection-noise robustness for quantum-enhanced metrology in collective spin systems," *Phys. Rev. A* **98**, 030303 (2018).
- ³⁶⁸S. S. Mirkhafal, S. P. Nolan, and S. A. Haine, "Robustifying twist-and-turn entanglement with interaction-based readout," *Phys. Rev. A* **97**, 053618 (2018).
- ³⁶⁹Q. Liu, T.-W. Mao, M. Xue, L.-N. Wu, and L. You, "Cyclic nonlinear interferometry with entangled non-Gaussian spin states," *Phys. Rev. A* **107**, 052613 (2023).
- ³⁷⁰M. S. Scharnagl, T. Kielinski, and K. Hammerer, "Optimal Ramsey interferometry with echo protocols based on one-axis twisting," *Phys. Rev. A* **108**, 062611 (2023).
- ³⁷¹Z. Li, S. Colombo, C. Shu, G. Velez, S. Pilatowsky-Cameo, R. Schmied, S. Choi, M. Lukin, E. Pedrozo-Peñafield, and V. Vuletić, "Improving metrology with quantum scrambling," *Science* **380**, 1381–1384 (2023).
- ³⁷²M. Affolter, W. Ge, B. Bullock, S. C. Burd, K. A. Gilmore, J. F. Lilieholm, A. L. Carter, and J. J. Bollinger, "Toward improved quantum simulations and sensing with trapped two-dimensional ion crystals via parametric amplification," *Phys. Rev. A* **107**, 032425 (2023).
- ³⁷³S. M. Brewer, J.-S. Chen, A. M. Hankin, E. R. Clements, C. W. Chou, D. J. Wineland, D. B. Hume, and D. R. Leibrandt, "²⁷Al⁺ quantum-logic clock with a systematic uncertainty below 10⁻¹⁸," *Phys. Rev. Lett.* **123**, 033201 (2019).
- ³⁷⁴J. M. Robinson, M. Miklos, Y. M. Tso, C. J. Kennedy, T. Bothwell, D. Kedar, J. K. Thompson, and J. Ye, "Direct comparison of two spin-squeezed optical clock ensembles at the 10⁻¹⁷ level," *Nat. Phys.* **20**, 208–213 (2024).
- ³⁷⁵I. D. Leroux, M. H. Schleier-Smith, and V. Vuletić, "Orientation-dependent entanglement lifetime in a squeezed atomic clock," *Phys. Rev. Lett.* **104**, 250801 (2010).
- ³⁷⁶S. Weyers, V. Gerginov, M. Kazda, J. Rahm, B. Lipphardt, G. Dobrev, and K. Gibble, "Advances in the accuracy, stability, and reliability of the PTB primary fountain clocks," *Metrologia* **55**, 789–805 (2018).
- ³⁷⁷R. Szmulik, V. Dugrain, W. Maineult, J. Reichel, and P. Rosenbusch, "Stability of a trapped-atom clock on a chip," *Phys. Rev. A* **92**, 012106 (2015).
- ³⁷⁸J. N. Eckstein, A. I. Ferguson, and T. W. Hänsch, "High-resolution two-photon spectroscopy with picosecond light pulses," *Phys. Rev. Lett.* **40**, 847–850 (1978).
- ³⁷⁹H. Katori, "Optical lattice clocks and quantum metrology," *Nat. Photonics* **5**, 203–210 (2011).
- ³⁸⁰X. Zheng, J. Dolde, V. Lochab, B. N. Merriman, H. Li, and S. Kolkowitz, "Differential clock comparisons with a multiplexed optical lattice clock," *Nature* **602**, 425–430 (2022).
- ³⁸¹J. Li, X.-Y. Cui, Z.-P. Jia, D.-Q. Kong, H.-W. Yu, X.-Q. Zhu, X.-Y. Liu, D.-Z. Wang, X. Zhang, X.-Y. Huang, M.-Y. Zhu, Y.-M. Yang, Y. Hu, X.-P. Liu, X.-M. Zhai, P. Liu, X. Jiang, P. Xu, H.-N. Dai, Y.-A. Chen, and J.-W. Pan, "A strontium lattice clock with both stability and uncertainty below 5 × 10⁻¹⁸," *Metrologia* **61**, 015006 (2024).
- ³⁸²W. J. Eckner, N. Darkwah Oppong, A. Cao, A. W. Young, W. R. Milner, J. M. Robinson, J. Ye, and A. M. Kaufman, "Realizing spin squeezing with Rydberg interactions in an optical clock," *Nature* **621**, 734–739 (2023).
- ³⁸³E. M. Kessler, P. Kómár, M. Bishof, L. Jiang, A. S. Sørensen, J. Ye, and M. D. Lukin, "Heisenberg-limited atom clocks based on entangled qubits," *Phys. Rev. Lett.* **112**, 190403 (2014).
- ³⁸⁴P. Komar, E. M. Kessler, M. Bishof, L. Jiang, A. S. Sørensen, J. Ye, and M. D. Lukin, "A quantum network of clocks," *Nat. Phys.* **10**, 582–587 (2014).
- ³⁸⁵T. Vanderbruggen, R. Kohlhaas, A. Bertoldi, S. Bernon, A. Aspect, A. Landragin, and P. Bouyer, "Feedback control of trapped coherent atomic ensembles," *Phys. Rev. Lett.* **110**, 210503 (2013).
- ³⁸⁶K. C. Cox, G. P. Greve, J. M. Weiner, and J. K. Thompson, "Deterministic squeezed states with collective measurements and feedback," *Phys. Rev. Lett.* **116**, 093602 (2016).
- ³⁸⁷D. B. Hume and D. R. Leibrandt, "Probing beyond the laser coherence time in optical clock comparisons," *Phys. Rev. A* **93**, 032138 (2016).
- ³⁸⁸W. Li, S. Wu, A. Smerzi, and L. Pezzè, "Improved absolute clock stability by the joint interrogation of two atomic ensembles," *Phys. Rev. A* **105**, 053116 (2022).
- ³⁸⁹W. Bowden, A. Vianello, I. R. Hill, M. Schioppo, and R. Hobson, "Improving the q factor of an optical atomic clock using quantum nondemolition measurement," *Phys. Rev. X* **10**, 041052 (2020).
- ³⁹⁰R. B. Hutson, W. R. Milner, L. Yan, J. Ye, and C. Sanner, "Observation of millihertz-level cooperative lamb shifts in an optical atomic clock," *Science* **383**, 384–387 (2024).
- ³⁹¹S. A. King, L. J. Spieb, P. Micke, A. Wilzewski, T. Leopold, E. Benkler, R. Lange, N. Huntemann, A. Surzhikov, V. A. Yerokhin, J. R. Crespo Lopez-Urrutia, and P. O. Schmidt, "An optical atomic clock based on a highly charged ion," *Nature* **611**, 43–47 (2022).
- ³⁹²N. Schine, A. W. Young, W. J. Eckner, M. J. Martin, and A. M. Kaufman, "Long-lived Bell states in an array of optical clock qubits," *Nat. Phys.* **18**, 1067–1073 (2022).
- ³⁹³C. J. Berglund, L. R. Hunter, D. Krause, Jr., E. O. Prigge, M. S. Ronfeldt, and S. K. Lamoreaux, "New limits on local Lorentz invariance from hg and cs magnetometers," *Phys. Rev. Lett.* **75**, 1879–1882 (1995).
- ³⁹⁴M. A. Taylor and W. P. Bowen, "Quantum metrology and its application in biology," *Phys. Rep.* **615**, 1–59 (2016).
- ³⁹⁵L. Thiel, D. Rohner, M. Ganzhorn, P. Appel, E. Neu, B. Muller, R. Kleiner, D. Koelle, and P. Maletinsky, "Quantitative nanoscale vortex imaging using a cryogenic quantum magnetometer," *Nat. Nanotechnol.* **11**, 677–681 (2016).

- ³⁹⁶M. V. Romalis and H. B. Dang, "Atomic magnetometers for materials characterization," *Mater. Today* **14**, 258–262 (2011).
- ³⁹⁷P. M. Carlton, J. Boulanger, C. Kervrann, J.-B. Sibarita, J. Salamero, S. Gordon-Messer, D. Bressan, J. E. Haber, S. Haase, L. Shao, L. Winoto, A. Matsuda, P. Kner, S. Uzawa, M. Gustafsson, Z. Kam, D. A. Agard, and J. W. Sedat, "Fast live simultaneous multiwavelength four-dimensional optical microscopy," *Proc. Natl. Acad. Sci. U. S. A.* **107**, 16016–16022 (2010).
- ³⁹⁸N. Wilson, P. Light, A. Luitjen, and C. Perrella, "Ultrastable optical magnetometry," *Phys. Rev. Appl.* **11**, 044034 (2019).
- ³⁹⁹C. Troullinou, V. G. Lucivero, and M. W. Mitchell, "Quantum-enhanced magnetometry at optimal number density," *Phys. Rev. Lett.* **131**, 133602 (2023).
- ⁴⁰⁰E. Turner, S.-H. Wu, X. Li, and H. Wang, "Real-time magnetometry with coherent population trapping in a nitrogen-vacancy center," *Phys. Rev. A* **105**, L010601 (2022).
- ⁴⁰¹S.-H. Wu, E. Turner, and H. Wang, "Continuous real-time sensing with a nitrogen-vacancy center via coherent population trapping," *Phys. Rev. A* **103**, 042607 (2021).
- ⁴⁰²G. Bevilacqua, V. Biancalana, E. Breschi, Y. Dancheva, L. Moi, C. Andreeva, S. Cartaleva, and T. Karaulanov, "Coherent population trapping spectra in presence of ac magnetic fields," *Phys. Rev. Lett.* **95**, 123601 (2005).
- ⁴⁰³Y. Hu, Y. Y. Feng, C. Xu, H. B. Xue, and L. Sun, "Loop-locked coherent population trapping magnetometer based on a fiber electro-optic modulator," *Appl. Opt.* **53**, 2158–2162 (2014).
- ⁴⁰⁴V. Andryushkov, D. Radnatarov, and S. Kobtsev, "Vector magnetometer based on the effect of coherent population trapping," *Appl. Opt.* **61**, 3604–3608 (2022).
- ⁴⁰⁵R. Fang, C. Han, X. Jiang, Y. Qiu, Y. Guo, M. Zhao, J. Huang, B. Lu, and C. Lee, "Temporal analog of Fabry-Pérot resonator via coherent population trapping," *npj Quantum Inf.* **7**, 143 (2021).
- ⁴⁰⁶V. Shah and M. V. Romalis, "Spin-exchange relaxation-free magnetometry using elliptically polarized light," *Phys. Rev. A* **80**, 013416 (2009).
- ⁴⁰⁷I. M. Savukov, "Spin exchange relaxation free (serf) magnetometers," in *High Sensitivity Magnetometers*, edited by A. Grosz, M. J. Haji-Sheikh, and S. C. Mukhopadhyay (Springer International Publishing, Cham, 2017), pp. 451–491.
- ⁴⁰⁸M. P. Ledbetter, I. M. Savukov, V. M. Acosta, D. Budker, and M. V. Romalis, "Spin-exchange-relaxation-free magnetometry with Cs vapor," *Phys. Rev. A* **77**, 033408 (2008).
- ⁴⁰⁹T. Karaulanov, I. Savukov, and Y. J. Kim, "Spin-exchange relaxation-free magnetometer with nearly parallel pump and probe beams," *Meas. Sci. Technol.* **27**, 055002 (2016).
- ⁴¹⁰Y. Liang, L. Jiang, J. Liu, W. Fan, W. Zhang, S. Fan, W. Quan, and J. Fang, "Biaxial signal decoupling method for the longitudinal magnetic-field-modulated spin-exchange-relaxation-free comagnetometer in inertial rotation measurement," *Phys. Rev. Appl.* **17**, 024004 (2022).
- ⁴¹¹G. Zhang, S. Huang, F. Xu, Z. Hu, and Q. Lin, "Multi-channel spin exchange relaxation free magnetometer towards two-dimensional vector magnetoencephalography," *Opt. Express* **27**, 597–607 (2019).
- ⁴¹²H.-G. Hong, S. E. Park, S.-B. Lee, M.-S. Heo, J. Park, T. H. Kim, H. Kim, and T. Y. Kwon, "Chip-scale ultra-low field atomic magnetometer based on coherent population trapping," *Sensors* **21**, 1517 (2021).
- ⁴¹³F. Wolfgramm, A. Ceré, F. A. Beduini, A. Predojević, M. Koschorreck, and M. W. Mitchell, "Squeezed-light optical magnetometry," *Phys. Rev. Lett.* **105**, 053601 (2010).
- ⁴¹⁴T. Horrom, R. Singh, J. P. Dowling, and E. E. Mikhailov, "Quantum-enhanced magnetometer with low-frequency squeezing," *Phys. Rev. A* **86**, 023803 (2012).
- ⁴¹⁵J. Duan, Z. Hu, X. Lu, L. Xiao, S. Jia, K. Mølmer, and Y. Xiao, Continuous field tracking with machine learning and steady state spin squeezing," (2024).
- ⁴¹⁶M. Zhuang, J. Huang, and C. Lee, "Many-body quantum lock-in amplifier," *PRX Quantum* **2**, 040317 (2021).
- ⁴¹⁷M. Kasevich and S. Chu, "Atomic interferometry using stimulated Raman transitions," *Phys. Rev. Lett.* **67**, 181–184 (1991).
- ⁴¹⁸P. Asenbaum, C. Overstreet, T. Kovachy, D. D. Brown, J. M. Hogan, and M. A. Kasevich, "Phase shift in an atom interferometer due to spacetime curvature across its wave function," *Phys. Rev. Lett.* **118**, 183602 (2017).
- ⁴¹⁹A. Peters, K. Y. Chung, and S. Chu, "High-precision gravity measurements using atom interferometry," *Metrologia* **38**, 25 (2001).
- ⁴²⁰M. Kritsotakis, S. S. Szigeti, J. A. Dunningham, and S. A. Haine, "Optimal matter-wave gravimetry," *Phys. Rev. A* **98**, 023629 (2018).
- ⁴²¹F. Anders, A. Idel, P. Feldmann, D. Bondarenko, S. Loriani, K. Lange, J. Peise, M. Gersemann, B. Meyer-Hoppe, S. Abend, N. Gaaloul, C. Schubert, D. Schlippert, L. Santos, E. Rasel, and C. Klemp, "Momentum entanglement for atom interferometry," *Phys. Rev. Lett.* **127**, 140402 (2021).
- ⁴²²D.-S. Ding, W. Zhang, Z.-Y. Zhou, S. Shi, G.-Y. Xiang, X.-S. Wang, Y.-K. Jiang, B.-S. Shi, and G.-C. Guo, "Quantum storage of orbital angular momentum entanglement in an atomic ensemble," *Phys. Rev. Lett.* **114**, 050502 (2015).
- ⁴²³T. Lévéque, A. Gauguet, F. Michaud, F. P. D. Santos, and A. Landragin, "Enhancing the area of a Raman atom interferometer using a versatile double-diffraction technique," *Phys. Rev. Lett.* **103**, 080405 (2009).
- ⁴²⁴P. Clade, S. Guellati-Khelifa, F. Nez, and F. Biraben, "Large momentum beam splitter using Bloch oscillations," *Phys. Rev. Lett.* **102**, 240402 (2009).
- ⁴²⁵N. Malossi, Q. Bodart, S. Merlet, T. Lévéque, A. Landragin, and F. P. D. Santos, "Double diffraction in an atomic gravimeter," *Phys. Rev. A* **81**, 013617 (2010).
- ⁴²⁶S. W. Chiow, T. Kovachy, H.-C. Chien, and M. A. Kasevich, "102 hz large area atom interferometers," *Phys. Rev. Lett.* **107**, 130403 (2011).
- ⁴²⁷H. Ahlers, H. Muntinga, A. Wenzlawski, M. Krutzik, G. Tackmann, S. Abend, N. Gaaloul, E. Giese, A. Roura, R. Kuhl, C. Lammerzahl, A. Peters, P. Windpassinger, K. Sengstock, W. P. Schleich, W. Ertmer, and E. M. Rasel, "Double Bragg interferometry," *Phys. Rev. Lett.* **116**, 173601 (2016).
- ⁴²⁸S. S. Szigeti, S. P. Nolan, J. D. Close, and S. A. Haine, "High-precision quantum-enhanced gravimetry with a Bose-Einstein condensate," *Phys. Rev. Lett.* **125**, 100402 (2020).
- ⁴²⁹S. A. Haine, J. Lau, R. P. Anderson, and M. T. Johnsson, "Self-induced spatial dynamics to enhance spin squeezing via one-axis twisting in a two-component Bose-Einstein condensate," *Phys. Rev. A* **90**, 023613 (2014).
- ⁴³⁰G. Ferrari, N. Poli, F. Sorrentino, and G. M. Tino, "Long-lived Bloch oscillations with bosonic sr atoms and application to gravity measurement at the micrometer scale," *Phys. Rev. Lett.* **97**, 060402 (2006).
- ⁴³¹V. V. Ivanov, A. Alberti, M. Schioppo, G. Ferrari, M. Artoni, M. L. Chiofalo, and G. M. Tino, "Coherent delocalization of atomic wave packets in driven lattice potentials," *Phys. Rev. Lett.* **100**, 043602 (2008).
- ⁴³²N. Poli, F.-Y. Wang, M. G. Tarallo, A. Alberti, M. Prevedelli, and G. M. Tino, "Precision measurement of gravity with cold atoms in an optical lattice and comparison with a classical gravimeter," *Phys. Rev. Lett.* **106**, 038501 (2011).
- ⁴³³Y. Ke, J. Huang, M. Zhuang, B. Lu, and C. Lee, "Compact gravimeter with an ensemble of ultracold atoms in spin-dependent optical lattices," *Phys. Rev. A* **98**, 053826 (2018).
- ⁴³⁴Y. Sugimoto, P. Pou, M. Abe, P. Jelinek, R. Perez, S. Morita, and O. Custance, "Chemical identification of individual surface atoms by atomic force microscopy," *Nature* **446**, 64–67 (2007).
- ⁴³⁵T. L. Gustavson, A. Landragin, and M. A. Kasevich, "Rotation sensing with a dual atom-interferometer Sagnac gyroscope," *Class. Quantum Gravity* **17**, 2385–2398 (2000).
- ⁴³⁶D. S. Durfee, Y. K. Shaham, and M. A. Kasevich, "Long-term stability of an area-reversible atom-interferometer Sagnac gyroscope," *Phys. Rev. Lett.* **97**, 240801 (2006).
- ⁴³⁷B. Canuel, F. Leduc, D. Holleville, A. Gauguet, J. Fils, A. Virdis, A. Clairon, N. Dimarcq, C. J. Bordé, A. Landragin, and P. Bouyer, "Six-axis inertial sensor using cold-atom interferometry," *Phys. Rev. Lett.* **97**, 010402 (2006).
- ⁴³⁸A. Gauguet, B. Canuel, T. Lévéque, W. Chaibi, and A. Landragin, "Characterization and limits of a cold-atom Sagnac interferometer," *Phys. Rev. A* **80**, 063604 (2009).
- ⁴³⁹I. Dutta, D. Savoie, B. Fang, B. Venon, C. L. Garrido Alzar, R. Geiger, and A. Landragin, "Continuous cold-atom inertial sensor with 1 mrad/sec rotation stability," *Phys. Rev. Lett.* **116**, 183003 (2016).
- ⁴⁴⁰R. Stevenson, M. R. Hush, T. Bishop, I. Lesanovsky, and T. Fernholz, "Sagnac interferometry with a single atomic clock," *Phys. Rev. Lett.* **115**, 163001 (2015).
- ⁴⁴¹D. Savoie, M. Altorio, B. Fang, L. A. Sidorenkov, R. Geiger, and A. Landragin, "Interleaved atom interferometry for high-sensitivity inertial measurements," *Sci. Adv.* **4**, aau7948 (2018).
- ⁴⁴²M. Gersemann, M. Gebbe, S. Abend, C. Schubert, and E. M. Rasel, "Differential interferometry using a Bose-Einstein condensate," *Eur. Phys. J. D* **74**, 203 (2020).

- ⁴⁴³M. Gebbe, J.-N. Siemb, M. Gersmann, H. Muntinga, S. Herrmann, C. Lammerzahl, H. Ahlers, N. Gaaloul, C. Schubert, K. Hammerer, S. Abend, and E. M. Rasel, "Twin-lattice atom interferometry," *Nat. Commun.* **12**, 2544 (2021).
- ⁴⁴⁴V. V. Soshenko, S. V. Bolshedvorskii, O. Rubinas, V. N. Sorokin, A. N. Smolyaninov, V. V. Vorobyov, and A. V. Akimov, "Nuclear spin gyroscope based on the nitrogen vacancy center in diamond," *Phys. Rev. Lett.* **126**, 197702 (2021).
- ⁴⁴⁵S. P. Nolan, J. Sabbatini, M. W. J. Bromley, M. J. Davis, and S. A. Haine, "Quantum enhanced measurement of rotations with a spin-1 Bose-Einstein condensate in a ring trap," *Phys. Rev. A* **93**, 023616 (2016).
- ⁴⁴⁶C. Luo, J. Huang, X. Zhang, and C. Lee, "Heisenberg-limited Sagnac interferometer with multiparticle states," *Phys. Rev. A* **95**, 023608 (2017).
- ⁴⁴⁷F. Yao, Y. Che, Y. Su, H. Liang, J. Pei, and X. Wang, "Enhancing the sensitivity of rotation in a multiatom Sagnac interferometer," *Phys. Rev. A* **99**, 052128 (2019).
- ⁴⁴⁸H.-N. Dai, B. Yang, A. Reingruber, X.-F. Xu, X. Jiang, Y.-A. Chen, Z.-S. Yuan, and J.-W. Pan, "Generation and detection of atomic spin entanglement in optical lattices," *Nat. Phys.* **12**, 783–787 (2016).
- ⁴⁴⁹M. Yu, D. Li, J. Wang, Y. Chu, P. Yang, M. Gong, N. Goldman, and J. Cai, "Experimental estimation of the quantum Fisher information from randomized measurements," *Phys. Rev. Res.* **3**, 043122 (2021).
- ⁴⁵⁰J. Guo, F. Sun, Q. He, and M. Fadel, "Assisted metrology and preparation of macroscopic superpositions with split spin-squeezed states," *Phys. Rev. A* **108**, 053327 (2023).
- ⁴⁵¹M. Zhuang, J. Huang, and C. Lee, "Entanglement-enhanced test proposal for local Lorentz-symmetry violation via spinor atoms," *Quantum* **6**, 859 (2022).
- ⁴⁵²W. Ji, Z. Liu, Y. Guo, Z. Hu, J. Zhou, S. Dai, Y. Chen, P. Yu, M. Wang, K. Xia, F. Shi, Y. Wang, and J. Du, "Correlated sensing with a solid-state quantum multisensor system for atomic-scale structural analysis," *Nat. Photonics* **18**, 230–235 (2024).
- ⁴⁵³J. T. Reilly, S. B. Jäger, J. Cooper, and M. J. Holland, "Adiabatic control of decoherence-free subspaces in an open collective system," *Phys. Rev. A* **106**, 023703 (2022).
- ⁴⁵⁴J. Jeske, J. H. Cole, and S. F. Huelga, "Quantum metrology subject to spatially correlated Markovian noise: Restoring the Heisenberg limit," *New J. Phys.* **16**, 073039 (2014).
- ⁴⁵⁵Y.-S. Wang, C. Chen, and J.-H. An, "Quantum metrology in local dissipative environments," *New J. Phys.* **19**, 113019 (2017).
- ⁴⁵⁶A. Shajii and C. M. Caves, "Qubit metrology and decoherence," *Phys. Rev. A* **76**, 032111 (2007).
- ⁴⁵⁷X.-M. Lu, S. Yu, and C. Oh, "Robust quantum metrological schemes based on protection of quantum Fisher information," *Nat. Commun.* **6**, 7282 (2015).
- ⁴⁵⁸E. M. Kessler, I. Lovchinsky, A. O. Sushkov, and M. D. Lukin, "Quantum error correction for metrology," *Phys. Rev. Lett.* **112**, 150802 (2014).
- ⁴⁵⁹W. Dür, M. Skotiniotis, F. Fröwis, and B. Kraus, "Improved quantum metrology using quantum error correction," *Phys. Rev. Lett.* **112**, 080801 (2014).
- ⁴⁶⁰T. Under, P. Balasubramanian, D. Louzon, Y. Vinkler, M. B. Plenio, M. Markham, D. Twitchen, A. Stacey, I. Lovchinsky, A. O. Sushkov, M. D. Lukin, A. Retzker, B. Naydenov, L. P. McGuinness, and F. Jelezko, "Quantum metrology enhanced by repetitive quantum error correction," *Phys. Rev. Lett.* **116**, 230502 (2016).
- ⁴⁶¹S. Zhou, M. Zhang, J. Preskill, and L. Jiang, "Achieving the Heisenberg limit in quantum metrology using quantum error correction," *Nat. Commun.* **9**, 78 (2018).
- ⁴⁶²H. P. Nautrup, N. Delfosse, V. Dunjko, H. J. Briegel, and N. Friis, "Optimizing quantum error correction codes with reinforcement learning," *Quantum* **3**, 215 (2019).
- ⁴⁶³T. Kapourniotis and A. Datta, "Fault-tolerant quantum metrology," *Phys. Rev. A* **100**, 022335 (2019).
- ⁴⁶⁴M.-X. Huo and Y. Li, "Learning time-dependent noise to reduce logical errors: Real time error rate estimation in quantum error correction," *New J. Phys.* **19**, 123032 (2017).
- ⁴⁶⁵M. Schlosshauer, "Decoherence, the measurement problem, and interpretations of quantum mechanics," *Rev. Mod. Phys.* **76**, 1267–1305 (2005).
- ⁴⁶⁶Q. Liu, Z. Hu, H. Yuan, and Y. Yang, "Optimal strategies of quantum metrology with a strict hierarchy," *Phys. Rev. Lett.* **130**, 070803 (2023).
- ⁴⁶⁷S.-Y. Bai and J.-H. An, "Floquet engineering to overcome no-go theorem of noisy quantum metrology," *Phys. Rev. Lett.* **131**, 050801 (2023).
- ⁴⁶⁸R. Demkowicz-Dobroński, J. Czajkowski, and P. Sekatski, "Adaptive quantum metrology under general Markovian noise," *Phys. Rev. X* **7**, 041009 (2017).
- ⁴⁶⁹M. Valeri, V. Cimini, S. Piacentini, F. Ceccarelli, E. Polino, F. Hoch, G. Bizzarri, G. Corrielli, N. Spagnolo, R. Osellame, and F. Sciarrino, "Experimental multiparameter quantum metrology in adaptive regime," *Phys. Rev. Res.* **5**, 013138 (2023).
- ⁴⁷⁰M. A. C. Rossi, F. Albarelli, D. Tamascelli, and M. G. Genoni, "Noisy quantum metrology enhanced by continuous nondemolition measurement," *Phys. Rev. Lett.* **125**, 200505 (2020).
- ⁴⁷¹Q.-S. Tan, Y. Huang, X. Yin, L.-M. Kuang, and X. Wang, "Enhancement of parameter-estimation precision in noisy systems by dynamical decoupling pulses," *Phys. Rev. A* **87**, 032102 (2013).
- ⁴⁷²Y. Dong, X.-D. Chen, G.-C. Guo, and F.-W. Sun, "Reviving the precision of multiple entangled probes in an open system by simple π -pulse sequences," *Phys. Rev. A* **94**, 052322 (2016).
- ⁴⁷³H. Zhou, J. Choi, S. Choi, R. Landig, A. M. Douglas, J. Isoya, F. Jelezko, S. Onoda, H. Sumiya, P. Cappellaro, H. S. Knowles, H. Park, and M. D. Lukin, "Quantum metrology with strongly interacting spin systems," *Phys. Rev. X* **10**, 031003 (2020).
- ⁴⁷⁴K. Bai, Z. Peng, H.-G. Luo, and J.-H. An, "Retrieving ideal precision in noisy quantum optical metrology," *Phys. Rev. Lett.* **123**, 040402 (2019).
- ⁴⁷⁵W. J. Huggins, S. McArdle, T. E. O'Brien, J. Lee, N. C. Rubin, S. Boixo, K. B. Whaley, R. Babbush, and J. R. McClean, "Virtual distillation for quantum error mitigation," *Phys. Rev. X* **11**, 041036 (2021).
- ⁴⁷⁶K. Yamamoto, S. Endo, H. Hakoshima, Y. Matsuzaki, and Y. Tokunaga, "Error-mitigated quantum metrology via virtual purification," *Phys. Rev. Lett.* **129**, 250503 (2022).
- ⁴⁷⁷Q. Yao, J. Zhang, X.-F. Yi, L. You, and W. Zhang, "Uniaxial dynamical decoupling for an open quantum system," *Phys. Rev. Lett.* **122**, 010408 (2019).
- ⁴⁷⁸J. Liu and H. Yuan, "Quantum parameter estimation with optimal control," *Phys. Rev. A* **96**, 012117 (2017).
- ⁴⁷⁹G. Wang, A. R. Barr, H. Tang, M. Chen, C. Li, H. Xu, A. Stasiuk, J. Li, and P. Cappellaro, "Characterizing temperature and strain variations with qubit ensembles for their robust coherence protection," *Phys. Rev. Lett.* **131**, 043602 (2023).
- ⁴⁸⁰C. Brif, B. P. Ruzic, and G. W. Biedermann, "Characterization of errors in interferometry with entangled atoms," *PRX Quantum* **1**, 010306 (2020).
- ⁴⁸¹M. Shuker, J. W. Pollock, R. Boudot, V. I. Yudin, A. V. Taichenachev, J. Kitching, and E. A. Donley, "Ramsey spectroscopy with displaced frequency jumps," *Phys. Rev. Lett.* **122**, 113601 (2019).
- ⁴⁸²C. Sanner, N. Huntemann, R. Lange, C. Tamm, and E. Peik, "Autobalanced Ramsey spectroscopy," *Phys. Rev. Lett.* **120**, 053602 (2018).
- ⁴⁸³J. Gray, L. Banchi, A. Bayat, and S. Bose, "Machine-learning-assisted many-body entanglement measurement," *Phys. Rev. Lett.* **121**, 150503 (2018).
- ⁴⁸⁴V. Cimini, M. Valeri, E. Polino, S. Piacentini, F. Ceccarelli, G. Corrielli, N. Spagnolo, R. Osellame, and F. Sciarrino, "Deep reinforcement learning for quantum multiparameter estimation," *Adv. Photonics* **5**, 016005 (2023).
- ⁴⁸⁵Y. Qiu, M. Zhuang, J. Huang, and C. Lee, "Efficient and robust entanglement generation with deep reinforcement learning for quantum metrology," *New J. Phys.* **24**, 083011 (2022).
- ⁴⁸⁶R. Kaubruegger, P. Silvi, C. Kokail, R. van Bijnen, A. M. Rey, J. Ye, A. M. Kaufman, and P. Zoller, "Variational spin-squeezing algorithms on programmable quantum sensors," *Phys. Rev. Lett.* **123**, 260505 (2019).
- ⁴⁸⁷J. Li, X. Yang, X. Peng, and C.-P. Sun, "Hybrid quantum-classical approach to quantum optimal control," *Phys. Rev. Lett.* **118**, 150503 (2017).
- ⁴⁸⁸C. Marciak, T. Feldker, I. Pogorelov, R. Kaubruegger, D. Vasilyev, R. Bijnen, P. Schindler, P. Zoller, R. Blatt, and T. Monz, "Optimal metrology with programmable quantum sensors," *Nature* **603**, 604–609 (2022).
- ⁴⁸⁹R. Kaubruegger, A. Shankar, D. V. Vasilyev, and P. Zoller, "Optimal and variational multiparameter quantum metrology and vector-field sensing," *PRX Quantum* **4**, 020333 (2023).
- ⁴⁹⁰M. Valeri, E. Polino, D. Poderini, I. Gianani, G. Corrielli, A. Crespi, R. Osellame, N. Spagnolo, and F. Sciarrino, "Experimental adaptive Bayesian

- estimation of multiple phases with limited data," *npj Quantum Inf.* **6**, 92 (2020).
- ⁴⁹¹Y. Qiu, M. Zhuang, J. Huang, and C. Lee, "Efficient Bayesian phase estimation via entropy-based sampling," *Quantum Sci. Technol.* **7**, 035022 (2022).
- ⁴⁹²V. Gebhart, R. Santagati, A. A. Gentile, E. Gauger, D. Craig, N. Ares, L. Banchi, F. Marquardt, L. Pezzè, and C. Bonato, "Learning quantum systems," *Nat. Rev. Phys.* **5**, 141 (2023).
- ⁴⁹³F. Belliardo, V. Cimini, E. Polino, F. Hoch, B. Piccirillo, N. Spagnolo, V. Giovannetti, and F. Sciarrino, "Optimizing quantum-enhanced Bayesian multiparameter estimation of phase and noise in practical sensors," *Phys. Rev. Res.* **6**, 023201 (2024).
- ⁴⁹⁴J. Huang, M. Zhuang, J. Zhou, Y. Shen, and C. Lee, "Quantum metrology assisted by machine learning," *Adv. Quantum Technol.* **2300329**, 1–29 (2024).
- ⁴⁹⁵I. Frerot, M. Fadel, and M. Lewenstein, "Probing quantum correlations in many-body systems: A review of scalable methods," *Rep. Prog. Phys.* **86**, 114001 (2023).
- ⁴⁹⁶B. Yadin, M. Fadel, and M. Gessner, "Metrological complementarity reveals the Einstein–Podolsky–Rosen paradox," *Nat. Commun.* **12**, 2410 (2021).
- ⁴⁹⁷J. Guo, F.-X. Sun, D. Zhu, M. Gessner, Q. He, and M. Fadel, "Detecting Einstein–Podolsky–Rosen steering in non-Gaussian spin states from conditional spin-squeezing parameters," *Phys. Rev. A* **108**, 012435 (2023).
- ⁴⁹⁸F. Fröwis, M. Fadel, P. Treutlein, N. Gisin, and N. Brunner, "Does large quantum Fisher information imply Bell correlations?," *Phys. Rev. A* **99**, 040101 (2019).
- ⁴⁹⁹J. Guo, J. Tura, Q. He, and M. Fadel, "Detecting Bell correlations in multipartite non-Gaussian spin states," *Phys. Rev. Lett.* **131**, 070201 (2023).
- ⁵⁰⁰M. Fadel, T. Zibold, B. Décamps, and P. Treutlein, "Spatial entanglement patterns and Einstein–Podolsky–Rosen steering in Bose–Einstein condensates," *Science* **360**, 409–413 (2018).
- ⁵⁰¹P. Kunkel, M. Prüfer, H. Strobel, D. Linnemann, A. Frölian, T. Gasenzer, M. Gärttner, and M. K. Oberthaler, "Spatially distributed multipartite entanglement enables EPR steering of atomic clouds," *Science* **360**, 413–416 (2018).
- ⁵⁰²K. Lange, J. Peise, B. Lücke, I. Kruse, G. Vitagliano, I. Apellaniz, M. Kleinmann, G. Tóth, and C. Klempert, "Entanglement between two spatially separated atomic modes," *Science* **360**, 416–418 (2018).
- ⁵⁰³Y. Jing, M. Fadel, V. Ivannikov, and T. Byrnes, "Split spin-squeezed Bose–Einstein condensates," *New J. Phys.* **21**, 093038 (2019).
- ⁵⁰⁴G. Vitagliano, M. Fadel, I. Apellaniz, M. Kleinmann, B. Lücke, C. Klempert, and G. Tóth, "Number-phase uncertainty relations and bipartite entanglement detection in spin ensembles," *Quantum* **7**, 914 (2023).
- ⁵⁰⁵M. Fadel and M. Gessner, "Relating spin squeezing to multipartite entanglement criteria for particles and modes," *Phys. Rev. A* **102**, 012412 (2020).
- ⁵⁰⁶B. K. Malia, Y. Wu, J. Martinez-Rincón, and M. A. Kasevich, "Distributed quantum sensing with mode-entangled spin-squeezed atomic states," *Nature* **612**, 661–665 (2022).
- ⁵⁰⁷M. Fadel, B. Yadin, Y. Mao, T. Byrnes, and M. Gessner, "Multiparameter quantum metrology and mode entanglement with spatially split nonclassical spin ensembles," *New J. Phys.* **25**, 073006 (2023).
- ⁵⁰⁸I. Frerot and T. Roscilde, "Quantum critical metrology," *Phys. Rev. Lett.* **121**, 020402 (2018).
- ⁵⁰⁹V. Montenegro, U. Mishra, and A. Bayat, "Global sensing and its impact for quantum many-body probes with criticality," *Phys. Rev. Lett.* **126**, 205001 (2021).
- ⁵¹⁰P. Zanardi, M. G. A. Paris, and L. Campos Venuti, "Quantum criticality as a resource for quantum estimation," *Phys. Rev. A* **78**, 042105 (2008).
- ⁵¹¹K. Petrovnik, J. Wang, M. Perelstein, P. Hakonen, and G. S. Paraoanu, "Microwave photon detection at parametric criticality," *PRX Quantum* **5**, 020342 (2024).
- ⁵¹²C. Invernizzi, M. Korbman, L. Campos Venuti, and M. G. A. Paris, "Optimal quantum estimation in spin systems at criticality," *Phys. Rev. A* **78**, 042106 (2008).
- ⁵¹³R. Liu, Y. Chen, M. Jiang, X. Yang, Z. Wu, Y. Li, H. Yuan, X. Peng, and J. Du, "Experimental critical quantum metrology with the Heisenberg scaling," *npj Quantum Inf.* **7**, 170 (2021).
- ⁵¹⁴M. Raghunandan, J. Wrachtrup, and H. Weimer, "High-density quantum sensing with dissipative first order transitions," *Phys. Rev. Lett.* **120**, 150501 (2018).
- ⁵¹⁵K. Gietka, "Squeezing by critical speeding up: Applications in quantum metrology," *Phys. Rev. A* **105**, 042620 (2022).
- ⁵¹⁶W. Chen, S. K. Ozdemir, G. Zhao, J. Wiersig, and L. Yang, "Exceptional points enhance sensing in an optical microcavity," *Nature* **548**, 192–196 (2017).
- ⁵¹⁷Y.-H. Lai, Y.-K. Lu, M.-G. Suh, Z. Yuan, and K. Vahala, "Observation of the exceptional-point-enhanced Sagnac effect," *Nature* **576**, 65–69 (2019).
- ⁵¹⁸H. Wang, Y.-H. Lai, Z. Yuan, M.-G. Suh, and K. Vahala, "Petermann-factor sensitivity limit near an exceptional point in a Brillouin ring laser gyroscope," *Nat. Commun.* **11**, 1610 (2020).
- ⁵¹⁹A. McDonald and A. A. Clerk, "Exponentially-enhanced quantum sensing with non-Hermitian lattice dynamics," *Nat. Commun.* **11**, 5382 (2020).
- ⁵²⁰J. Wiersig, "Prospects and fundamental limits in exceptional point-based sensing," *Nat. Commun.* **11**, 2454 (2020).
- ⁵²¹Y. Chu, Y. Liu, H. Liu, and J. Cai, "Quantum sensing with a single-qubit pseudo-Hermitian system," *Phys. Rev. Lett.* **124**, 020501 (2020).
- ⁵²²M. Zhang, W. Sweeney, C. W. Hsu, L. Yang, A. D. Stone, and L. Jiang, "Quantum noise theory of exceptional point amplifying sensors," *Phys. Rev. Lett.* **123**, 180501 (2019).
- ⁵²³J. C. Budich and E. J. Bergholtz, "Non-Hermitian topological sensors," *Phys. Rev. Lett.* **125**, 180403 (2020).
- ⁵²⁴L. Bao, B. Qi, D. Dong, and F. Nori, "Fundamental limits for reciprocal and nonreciprocal non-Hermitian quantum sensing," *Phys. Rev. A* **103**, 042418 (2021).
- ⁵²⁵X. Ou, J. Huang, and C. Lee, "Quantum exceptional points of non-Hermitian Hamiltonian and Liouvillian in dissipative quantum Rabi model," *Chin. Phys. B* **30**, 110309 (2021).
- ⁵²⁶A. Li, H. Wei, M. Cotrufo, W. Chen, S. Mann, X. Ni, B. Xu, J. Chen, J. Wang, S. Fan, C.-W. Qiu, A. Al, and L. Chen, "Exceptional points and non-Hermitian photonics at the nanoscale," *Nat. Nanotechnol.* **18**, 706–720 (2023).
- ⁵²⁷T. B. Magdalena Szczukulska and A. Datta, "Multi-parameter quantum metrology," *Adv. Phys. X* **1**, 621–639 (2016).
- ⁵²⁸F. Albarelli, M. Barbieri, M. Genoni, and I. Gianani, "A perspective on multi-parameter quantum metrology: From theoretical tools to applications in quantum imaging," *Phys. Lett. A* **384**, 126311 (2020).
- ⁵²⁹J. Liu and H. Yuan, "Control-enhanced multiparameter quantum estimation," *Phys. Rev. A* **96**, 042114 (2017).
- ⁵³⁰X.-M. Lu and X. Wang, "Incorporating Heisenberg's uncertainty principle into quantum multiparameter estimation," *Phys. Rev. Lett.* **126**, 120503 (2021).
- ⁵³¹L. Pezzè, M. A. Ciappini, N. Spagnolo, P. C. Humphreys, A. Datta, I. A. Walmsley, M. Barbieri, F. Sciarrino, and A. Smerzi, "Optimal measurements for simultaneous quantum estimation of multiple phases," *Phys. Rev. Lett.* **119**, 130504 (2017).
- ⁵³²J. Liu, H. Yuan, X.-M. Lu, and X. Wang, "Quantum Fisher information matrix and multiparameter estimation," *J. Phys. A* **53**, 023001 (2019).
- ⁵³³M. Gessner, L. Pezzè, and A. Smerzi, "Sensitivity bounds for multiparameter quantum metrology," *Phys. Rev. Lett.* **121**, 130503 (2018).
- ⁵³⁴M. Gessner, A. Smerzi, and L. Pezzè, "Multiparameter squeezing for optimal quantum enhancements in sensor networks," *Nat. Commun.* **11**, 3817 (2020).
- ⁵³⁵Z. Ren, W. Li, A. Smerzi, and M. Gessner, "Metrological detection of multipartite entanglement from young diagrams," *Phys. Rev. Lett.* **126**, 080502 (2021).
- ⁵³⁶L. Pezzè, "Entanglement-enhanced sensor networks," *Nat. Photonics* **15**, 74–76 (2021).
- ⁵³⁷P. Wang, Z. Yuan, P. Huang, X. Rong, M. Wang, X. Xu, C. Duan, C. Ju, F. Shi, and J. Du, "High-resolution vector microwave magnetometry based on solid-state spins in diamond," *Nat. Commun.* **6**, 6631 (2015).
- ⁵³⁸G. Wang, Y.-X. Liu, Y. Zhu, and P. Cappellaro, "Nanoscale vector ac magnetometry with a single nitrogen-vacancy center in diamond," *Nano Lett.* **21**, 5143 (2021).
- ⁵³⁹E. Roccia, V. Cimini, M. Sbroscia, I. Gianani, L. Ruggiero, L. Mancino, M. G. Genoni, M. A. Ricci, and M. Barbieri, "Multiparameter approach to quantum phase estimation with limited visibility," *Optica* **5**, 1171–1176 (2018).
- ⁵⁴⁰M. D. Vidrighin, G. Donati, M. G. Genoni, X.-M. Jin, W. S. Kolthammer, M. Kim, M. Barbieri, and I. A. Walmsley, "Joint estimation of phase and phase diffusion for quantum metrology," *Nat. Commun.* **5**, 3532 (2014).

- ⁵⁴¹M. Zhuang, J. Huang, and C. Lee, "Multiparameter estimation via an ensemble of spinor atoms," *Phys. Rev. A* **98**, 033603 (2018).
- ⁵⁴²J. Liu, X.-M. Lu, Z. Sun, and X. Wang, "Quantum multiparameter metrology with generalized entangled coherent state," *J. Phys. A* **49**, 115302 (2016).
- ⁵⁴³H. Xu, L. Wang, H. Yuan, and X. Wang, "Generalizable control for multiparameter quantum metrology," *Phys. Rev. A* **103**, 042615 (2021).
- ⁵⁴⁴R. Nichols, P. Liuzzo-Scorpo, P. A. Knott, and G. Adesso, "Multiparameter Gaussian quantum metrology," *Phys. Rev. A* **98**, 012114 (2018).
- ⁵⁴⁵J. S. Sidhu, Y. Ouyang, E. T. Campbell, and P. Kok, "Tight bounds on the simultaneous estimation of incompatible parameters," *Phys. Rev. X* **11**, 011028 (2021).
- ⁵⁴⁶M. Hayashi and Y. Ouyang, "Tight Cramér–Rao type bounds for multiparameter quantum metrology through conic programming," *Quantum* **7**, 1094 (2023).
- ⁵⁴⁷M. Hayashi and Y. Ouyang, "Finding the optimal probe state for multiparameter quantum metrology using conic programming," *arXiv:2401.05886* (2024).